31

ISOTOPIC, GEOCHEMICAL, AND GEOCHRONOLOGICAL CONSTRAINTS ON THE ORIGIN AND EVOLUTION OF CENOZOIC VOLCANISM, BAIKAL RIFT ZONE, SIBERIA

by

NANCY RUTH HARRIS

B.A. Geology, Rice University (1992)

Submitted to the Department of
Earth, Atmospheric, and Planetary Sciences
in Partial Fulfillment of the Requirements for the Degree of

DOCTOR OF PHILOSOPHY

at the MASSACHUSETTS INSTITUTE OF TECHNOLOGY

September, 1998

Signature of Author_____
Department of Earth, Atmospheric, and Planetary Sciences

Certified by_____
Samuel A. Bowring
Thesis Supervisor

Accepted by_____
Ronald Prinn
Department Head

ISOTOPIC, GEOCHEMICAL, AND GEOCHRONOLOGICAL CONSTRAINTS ON THE ORIGIN AND EVOLUTION OF CENOZOIC VOLCANISM, BAIKAL RIFT ZONE, SIBERIA

by

NANCY RUTH HARRIS

Submitted to the Department of Earth, Atmospheric, and Planetary Sciences at the Massachusetts Institute of Technology in partial fulfillment of the requirements for the degree of Doctor of Philosophy in Geology

ABSTRACT

The Cenozoic Baikal Rift Zone, one of the world's major continental rifts, is expressed as an approximately 1800 km-long southwest-northeast oriented system situated along a suture between the Archean Siberian craton and younger Paleozoic fold belts. Oligocene to Recent age volcanic rocks and associated mantle xenoliths are distributed in three major regions of the rift zone: the Udokan volcanic field in the northeast, the Vitim volcanic field ~200 km southeast of Lake Baikal, and a broad zone of volcanism to the southwest of Lake Baikal. This large-scale study investigates the geochemical evolution of the Baikal Rift Zone volcanism using major element, trace element, and isotopic (Sr, Nd, and Pb) geochemistry, as well as $^{40}Ar/^{39}Ar$ geochronology. In addition, a detailed isotopic study of megacrysts provides insight into the relationship between megacrysts and host lavas and the nature of the lithospheric mantle.

Results of this study suggest that the source region for Baikal Rift Zone volcanic rocks is remarkably homogeneous considering the large region and time span over which these rocks erupted, and that crustal contamination has not been a significant controlling factor. The Tunka Basin, Oka Plateau, and Tuva volcanic fields in the western Baikal Rift Zone, and the Vitim volcanic field southeast of Lake Baikal, have a fairly restricted compositional range from basaltic andesite, alkaline basalt and hawaiite, to basanite and mugearite. In the Udokan volcanic field in the northeast, a more evolved series of rocks ranging to trachytic compositions erupted across the suture between the Archean craton and Paleozoic fold belts. Major and trace elements indicate that fractional crystallization of pyroxene, olivine, and plagioclase produced the observed range in compositions.

The trace element and isotopic compositions of Baikal Rift Zone volcanic rocks are comparable to those observed in ocean island basalts. The Sr, Nd, and Pb isotope systematics can best be explained by mixing between the end-member mantle components DMM (typical of the depleted source of MORB mantle) and EMI (enriched mantle type 1). Megacrysts of clinopyroxene, amphibole, garnet, biotite, and anorthoclase mirror the isotope systematics of the host volcanic rocks, and suggest that the megacrysts were

derived from a melt closely related to their host rocks. Furthermore, megacrysts of clinopyroxene, as well as Cr-diopside from spinel lherzolites, have an unradiogenic Pb isotopic composition that may be representative of the EMI-like composition of the subcontinental lithospheric mantle.

Thesis supervisor: Samuel A. Bowring, Professor of Geology

Dedicated to my grandmothers:

ALICE NANCY HARRIS *and* RUTH ELIZABETH BONGARD

who are strong women and loving role models.

I am proud to carry their names.

ACKNOWLEDGMENTS

My geology career began my second semester at Rice University after I decided I didn't want to be a chemical engineer, and registered for a Historical Geology class (taught by Prof. Peter Vail). This was perhaps an unconventional introductory geology class since we learned how to correlate well logs and identify sequence boundaries before really knowing how to identify rocks! Nevertheless, we went on a field trip, and I was immediately hooked. Geology was perhaps a logical choice for me because of my exposure to so many wonderful and exotic places during my childhood growing up all over the world (8 different countries and 5 different U.S. states by the time I graduated from high school in Cairo, Egypt). However, I am sure that my parents would not have predicted my career choice. My mother loves to tell the story of how, when we lived on Réunion Island, they took me to see lava from a volcano flow down the mountain and into the Indian Ocean, and I told them it was "no big deal" !!

I was very fortunate to have stumbled upon the Department of Geology and Geophysics at Rice University: the small class sizes, interaction with graduate students, and many field trips and scholarships nurtured my interest in geology. I am especially grateful to Professor Jinny Sisson for inviting me to go the Chugach Mountains in southeastern Alaska in 1991, and generally taking me under her wing. Professor Jim Wright gave me my introduction to isotope geochemistry and igneous petrology, and actually let me run his mass spectrometer and work in his clean lab.

I benefitted from several non-academic geology experiences. In the summer of 1990, I worked as an intern for BHP-Utah Minerals in Côte d'Ivoire, West Africa. This was a very exciting experience since we were drilling exploratory holes looking for gold. I learned an incredible amount just by being around Howard Golden and John Mortimer (and asking lots of questions). After graduating from Rice, I got an internship at Amoco in Houston, and worked as a petroleum geologist for half a year before coming to M.I.T. Many thanks to Charlie Brewster for making that a fun experience.

I am grateful to my advisor, Sam Bowring, for providing me the opportunity to come to M.I.T. and work on the Baikal Rift project. I am appreciative of Sam's broad range of interests and knowledge about earth science. I am glad he encouraged me to interview with petroleum companies! Thanks to my thesis committee (Tim Grove, Todd Housh, Wicki Royden) for their insightful questions.

I wish to express my sincere thanks to Sergei Rasskazov for inviting me to the field in Siberia and sharing his extensive knowledge of the Baikal Rift Zone. Thanks also to Alexei Ivanov for help in the field. I am also grateful to Igor Ashchepkov for inviting me to the Vitim Plateau.

During my years here at M.I.T., I have benefitted from interaction with many, many people. I have had a number of officemates over the years (including Martha House, Meg Coleman, Mark Schmitz, and Simon Brocklehurst), and I offer my humble apologies to them for the disaster area surrounding my desk. I was very grateful for the arrival of Mark Schmitz several years ago - his enthusiasm for geology and hard work ethic inspired me, and we have had many good discussions about our research projects

and the lab. Special thanks to Anke Friedrich for working the same odd hours as me, especially in our marathon to finish, as well as being a good friend here. Thanks to the other graduate students I've served time at M.I.T. with: Audrey Huerta, Dave Hawkins, Jim van Orman, C.J. Northrup, Steve Parman, Alberto Saal, Kirsten Nicolaysen, Ken Koga, Deb Hassler, and many others.

A special thanks to Drew Coleman for teaching me the fundamentals of whole-rock column chemistry and - most importantly - how to run the mass spectrometer. I am also grateful that he went with me to Siberia in 1993. I learned a great deal about mass spectrometry from Bill Olszewski, who patiently answered my many questions, even though I'm sure I asked some of them more than once. Mark Martin was a welcome addition to the lab family last year. Kathy Davidek (Keefe) is an incredibly important part of the isotope lab, and has provided much guidance, support, and friendship over the years - thank you.

My dear friends Tonya and Drew St. John have always been there for me, and recently made me very happy by giving me a godson - Tullie. I also want to express my thanks to Brian Clifford for the good times and support during my first 4 years at M.I.T. Finally, I would never have been able to finish without the love and encouragement of my parents and my sister Lora. Thank you for believing in me.

TABLE OF CONTENTS

CHAPTER 1

INTRODUCTION AND OVERVIEW

INTRODUCTION AND OVERVIEW OF THE DISSERTATION

The Baikal Rift Zone (BRZ) in southeastern Siberia (Fig. 1.1) is one of the world's major active continental rifts, yet remains relatively poorly studied and understood in comparison to other major continental rifts. The BRZ is expressed as an approximately 1800 km-long southwest-northeast oriented system of rift valleys and faults situated along a suture between the Archean Siberian platform and younger Paleozoic fold belts, and associated with a broad area of domal uplift. Alkaline volcanic rocks of Oligocene to Recent age are associated with rifting and distributed in three major regions of the rift.

This introductory chapter (Chapter 1) will review major features of the BRZ, including: regional geology, faulting, rift depressions and sediments, seismicity, heat flow, geophysical data on deep structure of the rift, and volcanism. Various theories on the formation of the Baikal Rift, in particular the issue of an "active" versus "passive" origin, will be presented and discussed. In addition, the concept of mantle "components" (as defined by Hart and others), theoretically and empirically defined geochemical end-members thought to be present in the earth's mantle, will be discussed. This broad background information will provide a context for the main focus of the dissertation presented in the remaining chapters: the origin and temporal evolution of Baikal Rift

volcanic rocks and their inclusions, and their implications for continental magmatism and the nature of the subcontinental lithosphere and asthenosphere.

A major contribution of the work represented by this thesis is the development of a large set of geochemical data, especially isotopic data, for Cenozoic volcanic rocks of the BRZ. Isotopic data for this large and important rift has until now been almost absent. Chapters 2 - 4 each focus on one of the major regions of volcanism associated with the BRZ. Chapter 2 focuses on the large region of volcanism in the western BRZ, including the Tunka, Oka Plateau, and Tuva volcanic fields. A look at the temporal evolution of the geochemistry of this region is possible based on new $^{40}Ar/^{39}Ar$ geochronologic data, combined with age data from the literature. Chapter 3 focuses on the Udokan volcanic field, which partially overlaps the Archean craton, and therefore provides the most direct evidence for correlating isotopic variation in the lavas with variation in the lithosphere. Chapter 4 deals with the Vitim volcanic field, which is interesting due to its position farther away from the main axis of rifting (Lake Baikal), greater crustal thickness, and also perhaps deeper source of lavas.

A remarkable variety and abundance of megacrysts occurs in BRZ volcanic rocks. Chapter 5 presents a combined Sr, Nd, and Pb isotopic study of BRZ megacrysts, as well as pyroxenes separated from several lherzolite xenoliths. Megacrysts of clinopyroxene, anorthoclase, amphibole, garnet, and biotite are all found to have a range in isotopic compositions very similar to the lavas in which they are included, supporting their formation from a melt that is parental to the lava they erupted in. However, subtle differences in the isotopic compositions of the different minerals may indicate they

precipitated from the parental melt at slightly different times. Also, the clinopyroxene megacrysts extend to slightly less radiogenic Sr (lower $^{87}Sr/^{86}Sr$) and more radiogenic Nd (higher ε_{Nd}) than their host lavas, suggesting that the host lava may have interacted with the crust during ascent, while the megacrysts did not. Chapter 6 is a very brief summary of the main results of this dissertation.

REGIONAL GEOLOGIC BACKGROUND

The basement rocks of the BRZ are of a complex composition and structure formed through Precambrian and Phanerozoic tectonic, magmatic and metamorphic cycles (Delvaux et al., 1995). The oldest rocks of the BRZ are the Archean/lower Proterozoic crystalline basement of the Aldan Shield/Siberian Platform, occurring mainly to the west and north of Lake Baikal, but also east of the Lake. Upper Proterozoic rocks unconformably overlie lower Proterozoic rocks, and are weakly metamorphosed clastics and calcsilicates (Logatchev, 1993). They outcrop south of the Main Sayan Fault and shear zone, along the south shore of the Lake, in northern Mongolia, and also on the edges of the Siberian platform in the west and north (Logatchev and Zorin, 1992).

During the Silurian-Devonian, Precambrian "micro-continents" (Tuva-Mongol, Khamar-Daban, and Barguzin-Vitim) collided with the Siberian craton. This resulted in the accretion of the Sayan-Baikal fold belt of northwest-verging thrust sheets involving early Paleozoic sediments and volcanic sequences (Logatchev and Zorin, 1992). Huge

early and middle Paleozoic batholiths of the folded zone form the mountain ranges east of Lake Baikal, and granitoid magmatism makes up half of the rock mass of the BRZ.

The Baikal Rift region was relatively quiet during the Mesozoic. Jurassic sediments (shale and fine-grained clastics) were deposited on Cambrian rocks near the mouth of the Angara River and in a belt stretching northwest away from the lake parallel to the Main Sayan fault. There are isolated pockets of Cretaceous and Jurassic sediments preserved on rift basin flanks south of the Main Sayan fault in the southern part of the folded zone (Logatchev, 1993).

SAYAN-BAIKAL DOMAL UPLIFT

Most of the BRZ system of faults and depressions occurs within the Sayan-Baikal domal uplift, a broad area of mountain ranges and high plateaus surrounding rift valleys containing Paleogene, Neogene, and Quaternary sediments (Logatchev, 1993). The uplift is defined by the 1500 m elevation contour line of the Cretaceous-Paleogene planation surface, characterized by a kaolinite-laterite horizon (Delvaux et al., 1995). The domal uplift area has three culminations (high points) separated by the saddle-shaped depressions of the Selenga River delta and the Vitim plateau (Logatchev and Zorin, 1987). The saddle shape results from greater vertical uplift on the rift flanks than in the South Baikal area: 3000 - 3500 m elevation to the southwest and 2600 - 3000 m to the northeast (Logatchev, 1993). Lake Khubsugul in the southwest is almost 1200 m higher than Lake Baikal (Florensov, 1969).

BAIKAL RIFT BASINS AND FAULTS

The Baikal Rift Zone comprises 13 major rift basins. Lake Baikal itself, the largest (636 km long, 40 - 50 km wide) and deepest (1637 m deep) freshwater lake in the world, containing 20% of the world's fresh water (23,000 km^3), is formed by the two en-echelon depressions of North and South Lake Baikal (Logatchev, 1993). The average water depth in Lake Baikal is 730 m, and the surface of the Lake is 450 m above sea level. South Baikal basin, the deepest, is ~400 km long and 70 - 75 km wide (Logatchev, 1993). Based on multichannel seismic studies (Hutchinson et al., 1992), the South Baikal basin is believed to be filled with 7500 - 8000 m of sediments. It is separated from the North Baikal basin (390 km long) by the diagonal submarine Academician Ridge (Logatchev, 1993). The South Baikal Basin is also divided by bottom formed by deposition from rivers on opposing sides of Lake Baikal. South Baikal Basin can therefore be subdivided into a southern and central basin, but since the division is buried by sediments, Lake Baikal is still often described as only being two basins (Logatchev, 1993).

Most BRZ basins are asymmetric, including North and South Baikal, with higher and steeper northern flanks than southern flanks. In general, the north/northwestern margins are steep, basin-bounding faults which probably shallow out at depth, while the southern/southeastern margins are shallower smooth bends of basement rocks with some minor normal faults (Logatchev and Zorin, 1992). The north/northwestern fault scarps reach amplitudes of 1500 - 2000 m above the basin. The Primorye Fault runs along the northwestern boundary of Lake Baikal. Initiated in the early Proterozoic, pre-Cenozoic it was a sinistral oblique-slip thrust, but is now a dextral oblique-slip normal fault (Sherman,

1978). Vertical throw on this fault is estimated at more than 6 km. Most other BRZ faults have vertical throws of less than 1000 m (Sherman, 1978).

The other major Baikal depressions extend to the northeast and southwest of Lake Baikal in an intricate branching chain of sub-parallel basins separated by long, high ridges and mountains (Logatchev, 1993; Logatchev and Zorin, 1987). The direction and location of rift development was strongly influenced by the significant differences in lithospheric and deep-seated structures between the Archean platform and the Sayan-Baikal mobile belt (Logatchev and Zorin, 1992; Zamarayev and Ruzhich, 1978). South Baikal is thought to be the earliest rift depression based on the age of sediments found during drilling (at least old as Oligocene, perhaps Eocene?) (Logatchev and Zorin, 1987). The other rift valleys propagate away from it in both directions, but there is no evidence that rift development in both directions progressed uniformly or synchronously (Logatchev and Florensov, 1978). Narrow Pleistocene-Holocene fault trenches located alongside some large depressions could be the precursors of future basins (Florensov, 1969).

At the western end of Lake Baikal, the transverse Main Sayan fault, the largest dislocation in the BRZ, extends northwest for ~1000 km. Like many fault structures in the BRZ, it originated in the Late Archean to Early Proterozoic (Sherman, 1978). Pre-Cenozoic it was a dextral oblique-slip thrust, but in the Cenozoic has become a sinistral oblique-slip normal fault downthrown to the northeast (Sherman, 1978). Rifting is limited to the southwest by the east-west Bolnai Fault, a sinistral strike-slip shear zone separating the southwest culmination of the BRZ from the north-south rift structures of northern Mongolia (Logatchev, 1993). In the southwest, rift structures are more

dispersed, and the major rift basins of Khubsugul, Darkhat, and Busingol are north-south oriented. The Tunka Fault approaches the Main Sayan fault from the west and is a major influence on the location of depressions, distribution of sediments and development of the rift to the southwest. It is believed to have originated in the Riphean and is currently a series of sub-parallel en-echelon structures each 25 - 30 km long and extending over 200 km overall (Logatchev, 1993). Like the Main Sayan fault, it was dextral oblique-slip prior to the Cenozoic and is now sinistral oblique-slip normal (Sherman, 1978). The Tunka basin is an east-west-oriented graben bounded by the Tunka fault on the south and cut off by the Main Sayan Fault on the northeast (Sherman, 1978).

The Barguzin, Tsipa, Baunt, Upper Angara, and Muya rift basins extend the rift northeast away from North Baikal basin. The largest of these, the Barguzin basin, is ~200 km long and 30 - 40 km wide (Logatchev and Zorin, 1992). The Chara and Tokka basins are the last rift depressions to the northeast and actually occur within the Aldan Shield, but rift propagation appears to die out further northeastward within the strong cratonic lithosphere (Logatchev and Zorin, 1992).

Most Baikal rift depressions contain 1500 - 2500 m of sediments, with a maximum thickness of around 8000 - 8500 m in South Baikal. North Baikal basin holds ~4000 m of sediments (Logatchev and Zorin, 1992). The southwestern Khubsugul, Darkhat and Busingol basins contain only ~600 m of sediments, while the Tunka Basin contains 2500 - 3000 m of Cenozoic sediments (Logatchev and Zorin, 1992). Cenozoic sediments filling rift depressions are fluvial, proluvial, lacustrine, palustrine, glacial, fluvioglacial, and eolian in origin, corresponding to subtropical (Paleocene - Eocene) to

moderately warm (Oligocene - Miocene) climate conditions (Logatchev, Episodes; Logatchev, 1993).

Some researchers (e.g., Logatchev and Zorin, 1987, 1992; Moore et al., 1997) have proposed a "two-stage" development of the rift based on the age and type of sediment fill. The "first-stage" sediments of Paleocene (?), Eocene, Oligocene, Miocene, and Lower Pliocene (?) age are predominantly fine-grained and make up a package 1.5 - 2 km thick (5 km in S. Baikal). They comprise sandstones, siltstones, and clays (fluvial, marsh, and lacustrine) (Logatchev, 1993). Because no coarse-grained marginal facies have been found, it has been suggested that perhaps the sequence was once wider in aerial extent and was uplifted and eroded prior to deposition of the "second-stage" sediments (Logatchev, 1993). The "second-stage" sediments are Pliocene to Holocene and 1000 - 1200 m thick. They also comprise fluvial/lacustrine sediments, but coarser-grained sediments such as gravels and conglomerates prevail around the basin margins (Logatchev, 1993). This suggests increased vertical movements during the "second-stage" of rifting (Logatchev and Zorin, 1987). Based on these two "stages" of rifting and estimates of the amount of sediments deposited for each stage, Logatchev and Zorin (1987) calculated a subsidence rate of .07 - .15 mm/yr during the first stage, and .66 mm/yr during the second stage, and therefore termed the early stage "slow rifting" and the second stage "fast rifting".

SEISMICITY IN THE BRZ

The BRZ is an active zone of seismicity, with thousands of small earthquakes and a significant number of major earthquakes recorded each year (Logatchev, 1993). Most of

these earthquakes can be related to structures within the rift and extending into northern Mongolia. The majority of earthquakes are associated with rift-trend fractures, but some foci are associated with transverse zones (Golonetsky and Misharina, 1978).

In the region west of Lake Baikal, a seismically active zone along the Main Sayan Fault and its branches delineates the active area of Pribaikalye from the mostly aseismic Siberian platform (Solonenko, 1978). Belts of seismicity also extend to the northeast of Lake Baikal. The rift terminates in the Tokka depression, but east of the Chara graben, two embryonic depressions with arch uplifts are developing and high magnitude earthquakes (7.6 - 7) have occurred recently (Solonenko, 1978). Beyond the Sayan-Baikal area of domal uplift, a wide band of epicenters occurs across the Vitim Plateau.

BRZ HEAT FLOW

Heat flow in the BRZ is about 1.5 times that of surrounding regions, but is not uniform (Logatchev, 1993). Most measurements reported in the literature are from sites within Lake Baikal. The highest values are recorded in rift depressions and fault zones. In the northeast rift depressions of Chara, Muya, and Angara, the mean heat flow reported is 55 $\pm$17 mW m^{-2} (Lysak, 1987). Within the Lake Baikal depressions, the mean heat flow reported is 78 mW m^{-2}, but ranges from 15 to 300 mW m^{-2} (Lysak, 1987). In the central and deepest Lake Baikal depression and in the area of the Selenga River delta heat flow is less than 50 - 25 mW m^{-2}, the lower values as expected for regions of active sedimentation (Lysak, 1987). Local anomalous heat flows from 100 - 300 mW m^{-2} are associated with fault-related hydrothermal discharge (Lysak, 1987). On the southwest

flank of the BRZ heat flow reaches a high of 90 mW m^{-2} in the Tunka depression, which is also the only depression containing volcanic flows (Lysak, 1987). Regional heat flow outside the BRZ does not exceed 38 - 50 mW m^{-2} (Lysak, 1987).

BRZ VOLCANISM

Oligocene to Recent alkaline volcanic rocks are associated with Baikal rifting (Kiselev, 1987). However, they do not occur throughout the BRZ and are independent of rift valleys and faults. The total volume of volcanic rocks is less than 6000 km^3, several orders of magnitude less than other continental rift zones, such as the East African Rift (Logatchev, 1993).

Volcanism occurs in three main regions. Approximately 50% of the BRZ's volcanic rocks are found in the Sayan-Khamar-Daban-Northern Mongolia region west of Lake Baikal (Logatchev, 1993; Rasskazov, 1993). Many large and small lava sheets up to 500 - 600 m thick occur on highland plateaus and are modified by erosion (Kiselev, 1987). Rarer small cinder cones are found in the Oka Plateau, Tunka basin, Dzhida Basin, and Khamar-Daban (Kiselev, 1987). Volcanic rocks, in general, do not occur within rift depressions or along faults, but are located on the uplifted shoulders of rift valleys. The Tunka basin is the only exception, where basalts intercalated with sediments make up 20% of the basin fill (Kiselev, 1987; Kiselev and Popov, 1992).

The Udokan volcanic field partially overlaps the Archean Aldan Shield on the eastern end of the Baikal Rift. In the Miocene and Pliocene, fissure eruptions formed a 400 - 500 m thick lava plateau (Kiselev, 1987). By the Pleistocene, magmatism became

focused at Udokan in the form of central volcanoes erupted onto the eroded surface of the basalt plateau. The most recent known volcanic event in the Baikal Rift is a trachytic pyroclastic flow erupted in the Udokan field ~2,000 years ago (Kiselev, 1987).

The Vitim Plateau (3500 km^2) to the southeast of Lake Baikal actually occurs outside the boundaries of the Sayan-Baikal domal uplift (Kiselev, 1987). Sheets of lava also occur in Vitim, along with cinder cones, explosion craters and lava domes (Rasskazov, 1993; Kiselev, 1987; Rasskazov and Batyrmurzaev, 1985). The Vitim volcanic field is well-known for its many occurrences of upper mantle xenoliths, especially the rare garnet lherzolites (Ionov, 1993).

The largest volume of volcanic rocks was extruded in the early stages of rifting (Miocene), and has tapered off during the Quaternary, except at Udokan (Kiselev, 1987). The location of Plio-Pleistocene volcanic rocks is highly dependent on recent topography, with some filling river valleys (Kiselev, 1987; Rasskazov et al., 1990). Surprisingly, no basaltic rocks have yet been found in Lake Baikal (Logatchev, 1993). One would expect that the basin above the zone of maximum extension would be sufficiently weakened for basaltic rocks to intrude the sediment fill. However, the lack of flows within Lake Baikal reinforces the independence of rift basin formation and volcanic activity in the BRZ.

In all regions of BRZ volcanism, there are numerous occurrences of upper mantle xenoliths and megacrysts. Megacrysts are large (.5 - 10 cm) single crystals of various mineral types (most commonly clinopyroxene and anorthoclase, with rare amphibole, garnet, biotite, ilmenite, and zircon) that are found in alkaline volcanic rocks and kimberlites throughout the world. A wide variety of upper mantle xenoliths are found in

BRZ rocks, including rare garnet lherzolites found only in the Vitim volcanic field (Ionov et al., 1993; Ionov et al., 1992).

EXTENSIONAL TECTONICS OF THE BRZ

The amount of crustal extension in the BRZ has been difficult to estimate because the deep morphology of BRZ faults is poorly known. Zorin et al. (1989) estimated 15 - 30 km of extension in the central South Baikal depression and Selenga delta. Zorin and Cordell (1991) used a technique based on Bouguer gravity anomalies to calculate crustal extension for four profiles across the BRZ. They found a progressive increase in crustal extension from the northeast to southwest, from 0.9 to 19.3 km, which can be expressed in terms of finite rotation around an Euler pole located approximately at the northeastern terminus of the Chara depression. They also calculated a mean rotation velocity over 30 m.y. of 5.93×10^{-4} rad/m.y. By comparison, the Rio Grande Rift extensional velocity (calculated by the same method) is 30% higher, consistent with its higher heat flow and larger volume of volcanic rocks (Zorin and Cordell, 1991).

PASSIVE VS. ACTIVE RIFTING MODELS

Because the BRZ is far removed from active plate boundaries, the origin of and driving mechanism for rifting in the Baikal region remains a subject of extensive debate. The most controversial issue is whether rifting follows an "active" or "passive" model. The "active" model ascribes formation of the BRZ to active upwelling of asthenosphere ("anomalous mantle") beneath the rift and its intrusion into and replacement of the

lithosphere (e.g., Logatchev et al., 1993). The anomalous mantle region is characterized by high electrical conductivity, decreased density, and slower p-wave velocities (Logatchev and Zorin, 1992; Gao et al., 1994). The width of the zone of anomalous mantle appears to coincide with the domal uplift, and has been shown to have an asymmetric shape that mirrors the asymmetry of BRZ rift depressions (Gao et al., 1994). Logatchev and Zorin (1992) postulate that once the upwelling asthenosphere reaches the base of the Moho, it flows laterally towards the southeast since it has a higher density than the crust. Additionally, Zorin (1981) proposed that large dikes are intruded beneath the rift axis since heat-flow anomalies are localized to 30 - 40 km regions. A large velocity contrast and small density contrast between the crust and asthenosphere indicate there could be a small fraction of partial melt in the upwarped asthenosphere (Gao et al., 1994).

Alternatively, the passive model ascribes formation of the BRZ to plate tectonic motions between India and Eurasia, rather than active upwelling of asthenosphere (e.g., Molnar and Tapponnier, 1975, 1977; Tapponnier and Molnar, 1979; Zonenshain and Savostin, 1981). Evidence used to support this model includes the very low volume of rift magmatism, lack of basalts in Lake Baikal, and the non-dependence of volcanism on rift structures. Therefore the asthenosphere is thought to have risen passively to fill already extended lithosphere, rather than being the cause of that extension.

The most recent models have proposed the more moderate view that the cause of the BRZ is the complex interaction between stresses due to motions at far-away plate boundaries and a regional thermal anomaly causing upwelling of the asthenosphere (e.g., Dobretsov et al., 1996). The gravity modeling studies of Petit et al. (1997) and van der

Beek (1997), as well as the stress field studies of Petit et al. (1996) and Delvaux et al. (1995) have all concluded that the current lithospheric thinning and topography can be explained mostly by stresses propagated from plate motions occurring far away. After a certain amount of lithospheric thinning, the asthenosphere will rise up to compensate the crust. Therefore, the definition of "passive" versus "active" rifting takes on a limited meaning. At issue is really the *chronology* of rifting. Which came first: did the upwelling mantle cause lithospheric thinning, or did lithospheric extension cause the mantle to upwell?

A REVIEW OF MANTLE "COMPONENTS"

There has been extensive research on the isotope geochemistry of oceanic volcanic rocks. Based on this large data set, it has been observed that the Sr, Nd, and Pb isotopic systems are correlated, so that mixing between various end-member mantle "components" can explain the variation in oceanic volcanic rock data. Zindler et al. (1982) fit the data for oceanic rocks to a three-dimensional "mantle plane". Both Zindler and Hart (1986) and Hart (1988) extensively review the proposed end-members. The simplest and most commonly used are: DMM (depleted MORB mantle), EMI (enriched mantle I), EMII (enriched mantle II), and HIMU. Zindler et al. (1982) emphasized that the proposed end-member components are not necessarily physical reservoirs in the earth, but are rather a tool for explaining the data in a simple way.

DMM is defined as the source of typical MORB (mid-ocean ridge basalt) erupted away from plumes. This mantle component has a "depleted" isotopic characteristic, i.e.,

it has been depleted in easily removed components, such as large ion lithophile (LIL) elements, by multiple melting events (Hart, 1988). It has the following characteristics: low Rb/Sr (due to many melting events) and corresponding low $^{87}Sr/^{86}Sr$; high Sm/Nd (again due to melting) and high $^{143}Nd/^{144}Nd$ (positive ε_{Nd}); low U/Pb, with $^{206}Pb/^{204}Pb$ around 17.2 to 17.7, $^{207}Pb/^{204}Pb$ around 15.4; and Th/U around 2.4, giving $^{208}Pb/^{204}Pb$ around 37.2 to 37.4 (all ranges from Zindler and Hart, 1986).

HIMU is defined as a high U/Pb mantle component, first observed by Tatsumoto (1978). Like DMM, HIMU has low Rb/Sr and low $^{87}Sr/^{86}Sr$ (around 0.7029), but has moderate $^{143}Nd/^{144}Nd$. The most distinctive characteristic of the HIMU component, as its name implies, is its high U/Pb (and Th/Pb), leading to $^{206}Pb/^{204}Pb > 20.8$ (Zindler and Hart, 1986). A variety of origins for the HIMU component has been proposed, including: extraction of Pb by core formation, recycling of ancient continental crust or altered oceanic crust, or mantle metasomatism. Hart (1988) favors the origin of HIMU by mantle metasomatism that has mobilized Pb and Rb and removed them from some portion of the mantle.

The enriched mantle components (EMI and EMII) were needed to explain the ocean island basalt (OIB) data that can not be explained by mixing between only DMM and HIMU. They are called "enriched" components because they had to evolve in reservoirs with high (enriched) Rb/Sr and Nd/Sm (Hart, 1988). EMI has $^{87}Sr/^{86}Sr$ around 0.705 and low $^{143}Nd/^{144}Nd$, while EMII has more radiogenic $^{87}Sr/^{86}Sr > 0.722$ (Hart, 1988). EMI (first defined to explain data from the Walvis Ridge) has very unradiogenic Pb isotopic composition, with $^{206}Pb/^{204}Pb$ of 17.6 to 17.7, $^{207}Pb/^{204}Pb$ of 15.46 to 15.49,

and $^{208}Pb/^{204}Pb$ of 38.0 to 38.2. EMII is characterized by a high $^{207}Pb/^{204}Pb$ and $^{208}Pb/^{204}Pb$ for a given $^{206}Pb/^{204}Pb$ (Zindler and Hart, 1986; Hart, 1988). Like the HIMU components, the origin of the EM components is a subject of some debate. Various proposed sources for the EM characteristics include mixing of continental sediment or crust into the mantle, delamination of continental lithosphere and mixing into the mantle, and mantle metasomatism (Zindler and Hart, 1986). While EMII resembles upper continental crust or continentally derived sediment (Zindler and Hart, 1986), and has long been documented by xenoliths and xenolith-bearing basalts, the source of the EMI component was not initially so clear, and was hampered by a lack of Pb isotopic data for xenoliths.

Since the concept of mantle components was first put forth more than ten years ago, researchers have been actively searching for the EMI component in subcontinental lithospheric mantle and continental basalts. The Asian continent has been a very important source for much of this data because of its large amount of continental volcanism and many locations of xenolith-bearing alkaline basalts and kimberlites. Studies of peridotite xenoliths from China (Song and Frey, 1989; Tatsumoto et al., 1992), as well as alkaline volcanic rocks of eastern China (Basu et al., 1991; Peng et al., 1986; Song et al., 1990) and the south China basin (Nguyen et al., 1996; Tu et al., 1991) have all recorded an EMI-type component. This dissertation will also present evidence for an EMI component in BRZ volcanic rocks and inclusions.

In addition to the end-member mantle components, it has been observed that there seems to be a global distribution of certain components. Hart (1984) and Hart et al.

(1986) defined the Northern Hemisphere Regression Line (NHRL), a regression line through the Pb isotopic data for average northern hemisphere oceanic basalt data. They found that there appeared to be a belt of data from the southern hemisphere with high $^{87}Sr/^{86}Sr$ (> 0.705) that all had Pb isotopic compositions that plotted above the NHRL. Hart called this set of data the DUPAL anomaly (after Dupré and Allègre). Deviations from the NHRL can be calculated based on Hart's equation for the NHRL (1984). The DUPAL anomaly has Δ8/4 (deviation of $^{208}Pb/^{204}Pb$ from the NHRL) > +60. The significance of the DUPAL anomaly has been questioned, since the EMI and EMII components are probably related to processes that occur throughout the globe, and should not occur just in the sub-equatorial regions. Hart (1988) proposed that the DUPAL anomaly is related to repeated cycles of continental break-up and amalgamation that have concentrated subduction zones in the latitudes of the DUPAL anomaly. However, recent studies have shown that a DUPAL-like signature is not restricted to the southern hemisphere, since it has been documented in the South China Basin (Tu et al., 1992; Flower et al., 1992), the Philippines (Chen et al., 1990; Mukasa et al., 1987), and Taiwan (Chung and Sun, 1992; Chung et al., 1995). The results of this thesis will also demonstrate a DUPAL-like signature for BRZ volcanism.

REFERENCES

Basu, A. R., Junwen, W., Wankang, H., Guanghong, X., and Tatsumoto, M., 1991, Major element, REE, and Pb, Nd and Sr isotopic geochemistry of Cenozoic volcanic rocks of eastern China: implications for their origin from suboceanic-type mantle reservoirs: Earth and Planetary Science Letters, v. 105, p. 149-169.

Chen, C.-H., Shieh, Y.-N., Lee, T., Chen, C.-H., and Mertzman, S. A., 1990, Nd-Sr-O isotopic evidence for source contamination and an unusual mantle component under Luzon Arc: Geochimica et Cosmochimica Acta, v. 54, p. 2473-2483.

Chung, S.-L., and Sun, S.-s., 1992, A new genetic model for the East Taiwan Ophiolite and its implications for Dupal domains in the Northern Hemisphere: Earth and Planetary Science Letters, v. 109, p. 133-145.

Chung, S.-L., Jahn, B.-M., Chen, S.-J., Lee, T., and Chen, C.-H., 1995, Miocene basalts in northwestern Taiwan: evidence for EM-type mantle sources in the continental lithosphere: Geochimica et Cosmochimica Acta, v. 59, p. 549-555.

Delvaux, D., Moeys, R., Stapel, G., Melnikov, A., and Ermikov, V., 1995, Palaeostress reconstructions and geodynamics of the Baikal region, Central Asia, Part I. Palaeozoic and Mesozoic pre-rift evolution: Tectonophysics, v. 252, p. 61-101.

Dobretsov, N. L., Buslov, M. M., Delvaux, D., Berzin, N. A., and Ermikov, V. D., 1996, Meso- and Cenozoic tectonics of the central Asian mountain belt: effects of lithospheric plate interaction and mantle plumes: International Geology Review, v. 38, p. 430-466.

Florensov, N. A., 1969, Rifts of the Baikal mountain region: Tectonophysics, v. 8, p. 443-456.

Flower, M. F. J., Zhang, M., Chen, C.-Y., Tu, K., and Xie, G., 1992, Magmatism in the South China Basin 2. Post-spreading Quaternary basalts from Hainan Island, south China: Chemical Geology, v. 97, p. 65-87.

Gao, S., Davis, P. M., Liu, H., Slack, P. D., Zorin, Y. A., Logatchev, N. A., Kogan, M., Burkholder, P. D., and Meyer, R. P., 1994, Asymmetric upwarp of the asthenosphere beneath the Baikal rift zone, Siberia: Journal of Geophysical Research, v. 99, p. 15,319-15,330.

Golonetsky, S. I., and Misharina, L. A., 1978, Seismicity and earthquake focal mechanisms in the Baikal rift zone: Tectonophysics, v. 45, p. 71-85.

Hart, S. R., Gerlach, D. C., and White, W. M., 1986, A possible new Sr-Nd-Pb mantle array and consequences for mantle mixing: Geochimica et Cosmochimica Acta, v. 50, p. 1551-1557.

Hart, S. R., 1988, Heterogeneous mantle domains: signatures, genesis and mixing chronologies: Earth and Planetary Science Letters, v. 90, p. 273-296.

Hutchinson, D. R., Golmshtok, A. J., Zonenshain, L. P., Moore, T. C., Scholz, C. A., and Klitgord, K. D., 1992, Depositional and tectonic framework of the rift basins of Lake Baikal from multichannel seismic data: Geology, v. 20, p. 589-592.

Ionov, D. A., Kramm, U., and Stosch, H., 1992, Evolution of the upper mantle beneath the southern Baikal rift zone: an Sr-Nd isotope study of xenoliths from the Bartoy volcanoes: Contrib. Mineral. Petrol., v. 11, p. 235-247.

Ionov, D. A., Ashchepkov, I. V., Stosch, H., Witt-Eickschen, G., and Seck, H. A., 1993, Garnet peridotite xenoliths from the Vitim volcanic field, Baikal region: the nature of the garnet-spinel peridotite transition zone in the continental mantle: Journal of Petrology, v. 34, p. 1141-1175.

Kiselev, A. I., 1987, Volcanism of the Baikal rift zone: Tectonophysics, v. 143, p. 235-244.

Kiselev, A. I., and Popov, A. M., 1992, Asthenospheric diapir beneath the Baikal rift: petrological constraints: Tectonophysics, v. 208, p. 287-295.

Logatchev, N. A., and Florensov, N. A., 1978, The Baikal system of rift valleys: Tectonophysics, v. 45, p. 1-13.

Logatchev, N. A., Zorin, Y. A., and Rogozhina, V. A., 1983, Baikal Rift: active or passive? - comparison of the Baikal and Kenya rift zones: Tectonophysics, v. 94, p. 223-240.

Logatchev, N. A., and Zorin, Y. A., 1987, Evidence and causes of the two-stage development of the Baikal rift: Tectonophysics, v. 143, p. 225-234.

Logatchev, N. A., and Zorin, Y. A., 1992, Baikal rift zone: structure and geodynamics: Tectonophysics, v. 208, p. 273-286.

Logatchev, N. A., 1993, History and geodynamics of the Lake Baikal rift in the context of the eastern Siberia rift system: a review: Bull. Centres Rech. Explor.-Prod. Elf Aquitaine, v. 17, p. 353-370.

Lysak, S. V., 1987, Terrestrial heat flow of continental rifts: Tectonophysics, v. 143, p. 31-41.

Molnar, P., and Tapponnier, P., 1975, Cenozoic tectonics of Asia: effects of a continental collision: Science, v. 189, p. 419-426.

Molnar, P., and Tapponnier, P., 1977, Relation of the tectonics of eastern China to the India-Eurasia collision: application of slip-line field theory to large-scale continental tectonics: Geology, v. 5, p. 212-216.

Moore, T. C., Klitgord, K. D., Gomshtok, A. J., and Weber, E., 1997, Sedimentation and subsidence patterns in the central and north basins of Lake Baikal from seismic stratigraphy: Geological Society of America Bulletin, v. 109, p. 746-766.

Mukasa, S. B., McCabe, R., and Gill, J. B., 1987, Pb-isotopic compositions of volcanic rocks in the West and East Philippine island arcs: presence of the Dupal isotopic anomaly: Earth and Planetary Science Letters, v. 84, p. 153-164.

Nguyen, H., Flower, M. F. J., and Carlson, R. W., 1996, Major, trace element, and isotopic compositions of Vietnamese basalts: interaction of hydrous EMI-rich asthenosphere with thinned Eurasian lithosphere: Geochimica et Cosmochimica Aca, v. 60, p. 4329-4351.

Peng, Z. C., Zartman, R. E., Futa, K., and Chen, D. G., 1986, Pb-, Sr- and Nd-isotopic systematics and chemical characteristics of Cenozoic basalts, eastern China: Chemical Geology, v. 59, p. 3-33.

Petit, C., Deverchere, J., and Houdry, F., 1996, Present-day stress field changes along the Baikal rift and tectonic implications: Tectonics, v. 15, p. 1171-1191.

Petit, C., Burov, E., and Deverchere, J., 1997, On the structure and mechanical behaviour of the extending lithosphere in the Baikal Rift from gravity modelling: Earth and Planetary Science Letters, v. 149, p. 29-42.

Rasskazov, S. V., and Batyrmurzaev, A. S., 1985, Cenozoic basalts of the Vitim Plateau and their age determination: Geologiya i Geofizika, v. 26, p. 20-27.

Rasskazov, S. V., Batyrmurzaev, A. S., and Magomedev, S. A., 1990, K-Ar dating of cenozoic basalts of the Oka tableland (eastern Sayan): Geologiya i Geofizika, v. 31, p. 100-105.

Rasskazov, S. V., 1993, Magmatism of the Baikal rift zone: Novosibirsk, Nauka, 273 p.

Sherman, S. I., 1978, Faults of the Baikal rift zone: Tectonophysics, v. 45, p. 31-39.

Solonenko, V. P., 1978, Seismotectonics of the Baikal rift zone: Tectonophysics, v. 45, p. 61-69.

Song, Y., and Frey, F. A., 1989, Geochemistry of peridotite xenoliths in basalt from Hannuoba, Eastern China: implications for subcontinental mantle heterogeneity: Geochimica et Cosmochimca Acta, v. 53, p. 97-113.

Song, Y., Frey, F. A., and Zhia, X., 1990, Isotopic characteristics of Hannuoba basalts, eastern China: implications for their petrogenesis and the composition of subcontinental mantle: Chemical Geology, v. 85, p. 35-52.

Tapponnier, P., and Molnar, P., 1979, Active faulting and Cenozoic tectonics of the Tien Shan, Mongolia, and Baykal regions: Journal of Geophysical Research, v. 84, p. 3425-3459.

Tatsumoto, M., 1978, Isotopic composition of lead in oceanic basalt and its implication to mantle evolution: Earth and Planetary Science Letters, v. 38, p. 63-87.

Tatsumoto, M., Basu, A. R., Wankang, H., Junwen, W., and Guanghon, X., 1992, Sr, Nd, and Pb isotopes of ultramafic xenoliths in volcanic rocks of eastern China: enriched components EMI and EMII in subcontinental lithosphere: Earth and Planetary Science Letters, v. 113, p. 107-128.

Tu, K., Flower, M. F. J., Carlson, R. W., Zhang, M., and Xie, G., 1991, Sr, Nd, and Pb isotopic compositions of Hainan basalts (south China): implications for a subcontinental lithosphere Dupal source: Geology, v. 19, p. 567-569.

Tu, K., Flower, M. F. J., Carlson, R. W., Xie, G., Chen, C.-Y., and Zhang, M., 1992, Magmatism in the South China Basin 1. Isotopic and trace-element evidence for an endogenous Dupal mantle component: Chemical Geology, v. 97, p. 47-63.

van der Beek, P., 1997, Flank uplift and topography at the central Baikal Rift (SE Siberia): A test of kinematic models for continental extension: Tectonics, v. 16, p. 122-136.

Zamarayev, S. M., and Ruzhich, V. V., 1978, On relationships between the Baikal rift and ancient structures: Tectonophysics, v. 45, p. 41-47.

Zindler, A., Jagoutz, E., and Goldstein, S., 1982, Nd, Sr and Pb isotopic systematics in a three-component mantle: a new perspective: Nature, v. 298, p. 519-523.

Zindler, A., and Hart, S., 1986, Chemical geodynamics: Annual Reviews in Earth and Planetary Science, v. 14, p. 493-571.

Zonenshain, L. P., and Savostin, L. A., 1981, Geodynamics of the Baikal rift zone and plate tectonics of Asia: Tectonophysics, v. 76, p. 1-45.

Zorin, Y. A., 1981, The Baikal rift: an example of the intrusion of asthenospheric material into the lithosphere as the cause of disruption of lithopheric plates: Tectonophysics, v. 73, p. 91-104.

Zorin, Y. A., Kozhevnikov, V. M., Novoselova, M. R., and Turutanov, E. K., 1989, Thickness of the lithosphere beneath the Baikal rift zone and adjacent regions: Tectonophysics, v. 168, p. 327-337.

Zorin, Y., and Cordell, L., 1991, Crustal extension in the Baikal rift zone: Tectonophysics, v. 198, p. 117-121.

FIGURE CAPTIONS

Figure 1.1 General map of the Baikal Rift Zone (BRZ) showing locations of the major Cenozoic volcanic fields and other major features. TV is the Tuva volcanic field; OP is the Oka Plateau; T is the Tunka Basin, and D is the Dzhida Basin. Other rift basins according to number label are: 1) Busingol, 2) Darkhat, 3) Khubsugul, 4) Barguzin, 5) Upper Angara, 6) Tsipa, 7) Baunt, 8) Muya, 9) Chara, and 10) Tokka. The 1500 m contour line of the Sayan-Baikal domal uplift is indicated.

Figure 1.1

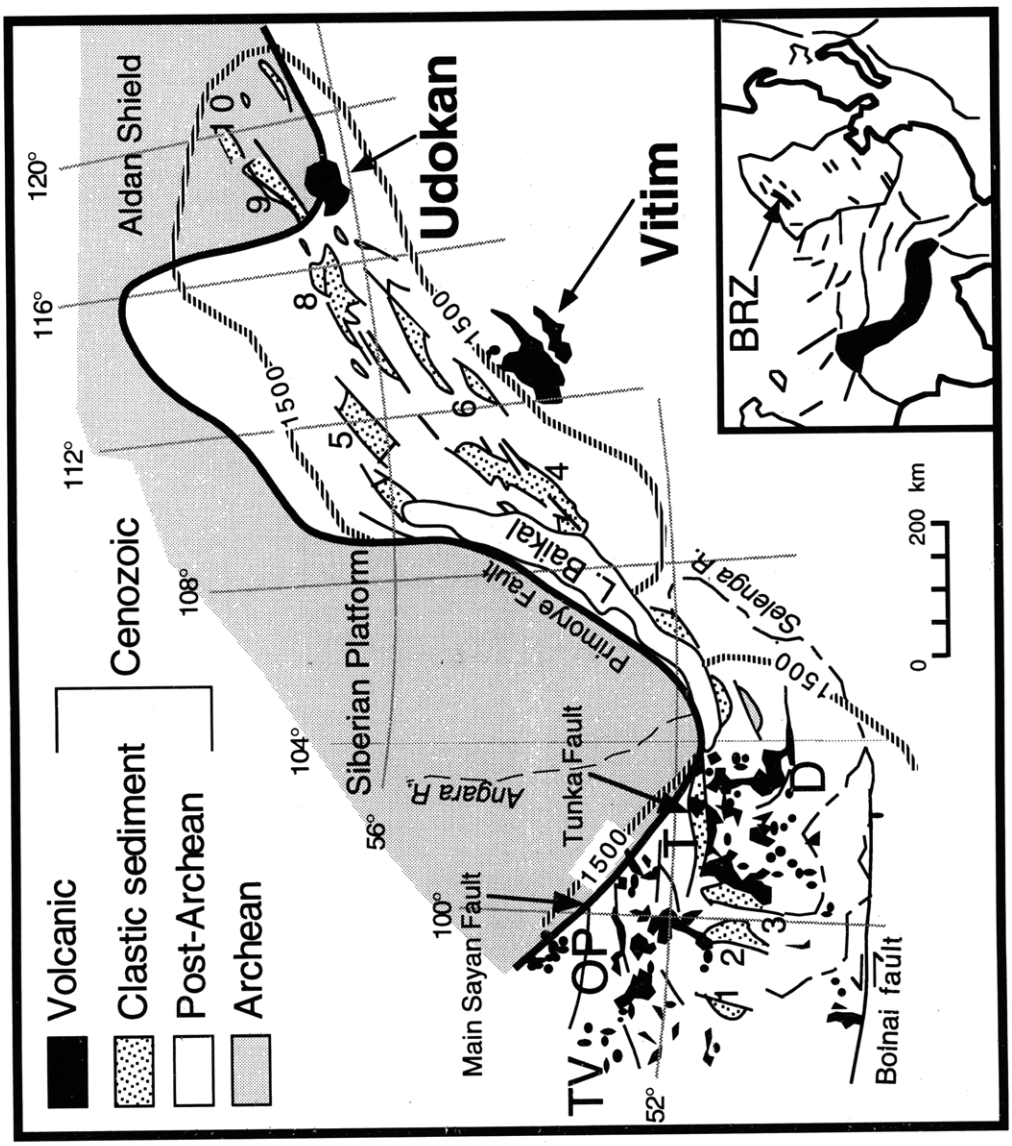
Volcanic
Clastic sediment
Cenozoic
Post-Archean
Archean
Aldan Shield
Udokan
Vitim
Siberian Platform
Primorye Fault
L. Baikal
Angara R.
Tunka Fault
Main Sayan Fault
Selenga R.
Bolnai fault
TV
OP
T
D
BRZ
1500
200 km
0
52°
56°
100°
104°
108°
112°
116°
120°

CHAPTER 2

VOLCANISM OF THE WESTERN BAIKAL RIFT ZONE: GEOCHEMISTRY OF THE TUNKA, OKA PLATEAU, AND TUVA VOLCANIC FIELDS

ABSTRACT

A large region of Cenozoic volcanism occurs in the western Baikal Rift Zone, Siberia, and includes the Tunka, Oka Plateau, and Tuva volcanic fields. Lavas have a restricted range in composition, comprising alkaline/subalkaline basalt, basanite, hawaiite/trachybasalt, and a few mugearites. Likewise, their rare earth and incompatible element abundances are similar. The observed major and trace element geochemical variations are consistent with derivation of the magmas from a relatively homogeneous source, followed by fractional crystallization of olivine, pyroxene, and plagioclase.

Sr, Nd, and Pb isotopic compositions are comparable to the range for ocean island basalts, and can best be explained by mixing between a depleted mantle component (DMM) and enriched mantle type I (EMI). It appears that Sr isotopic compositions may have become more radiogenic from the Oligocene to the Pliocene, while Nd became less radiogenic, suggesting the source of the western Baikal Rift Zone lavas became more "lithospheric" rather than "asthenospheric" with time, contrary to what has been documented in other rifts. This temporal variation could be caused by progressive incorporation of the lithosphere into the asthenosphere beneath the Baikal Rift Zone.

INTRODUCTION

The Tunka, Oka Plateau, and Tuva volcanic fields occur within a large region of diffuse Cenozoic volcanic activity west of Lake Baikal. Together with the Dzhida and Khamar-Daban volcanic fields, they form one of the three major regions of Cenozoic volcanism associated with the Baikal Rift Zone, Siberia (Fig. 2.1). As is the case for the Udokan and Vitim volcanic fields of the BRZ, volcanism began in the Oligocene and continued to the Holocene, although the majority of eruptions occurred during the Miocene. The composition of lavas of the western BRZ range from alkaline basalt to basanite, hawaiite, and mugearite.

The Oka Plateau and Dzhida volcanic fields are some of the most comprehensively studied fields in the BRZ (Rasskazov, 1994; Rasskazov, 1993), while study of the remote Tuva volcanic field is still in its infancy. There is little radiogenic isotope data, or geochronology, for the western BRZ volcanic rocks in comparison to major element and trace element data. This study presents extensive new isotopic data (104 samples) for this region, as well as major and trace element data (118 samples), and $^{40}Ar/^{39}Ar$ geochronology (26 samples).

REGIONAL GEOLOGY

The Baikal Rift Zone (BRZ) in southern Siberia is one of the world's major continental rifts. It is expressed as an ~1800 km-long series of southwest-northeast-oriented rift depressions and faults situated along a suture between the Archean Siberian craton to the north and younger accreted Paleozoic terranes to the south (Fig. 2.1). Most

of the BRZ is encompassed by the Sayan-Baikal domal uplift, a broad region of mountain ranges and high plateaus surrounding rift basins containing Paleogene, Neogene, and Quaternary sediments. The domal uplift is defined by the 1500m elevation contour line of the Cretaceous-Paleogene erosion surface, characterized by a kaolinite-laterite horizon(Logatchev and Florensov, 1978).

The BRZ comprises 13 major rift basins, with the two largest basins forming Lake Baikal itself, the world's largest (23,000 km^3) and deepest (maximum 1637 m) freshwater lake. Based on the age of sediment fill, rifting is thought to have begun in the Paleocene, starting with the South Baikal basin (Logatchev, 1993). Sediments of the BRZ seem to suggest a two-stage rifting process. The "first-stage" sediments of Paleocene to Lower Pliocene age form a predominantly fine-grained sedimentary package of sandstones, siltstones, and clays 1.5 - 2 km thick (5 km in South Baikal basin). The "second-stage" sediments of Pliocene to Holocene age form a package 1000 - 1200 m thick, and include coarser-grained sediments such as gravels and conglomerates in addition to the fluvial/lacustrine sediments found in the "first-stage". Based on estimates of the amount of sediments deposited during each stage, Logatchev and Zorin (1987) termed the early stage "slow rifting" and the second stage "fast rifting".

There are three major areas of Cenozoic volcanism associated with the BRZ, the largest of which is the broad zone at the western end of Lake Baikal. The western zone of Baikal Rift volcanism extends ~500 km west from the southwestern tip of Lake Baikal, north to the boundary with the Siberian shield, and south to the Mongolian border region (Fig. 2.1). There are additional volcanic fields located south of this region in Mongolia

which are part of the broad domal uplift region (i.e., Dariganga plateau, Lake Khubsugul, etc.). However, this study does not include them because they lie south of the east-west trending Bolnai shear zone, and are considered to be outside of the Baikal Rift Zone proper. The other two major volcanic fields of the BRZ are the Udokan volcanic field, which partially overlaps the Siberian shield on the northeast end of the rift, and the Vitim volcanic field, located on a plateau several hundred km east of Lake Baikal and offset from BRZ extensional structures and the axis of rifting. The lavas of the Tunka, Oka Plateau, and Tuva volcanic fields of the western BRZ are the subject of this chapter.

GEOLOGIC BACKGROUND OF VOLCANIC FIELDS OF THE WESTERN BRZ

Tunka Basin

The Tunka Basin is an asymmetric graben that extends over 200 km in an east-west direction away from the southwest end of Lake Baikal (Fig. 2.1, 2.2). It is bounded to the north by the Tunka Fault, a series of sub-parallel en echelon structures that currently have sinistral oblique-slip normal movement (Sherman, 1978). The Tunka Basin is cut off to the northeast by the Main Sayan Fault. Unlike other BRZ depressions, drilling in Tunka has revealed a significant amount of fissure-type eruptions (~20% of fill) intercalated with sediments (Logatchev, 1993; Rasskazov, 1993). 65 basalt bodies (totaling ~400 m) are interbedded with coal-bearing sediments (Kiselev, 1987). Additionally, there appears to be a higher volume of lavas on the northern, most downwarped side of the graben (Logatchev and Florensov, 1978). Volcanism in Tunka

may have started in the Paleogene, but was most intense in the Middle-Early Pliocene during maximum subsidence of the rift depression (Kiselev, 1987). An explosive phase of eruptions occurred in the Early Pleistocene when 200 - 240 m of volcaniclastics were deposited in the Tunka basin. During the final phase of eruptions in the Pleistocene, basalts were erupted on intradepressional basin uplifts, and ~150m are interlayered with Quaternary sediments in the Tunka basin itself. Volcanism in the Tunka area ended at the Pleistocene-Holocene boundary with the eruption of single cinder and lava cones (~20 in number) rising 40 - 50m above the surface of the Tunka depression (Kiselev, 1987).

Oka Plateau/East Sayan volcanic region

The Oka Plateau/East Sayan region is a large dispersed region of volcanism west of the Tunka Basin in the western zone of the BRZ. This region extends west of the Tunka Basin and fault and is bounded to the north by the transverse Main Sayan Fault (Fig. 2.1, 2.3). The East Sayan Mountain Range separates the Oka Plateau from the Tuva volcanic field to the west. As in other volcanic areas of the western BRZ, volcanism was most voluminous in the Miocene and Pliocene, and less voluminous and more diffuse in the later Pliocene to Holocene (Rasskazov et al., 1990). The Miocene-Pliocene basalt plateaus are 300 - 500 m thick and are currently 1440 - 2500 m above sea level (Rasskazov, 1993). The youngest known volcanism of the Oka area is the Holocene Zhom-Bolock basalt, an 85 km-long basalt flow in a river valley with three cinder cones on its surface (Kiselev, 1987).

As in other areas of BRZ volcanism, Pliocene and Quaternary volcanic rocks flowed down valleys incised in the Miocene lava plateau, creating an inverted stratigraphic relationship. Rasskazov et al. (1990) subdivide the Miocene-Pliocene group of rocks into four types: mostly hypersthene normative subalkali olivine basalts with low alkalis (~5 wt.%), differentiated lavas flows with segregation lenses found in the Yamata R., alkalic lavas (basanites) in the western part of the Oka Plateau which contain mantle xenoliths, and very young (Quaternary?) "valley" basalts of intermediate alkalinity on the paleoterrace of the Oka River.

Tuva volcanic region

The Tuva volcanic field is the westernmost expression of BRZ volcanism, located in the remote region west of the axial, uplifted East Sayan Mountain Range and north of the Mongolian border (Fig. 2.1, 2.4). The largest area of volcanism within the Tuva region is the East Tuva Lava Field (ETLF), situated between the East Sayan Mountains and the Ulug-Arga ridge. This large lava field (2400 km^2) is made up of coalescing post-plateau shield volcanoes of Pleistocene-Quaternary age, including the Shivit-Taiga, Derbi-Taiga, and Prioserniy volcanoes. Outside of the ETLF, smaller basalt outliers are spread out over the rest of the Tuva volcanic area (45,000 km^2) (Rasskazov et al., 1989).

Rasskazov et al. (1989) presented data on volcanic rocks of the Ulug-Arga ridge (Fig. 2.4) and the area north of it. The Ulug-Arga ridge is believed to have been uplifted relatively recently, after the formation of the ETLF, since remnants of Miocene basalt are found at different levels of the stepped paleo-topography of the ridge. Young basalts of

the ETLF overlap the lowest level watersheds in which the modern river valleys are incised on the Ulug-Arga ridge, as well as to the north and west of the ETLF. K-Ar data of Rasskazov et al. (1989) indicate that the Ulug-Arga ridge volcanic sequence is 16.1 to 17.5 Ma, and the young basalts which lap onto the ridge are 2.32 Ma.

SAMPLE DESCRIPTIONS AND LOCATIONS

Volcanic rocks of the western BRZ were sampled during field excursions in 1988, 1989, 1991, 1992, and 1993, and supplemented by our Russian collaborator, Sergei Rasskazov, of the Institute for the Earth's Crust in Irkutsk, Siberia. Sample locations are shown on the maps and cross-sections of Figures 2.1 to 2.4. Appendix 2.C provides a complete sample listing and details of field relationships .

Tunka Basin Samples

Samples BK-1 to BK-13 from the Tunka Basin were collected in 1988 by M. Dungan, P. Lipman, and C. Chapin. Samples p506, p508, and p528A were collected by S. Rasskazov. Samples BK-161 and 162 were collected in 1989. Sample locations are shown on the map of Figure 2.2.

Oka Plateau/East Sayan Samples

The Oka Plateau/East Sayan volcanic region is the most extensively sampled region of the western BRZ included in this study. Figure 2.3 shows the Oka Plateau volcanic field along with sample locations. Not shown on Figure 2.3 is the sequence of

rocks of probably Pliocene age from the Kitoy Ridge (BK-201 to BK-207, bottom to top), east of the Oka area. Also not shown on Figure 2.3 are samples BK-242 to BK-246 from the Hurugaycha volcano northeast of the town of Mondi.

Tuva Region Samples

Samples from the Tuva region (Fig. 2.4) are from the Miocene sequence on the Ulug-Arga ridge studied by Rasskazov et al. (1989), as well as Pliocene lavas of the East Tuva Lava Field (Fig. 2.4a) which onlap onto the Ulug-Arga ridge. Figure 2.4b is a cross-section of the Ulug-Arga ridge showing sample locations. Additional samples from Tuva were obtained by A. Ivanov and Rasskazov in 1994, and locations are shown on Figure 2.4a. These include samples of the Shivit-Taiga, Derbi-Taiga, and Prioserniy post plateau shield volcanoes of the East Tuva Lava Field.

SAMPLE PREPARATION AND ANALYTICAL TECHNIQUES

Great care was taken to collect the freshest possible samples in the field. Samples were crushed to gravel size wrapped in heavy plastic to reduce contamination from metal hammers. The gravel was then ultrasonically cleaned in deionized water to remove adhering rock dust, followed by drying in an oven. Dried samples were carefully examined and the freshest, inclusion-free fragments were chosen for powdering in an alumina ceramic shatterbox.

Major element and some trace element abundances were determined by X-ray fluorescence (XRF) at both Washington University, St. Louis - according to methods of

Couture et al. (1993) - and at the University of Massachusetts at Amherst - according to the methods described by Rhodes (1983). Selected samples were analyzed for rare earth element (REE) abundances by instrumental neutron activation analysis (INAA) at the Massachusetts Institute of Technology, following methods of Ila and Frey (1984), and at Washington University, St. Louis. Additional samples were analyzed for trace element abundances, including REE, by inductively coupled plasma mass spectrometry (ICP-MS) on the Fisons Plasma Quad 4+S at the Massachusetts Institute of Technology. Details of the ICP-MS analytical method are given in Appendix 2.A.

Isotopic compositions were determined on a VG sector-54 mass spectrometer at the Massachusetts Institute of Technology, except where noted in Tables 2.3a and 2.3b. Approximately 300 mg of whole-rock powder was dissolved in Teflon beakers in concentrated HF-HNO_3, followed by conversion to chloride form. Rare earth elements were separated by cation exchange columns with HCl as eluant. Sm and Nd were separated using HDEHP-coated BioBead resin with HCl as eluant. Sr separation was accomplished in Teflon micro-columns using Sr-spec resin and HNO_3 chemistry. Pb was separated using HBr-based chemistry on 200 - 400 mesh anion exchange resin in Teflon microcolumns. All reagents used were distilled to reach ultrahigh purity for trace elements. Total procedural blanks are estimated to be <100pg for Sr, <400pg for Nd, and <10pg for Pb.

Sr and Nd isotopic compositions were measured in dynamic multicollector mode. Sr isotopic ratios are normalized to $^{86}Sr/^{88}Sr = 0.1194$, and Nd isotopic ratios are normalized to $^{146}Nd/^{144}Nd = 0.7219$. Pb isotopic compositions were measured in static

multicollector mode. Sr and Nd isotopic ratios are corrected for isotopic fractionation using an exponential law. Based on analyses of NBS-981, Pb isotopic ratios are corrected by 0.12%/a.m.u. to account for mass fractionation during analysis.

$^{40}Ar/^{39}Ar$ GEOCHRONOLOGIC CONSTRAINTS ON TIMING OF VOLCANISM

Due to the paucity of existing age information for volcanism in the Oka Plateau and Tuva regions, we chose 26 samples for Ar-Ar geochronology. Some samples are from geochemically studied basalt sequences whose absolute age was unknown. Other samples were dated to augment existing age information obtained by other less robust methods for the same or related sequences, and to attempt to resolve outstanding geochronological questions suggested by our colleague Sergei Rasskazov, an expert on volcanic rocks of the western BRZ. Details of the analytical procedure, complete tables of the argon geochronologic results, and a discussion of the age information are given in Appendix 2.B, and summarized in Table 2.1.

GEOCHEMICAL RESULTS

Major elements

Major and trace element data for the western BRZ volcanic rocks are given in Table 2.2a-c. The major element composition of samples from all three volcanic fields of the western BRZ is fairly restricted, as shown in the total alkali silica (TAS) diagram (Fig. 2.5). Based on the TAS classification scheme of Le Bas et al. (1986), the majority of samples from all areas are hawaiites or potassic trachybasalts, with SiO_2 from 45 to 52%,

and $Na_2O + K_2O$ from 5 to 7%. A smaller number of samples, from Tunka and Oka only, are alkaline/subalkaline basalts, with SiO_2 from 48 to 51%, and $Na_2O + K_2O$ from 4 to 5%. A few basanites are sampled from the Tunka and Oka fields. As observed by other BRZ researchers (e.g., Kiselev, 1987; Rasskazov, 1993), most BRZ lavas do not exhibit trends to highly evolved compositions such as benmoreites and trachytes, except in the Udokan volcanic field on the northeastern end of the BRZ (Rasskazov et al., 1997; Rasskazov, 1985). A small number of samples from the Oka and Tuva volcanic fields reach mugearite compositions, with SiO_2 from 50 to 54%, and $Na_2O + K_2O$ from 5 to 7%. The one sample of basaltic andesite composition is a dike from the southern Oka Plateau volcanic field that cross-cuts granitic basement rocks of probable Devonian age (pers. comm., Rasskazov).

Mg# (Mg# = 100 * molecular $Mg/(Mg + Fe^{2+})$) for all western BRZ lavas ranges from 47 to 68 (Fig. 2.6). Lavas of the Tunka volcanic field have Mg# from 54 to 68 and are approximately bimodally distributed between hypersthene normative and nepheline normative compositions. Oka lavas have the widest range in Mg# (47 to 66) and normative nepheline (up to 15%) and hypersthene (up to 22%). Tuva lavas have a range in Mg# (52 to 64) comparable to the Tunka lavas, but all are nepheline normative with the exception of sample p901/2.

Major element data are plotted as a function of MgO % for each volcanic field in Figures 2.7a-c. In general, all three volcanic fields of the western BRZ have almost identical ranges in major element oxides. MgO ranges from 6 to 11% for the Tunka volcanic field, from 4 to 10% for the Oka volcanic field, and from 5 to 9% for the Tuva

volcanic field. For all three volcanic fields, MgO is negatively correlated with Al_2O_3 and Na_2O and positively correlated with CaO and MnO. MgO is weakly positively correlated with FeO* (FeO* = .15*Fe_2O_{3total}) for the Oka and Tuva volcanic fields, and weakly negatively correlated with P_2O_5 for the Tunka volcanic field. For all volcanic fields, K_2O shows the widest variation, most likely resulting from mobility during weathering, despite care taken to avoid such samples.

Trace elements

Rare earth elements (REE)

Chondrite normalized rare earth element patterns (using C1 chondrite values of Sun and McDonough, 1989) for all three volcanic fields are quite similar and are roughly sub-parallel (Fig. 2.8a-c), with light rare earth elements (LREE) enriched over heavy rare earth elements (HREE). $(La/Yb)_N$ ranges from 7 to 14 for Tunka, from 3 to 17 for Oka, and from 9 to 14 for Tuva. In addition to having very similar slopes from light to heavy rare earth elements, REE abundances of the lavas are also very similar, with the majority having La_N from 60 to 200 times chondrite. The basaltic andesite from the Oka volcanic field has a nearly flat REE pattern, at about 10 to 20 times chondrite. None of the lavas has a pronounced Eu anomaly.

Incompatible elements

The incompatible elements Rb, Ba, Sr, and Zr are plotted as a function of MgO in Figure 2.9a-c. There is no correlation between MgO and Rb, although the alkaline and subalkaline basalts from the Oka field may be weakly positively correlated with MgO

(Fig. 2.9b). There is no correlation between MgO and Zr or Sr for any of the volcanic fields. A weak positive correlation between MgO and Ba occurs at the Tuva volcanic field only (Fig. 2.9c).

Plots of Th versus incompatible elements (Rb, Ba, Zr, Sr; Fig. 2.10a-c) demonstrate that incompatible elements are correlated with each other. The Oka volcanic field again shows greater variation than the Tunka and Oka fields in the abundance of the large ion lithophile elements Ba and Sr.

Primitive mantle normalized (Sun and McDonough, 1989) incompatible element diagrams are shown in Figure 2.11. Incompatible element abundances are roughly similar for all three volcanic fields, as are the incompatible element patterns. All volcanic fields have a relative Ba and Sr enrichment, relative Th depletion, and overall enrichments in Nb, Ta, and K. The basaltic andesite dike from the Oka Plateau has very different and much lower incompatible element abundances than any of the other samples, with strong relative enrichments in K and Sr, and weak relative enrichment in Ti. The Tuva volcanic field has the highest degree of variability in the degree of relative enrichment or depletion of trace elements. The hawaiite sample p908/4 has the most extreme relative enrichments and depletions, and extremely low heavy rare earth elements with chondritic Yb and Lu abundances.

Compatible trace elements

The compatible trace elements Ni, Cr and Co are all highly correlated with MgO for all volcanic fields (Fig. 2.12a-c). Ni ranges from 70 to 250 ppm for Tunka, 20 to 140 ppm for Tuva, and 20 to 200 ppm for Oka. Cr ranges from 125 to 296 for Tunka, 88 to

256 for Oka, and 65 to 265 for Tuva. The abundances of these compatible elements does not appear to be correlated with the composition of the lavas, since the range in composition for each rock type overlaps. However, the compatible elements are weakly correlated with modal normative olivine (Fig. 2.13).

Isotopic data

Isotopic data for each of the volcanic fields of the western BRZ is given in Table 2.3a-c and plotted in Figures 2.14, 2.15, and 2.16. The total range in $^{87}Sr/^{86}Sr$ for the Tunka, Oka Plateau, and Tuva volcanic fields is 0.70380 to 0.70667, and the range for ε_{Nd} is +3.8 to -0.4. In the Tunka volcanic field, the lowest $^{87}Sr/^{86}Sr$ and highest ε_{Nd} is for a basanite, but isotopic compositions overlap for all rock types. The Oka volcanic field has the highest degree of variation in Sr and Nd isotopic compositions, but also has the most samples. For Oka, there does not appear to be any correlation between rock type and isotopic composition, although the basaltic andesite has the highest ε_{Nd}. The samples with the lowest (least radiogenic) Nd isotopic composition are a series of hawaiites from the southern Oka volcanic field (Fig. 2.3). The three samples with very radiogenic Sr (BK-215, BK-216, BK-219) are all from the lowest part of a sequence of basalts on the Bokson River (Fig. 2.3). The Sr and Nd isotopic compositions of the Tuva volcanic field samples appear to be somewhat correlated with major element composition, since the potassic trachybasalts are systematically offset to higher $^{87}Sr/^{86}Sr$ for a given ε_{Nd} when compared to the hawaiites. The distinction between hawaiite and trachybasalt is made on

the basis of whether wt.% Na_2O - 2 is > K_2O (Le Bas et al., 1986), so the offset may be indicative of post-magmatic remobilization of large ion lithophile elements.

The Tunka and Oka volcanic fields have a large range in Pb isotopic compositions (Fig. 2.15), with $^{206}Pb/^{204}Pb$ from 17.3 to 18.3, $^{207}Pb/^{204}Pb$ from 15.38 to 15.52, and $^{208}Pb/^{204}Pb$ from 37.5 to 38.1. The Tuva volcanic field has a more restricted range in $^{206}Pb/^{204}Pb$ (17.7 to 18.2), a similar range in $^{207}Pb/^{204}Pb$ (15.38 to 15.5), and a larger range in $^{208}Pb/^{204}Pb$ (37.3 to 38.2). There does not appear to be any correlation between rock type and Pb isotopic composition for the Tunka, Tuva or Oka volcanic fields.

$^{206}Pb/^{204}Pb$ - $^{87}Sr/^{86}Sr$ and $^{206}Pb/^{204}Pb$ - ε_{Nd} diagrams are shown in Figure 2.16. The majority of data for the Tunka, Tuva, and Oka volcanic fields falls on a trend of slightly increasing $^{87}Sr/^{86}Sr$ and decreasing ε_{Nd} with changing $^{206}Pb/^{204}Pb$. There is a weaker trend of greatly increasing $^{87}Sr/^{86}Sr$ and decreasing ε_{Nd} with a smaller change in $^{206}Pb/^{204}Pb$, in particular for the Oka field. The combination of the two trends gives the data a roughly triangular shape on the $^{206}Pb/^{204}Pb$ - $^{87}Sr/^{86}Sr$ and - ε_{Nd} diagrams.

DISCUSSION

Origin of volcanic rocks of the western BRZ

One of the most remarkable features of the lavas of the western BRZ is their relative homogeneity in major element compositions (Fig. 2.5) when compared to other occurrences of continental volcanic rocks. In particular, unlike the other occurrences of continental volcanism in Asia, such as those in eastern China studied by Zhi et al. (1990) and Peng et al. (1986) which are bimodally split between tholeiitic and alkaline

compositions, the BRZ is almost completely devoid of tholeiitic compositions. Additionally, with the exception of the Udokan Volcanic Field, the BRZ also lacks the highly evolved felsic series of rocks (trachytes, phonolites, rhyolites) present in other rifts such as the East African Rift. This restricted compositional range and lack of tholeiitic compositions is strong evidence that the melting process and depth of melting has been quite consistent over the history of the BRZ.

Inspection of the MgO variation diagrams (Fig. 2.7a-c) shows that while there are covariation trends with the other major oxides, most of the samples have a fairly restricted range of MgO content (7 - 9%), although there is a sizable amount of scatter in the other major oxides for this range in MgO. Correlations between MgO% and the major oxides Al_2O_3, Na_2O, and CaO (Fig. 2.5a-c), as well as with the CaO/Al_2O_3 ratio and compatible trace elements (Ni, Cr, Co) (Fig. 2.12a-c) demonstrate that fractional crystallization of pyroxene, olivine, and plagioclase from a parental melt has been an important control on composition. The range in Mg# for the western BRZ lavas (47 to 68) (Fig. 2.6) indicates that the lavas have evolved to varying degrees from their original parental melt composition. The Tuva volcanic field also shows a trend of decreasing Mg# with increasing degree of silica undersaturation (normative nepheline) (Fig. 2.6), indicative of fractional crystallization.

Another way to look at the evolution of the lavas is with a plot of the differentiation index (DI = normative quartz + nepheline + orthoclase + albite) versus Mg# (Fig. 2.17). For a normal fractional crystallization sequence, the DI should increase with decreasing Mg#, as is the case for the western BRZ lavas. This diagram illustrates

that the Tuva lavas are restricted to a DI > 38, as opposed to the other two volcanic fields which start with a DI of 30. The explanation for this difference may be that the Tuva lavas were generated at higher pressure and had more time to undergo fractional crystallization prior to eruption, or stagnated for some time in a shallow magma chamber, so that the lower DI melts are not represented on the surface. Additionally, since the Tuva lava field is one of the youngest regions in the BRZ (Rasskazov et al., 1989; Table 2.1), the more restricted range in DI may reflect the fact that it is more difficult for melts to reach the surface in the Tuva area because magmatic conduits have not been established for as long as they have been in the Oka and Tunka volcanic fields.

There is a general lack of consensus on the pressure and temperature at which continental alkaline rocks are generated. The majority of experimentally calibrated models for magma generation were developed to explain the variation in major element geochemistry along mid-ocean ridges. One such model, developed by Yang et al. (1996) on the basis of natural and basalt-analog experiments, describes temperature, Al, Ca, and Mg molar fractions as a function of Si, Fe, Na, Ti, and K molar fractions and pressure. Since the majority of BRZ rocks are silica undersaturated, we can only try this model for a small subset of the samples which are hypersthene normative. To estimate the pressure at which the melts were saturated with olivine, plagioclase, and augite, we compared the observed composition with a range of compositions calculated at different pressures using the equations of Yang et al. (1996). This is best accomplished by plotting compositions on the Ol-Cpx-Qtz ternary using the projection scheme of Grove et al. (1993).

In Figures 2.18a-e, the resulting ternary plots are shown for samples from the Oka Plateau and Tunka Basin (no samples from Tuva were hypersthene normative). Also shown in the figures are the best estimate for pressure, and the corresponding calculated temperature for each sample. The results seem to be remarkably consistent. The Tunka Basin samples range in pressure from 7.5 to 9 kbar and 1195 to 1217° C. The alkaline Oka Plateau samples range in pressure from 5.5 to 8 kbar and 1183 to 1216°C, while the tholeiitic sample (OP-9) is estimated at 4 kbar and 1162°C. Samples BK-208, 209, 211, and 212 are from a continuous sequence of basalts, with BK-208 being the stratigraphically highest flow. It appears that the lower flows BK-211 and BK-212 give a lower pressure than the higher flows BK-208 and BK-209.

The pressures and temperatures calculated according to Yang et al.'s (1996) model correspond to depths of ~19 to 30 km for the alkaline samples , and ~13 km for the tholeiitic samples. Estimated crustal thicknesses for the BRZ, based on gravity and seismic data (Zorin et al., 1989; Gao et al., 1994), are from <30 km beneath Lake Baikal, to ~45 km on the rift flanks. Beneath the western BRZ, however, crustal thickness is estimated to be between ~42 and 45 km. Lithospheric thickness (depth to anomalous mantle) ranges from 30 km beneath Lake Baikal (i.e., there is no lithospheric mantle), to >150 km beneath the rift flanks and the Siberian craton. However, in most of the Baikal area the estimated lithospheric thickness is ~50 km, indicating that there is not much lithospheric mantle present, or that the lithospheric mantle has been thermally converted to asthenospheric mantle and is therefore indistinguishable from upwelling mantle. Accordingly, the pressures calculated by Yang et al.'s (1996) model indicate the magmas

were last olivine-plagioclase-augite saturated at depths within the sub-BRZ crust. Because it is highly unlikely that the melts were produced within the crust, since they contain upper mantle xenoliths, the calculated pressures may reflect the depth of the crustal magma chambers in which fractional crystallization occurred. Unfortunately, there is no good way to try to back-calculate the fractional crystallization sequence of these rocks to get to a "primary" melt composition for several reasons: 1) there are no samples that appear to be "parental" melts for these sequences, 2) the sequences of plateau lavas in the western BRZ can be up to 500 m thick, but usually show little stratigraphic variation that would be useful for calculation of a fractional crystallization trend (see Figures 2.23a-d), and 3) it does not seem geologically reasonable to make up for this lack of local geochemical variation by trying to relate samples erupted hundreds of kilometers apart, and of different ages. Therefore the calculated pressures must be considered minimum pressures (and temperatures). An additional caveat is that Yang et al.'s model was developed for anhydrous, oceanic rocks quite different from the BRZ alkaline rocks which have an order of magnitude more K. The affect of the higher proportion of K is not known.

The pattern of enrichment of LREE over HREE (Fig. 2.8) indicates that either garnet is residual in the source region, or that the magmas originated from small degree partial melts of the source. $(La/Yb)_N$ ranges from 3 to 16, and decreases with decreasing Mg# (Fig. 2.19). This trend does not support fractional crystallization of garnet from the parental melt in the evolution of the magmas, since crystallization of garnet would

decrease the amount of HREE in the melt and increase the $(La/Yb)_N$ ratio. The basaltic andesite clearly was formed by a different process than the alkaline rocks.

Comparison of the Tunka, Oka Plateau, and Tuva volcanic fields

As discussed above, the major element chemistry of the Tunka, Oka Plateau, and Tuva volcanic fields are very much alike. However, there are some systematic differences in the isotopic signatures of the three fields. Although the range in isotopic ratios for each field is quite similar, the Tuva volcanic field has $^{87}Sr/^{86}Sr$ offset to less radiogenic values for a given ε_{Nd} when compared to the other fields (Fig. 2.14), including the range for lavas from the Dzhida volcanic field as reported by Housh et al., (in prep.). The difference also extends to the Pb isotopic system, where Tuva lavas have consistently lower $^{208}Pb/^{204}Pb$ for a given $^{206}Pb/^{204}Pb$ compared to the Oka Plateau and Tunka volcanic fields (Fig. 2.15).

Crustal contamination?

The consistency in major and trace element variations for lavas of the western BRZ argues against significant amounts of crustal contamination, although the high abundances of K, Na, Ba, and Sr may reflect derivation from a metasomatized source region. The high abundance of Sr in many of the lavas (400-1000ppm) means that assimilation of crustal material would not have much of an affect on the Sr isotopic composition. Likewise, the Nd abundance of the BRZ lavas is higher than typical MORB, although interaction with a highly LREE enriched crustal rock might affect the Nd isotopic composition. Mixing with a typical Archean or Proterozoic granitic rock

with $\varepsilon_{Nd} < -30$ would significantly alter the Nd isotopic composition. However, we do not observe $\varepsilon_{Nd} < -1$ in the western BRZ (Fig. 2.14, Table 2.3a-c). For volcanic rocks, the Pb isotopic system is the most sensitive to crustal contamination because of the extremely low concentration of Pb in volcanic rocks (~1-3 ppm) compared to crustal rocks. There does appear to be more variability in the Pb isotopic data than the Sr and Nd isotopic data, suggesting that some crustal contamination has occurred, but the range in measured Pb isotopic compositions is well within the range observed for OIB.

Implications for the western BRZ source region

The isotope geochemistry of the western BRZ volcanic rocks is comparable to that for ocean island basalts. Most of the variation in Sr and Nd isotopic compositions can be explained by mixing between a depleted MORB mantle component (DMM) and an enriched mantle type I component (EMI) (Hart, 1988) (Fig. 2.14). The samples with higher $^{87}Sr/^{86}Sr$ for a given ε_{Nd} could possibly be explained by mixing between a DMM component and sediment or other crustal component. The $^{206}Pb/^{204}Pb$ -$^{207}Pb/^{204}Pb$ and $^{206}Pb/^{204}Pb$ -$^{208}Pb/^{204}Pb$ diagrams (Figure 2.15) illustrate that all the western BRZ samples (with the exception of a few samples from Tuva) plot above the Northern Hemisphere Regression Line (Hart, 1984). A few samples from the Tunka Basin and several from the Oka Plateau have isotopic compositions similar to the proposed EMI end-member component, with $^{206}Pb/^{204}Pb$ between 17.6 and 17.7, $^{207}Pb/^{204}Pb$ between 15.46 and 15.49, and $^{208}Pb/^{204}Pb$ between 38.0 and 38.2 (Hart, 1988). All other western BRZ volcanic rock data can be explained by mixing between an EMI component and a typical

MORB or DMM component. The data array does not extend to the more radiogenic Pb ratios that would indicate mixing with an EMII component. The $^{206}Pb/^{204}Pb$ - $^{87}Sr/^{86}Sr$ diagram also illustrates that most data occur on a mixing line between DMM and an EMI component. The samples which trend to higher $^{87}Sr/^{86}Sr$ do not have the radiogenic $^{206}Pb/^{204}Pb$ needed to indicate mixing with EMII (Fig. 2.16). The $^{206}Pb/^{204}Pb$ - ε_{Nd} diagram also illustrates this point (Fig. 2.16).

The fact that most of the western BRZ data plot above the NHRL gives them a DUPAL-like Pb isotopic signature (Fig. 2.15). Hart (1984) first defined the DUPAL anomaly based on the global distribution of a belt of southern hemisphere oceanic basalts with high $^{87}Sr/^{86}Sr$ (> 0.705) and Pb isotopic ratios above the NHRL. Since then, the DUPAL anomaly has also been observed in Northern Hemisphere oceanic basalts as well as continental basalts (South China Basin: Tu et al., 1992; Flower et al., 1992; the Philippines: Chen et al., 1990; Mukasa et al., 1987; Taiwan: Chung and Sun, 1992; Chung et al., 1995). Because the BRZ lavas mostly do not have $^{87}Sr/^{86}Sr > 0.705$, they cannot be strictly considered DUPAL-like. However, many of them do have $\Delta^{208}Pb/^{204}Pb$ (deviation from the NHRL) > +60 (Fig. 2.20). As seen on the $\Delta^{208}Pb/^{204}Pb$ - $^{87}Sr/^{86}Sr$ diagram (Fig. 2.20), many of the lavas lie along the EMI branch, which is the line for mixing between DMM and an EMI component (Hart, 1988). The high $^{87}Sr/^{86}Sr$ samples lie along the EMII branch (lines takens directly from Hart, 1988), although as described earlier they do not have radiogenic enough Pb isotopic ratios to actually be mixing with EMII.

Allègre and Turcotte (1985) proposed that the DUPAL anomaly was related to recycling of sediments and delamination of subcontinental lithosphere in subduction zones related to repeated cycles of continental break-up and assembly concentrated at the lower latitudes. Hart (1988), however, speculated that the anomaly was metasomatic in nature, and was related to upwelling originating at the core/mantle boundary layer. The existence of a DUPAL-like signature in continental alkaline volcanic rocks can be interpreted in several ways: 1) global mantle convection and recycling of sediments has redistributed the subduction-zone/DUPAL anomaly characteristics to the asthenosphere beneath the continents, 2) the signature is derived from subcontinental plumes, or 3) since the DUPAL signature may be caused by mixing of DMM with two types of continental lithosphere (upper crust = EMII, and subcontinental lithospheric mantle = EMI), the DUPAL-like isotopic characteristics have been derived directly from the base of the lithosphere by delamination due to lithospheric thinning or thermal conversion/erosion due to a regional thermal anomaly. A higher proportion of mixing with an EMI component over an EMII component in continental volcanic rocks could explain their Pb isotopic DUPAL signature without the same Sr isotopic DUPAL signature (i.e., $^{87}Sr/^{86}Sr > .705$) as oceanic rocks. Continental rift zones, such as the BRZ, are clearly areas where the source of EMI (the subcontinental lithospheric mantle) is readily available.

Temporal variation in geochemical characteristics

The temporal variation in geochemical characteristics of rift-related volcanic rocks may have significant implications for the process of rifting. Studies of other rifts, such as

the Rio Grande Rift of North America (Gibson et al., 1992; Lipman et al., 1989), have revealed that lavas became progressively less radiogenic in Sr and more radiogenic in Nd isotopic composition with time, i.e., became more "asthenospheric", or like the source of normal MORB. A proposed explanation for this variation is that it was more difficult for early magmas to make it through the crust, and therefore they had more time to evolve in shallow magma chambers or interact with the crust, as well as melting out any easily fusible components in the crust. As rifting progressed, the lithosphere thinned and magmatic conduits became well-established, making it easier for magmas to erupt through the crust without interaction, and leading to a clearer asthenospheric signature.

We obviously would like to know whether this sort of temporal relationship exists for the BRZ. Although there is limited absolute age information, we can classify most of the analyzed western BRZ rocks by known or assumed time period (Oligocene, Miocene, Pliocene, Quaternary). The isotopic data are thus plotted as a function of time period in Figure 2.21.

As seen in Figure 2.21, condensing data for all lavas from time periods that span up to 15 million years results in a wide range in isotopic ratios for each time period. The range in $^{87}Sr/^{86}Sr$ appears to increase from the Oligocene to the Pliocene, as does the maximum measured $^{87}Sr/^{86}Sr$, followed by a drastic decrease in the Quaternary. The range in ε_{Nd} is greatest during the Miocene. This is also the time period with the lowest measured ε_{Nd} (-1). The Pliocene and Quaternary rocks have approximately the same range in ε_{Nd}. The plot of time period versus $^{206}Pb/^{204}Pb$ shows the most dramatic trend of the three isotopic systems: the lowest $^{206}Pb/^{204}Pb$ measured for each time period

increases from the Miocene to the Quaternary. The Miocene rocks have the largest range in Pb isotopic composition, and include the most radiogenic Pb isotopic compositions of any of the time periods.

Based on the newly acquired $^{40}Ar/^{39}Ar$ data of this study (summarized in Table 2.1; details in Appendix 2.B), as well as some age information taken from the Russian literature (see Table 2.4), it is also possible to look at the variation in isotopic ratios as a function of a well-defined age for some of the samples. The majority of samples with well-known ages are from the Oka Plateau volcanic field. In Figure 2.22, it can be seen that there is some variation in isotopic composition for each age increment. It appears that the $^{87}Sr/^{86}Sr$ ratio may have decreased through time (from 20 to 5 Ma) for the Oka volcanic field, followed by a sharp increase in $^{87}Sr/^{86}Sr$. The youngest samples are often the ones which flowed down into river valleys incised in the Miocene lava plateau, and may have been more susceptible to weathering. The two Oka samples that have elevated $^{87}Sr/^{86}Sr$ and are ~ 5 Ma (93-OP-3, 93-OP-3A; Table 2.1b) are young flows sitting very near to the present-day river level. However, these samples also have relatively high Sr concentration (1141 and 727 ppm, respectively), so it would be very difficult for their Sr isotopic composition to have been disturbed, for example, by interaction with carbonate-rich river water. The youngest samples, from the Tuva volcanic field, are some of the least radiogenic of the set of samples of known age, although some Miocene age Tuva lavas have almost identical Sr isotopic composition.

The variation in ε_{Nd} with time (Fig. 2.22) is very intriguing because it appears that the Oka Plateau lavas have systematically become less radiogenic (lower ε_{Nd}) with time.

This contrasts with the trend (at Oka) toward less radiogenic Sr with time, since the two isotopic systems are usually anti-correlated. This raises two possibilities - either 1) there is a trend to higher (more radiogenic) $^{87}Sr/^{86}Sr$ with time, or 2) the observed trend is merely a coincidental result of our limited sampling. The Nd isotopic compositions of the Tuva and Tunka lavas are quite scattered and not correlated with age. The Pb isotopic composition is highly variable for each given time increment. As discussed previously, this is most likely a result of the greater sensitivity of the Pb isotopic system to mixing with a component with much higher Pb concentration, such as a crustal contaminant.

Another approach to the question of the temporal evolution of BRZ magmas is to look in greater detail at the stratigraphic sequences of lavas (Fig. 2.23a-d). There are four such sequences in the Oka Plateau volcanic field (Fig. 2.3): a sequence from the Kitoy Ridge (BK-201 to 207), a sequence above the Bokson River (BK-218 to BK-208), a sequence above the Shibit River (BK-229 to BK-224), and a sequence above the Tissa River (BK-316 to BK-320). From top to bottom for the Kitoy Ridge sequence (Fig. 2.23a), $^{87}Sr/^{86}Sr$ increases from 0.70430 to 0.70518, ε_{Nd} ranges from +2.1 to +2.9, and $^{206}Pb/^{204}Pb$ increases from 17.91 to 18.02. The Bokson River sequence(Fig. 2.23b) has a range in $^{87}Sr/^{86}Sr$ from 0.70414 to 0.70570, ε_{Nd} from +0.16 to +2.77, and $^{206}Pb/^{204}Pb$ from 17.42 to 17.88. The Sr isotopic composition of the stratigraphically higher (younger) Bokson River lavas is less radiogenic than the lower (older) samples, although the Nd isotopic composition remains almost the same for the whole sequence. The youngest samples have a significantly less radiogenic Nd isotopic composition. The Pb isotopic composition for the Bokson River sequence remains essentially steady. Lavas of the

Shibit River (Fig. 2.23c) sequence fluctuate slightly from top to bottom, with no clear trend, with $^{87}Sr/^{86}Sr$ from 0.70416 to 0.70465, ε_{Nd} from 0.25 to 2.64, and $^{206}Pb/^{204}Pb$ from 17.72 to 18.04. The Tissa River sequence (Fig. 2.23d) samples show a trend of slightly increasing $^{87}Sr/^{86}Sr$ with time, from 0.70429 to 0.70450. The Nd isotopic composition remains nearly constant until the last sample (BK-320) which has more radiogenic Nd (ε_{Nd} = +2.8). The same is true of the Pb isotopic composition, with the top lava having a more radiogenic composition with $^{206}Pb/^{204}Pb$ = 17.82.

The lack of dramatic changes in isotopic composition from top to bottom for each of the discussed lava sequences is not unexpected, since these lavas were probably erupted within a fairly short time period and are of very similar composition. The Sr isotopic composition seems to exhibit the largest variation, and for the Bokson River and Kitoy Ridge sequence appears to become less radiogenic with time. The Tissa River sequence exhibits the opposite trend.

While it is a useful exercise to look in detail at the geochemical variation in these stratigraphic series of samples, the lack of significant variation due to the short time-span covered by these eruptions illustrates once more the need to develop a larger data base of absolute age information for the BRZ. It is tempting, even at this early stage of geochronologic data collection, to speculate on the cause of the apparent trend to less radiogenic Nd isotopic compositions for the Oka volcanic field, which if real is the exact opposite of the trend observed for the Rio Grande Rift. One possible explanation could be that since the major eruptions in the Oka volcanic field occurred during the Miocene, followed by a hiatus, the youngest Oka lavas represent a renewed episode of volcanism

that was derived from a different source. Volcanism did not develop synchronously in all parts of the rift, or with position along strike, nor was it by any means continuous. Rather, episodic pulses of magmatism occurred, so the temporal variation must be interpreted accordingly.

The BRZ is continuing to grow, with rifts propagating away from each end of the rift zone, as evidenced by earthquake activity and development of new fault scarps (Solonenko, 1978). The Tuva volcanic field contains some of the youngest BRZ volcanic rocks in its large post-plateau shield volcanoes (Rasskazov et al., 1989). The study of this large volcanic field is only just barely beginning, and results of new $^{40}Ar/^{39}Ar$ studies may reveal as yet undiscovered extremely young volcanism.

CONCLUSIONS

The large amount of data presented here for rocks from three different volcanic fields of the western BRZ has produced an unexpected outcome: the major element, trace element, and Sr, Nd, and Pb isotopic compositions are overall quite similar, despite the wide variation in age and type of lithosphere through which the lavas erupted. This is quite convincing evidence that crustal contamination has not had a significant impact on the geochemistry of the western BRZ volcanic rocks. Rather, the BRZ lavas appear to have been derived from a fairly homogeneous mantle source.

Correlations between MgO and major oxides (Fig. 2.7a-c), as well as CaO/Al_2O_3, and compatible elements (Fig. 2.12a-c) indicate that fractional crystallization of pyroxene, olivine, feldspar, and minor Fe-Ti oxide occurred to produce the observed geochemical

variations. A moderate enrichment of LREE over HREE (Fig. 2.8) suggests that the source region may contain residual garnet, although it is more likely that the LREE enriched pattern is caused by small degrees of partial melting.

Although the western BRZ lavas of all three volcanic fields are quite similar, there are small systematic differences between the three volcanic fields. The Tuva volcanic field has $^{87}Sr/^{86}Sr$ offset to slightly less radiogenic values for a given ε_{Nd} compared to the other fields (Fig. 2.14). Also, Tuva lavas are restricted to higher differentiation values (Fig. 2.17) and have the most extreme relative enrichments and depletions in incompatible elements (Fig. 2.11). These features may indicate that the Tuva lavas were derived from higher pressures, and may have evolved more significantly during ascent or stagnation in lower-pressure magma chambers.

Based on the data of this study, the temporal evolution of the isotopic composition of the western BRZ lavas appears to be the opposite of that observed in other rifts, such as the Rio Grande Rift (Gibson et al., 1992). The western BRZ lavas increased in $^{8}7Sr/^{86}Sr$ and decreased in ε_{Nd} from the Oligocene to the Pliocene, followed by a steep drop in $^{87}Sr/^{86}Sr$ in the Quaternary, so did not become more "asthenospheric"; rather they became more "lithospheric". It is difficult to discern whether the Pb isotopic composition became more or less radiogenic, although the range in Pb isotopic composition certainly became more restricted. The temporal evidence could be interpreted in two ways: 1) as the level of volcanic activity tapered off and became more sporadic from the Miocene to the Pliocene, perhaps the magma conduits had to be reestablished or the lithosphere cooled, leading to more interaction between the ascending

melts and the crust, or 2) as rifting progressed and extension increased, *more* of the lithosphere was mixed into the upwelling asthenosphere by either delamination or thermal conversion. As discussed in the section on implications for the source region, the DUPAL-like Pb isotopic signature of the BRZ lavas (in particular the evidence for mixing with an EMI component) certainly supports considerable involvement of the lithospheric mantle. Based on the data of this study as well as common sense spatial arguments related to the thinning of the lithosphere (where is the lithosphere going if not into the mantle?), I would predict that the geochemistry of western BRZ volcanic rocks is controlled by input from the lithosphere, and will fluctuate between "asthenospheric", (more DMM-like) and "lithospheric" (EMI-like) compositions based on the rate and continuity of the rifting process. Clearly, additional geochronologic data as well as more isotopic data for Quaternary volcanic rocks would help to resolve this question, since progressive incorporation of lithospheric mantle beneath the rift would require the Pb isotopic compositions to become more EMI-like.

REFERENCES

Allègre, C. J., and Turcotte, D. L., 1985, Geodynamic mixing in the mesosphere boundary layer and the origin of oceanic islands: Geophysical Research Letters, v. 12, p. 207-210.

Cebula, G. T., Kunk, M. J., Mehnert, H. H., Naeser, C. W., Obradovich, J. D., and Sutter, J. F., 1986, The Fish Canyon Tuff, a potential standard for the ^{40}Ar/39Ar and fission-track dating methods, in Sixth International Conference on Geochronology, Cosmochronology and Isotope Geology.

Chen, C.-H., Shieh, Y.-N., Lee, T., Chen, C.-H., and Mertzman, S. A., 1990, Nd-Sr-O isotopic evidence for source contamination and an unusual mantle componentunder Luzon Arc: Geochimica et Cosmochimica Acta, v. 54, p. 2473-2483.

Chung, S.-L., and Sun, S.-s., 1992, A new genetic model for the East Taiwan Ophiolite and its implications for Dupal domains in the Northern Hemisphere: Earth and Planetary Science Letters, v. 109, p. 133-145.

Chung, S.-L., Jahn, B.-M., Chen, S.-J., Lee, T., and Chen, C.-H., 1995, Miocene basalts in northwestern Taiwan: evidence for EM-type mantle sources in the continental lithosphere: Geochimica et Cosmochimica Acta, v. 59, p. 549-555.

Couture, R. A., Smith, M. S., and Dymek, R. B., 1993, X-ray fluorescence analysis of silicate rocks using fused glass discs and a side-window Rh source tube: accuracy, precision and reproducibility: Chemical Geology, v. 110, p. 315-328.

Eggins, S. M., Woodhead, J. D., Kinsley, L. P. J., Mortimer, G. E., Sylvester, P., McCulloch, M. T., Hergt, J. M., and Handler, M. R., 1997, A simple method for the precise determination of ≥ 40 trace elements in geological samples by ICPMS using enriched isotope internal standardisation: Chemical Geology, v. 134, p. 311-326.

Flower, M. F. J., Zhang, M., Chen, C.-Y., Tu, K., and Xie, G., 1992, Magmatism in the South China Basin 2. Post-spreading Quaternary basalts from Hainan Island, south China: Chemical Geology, v. 97, p. 65-87.

Gibson, S. A., Thompson, R. N., Leat, P. T., Dickin, A. P., Morrison, M. A., Hendry, G. L., and Mitchell, J. G., 1992, Asthenosphere-derived magmatism in the Rio Grande rift, western USA: implications for continental break-up, in Storey, B. C., Alabaster, T., and Pankhurst, R. J., eds., Magmatism and the Causes of Continental Break-up, Geological Society Special Publication, V. 68, p. 61-89.

Govindaraju, K., 1987, 1987 compilation report on Ailsa Craig granite AC-E with the participation of 128 GIT-IWG laboratories: Geostandards Newsletter, v. 11, p. 203-255.

Hart, S. R., 1984, A large-scale isotope anomaly in the Southern Hemisphere mantle: Nature, v. 309, p. 753-757.

Hart, S. R., Gerlach, D. C., and White, W. M., 1986, A possible new Sr-Nd-Pb mantle array and consequences for mantle mixing: Geochimica et Cosmochimica Acta, v. 50, p. 1551-1557.

Hart, S. R., 1988, Heterogeneous mantle domains: signatures, genesis and mixing chronologies: Earth and Planetary Science Letters, v. 90, p. 273-296.

Hodges, K. V., Hames, W. E., Olszewski, W., Burchfiel, B. C., Royden, L. H., and Chen, Z., 1994, Thermobarometric and $^{40}Ar/^{3}9Ar$ geochronologic constraints on Eohimalayan metamorphism in the Dinggye area, southern Tibet: Contributions to Mineralogy and Petrology, v. 117, p. 151-163.

Ila, P., and Frey, F. A., 1984, Utilization of neutron activation analysis in the study of geologic materials, in use and development of low and medium flux research reactors., in Harlin, O. K., Clark, L., and von der Hardt, P., eds., Suppl. Atomkernenerg. Kerntech., p. 710-716.

Kiselev, A. I., 1987, Volcanism of the Baikal rift zone: Tectonophysics, v. 143, p. 235-244.

Le Bas, M. J., Le Maitre, R. W., Streckeisen, A., and Zanettin, B., 1986, A chemical classification of volcanic rocks based on the total alkali-silica diagram: Journal of Petrology, v. 27, p. 745-750.

Lipman, P. W., Logatchev, N. A., Zorin, Y. A., Chapin, E. E., Kovalenko, V., and Morgan, P., 1989, Intracontinental Rift Comparisons: Baikal and Rio Grande rift systems: EOS, Transactions American Geophysical Union, v. 70, p. 578-579, 586-588.

Logatchev, N. A., and Florensov, N. A., 1978, The Baikal system of rift valleys: Tectonophysics, v. 45, p. 1-13.

Logatchev, N. A., and Zorin, Y. A., 1987, Evidence and causes of the two-stage development of the Baikal rift: Tectonophysics, v. 143, p. 225-234.

Logatchev, N. A., and Zorin, Y. A., 1992, Baikal rift zone: structure and geodynamics: Tectonophysics, v. 208, p. 273-286.

Logatchev, N. A., 1993, History and geodynamics of the Lake Baikal rift in the context of the eastern Siberia rift system: a review: Bull. Centres Rech. Explor.-Prod. Elf Aquitaine, v. 17, p. 353-370.

Mukasa, S. B., McCabe, R., and Gill, J. B., 1987, Pb-isotopic compositions of volcanic rocks in the West and East Philippine island arcs: presence of the Dupal isotopic anomaly: Earth and Planetary Science Letters, v. 84, p. 153-164.

Peng, Z. C., Zartman, R. E., Futa, K., and Chen, D. G., 1986, Pb-, Sr- and Nd-isotopic systematics and chemical characteristics of Cenozoic basalts, eastern China: Chemical Geology, v. 59, p. 3-33.

Zindler, A., and Hart, S., Rasskazov, S. V., 1985, The Udokan Basaltoids: Novosibirsk, Nauka Publishers.

Rasskazov, S. V., Maslovskaya, M. N., Batyrmurzaev, A. S., Matsera, A. V., Zelenkov, P. Y., Avdeev, V. A., Omarova, M. R., Gargatsev, I. O., and Magomedov, S. A., 1989, Composition, strontium isotopy, and K-Ar dating of recent basalts of Tuva: Geologiya i Geofizika, v. 30, p. 77-85.

Rasskazov, S. V., Batyrmurzaev, A. S., and Magomedev, S. A., 1990, K-Ar dating of cenozoic basalts of the Oka tableland (eastern Sayan): Geologiya i Geofizika, v. 31, p. 100-105.

Rasskazov, S. V., 1993, Magmatism of the Baikal rift zone: Novosibirsk, Nauka, 273 p.

Rasskazov, S. V., 1994, Magmatism related to the eastern Siberia rift system and the geodynamics: Bull. Centres Rech. Explor.-Prod. Elf Aquitaine, v. 18, p. 437-452.

Rasskazov, S. V., Boven, A., Andre, L., Liegeois, J.-P., Ivanov, A. V., and Punzalan, L., 1997, Evolution of magmatism in the northeastern Baikal Rift system: Petrologiya, v. 5, p. 115-136.

Rhodes, J. M., 1983, Homogeneity of lava flows: chemical data for historic Mauna Loan eruptions: Journal of Geophysical Research, v. 88 (Suppl.), p. A869-A879.

Sherman, S. I., 1978, Faults of the Baikal rift zone: Tectonophysics, v. 45, p. 31-39.

Solonenko, V. P., 1978, Seismotectonics of the Baikal rift zone: Tectonophysics, v. 45, p. 61-69.

Sun, S., and McDonough, W. F., 1989, Chemical and isotopic systematics of oceanic basalts: implications for mantle composition and processes, in Saunders, A. D., and Norry, M. J., eds., Magmatism in the Ocean Basins, Geological Society Special Publication, V. 42, p. 313-345.

Tu, K., Flower, M. F. J., Carlson, R. W., Xie, G., Chen, C.-Y., and Zhang, M., 1992, Magmatism in the South China Basin 1. Isotopic and trace-element evidence for an endogenous Dupal mantle component: Chemical Geology, v. 97, p. 47-63.

Zhi, X., Song, Y., Frey, F. A., Feng, J., and Zhai, M., 1990, Geochemistry of Hannuoba basalts, eastern China: constraints on the origin of continental alkalic and tholeiitic basalt: Chemical Geology, v. 88, p. 1-33.

Zindler, A., and Hart, S., 1986, Chemical geodynamics: Annual Reviews in Earth and Planetary Science, v. 14, p. 493-571.

Zorin, Y. A., Kozhevnikov, V.M., Novoselova, M.R., and Turutanov, E.K., 1989, Thickness of the lithosphere beneath the Baikal rift zone and adjacent regions: Tectonophysics, V. 168, p. 327-337.

APPENDIX 2.A: ICP-MS ANALYTICAL METHODS

100 mg of whole-rock powders were dissolved in a two step HF-HNO_3-HCl process in Teflon beakers, following a procedure modified after Eggins et al (1997). After complete dissolution and dilution to 200 mL, the samples were spiked with a mixed solution of Se, In and Bi as internal drift correction standards. Solutions of the whole-rock samples were introduced into the plasma by standard nebulization using a peristaltic pump with a sample uptake rate of 0.75 ml/min, a nebulizer gas flow of 0.75 L/min, auxiliary gas flow of 0.9 L/min, and a coolant gas flow of 14 L/min. Using an autosampler, up to 44 samples were analyzed during each analytical session including drift monitors, blanks, calibration standards, and unknowns. Time and mass-dependent variations in machine sensitivity were monitored and corrected for using a combination of internal standards and external monitor solutions run periodically (every 4 - 5 samples) during the course of each analytical session. Analytical blanks were negligible for all masses analyzed, not exceeding 0.5% of the total counts for each mass. Calibration curves were generated using multiple USGS rock standards analyzed during each analytical session. Accepted values for the elements in these rock standards were taken from the compilations of Govindaraju (1987) and Eggins et al. (1997). Regression lines forced through the origin consistently gave correlation coefficients >0.995. Analytical precision and accuracy were estimated from multiple analyses of standard reference materials analyzed as unknowns over the course of the analytical work. Based on repeat analyses of standards, detection limits range from <1-10 ng/g for elements with mass >80

amu, and <10 ng/g to 1 μg/g for elements with mass <80 amu. Analytical precision (1σ) for elements with mass >80 amu is <2% RSD (relative standard deviation), and that for elements with mass <80 amu is <4% RSD. Residuals between average and accepted values for all elements commonly were less than the estimated analytical precision, confirming the quality of the data. Additionally, as a check on reproducibility, a number of aliquots both from the same prepared solution and from different dissolutions of the same sample were analyzed. In all cases the values obtained for these samples were in agreement within the estimated analytical precision.

APPENDIX 2.B

$^{40}Ar/^{39}Ar$ GEOCHRONOLOGY: TECHNIQUES AND RESULTS

Argon Technique

Since most BRZ volcanic rocks do not contain large or abundant phenocrysts of feldspar, a whole-rock basalt $^{40}Ar/^{39}Ar$ method was applied. The freshest and most fine-grained samples were selected for dating. One set of samples was analyzed in 1995, and a second set in 1997. In both cases, samples were finely crushed with a mortar and pestle and then sieved to 500 μm mesh size, followed by ultrasonic cleaning in ethanol to remove adhering powder. Samples analyzed in 1997 were prepared with a modified procedure to improve the quality of analytical material. After crushing, sieving, and ultrasonic cleaning in ethanol, a Franz magnetic separator was used to remove any olivine because olivine has been found to cause problems with excess Ar. Any other visible phenocrysts or more magnetic material was also magnetically removed. ~100 mg of sample was packaged for irradiation. All samples were irradiated at the research reactor at McMaster University. Fast neutron flux was monitored using Fish Canyon sanidine (27.95 Ma; Cebula et al., 1986). Irradiated samples were analyzed on a resistance-furnace gas-extraction system and MAP 215-50 mass spectrometer at the Cambridge Laboratory for Argon Isotopic Research at MIT. See Hodges et al. (1994) for a thorough discussion of the laboratory procedures. All samples were analyzed by furnace step-heating. Four steps were measured for 1995 samples, and six steps for 1997 samples.

Results

$^{40}Ar/^{39}Ar$ results for rocks from the Oka Plateau and Tuva volcanic fields are listed in Table 1. Most samples give plateau dates and inverse isochron dates which agree with each other within error. The isochron date is the preferred age in those instances. Several samples gave no plateau or isochron and therefore the ^{39}Ar weighted mean date is the best estimate. Two samples were irradiated in two different packages (BK-318 and BK-317) and the dates for these samples from the different irradiations give the same age within error.

A number of analyzed samples were purposely chosen from sequences of basalts where their relative stratigraphic position is known as a further check on the quality of the data. These four sequences are indicated in the data table by brackets, and samples within the brackets are listed in stratigraphic order (oldest at bottom). Samples 93-OP-3 and 93-OP-3A have the same age within error. For the series 93-OP-19 (bottom) to 93-OP-16 (top), the bottom two samples have the same age within error, while the top two samples (93-OP-15 and 93-OP-16) have progressively younger ages that are statistically different from each other and from the bottom two samples. In the sequence 93-OP-38 (bottom) to 93-OP-33 (top), the bottom three samples (93-OP-38, 37, 36) have the same age within error, 93-OP-36 and 93-OP-34 are the same age within error, and 93-OP-33 is significantly younger than the samples below it. In the sequence BK-316 (lowest) to BK-318 (highest), samples BK-317 and BK-318 have the same age within error. However, the stratigraphically lowest sample (BK-316) gives a younger age than the samples above it. Its ^{39}Ar weighted mean age is highlighted as the most reasonable age given that this

sample gave no plateau and the isochron is calculated with increments totaling <50% of the cumulative ^{39}Ar. Based on the additional information that BK-316 gives an age which conflicts with its stratigraphic position relative to two samples with very good analyses leads to the conclusion that the best estimate for its age is >16.50 ±.32 Ma, the age of the sample directly above it.

APPENDIX 2.C: SAMPLE DESCRIPTIONS

Tunka Basin Samples collected in 1988:

BK-1 alkali olivine basalt from Anchuk, Miocene volcanic neck. 51° 45.5, 103° 25.5

BK-2 Hawaiite dike cutting cinder cone, Talja village quarry, N. Tunka basin. 51° 50.0, 102° 28.5

BK-3 Basanite, Yelofski Spur of Khobok valley, Tunka basin.

BK-4a Hawaiite, uppermost in vertical traverse through Miocene section on right side of Khobok River. 51° 52.0, 102° 36.5
BK-4b Hawaiite, lower than BK-4a in same section.
BK-4c Hawaiite, lower than BK-4b in same section.
BK-5 Trachybasalt, base of section, below BK-4c.

BK-6a Trachybasalt with peridotite and pyroxenite xenoliths, on left side of Khobok River, same location as BK-5, same height.

BK-7 Basanite with peridotite and pyroxenite xenoliths, E. side of Zun-Murin River, SE margin of Tunka Basin (10.1 ± 0.5 Ma). : 51° 38.5, 102° 54.0
BK-8 Subalkaline basalt, same location as BK-7 but lower in section.
BK-9 Hawaiite, same location as BK-7, but higher than BK-7 (8.3±0.3Ma)

BK-10 Trachybasalt from southern part of Komar Ridge, next to Khamardaban Weather Station. 51° 32.0, 103° 34.5
BK-11 Subalkaline basalt, next flow up from BK-10.
BK-12 Subalkaline basalt, next flow up from BK-11.
BK-13 Subalkaline basalt, top of section above BK-12.

Samples collected in 1989 (from field notes of S. Bowring):

BK-100: Sawmill in valley of Zakirka River. Cretaceous (?) basalts. A lower porphyritic flow (plag, augite) overlain by an aphyric, vesicular flow. Sample is from porphyritic flow.

BK-101: Mugeraite with crustal xenoliths. One looked like limestone. Flows believed to be Jurassic (?). Seems questionable given freshness. Location is after fork in road after crossing Bartoy River, in watershed between Bartoy and Mila Rivers.

BK-102,103,104: Mike Dungan

Lowermost was 102- finest groundmass, olivine phenocrysts. Sergey reports that these sit on sequence of conglomerates. No flow contacts exposed, then 103 which was much coarser grained. 104- intermediate groundmass, vesicle fillings. 50, 46.0, 103, 25.5

BK-105: Basalt from top of ridge near (2km north) of village of Mila. Thought to be about 26 Ma. Overlies granite and diorite of proable Silurian-Devonian age.

BK-106: Basalt II or III? Sitting on BK-105. Down the ridge ~.2 mi. From massive core of flow, vesicular bottom and top.

BK-107: Flow III? down ridge .1-.2mi. From massive flow center. Each flow about 15-20m?

BK-108: Flow IV again from massive flow center.

105-108: 50°, 47.0', 103° 24.0'

BK-109: olivine + pyx bearing basalt which flooded valley just south of village of Mila. 50°, 44.0', 103°, 26.5'

BK-110: olivine-bearing basalt from south side of Mita River. Just other side of river from BK-109. Pyx looks fairly fresh. It is vesicular. 50° 43.0', 103° 27.0'

BK-111-116: Big section on hill with antennae south of Mita river. In watershed between Mita and Bartoy Rivers. 50°42.0', 103° 26.0'.
BK-111=1420m

These are all assumed to be Oligocene. Quite a bit of variation in mineralogy.

BK-112

BK-113

BK-114: contains megacrysts of plagioclase and olivine locally although not all that common. Range in size from 1-2mm for olivine to up to 10mm plagioclase.

BK-115: flow from near microwave tower

BK-116: From very top of hill (1580m)

BK-117: Distal Bartoy flow 200m north of Darkhintzy River. contains abundant megarysts of plag, pyx, and lherzolite inclusion. So distal it is basically a colluvium although this is as far from cone as we will see. 50° 38.5', 103° 26.0'

BK-118: Probable Devonian age granite which is probable basement to all basalts collected today. Contains very large phenocrysts of biotite, no hornblende visible. Outcrop from roadcut on road just opposite ultramagic. Watershed between Darkentey River and Sacerkivil Rivers. 50° 37.9', 103° 26.8'

8/16/89 - Zutamensk

BK-119: Sample of coarse-grained pyroxenite from Kchasurtey River - just opposite mouth of Dolon-moodon, not far from Mongolia
Pyroxenite occurs as large blocks within serpentinites. 50° 19.5', 103° 33.0'

BK-120: pillow basalt from ophiolitics sequence. Or Ubur inkur River . 50° 19.7', 103° 34.8'

BK-121: another pillow sample of basalt. 50° 19.7, 103° 34.0

BK-122: Tsakir cinder cone NE of Z. Took sample from core of bomb, reasonably fresh olivine present. 50°38.5, 103° 21.0

BK-123: pyroxene, olivine flow. Contains visible 5-10cm crustal xenoliths with quartz and feldspar. Large sample contains the xenolith. Both samples are from large blocks along river N of cone. 50° 29.5, 103° 22.0

BK-124: pyroxene, olivine flow about 500m N 30 E of cinder cone. 50° 29.5, 103° 22.0

Dzhida river:
BK-125: N side of Dzhida River - looks identical to BK-123,124. Its relationship to cinder cone is uncertain.

BK-126: aphanitic to slightly porphyritic flow apparently below 125. Separated by vesicular flow top.

BK-127: From bottom of the river - back to more porphyritic stuff. Could be settled equivalent of 126. No obvious breaks.
125-127: 50° 26.5', 103° 24.0.

8/17/89
Bartoy flows at intersection of Partanty River and Bartoy rivers. Top of hill is a basanite vescular with lherzolite inclusions.

BK-128: basanite with large anorthosite megacryst. Two samples hre, one is the host and remnant megacryst and the other is the separated megacryst. (Also added abundant xenocrysts and xenoliths:

3 anorthoclase + host rock
1 big augite
"d" 1 websterite with tape
"e" 1 large pyroxene
"f" kaersutite
"g" websterite
"h" garnet pyroxenite
"i" lherzolite

BK-129: basanite ~3m from top of flow or at least outcrop may be base of the flow. Contains anorthoclase and lherzolite xenoliths

BK-130: basanite as before, 1-2m from the top

BK-131: basanite underlain by coarser grained flow about 8m thick. It is some sort of alkali basalt

128-131: 50° 38.5', 103° 27.0'

BK-132: Sample of basanite near bridge over Bartoy River near the cones. Collected very large anorthoclase megacryst and host lava. Random sample of pyroxenite and garnet pyroxenite. 50° 43.0', 103° 18.0'

BK-133: Sample of vesicular basanite fro SW side of cone A. Chock full of xenocrysts. Olivine, pyroxene, anorthosite, and possible kaersutite. Sample came from bottom of circular trench. Bolshoi Cone=A

BK-134: Suite of xenocrysts from lava ta crest of cone A. Small crustal xenoliths, garnet anorthoclase, pyroxene. Sergey reports garnet megacrysts the size of baseballs. Also took a sample of
vesicular basalt with same number. 50° 43.0', 103° 17.5'

Ot Kriitiky= cone E

BK-135: From west side of cone along Bartoy River within largely spatter accumulation is large block of coherent material. 50°, 43.5', 103°, 17.5'

Razvalina= cone D

BK-136: from crest of cone (west side). contains large pyroxene megacrysts . One very large one is wrapped in toilet paper. Also one very large mica xenocryst also wrapped in toilet paper. 50° 43.5', 103° 16.0.

BK-137: sample of vesicular basanite with olivine megacrysts and autobreccieated blocks of less vesicular basalt. 50° 43.5', 103° 16.0.

Cone C: on south side of crest, vesicular, not the best in the world sample with lherzolite, pyroxene, and crustal xenoliths

BK-138: bag 1, bag 2 has two pieces of sheared lherzolite (first sheared stuff we have seen). 50° 43.0, 103° 15.5

8/18/89 Bartoy Field Part II

SE side of Bolshoi cone for lava sample that Sergey sent us to. Large boulders occur in the field along a road. Two slightly different samples, one slightly coarser grained or at least contains more lherzolite

BK-139: coarser more xenolith rich sample. 50° 43.5', 103° 18.0.

BK-140: finer grained

BK-141: xenoliths and xenocrysts from assorted blocks in area

BK-142: a collection of megacrysts from quarry at site of sample BK-132. 142g: tiny garnet- be very careful when unwrapping.
50° 43.0, 103° 18.0.

BK-143: samples of weird black shit. It could be some sort of glass as some of it has vesicles. Very strange. Head of the Geological Survey agrees that glass may be best explanation. These came from some quarry and then along the road. They are said to be very locally distributed. 50° 43.0', 103° 18.0.

BK-144: volcano Nizkii (low). sample of aphanitic basalt without much in way of inclusions. 50° 43.0', 103° 17.5.

BK-145: assorted xenocrysts from cone Razvolina (east flank) and cone B. Lots of garnet pyroxenites, garnet megacrysts, pyroxene megacrysts.

BK-146: bags of miscelaneous xenoliths collected by survey party from same place as BK-145. Mixture of Razvolina and drainage of cone B. (Combined with BK-145, so no BK-145) 50° 43.0, 103° 16.5

BK-148-153: From bottom to top sequence of probable Miocene basalts. Alkali olivine asalts with very rare deep seated inclusions. 50° 45.5', 103° 13.0'.

BK-154: on trip to train, tholeiitic basalt from Uleygchin River below its mouth where it enters Dzhida. 50° 27.5', 103° 19.5'

Samples collected from Oka Plateau in 1991 (from field notes of J. Luhr):

Kitoy River sequence (BK-201 to BK-207): cliff outcrop ~120m high, consists of many lava flows with vesicular tops and massive interiors. Many of the vesicular zones are badly altered with calcite and zeolites in vesicles and red-brown biotite disseminated. The biotite may have formed after smectite after olivine.
BK-201: ~2m dense lava
BK-202: platy zone above vesicular horizon above BK-201, and below a columnar horizon
BK-203: ~8m lava flow with 2m vesicular zone
BK-204: dense lava; ~8m flow with 2m vesicular zone
BK-205: from ~8m flow
BK-206: from a small 2-m high knob above BK-205
BK-207: lava from ~20m below top

Bokson River sequence (BK-208 down to BK-216):
BK-208: oliv + plag-rich basalt. In base many signs of quench rims on lava blocks
BK-209: cpx-rich lava, badly altered where vesicular.
BK-210 to BK-214: sequence of flows in descending order below BK-209; BK-213 is altered to a green color (smectite?) with only small core portions still blue.
BK-214 to 216: flows below ~50m grassy slope; have green alteration along numerous fracture planes.
BK-217: horizontal columnar basalt (see explanation below)
BK-218: piece from talus piles (see below)
BK-218A: piece collected later in trip to try to get fresher material; collected small pieces and 2 large blocks of freshest stuff.

Below BK-216 landscape becomes hummocky as if caused by landsliding. Nonetheless, coherent outcrops of flat-lying basalt can be found. Perhaps a falt along the base of the cliff has chopped up the landscape. At the base of the cliff are highly jointed basalts that show horizontal columnar jointing in the few remaining outcrops. Mostly they have disaggregated into talus piles of 30-100cm blocks. We interpret these jointed flows as younger than the cliff lavas, having travelled down an early canyon of the Bokson R., quenching against the canyon wall to form horizontal columns. These flows spread out on a morrainal terrace.

BK-219: Columnar jointed basalt on right side of road ~1-2km past Orlik. Basalt is ~5-6m thick and even when freshest shows dark sponts on light blue background. Plag may be large enough to separate for dating.
BK-220: from same outcrop, farther back towards Orlik, from vertical columns with no spotting.

BK-221, BK-222 (top flow) and BK-223 (lower flow): lava flows in Oka R. cliffs from Holocene flow front. Two different lava flows with columnar jointing. Total thickness 25-30m. According to Sergei, a section of these lava flows was studied up river. An early lava flowed down over sediments which were dated by TL as 12,000±4,000 yrs. The lava was then dissected before the main portion of the lava erupted, that which flowed 75km and which we collected. BK-223 is relatively vesicular and has a white mineral (calcite?) lining some vesicles and patches of green and white porous grains that may be hydrothermal.

Shibit River (BK-224 down to BK-229): 51°57.22',99°45.17'
BK-224: top of ridge on left side of river, relatively porphyritic cpx-oliv basalt, plag is relatively coarse-grained and might be dated.
BK-225: ~30m from summit is a black (hawaiite?) lava flow with small spinel lherzolite and small spinel crystals. Otherwise, very fine grained. Sergei has found this same laa in sections just to the E. Not very fresh, but we combined the blackest pieces from 6 or so different lava fragments.
BK-226: Next flow down is fine-medium grained gray lava with small vesicles. One granitic xenolith seen (2cm diameter).

Below BK-226 are 3 or 4 flows of similar appearance. Then comes the main cliff forming sequence. This is a series of vesicular lavas. Coarsely vesicular tops with fine vesicles (usually filled with green sheet silicates). Individual flows are 2-3m thicks, total sequence is ~40m. Some very prominent gas pipes filled with coarsely vesicular lava and interconnected with thin (2-10cm) horizontla veins of the same material. BK-227 is sample of this material.

BK-228: a black massivle lava flow ~40m thick below BK-227.
BK-229: ~30m of more vesicular, altered lavas with pipe strucutres and horizontal veins occur below BK-228. BK-229 is sample of more dense portion at base.

Upper Hore (Xore) River Cirque, left side (BK-230-238): 51°47.72', 99° 58'

BK-230: basalt flow ~25-30m thick; flow not present in the W, NW, SW, or S walls of cirque.. Contains much lherzolite debris. Many samples of spinel lherzolite, anorthoclase, and cpx megacryst also taken from this location.

BK-231 down to BK-237, sequence of flows that underlie BK-230:

BK-231: uppermost flow, lherzolite free, fine gray lava. Mostly very vesicular. Many subhorizontal vesicular zones. Sample from relatively dense layer ~2m from top.
BK-232: sequence continues downward for ~30m. Took another dense samples between vesicular zones.
BK-232, 233: Beneath BK-232, a basalt with small 1-2cm lherzolites and anorthoclase. Took anorthoclase sample for dating. Flow is ~2m thick.
BK-234: another similar flow with small lherzolite underlies BK-233, and is ~10m thick. Vesicular and hard to collect good sample.
BK-235: Beneath BK-234 is ~2m of vesicular lava and then comes this sample from ~12m of strongly jointed lava with both horizontal and vertical joints.
BK-236: first small ledge sticking out of talus below BK-235, contains small lherzolite
BK-237: ~15m below BK-236, last outcrop

BK-238: uppermost lava in the section is ~12m thick and forms a ridge from from the cirque rim to the north above BK-230.

BK-239: olivine rich young lava flow, 51°52.58', 99°52'30"
BK-240: another young lava flow, 51°54.5', 99°51.33'

BK-241: ~1/2km west of studied Shibit R. sequence. Here a canyon-filling lava flow forms a low terrace ~8km above the present river. A rather altered sample.

Hurugaycha Volcano E. of Mondi:
A hyaloclastic cone with black glass in yellow ash. Cone is cut by several dikes and a larger (conduit?) mass of lava, and overlain by several lava flows. The lavas flowed from this vent to SE in canyons. Thus landscape was dissected when it erupted. Spores and pollen of middle Miocene age were reported from sediments above these outlying lavas, and a K-Ar age of 16.5Ma was recently reported for a Hurugaycha lava. Other basalts in the same area have been dated at 15.7Ma.
BK-242: sample from conduit rock on W side of Hurugaycha River, just above talus slope.
BK-243: oldest lava flow in series of lavas with strong tilt (tectonic rotation) ~45°SE above hyaloclastite cone.
BK-244: Micro-vesicular flow above BK-243 with slightly brownish olivine.
BK-245: porphyritic lava moderately altered. Olivine is still fresh but some smectite is evident.
BK-246: highest basalt in the section is black, fine-grained basanite.

BK-247, 247A: ~5-10km E of Mondi in roadcut on N side of road is a coarse-grained basalt (diabase) with segregation veins and lenses of very coarse grained (ilmenite up to 1cm) vesicular material. Saw same basalt used for riprap and asphal in other places. BK-247 = basalt; BK-247A= segregation veins.

Samples collected from the Oka Plateau in 1992 (from field notes of S. Bowring and T. Housh):

BK-308: Sample of trachybasalt (lower) sitting on top of ophiolite marginal to Gargan block, 52° 08.52, 100° 21.40
BK-309: Sample of trachybasalt from middle flow of same outcrop as BK-308.
BK-310: Sample of trachybasalt from flow above BK-309.
BK-311: Sample of top trachybasalt flow in sequence. Zeolites present in flow breccia and vesicular basalt at base of top flow (BK-311). Therefore, according to Sergei Rasskazov, these flows are part of the older sequence (~16Ma).

BK-314: East bank of Tissa River, trachybasalts capping ridge. Lowermost flow is "dawgshit" but next one is pretty good. ~2170m, 52° 21.28, 99° 07.86
BK-315: Moved north about 200m to drainage. This is probably below 314 but hard to tell. Lots of vesicles, pretty much dawgshit.
BK-316: Next flow up, maybe ~= BK-314
BK-317: Next flow up, massive base, most of flow is vesicular. Looks pretty good.
BK-318: Next one up.
BK-319: Fairly fresh trachybasalt, about 8m above BK-318.

BK-320: Looks like top of the hill, trachybasalt with fresh plagioclase for dating, 2245m, 52° 21.47, 99° 08.06

BK-321, 322,323: Fresh mugearites overlying Shuttuly blocks, small anorthoclase xenocrysts in BK-323, 52° 24.29, 99° 08.10, 2302m

BK-328: Trachybasalt that sits in the river bottom. Fairly fresh. A few small inclusions. Sample is from an area known as Dodo Tergede. 52° 23.75, 99° 33.82, 1467m

Samples collected from Oka Plateau in 1993 (from field notes of N. Harris and D. Coleman):

93-OP-1: Hawaiite, finegrained, ~16Ma flow?, collected ~20m from contact with basement, basement is late Proterozoic, lower Cambrian limestone; ~10m from top of flow; most basalt very weathered, amygdoidal; sampled massive part of flow, 52° 05' 72", 100° 14' 64",

93-OP-2: Stop by road by Bokson R., trachybasalt in roadcut; when fresh showed contact aureole with ~2Ma?? terrace sediments; basalt also occurs above as pillow lavas with quenched rims, probably equivalent to BK-218; finegrained to coarsegrained,

contains small blobs of olivine, outcrop very weathered because on paleoterrace, 52° 08' 12", 100° 18' 82"

93-OP-3A: Hawaiite flow from below OP-3.

93-OP-3: Hawaiite from above Oka River.

93-OP-4: Fresh olivine basalt from near top of ridge, olivine phenocrysts up to 1cm, "frothy" vesicles, 4.75Ma K-Ar age from nearby locality, located above OP-3, 52° 10' 97", 100° 18' 9", 1778m?

93-OP-5: dense olivine basalt, ~16.2 Ma, from ridge above OP-4; sample from dense, vesicle-free zone above pillow base about 5-10m below top of flow, 52° 10.83, 100° 18.20

93-OP-6: Basaltic andesite from top of ridge, abundant plagioclase (laths) and large px, some very altered lherzolite xenoliths; contains many (yucky) crustal inclusions (qtz mostly) in lower part of flow, end of arête between head of Debe and Khore rivers close to Mongolian border, 51° 45.62, 99 55.45

93-OP-7: Hawaiite from base of OP-6, contains more ol, less px, sampled ~5m above base of flow.

93-OP-8: Hawaiite flow below OP-7

.

93-OP-9: 2m thick basaltic andesite dike, very glassy, age unconstrained, but younger than Devonian because unmetamorphosed, hosted by granite with Rb-Sr isochron 452Ma, ~E-W shallow dip, 51° 46.65, 99° 56.26, ~2740m

93-OP-10: Same as OP-7, from Oka Plateau proper; flow is probably on basement here, lower flow present at OP-8 missing, 51° 47.09, 99° 56.90, ~2658m

93-OP-11: Flow above OP-10, finegrained with ol phenos up to 1mm, platy flow which caps 2nd bench on Oka Plateau, abundant granite xenoliths partially to completely reacted with basalt, flows over 452 Ma granite.

93-OP-12: Coarsely crystalline ol-rich basalt, sample from flow front, along Oka River near small settlement Hara-Huzhir, Sergey thinks it is one of the valley-filling basalts. 52° 36.63, 99° 42.76

93-OP-13: Hand sample only, at top of hill: huge area of very weathered basalt, thick forest so little outcrop, spectacular ~4m columnar joints, not sampleable, smaller olivines

than in OP-12, groundmass brown, Sergei thinks similar to 13-14Ma basalts, 52° 38.62, 99° 46.01, ~1750m

93-OP-14: Lower basalt flow, similar to OP-13 but less weathered, small olivines, 52° 38.39, 99° 45.89, ~1670m

Shibit River Valley:
93-OP-15: Basalt on top of low hill, perhaps equivalent to OP-11, abundant crustal xenoliths, blocky appearance, pumice/glassy vesicles, olivine altered,; we collected best we could, but olivine not fresh, full of variably reacted crustal xenos, so not good for basalt geochem anyways, blocks of granitic basement nearby, 51° 55.74, 99°48.41, ~1667m.

93-OP-16: Top flow above Zabit River, light grey, finer grained, less olivine than below, massive outcrop, no crustal xenos apparent, "frothy" appearance due to tiny vesicles, very homogeneous flow, not very dense at all, ~75m thick, fairly fresh

93-OP-17: Below OP-16, more vesicles, less ol, some px.

93-OP-18: Below OP-17, coarsegrained, full of large ol phenocrysts and ol glomerocrysts and reacted crustal xenos, questionable freshness.

93-OP-19: Below OP-18 (flow above river), very finegrained, darker grey, silicic flow, no ol apparent, dense, calcite filling vesicles, perhaps a basanite, fairly planar with platy outcrop.

OP-16-19: 52° 04.11, 99° 36.55, top~2253m, bottom~1980m

Muya-Gol River:
93-OP-20: Mantle xenolith locality ~5m below top of hill where basalts resemble OP-16, host basalt reddish, vesicular at top, xenos 2-8cm of ol +px, weathered host and small xenos, a few collected as hand samples, 52° 06.80, 99° 34.64

93-OP-21: another location lower than OP-20, fresher host, larger xenoliths

93-OP-21: host a basanite (?), fg, no ol except occasional glomerocrysts (xenocrysts?), some areas it is mottled reddish brown and grey, or light grey and grey: Sergey says he has analyzed the different parts and found red to be K and Ba enriched therefore thinks feature a result of liquid immiscibility, abundant and varied xenoliths ranging from .5cm to 20cm diameter, most weathered.
Varieties are:

ol only (dunite?)
spinel lherzolite (most common)

Cr-diopside rich
garnet lherzolite (very rare), garnets occur as altered
porphyroblasts
orthopyroxene rich kind
several big samples with vein of opx (?) in center
possible kaersutite
no crustal xenos really
opx also occurs as porphyroblasts in spinel lherzolite

93-OP-30: ol basalt with ol up to 1cm and 2cm as glomerocrysts on hill across valley from 250m section of 8/4/93, flow same as OP-18, but fresher. Collected within 5m of top of flow. Next flow exposed different than capping flows described on either side

93-OP-31: Platy-foliated ol (?) plag basalt, fairly cg matrix with crystals up to 1mm, no phenos; ol(?) in groundmass looks partially altered to iddingsite, but freshest material abailable. Lies directly above OP-30.

Next flow up identical to OP-18 and 30, could be that OP-31 is correlative with OP-19 and OP-30 lies below. If this is OP-18, it is much thinner at this locality-may explain absence on next hill to west (where xenos are). Flow above OP-31 same as capping flows to the east and west, but contains more dense sections and generally more altered.

93-OP-32: capping flow very fresh at top, badly weathered below, ol basalt with ol phenos up to 2mm, groundmass mg, intergrown plag laths, flow is "frother" here, but in general less vesicular than to the east and west. Very platy, foliated. Top of section 52° 05.59, 99° 36.66, ~2160m

93-OP-33,34,35,36: Pliocene (?) basalts

93-OP-37,38: Miocene? 33 top, 38 bottom

Tuva Volcanic Field Samples:

The following samples are from the Ulug-Arga Ridge and adjacent area, and were collected by Sergei Rasskazov. The Ulug-Arga Ridge section is well-described in his light blue book (Rasskazov, 1993) and in a paper on the Tuva basalts (Rasskazov et al., 1989).

p901/1 to p901/4
p904/1, 6, 11, 13
p905
p906/2
p908/4, 5
p909/2, 3

p915
p919

The following samples were collected by A. Ivanov and S. Rasskazov in 1994, and are referenced on the Tuva Map:

TV-3: Sarikta pass; Late-Middle Pliocene? 52°18.25 N, 98°42.35E

TV-4: Sarikta pass; Pleistocene? 52°18.21N, 98°39.12E

TV-6: Dulaa-Hol-Tanma River; Middle Pleistocene? 52°20.45N, 98°23.13D

TV-10: Ulug-Arga volcano, major cone
TV-12: Ulug-Arga volcano, satellite cone
Holocene?

TV-13: Plateau basalts, right side of the Shivit River; Middle Pleistocene?
52°25.15N, 98°21.22E, alt. of 2120m

TV-14: Plateau basalt

TV-20: Shivit-Tayga volcano; post-plateau shield volcano; 52°26.48N, 98°22.57E

TV-25: Shivit-Tayga volcano, near to 52°27.15N, 98°24.26E

TV-27, TV-29: Derbi-Tayga volcano, dikes?, 52°22.12N, 98°14.33E

TV-31: vein from Derbi-Tayga volcano

TV-35: lava flow from near top of Derbi-Tayga volcano

TV-36, TV-41: Priosernity volcano (Karabalyk Lake volcano); 52°20.45N, 98°32.01E;
post-plateau shield volcano

FIGURE CAPTIONS

Figure 2.1 General map of the Baikal Rift Zone (BRZ) showing locations of the major Cenozoic volcanic fields and other major features. TV is the Tuva volcanic field; OP is the Oka Plateau; T is the Tunka Basin, and D is the Dzhida Basin. Other rift basins according to number label are: 1) Busingol, 2) Darkhat, 3) Khubsugul, 4) Barguzin, 5) Upper Angara, 6) Tsipa, 7) Baunt, 8) Muya, 9) Chara, and 10) Tokka. The 1500 m contour line of the Sayan-Baikal domal uplift is indicated.

Figure 2.2 Map of the Tunka Basin, including sample locations, modified after Rasskazov (1993, 1994).

Figure 2.3 Map of the Oka Plateau volcanic field showing Cenozoic lavas and sample locations.

Figure 2.4 a) Map of a portion of the East Tuva Lava Field (ETLF), showing major volcanoes and sample locations. b) Simplified cross-section of the Miocene lavas of the Ulug-Arga Ridge, modified after Rasskazov et al., (1989, 1993). Samples p904/1-15 are a sequence of basalts up the ridge.

Figure 2.5 Total Alkali Silica diagram (TAS), showing classification of volcanic rocks according to Le Bas et al., (1986), plotted for each volcanic field of the western BRZ. A legend is presented defining symbols used in subsequent diagrams.

Figure 2.6 Diagram of Mg# (Mg# = 100 * molecular Mg/(Mg + Fe^{2+}), where Fe^{2+} = .15 *Fe_{total}) versus normative nepheline or hypersthene, plotted for each volcanic field of the western BRZ.

Figure 2.7 Plots of MgO% versus major oxides. a) Tunka volcanic field, b) Oka Plateau volcanic field, c) Tuva volcanic field. Symbols as given in Legend of Figure 2.5.

Figure 2.8 Chondrite normalized REE diagrams for western BRZ volcanic rocks, using values of Sun and McDonough (1989) for C1 chondrite. a) Tunka volcanic field, b) Oka Plateau volcanic field, c) Tuva volcanic field. Symbols as given in legend of Figure 2.5.

Figure 2.9 Plots of MgO% versus the incompatible elements Rb, Ba, Sr, and Zr. a) Tunka volcanic field, b) Oka Plateau volcanic field, c) Tuva volcanic field. Symbols as given in Legend of Figure 2.5.

Figure 2.10 Plots of Th versus incompatible elements Rb, Ba, Sr, and Zr. a) Tunka volcanic field, b) Oka Plateau volcanic field, c) Tuva volcanic field. Symbols as given in legend of Figure 2.5.

Figure 2.11 Incompatible element abundance patterns for each of the volcanic fields of the western BRZ, using values for primitive mantle from Sun and McDonough (1989). Symbols as given in legend of Figure 2.5.

Figure 2.12 Plots of MgO% versus the compatible elements Cr, Co, and Ni, as well as the CaO/Al_2O_3 ratio. a) Tunka volcanic field, b) Oka Plateau volcanic field, c) Tuva volcanic field. Symbols as given in legend of Figure 2.5.

Figure 2.13 Diagram of normative olivine versus the compatible element Ni with symbols for each of the western BRZ volcanic fields.

Figure 2.14 $^{87}Sr/^{86}Sr$ - ε_{Nd} diagram for western BRZ volcanic rocks. Shown on the diagram is the field of Housh et al.'s data (in prep.) for the Dzhida Basin volcanic field, also in the western BRZ. The end-member mantle components (Hart, 1988; Zindler and Hart, 1986) DM (depleted mantle) and EMI (enriched mantle 1) are shown for reference. Calculated mixing lines between DM (Sr=150ppm, Nd=10ppm, Pb=0.5ppm, $^{87}Sr/^{86}Sr$=0.703, ε_{Nd} =+7, $^{206}Pb/^{204}Pb$=18.5) and EMI (Sr=100ppm, Nd=15ppm, Pb=1ppm, $^{87}Sr/^{86}Sr$=0.705, ε_{Nd} =-1, $^{206}Pb/^{204}Pb$=17.4), and DM and a possible crustal component (Sr=100ppm, Nd=22ppm, Pb=1ppm, $^{87}Sr/^{86}Sr$=0.709, ε_{Nd} =+1, $^{206}Pb/^{204}Pb$=18.2) are shown. Numbers next to tick marks on mixing lines are percent of assimilant (either EMI or crust).

Figure 2.15 $^{206}Pb/^{204}Pb$ - $^{207}Pb/^{204}Pb$ and $^{206}Pb/^{204}Pb$ - $^{208}Pb/^{204}Pb$ diagrams for western BRZ lavas. The field of data for the Dzhida volcanic field (Housh et al., in prep.) is shown for comparison. The Northern Hemisphere Reference Line (NHRL), defined by Hart (1984), is a regression through average northern hemisphere oceanic rocks. The end-member mantle component EMI is also labeled.

Figure 2.16 $^{206}Pb/^{204}Pb$ - $^{87}Sr/^{86}Sr$ and $^{206}Pb/^{204}Pb$ - ε_{Nd} diagrams for western BRZ lavas. Calculated mixing lines between DM and EMI and a crustal component are shown (parameters as in Figure 2.14).

Figure 2.17 Plot of differentiation index (DI) versus Mg#. DI = normative Q + Or + Ab + Ne.

Figure 2.18a, b, c, d, e. Cpx-Ol-Qtz ternary diagrams showing a range in predicted melt compositions using the model of Yang et al. (1996), compared to the projected composition of actual samples. For each sample, the legend lists in parentheses the plotted range in pressures in 1kbar increments. By comparing the predicted and observed compositions, a best estimate for pressure is obtained. The chosen pressure estimates and corresponding calculated temperatures are listed with each sample in the legend.

Figure 2.19 Plot of Mg# versus $(La/Yb)_N$ by volcanic field.

Figure 2.20 Plots of $\Delta^{208}Pb/^{204}Pb$ versus $\Delta^{207}Pb/^{204}Pb$ and $^{87}Sr/^{86}Sr$. $\Delta^{208}Pb/^{204}Pb$ and $\Delta^{207}Pb/^{204}Pb$ are calculated deviations from the NHRL, according to Hart et al. (1986).

Figure 2.21 Diagrams showing the variation in Sr, Nd, and Pb isotopic compositions of the western BRZ volcanic rocks as a function of time period from the Oligocene to the Quaternary.

Figure 2.22 Plots of age (Ma) versus $^{87}Sr/^{86}Sr$, ε_{Nd}, and $^{206}Pb/^{204}Pb$ for western BRZ lavas using the $^{40}Ar/^{39}Ar$ data of this study (Appendix 2.B, Table 2.1) and K-Ar data from the literature (Table 2.4).

Figure 2.23 Diagram showing the variation in Mg#, normative nepheline or hypersthene, $^{87}Sr/^{86}Sr$, ε_{Nd}, and $^{206}Pb/^{204}Pb$ for four stratigraphic sequences in the Oka Plateau (Fig. 2.3). a) Kitoy Ridge, b) Bokson R. sequence, c) Shibit R. sequence, d) E. bank of the Tissa R.

Figure 2.1

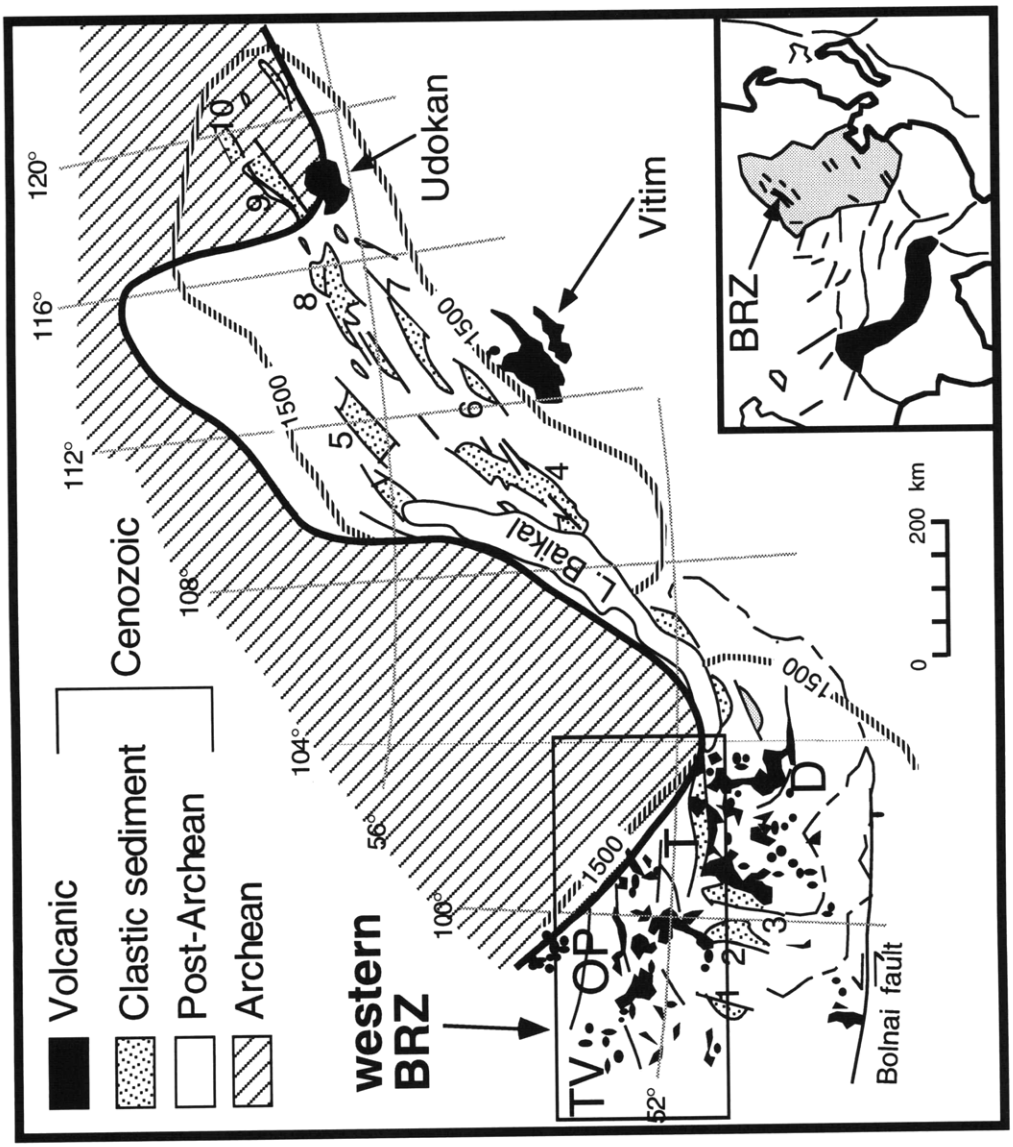
Volcanic
Clastic sediment
Cenozoic
Post-Archean
Archean
western BRZ
Udokan
Vitim
L. Baikal
BRZ
TV
OP
D
Bolnai fault
1500
112°
116°
120°
108°
104°
100°
56°
52°
0
200 km

Figure 2.2

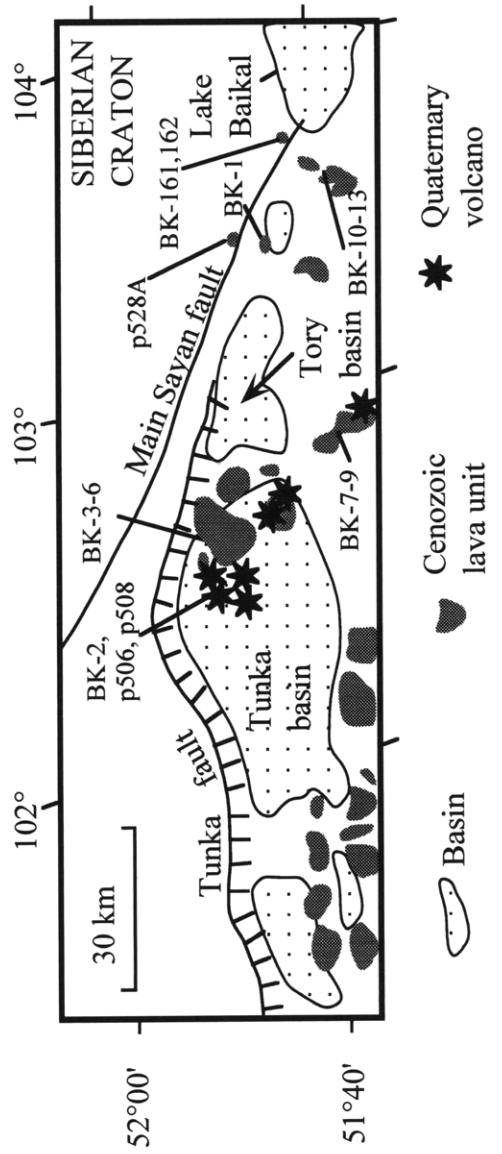
SIBERIAN CRATON
Lake Baikal
BK-161,162
BK-1
BK-10-13
p528A
Main Sayan fault
Tory basin
BK-3-6
BK-2, p506, p508
BK-7-9
Tunka basin
Tunka fault
30 km
102°
103°
104°
52°00'
51°40'
Basin
Cenozoic lava unit
Quaternary volcano

Figure 2.3

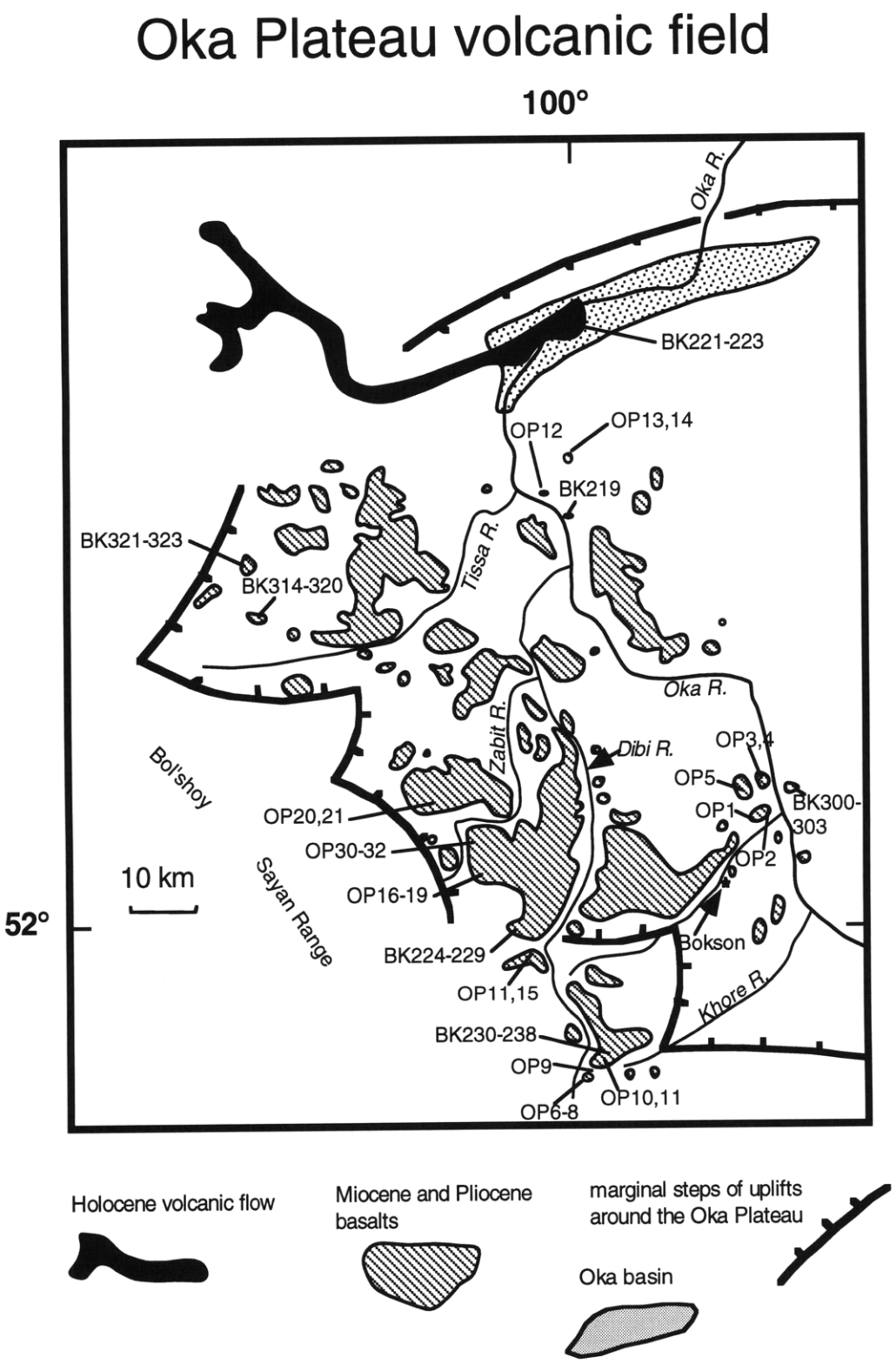
Oka Plateau volcanic field
100°
52°
Oka R.
BK221-223
OP12
OP13,14
BK219
BK321-323
BK314-320
Tissa R.
Oka R.
Zabit R.
Dibi R.
OP3,4
OP5
OP1
BK300-303
OP2
Bol'shoy
OP20,21
OP30-32
OP16-19
10 km
Sayan Range
Bokson
BK224-229
OP11,15
Khore R.
BK230-238
OP9
OP10,11
OP6-8
Holocene volcanic flow
Miocene and Pliocene basalts
marginal steps of uplifts around the Oka Plateau
Oka basin

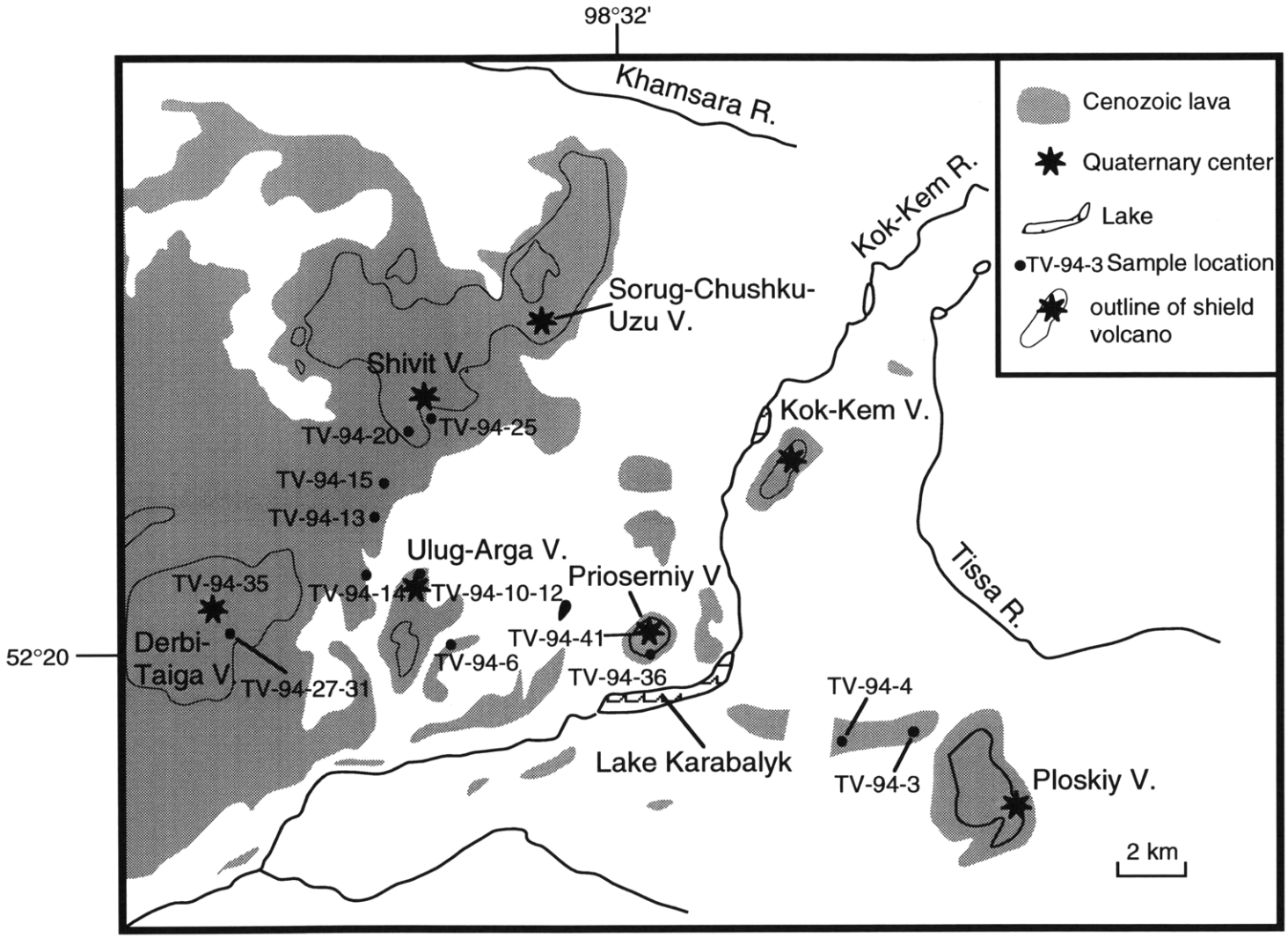

Figure 2.4a

The Ulug-Arga Ridge (samples p901-909, p915, p919) is located ~50km west of the portion of the East Tuva Lava Field shown in this map.

Figure 2.4b

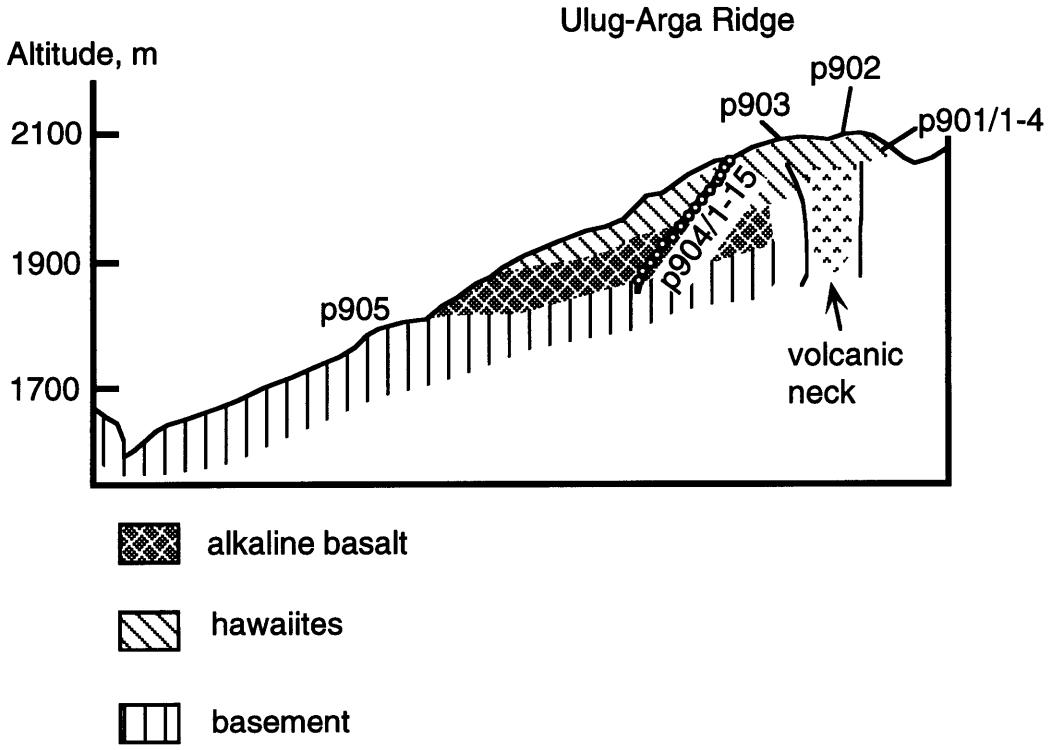
Ulug-Arga Ridge
Altitude, m
2100
1900
1700
p905
p904/1-15
p903
p902
p901/1-4
volcanic
neck
alkaline basalt
hawaiites
basement

Figure 2.5

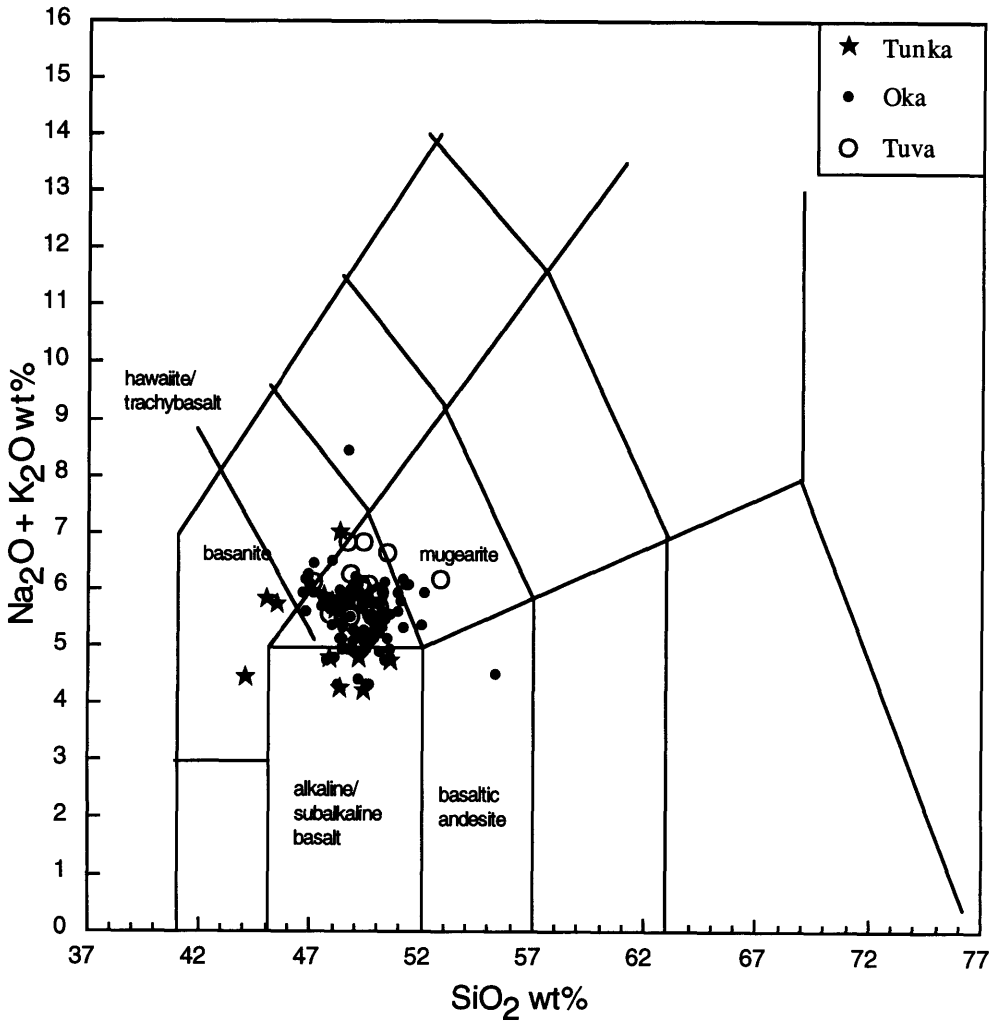
Tunka
Oka
Tuva
hawaiite/
trachybasalt
basanite
mugearite
alkaline/
subalkaline
basalt
basaltic
andesite
$Na_2O + K_2O$ wt%
SiO_2 wt%
0
1
2
3
4
5
6
7
8
9
10
11
12
13
14
15
16
37
42
47
52
57
62
67
72
77

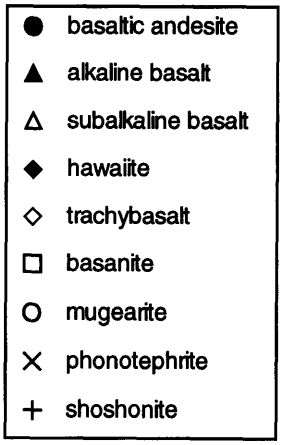
basaltic andesite
alkaline basalt
subalkaline basalt
hawaiite
trachybasalt
basanite
mugearite
phonotephrite
shoshonite

Figure 2.6

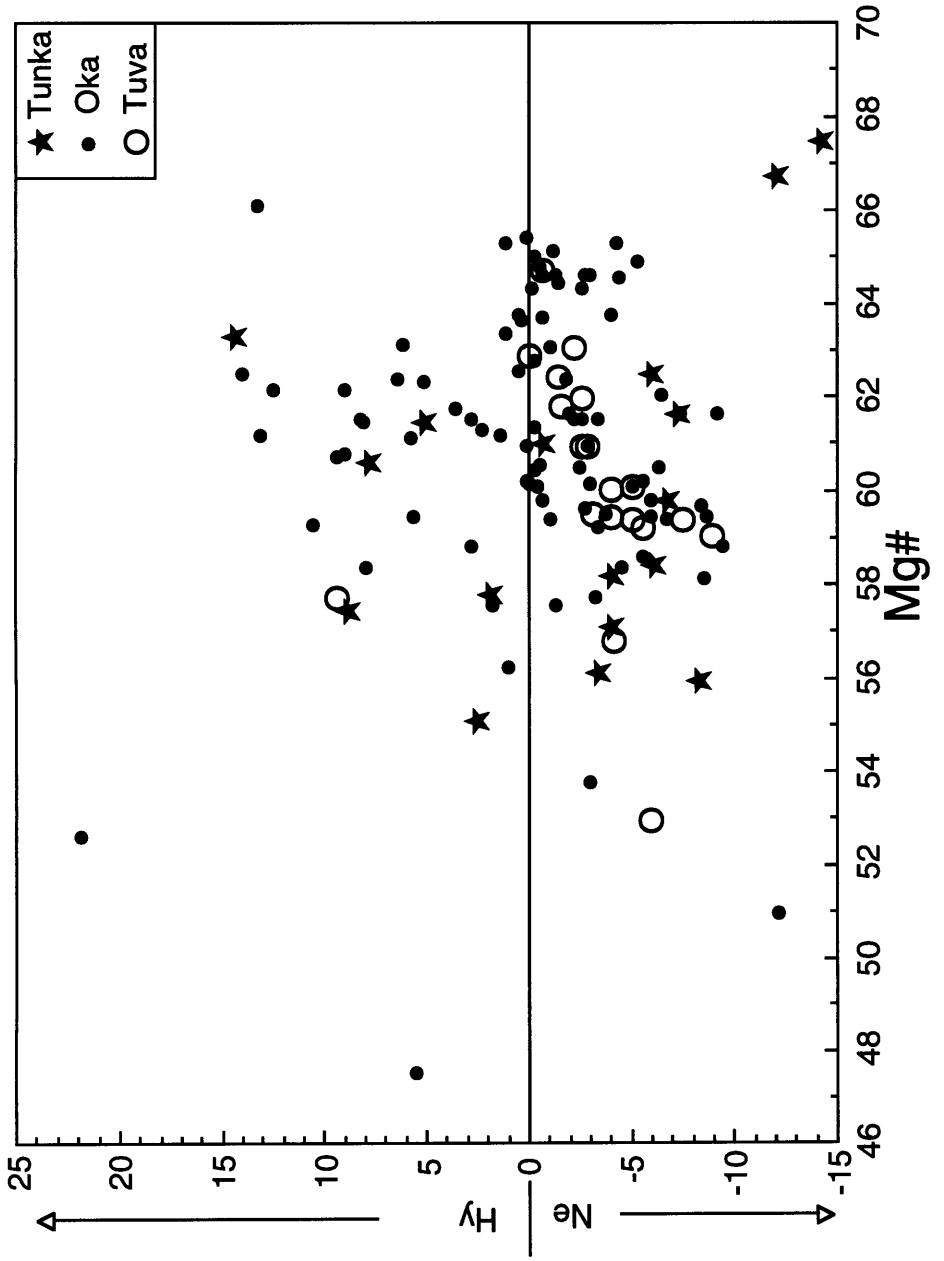
Tunka
Oka
Tuva
Hy
Ne
Mg#
25
20
15
10
5
0
-5
-10
-15
46
48
50
52
54
56
58
60
62
64
66
68
70

Figure 2.7a Tunka

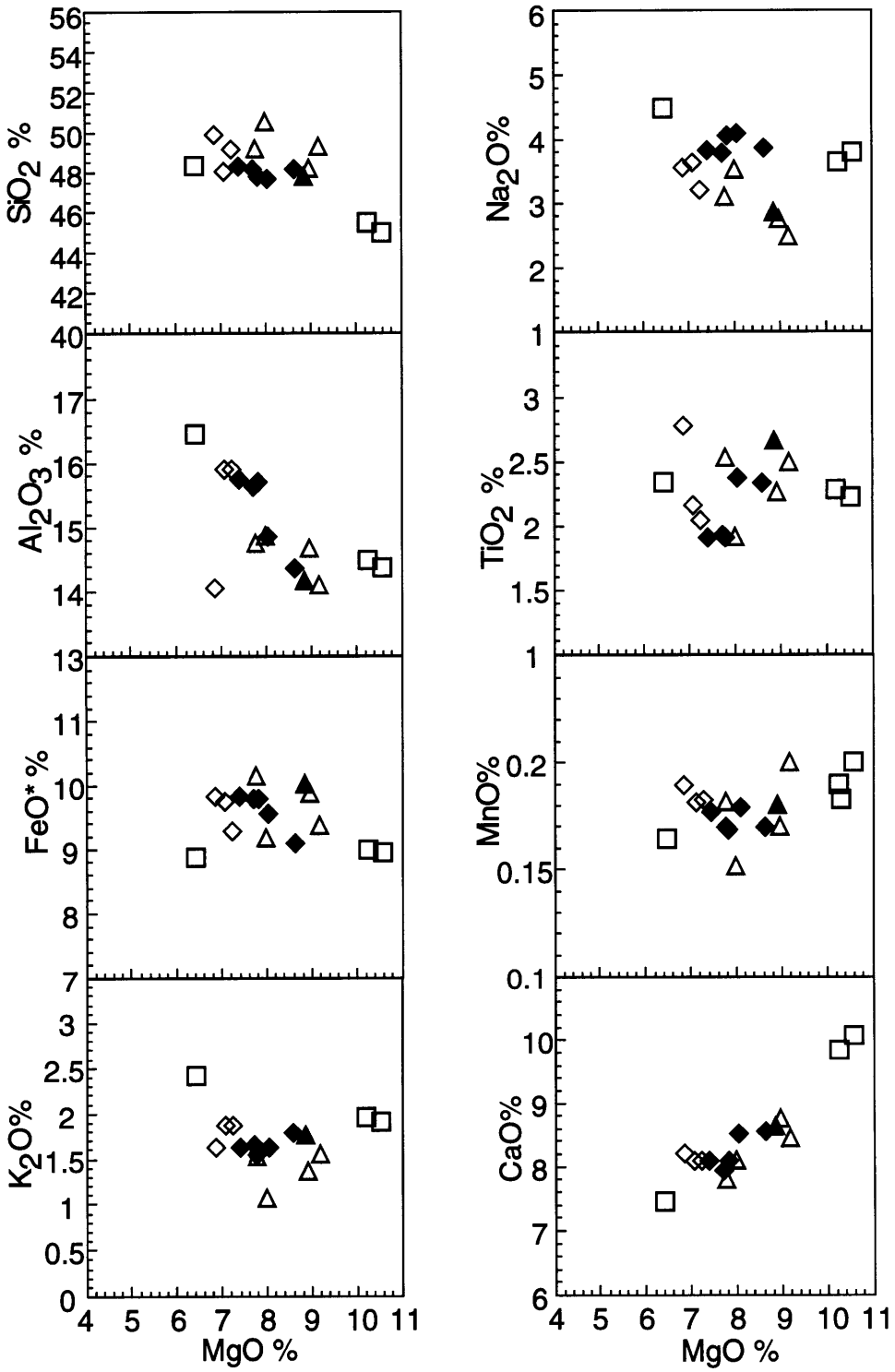

Figure 2.7b Oka Plateau

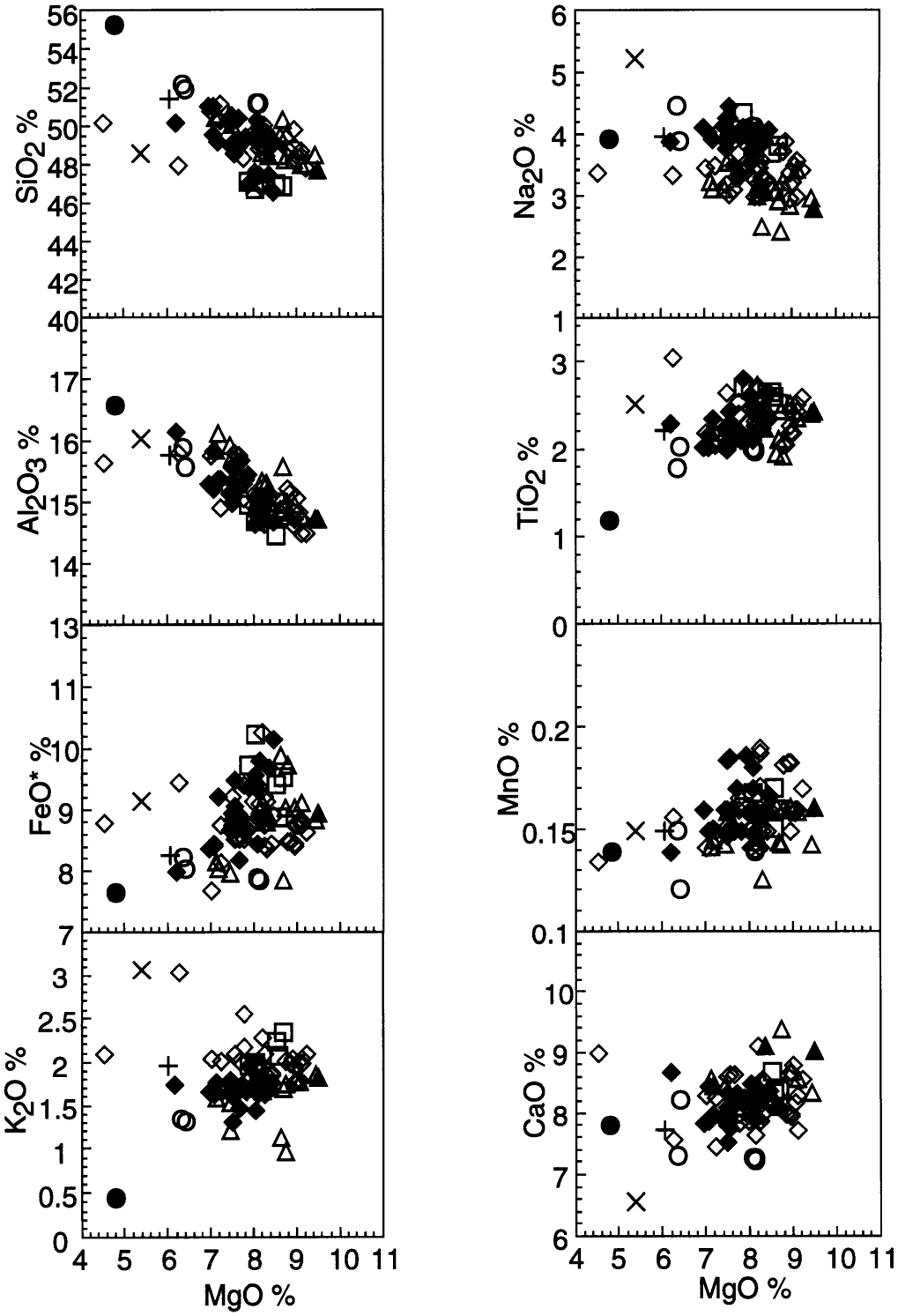

Figure 2.7c Tuva

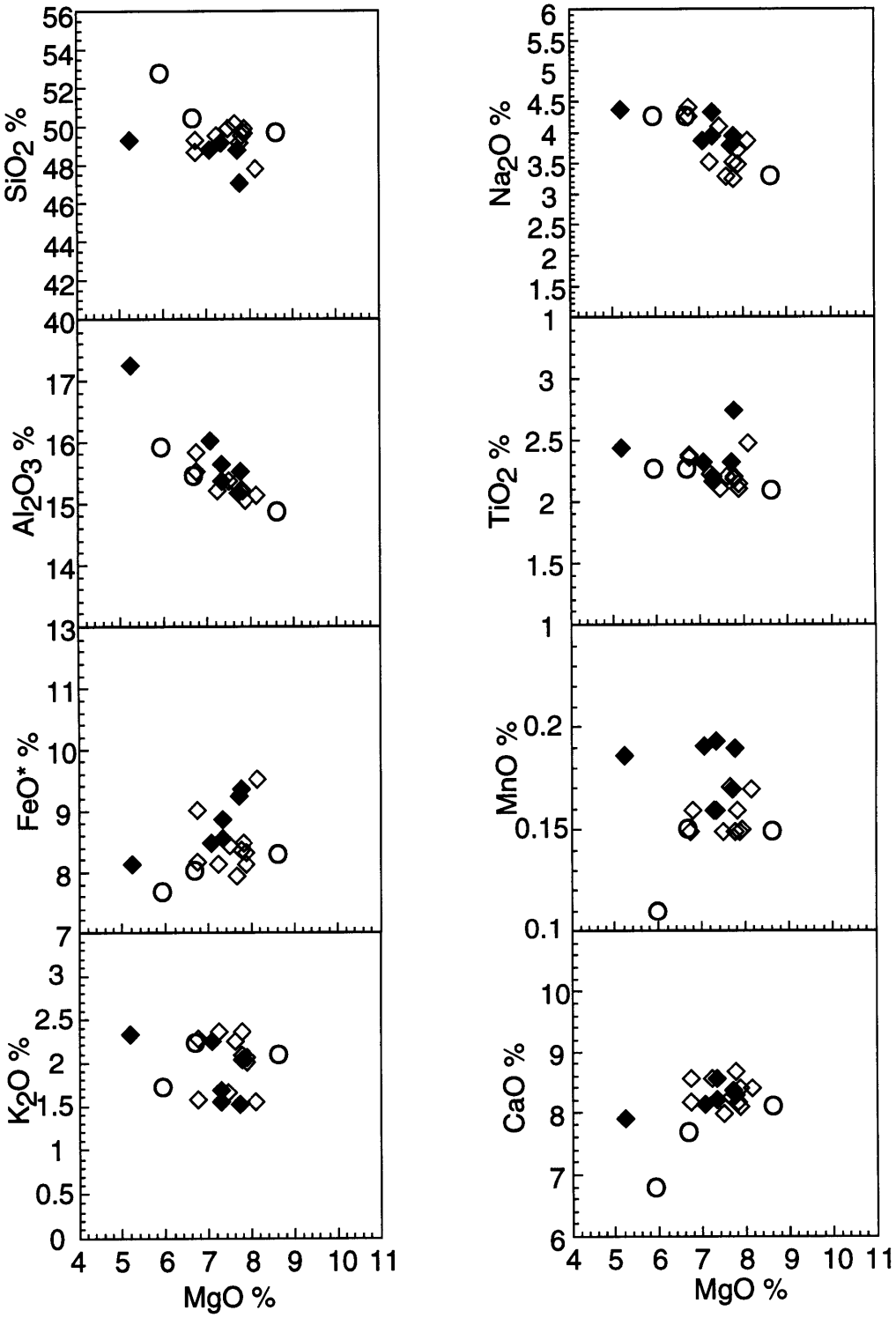

Figure 2.8

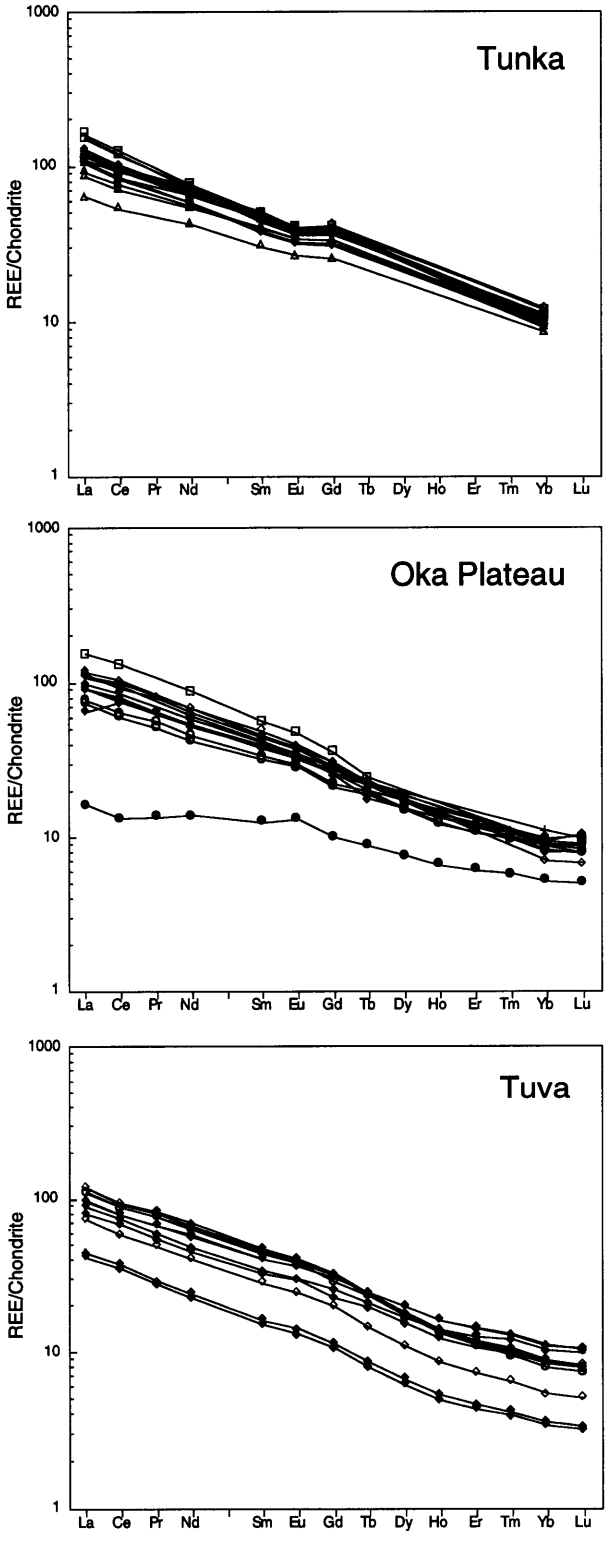
Tunka
Oka Plateau
Tuva
REE/Chondrite
1000
100
10
1
La Ce Pr Nd Sm Eu Gd Tb Dy Ho Er Tm Yb Lu

Figure 2.9a Tunka

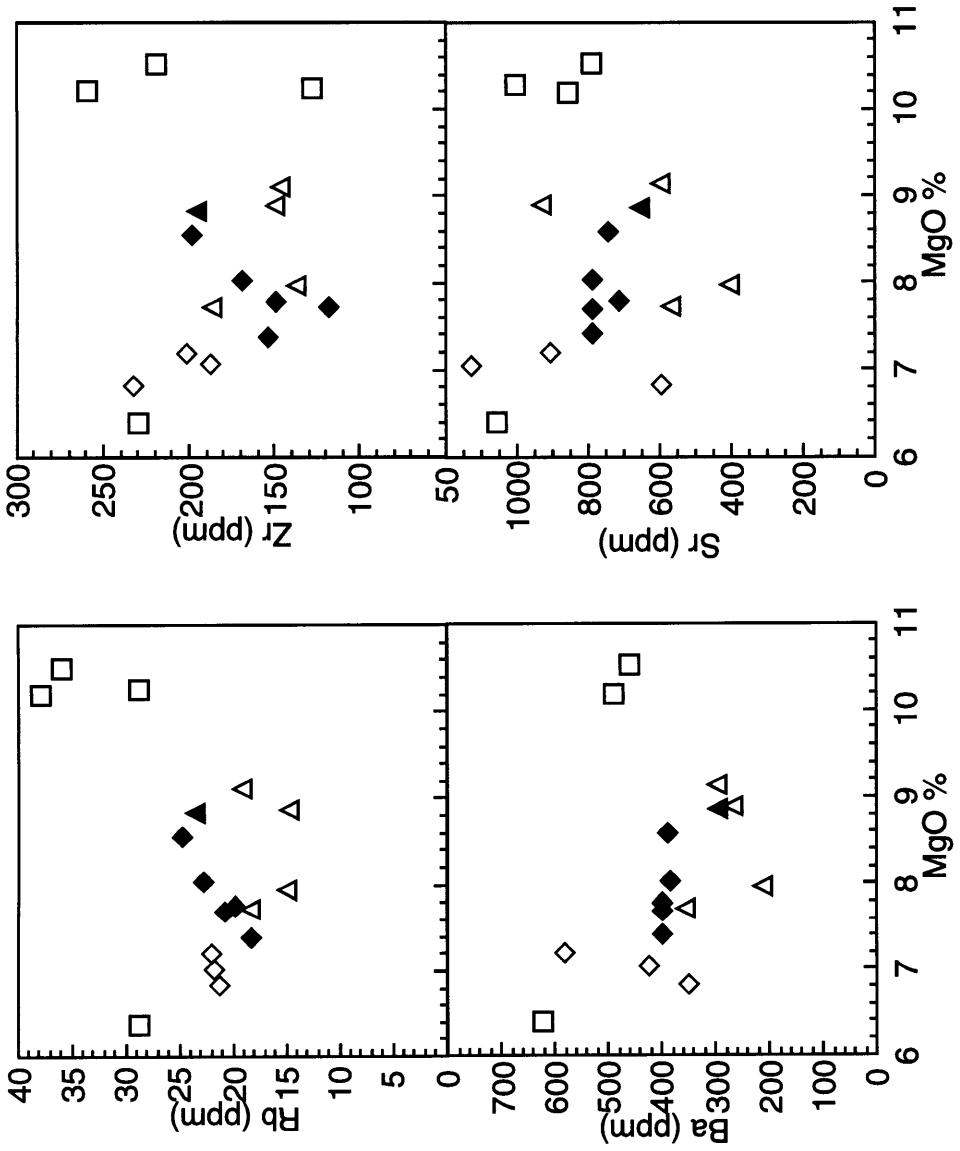

Figure 2.9b Oka Plateau

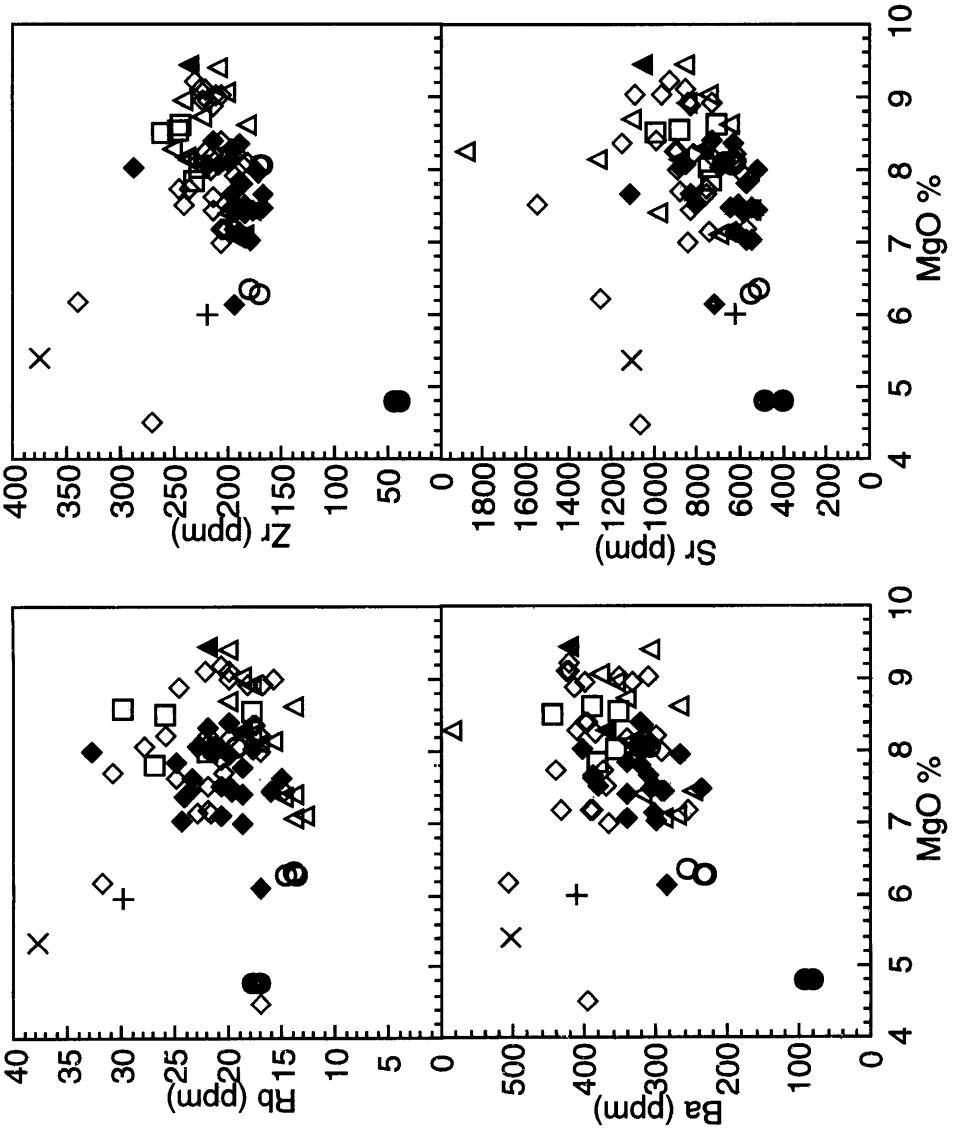

Figure 2.9c Tuva

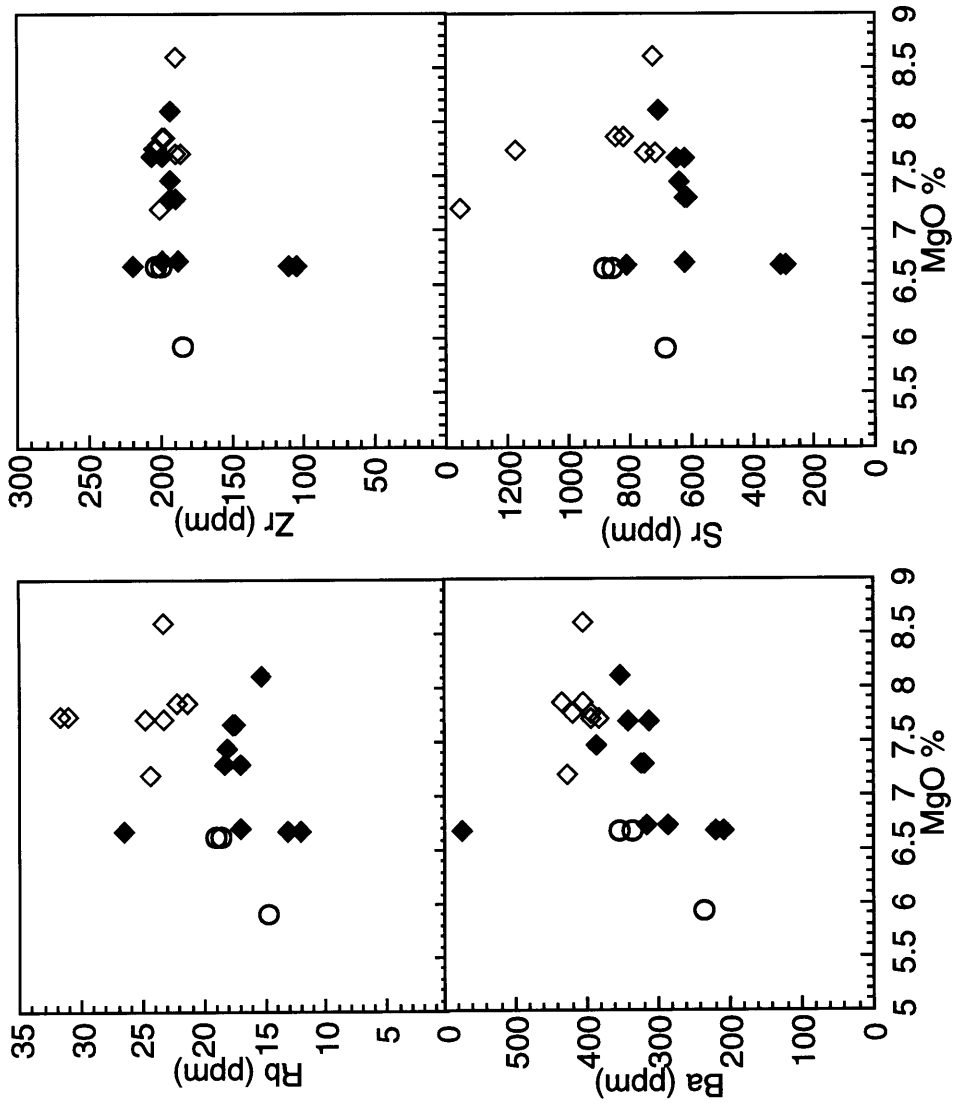

Figure 2.10a Tunka

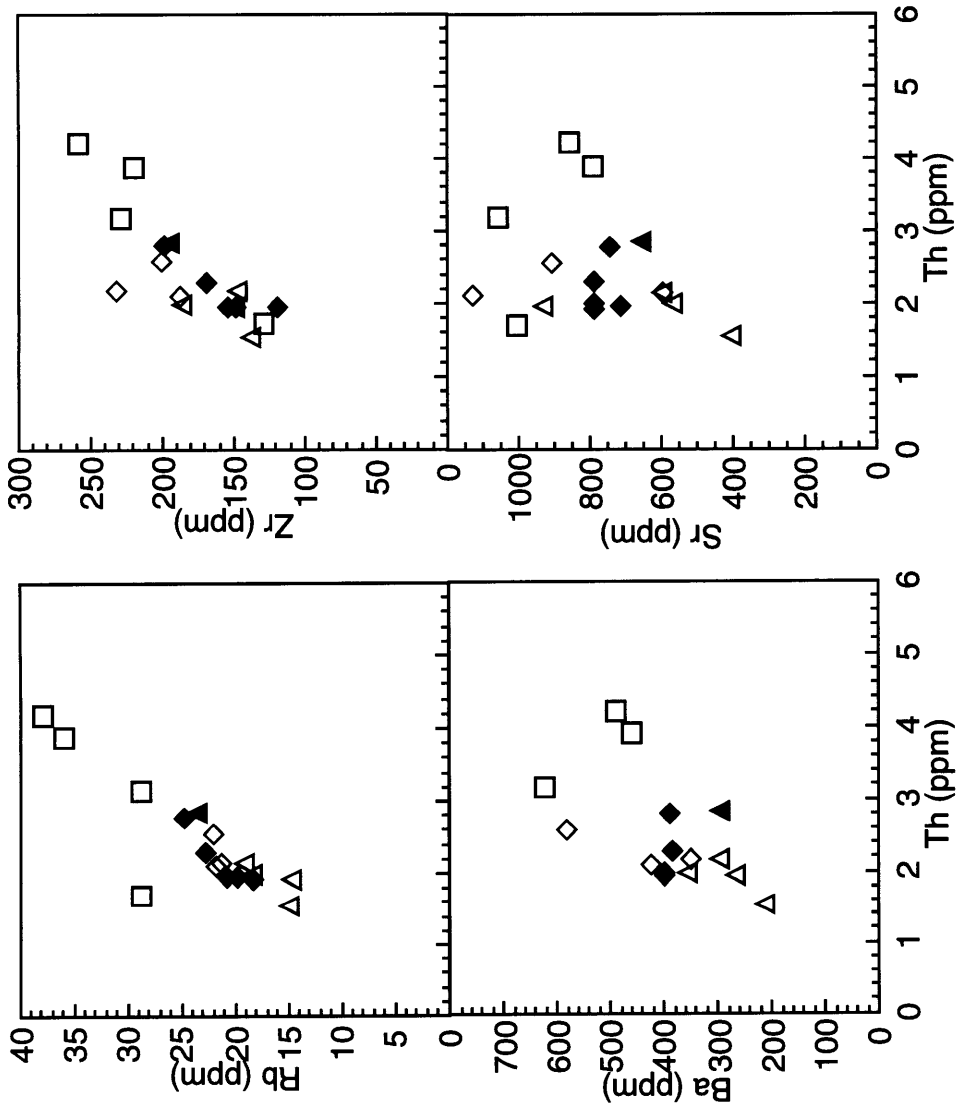

Figure 2.10b Oka Plateau

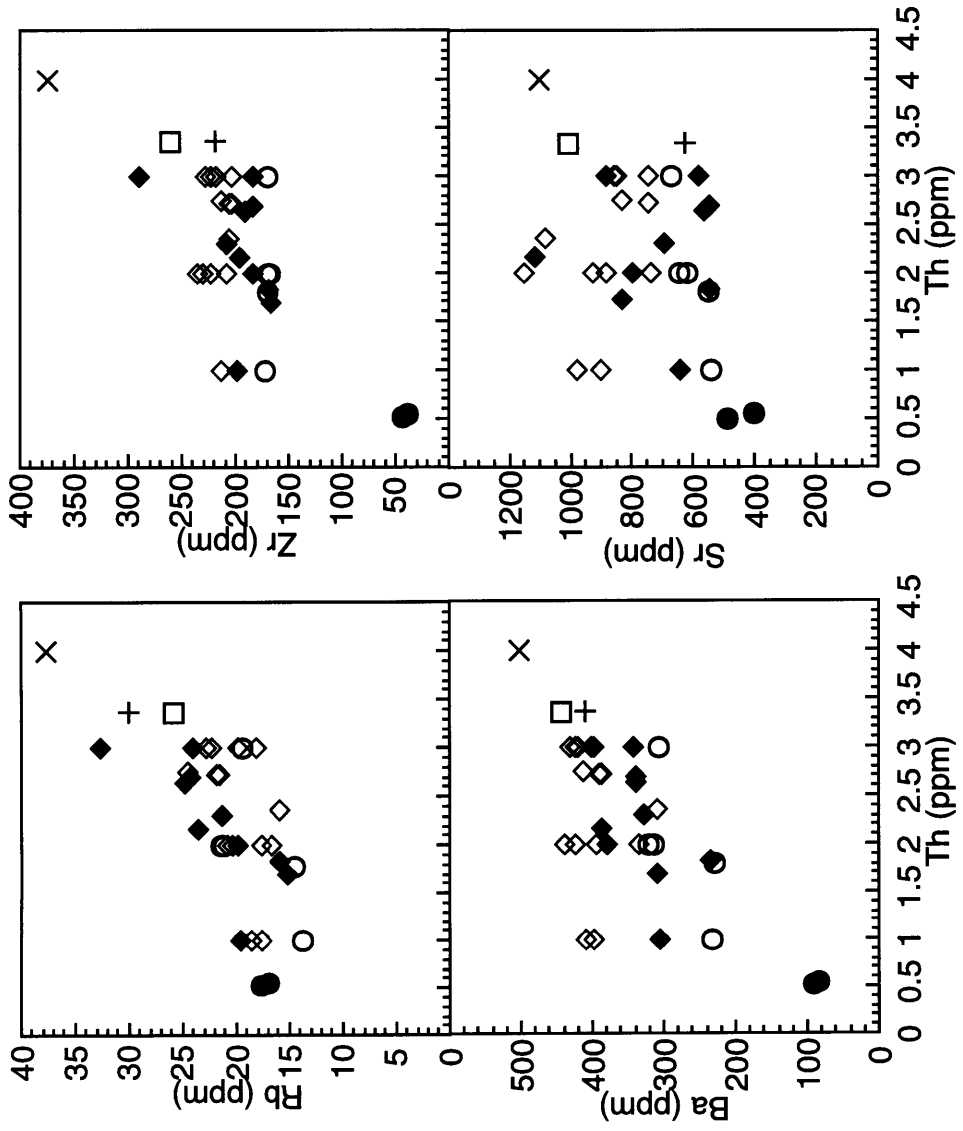

Figure 2.10c Tuva

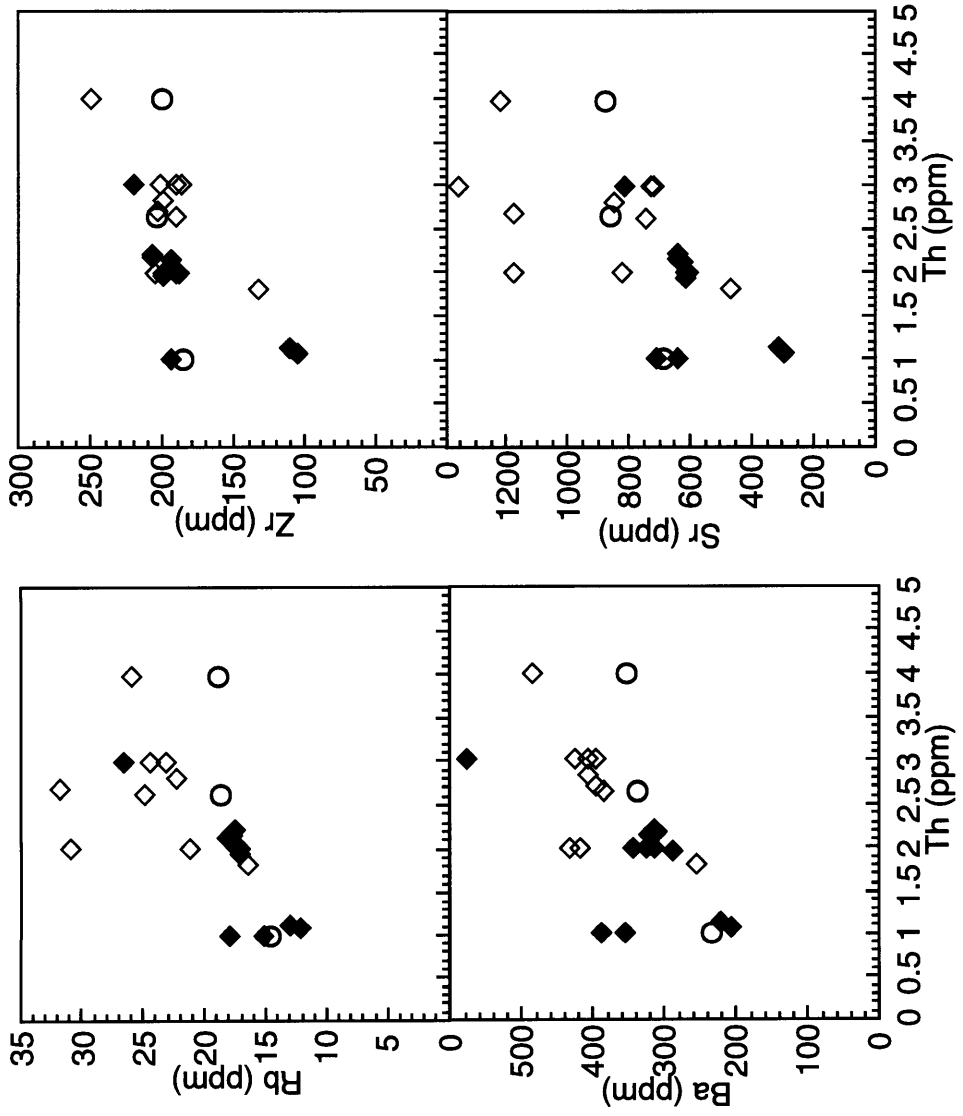

Figure 2.11

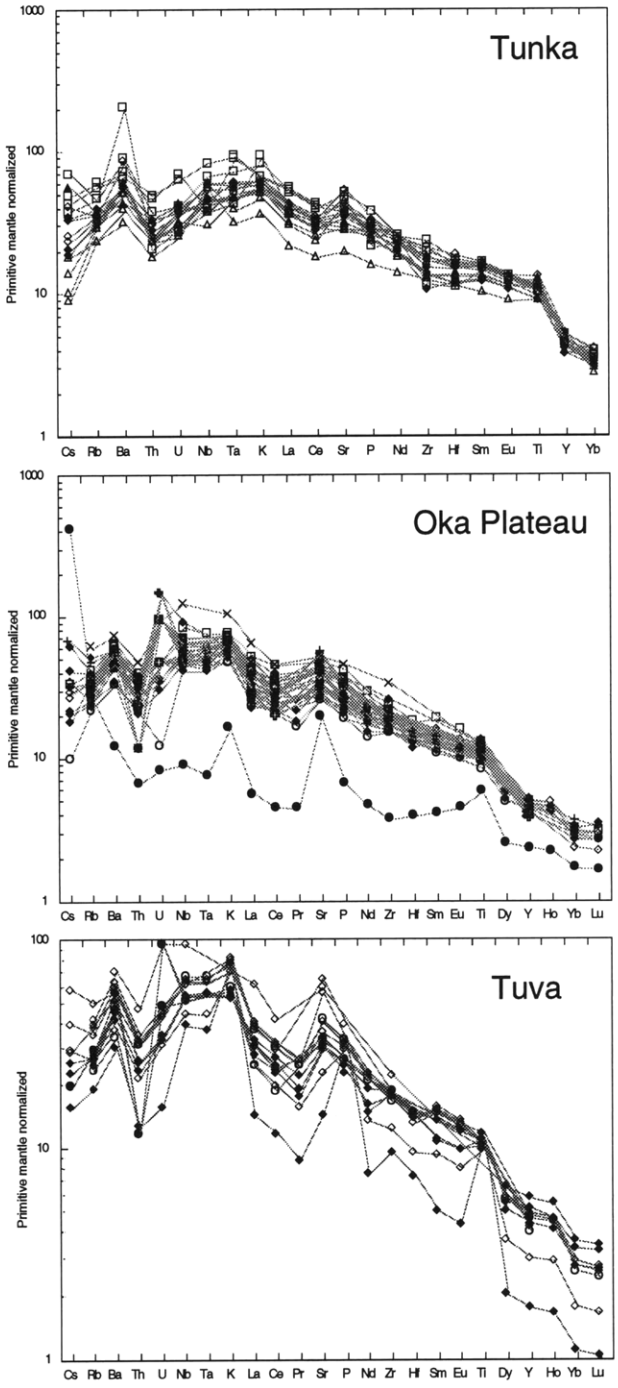
Tunka
Primitive mantle normalized
1000
100
10
1
Cs Rb Ba Th U Nb Ta K La Ce Sr P Nd Zr Hf Sm Eu Ti Y Yb
Oka Plateau
Primitive mantle normalized
1000
100
10
1
Cs Rb Ba Th U Nb Ta K La Ce Pr Sr P Nd Zr Hf Sm Eu Ti Dy Y Ho Yb Lu
Tuva
Primitive mantle normalized
100
10
1
Cs Rb Ba Th U Nb Ta K La Ce Pr Sr P Nd Zr Hf Sm Eu Ti Dy Y Ho Yb Lu

Figure 2.12a Tunka

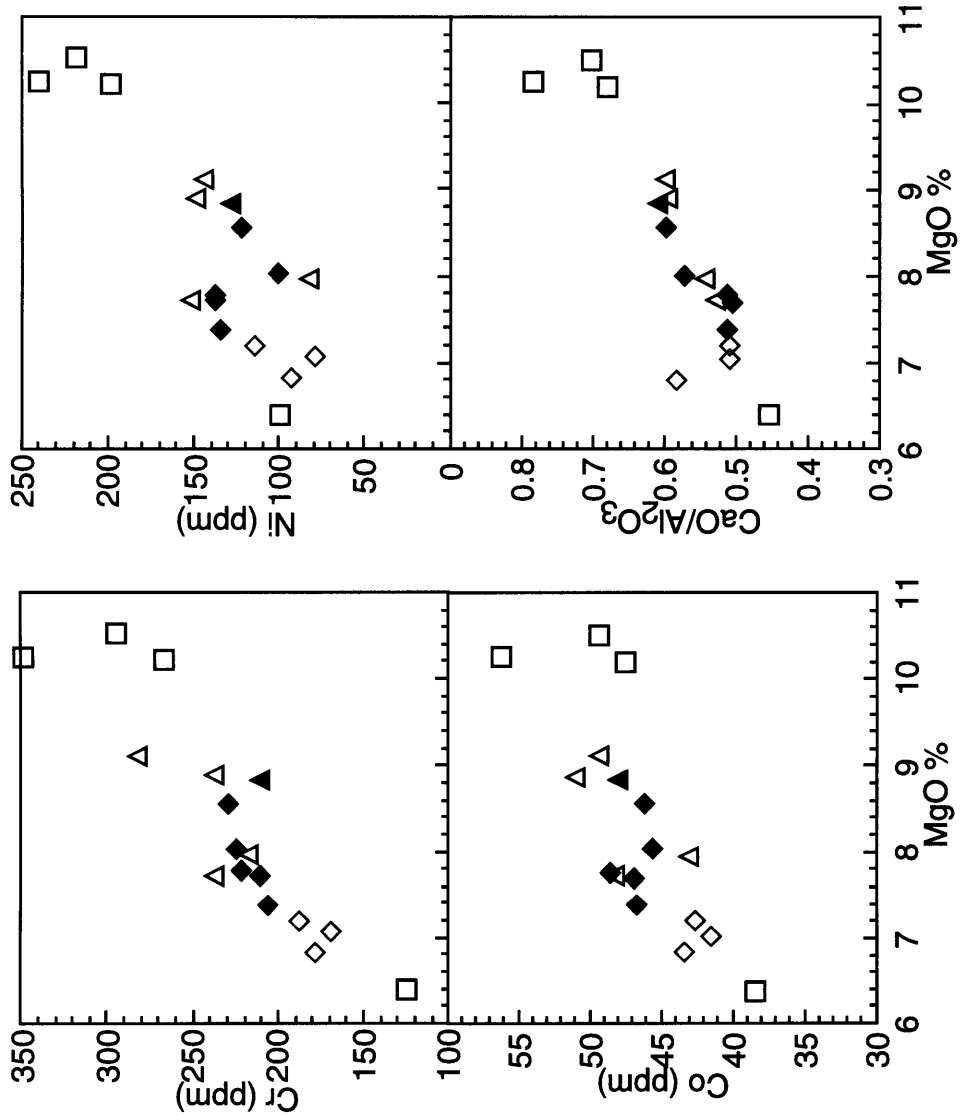

Figure 2.12b Oka Plateau

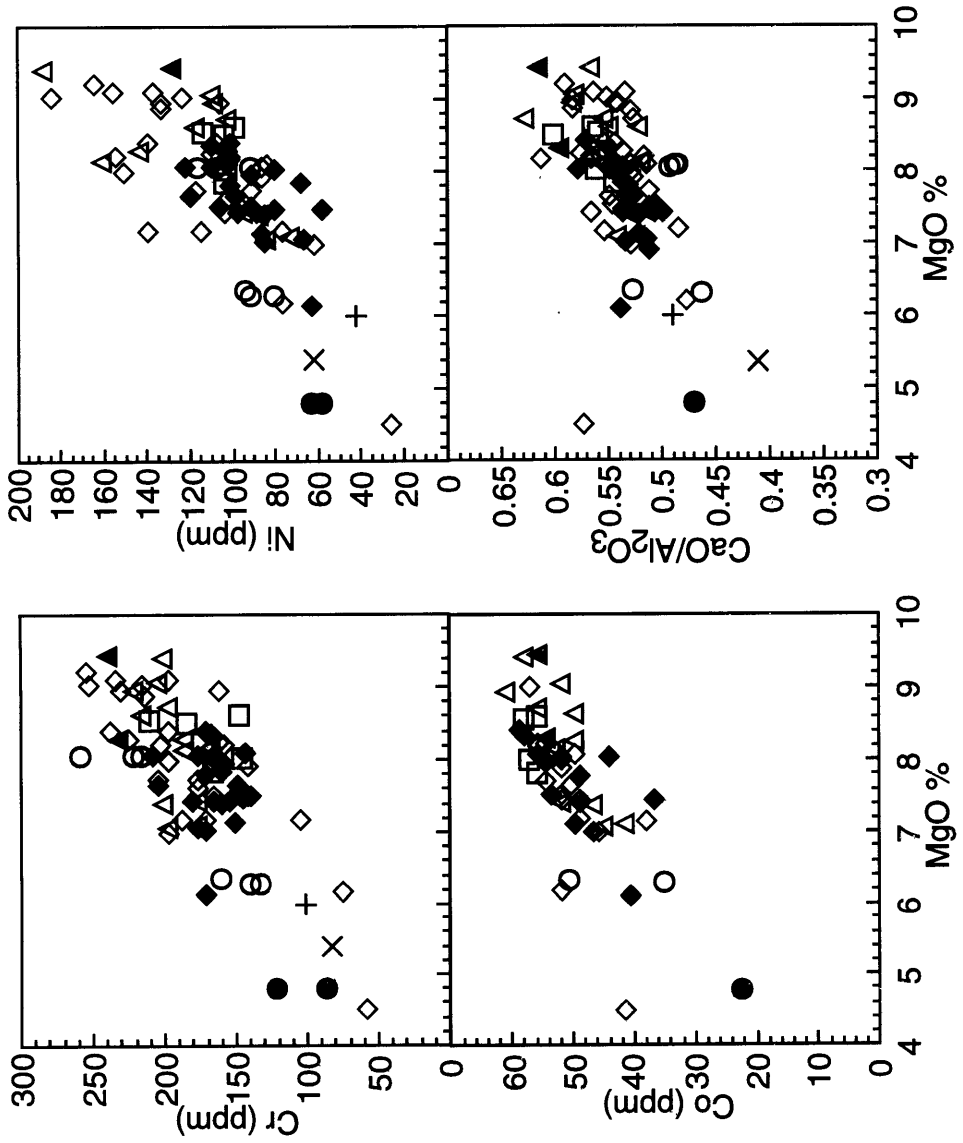

Figure 2.12c Tuva

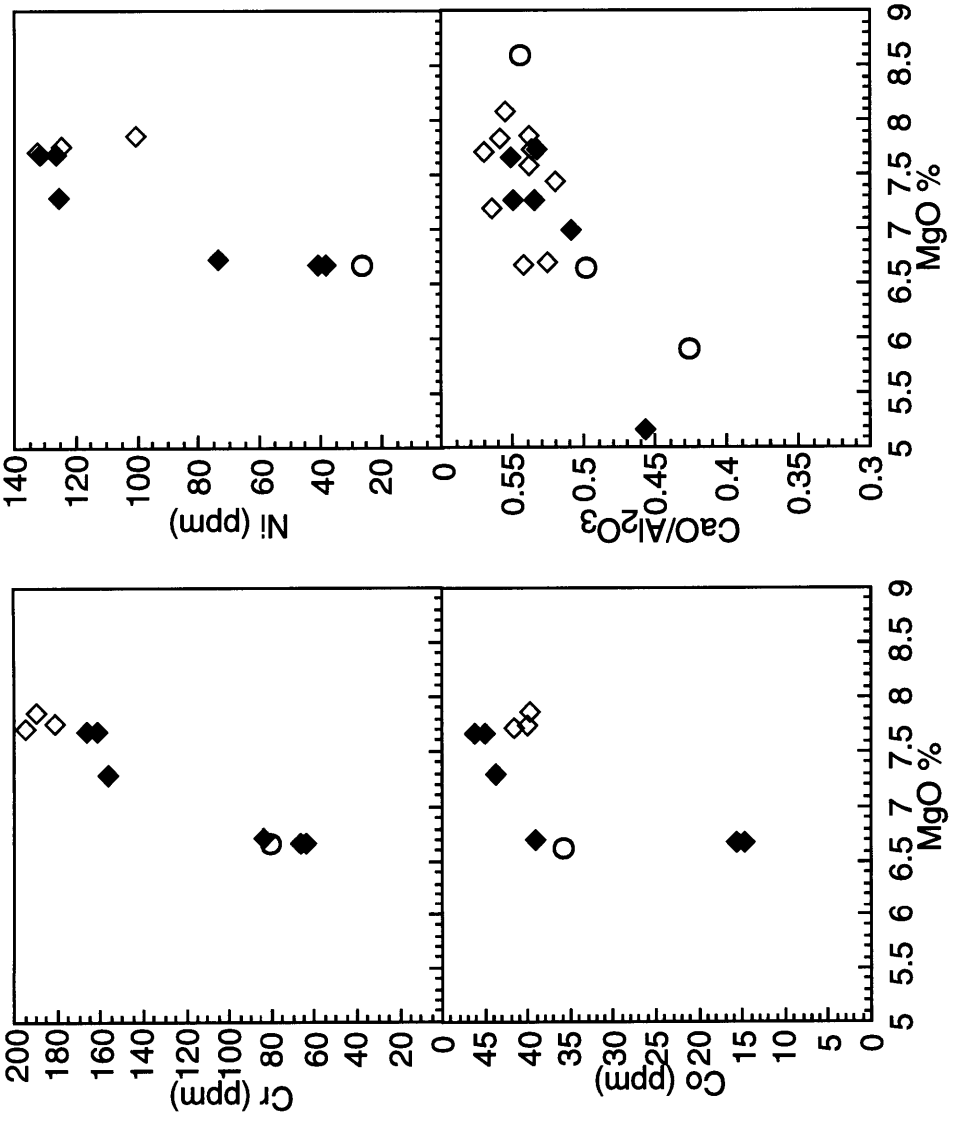

Figure 2.13

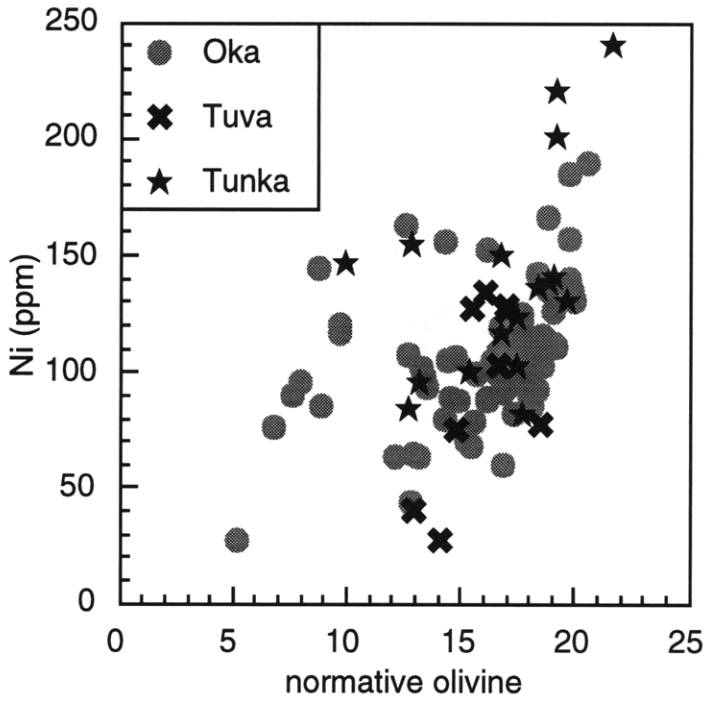
Oka
Tuva
Tunka
Ni (ppm)
250
200
150
100
50
0
0
5
10
15
20
25
normative olivine

Figure 2.14

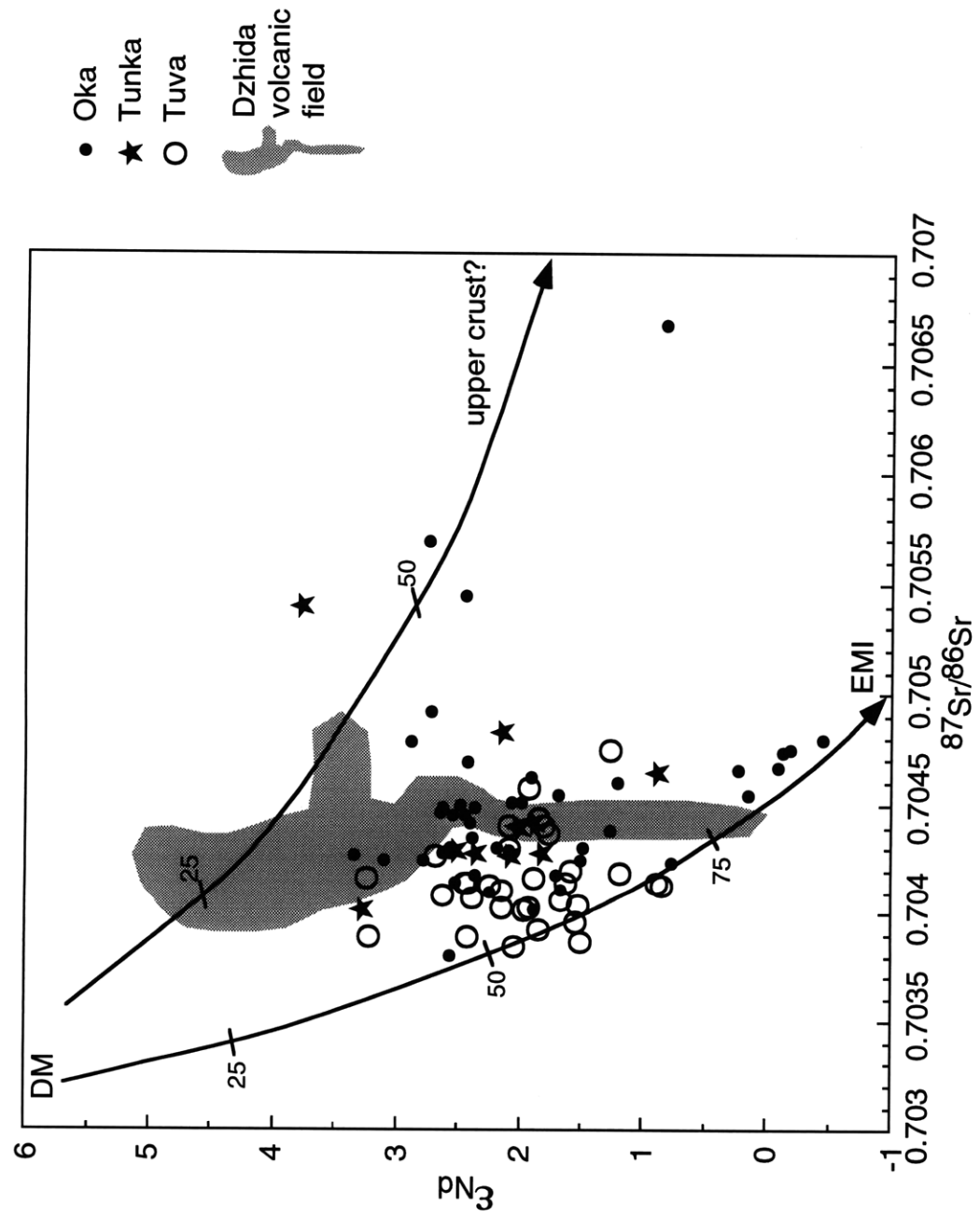
Oka
Tunka
Tuva
Dzhida volcanic field
upper crust?
EMI
DM
25
50
75
50
25
εNd
87Sr/86Sr
6
5
4
3
2
1
0
-1
0.703
0.7035
0.704
0.7045
0.705
0.7055
0.706
0.7065
0.707

Figure 2.15

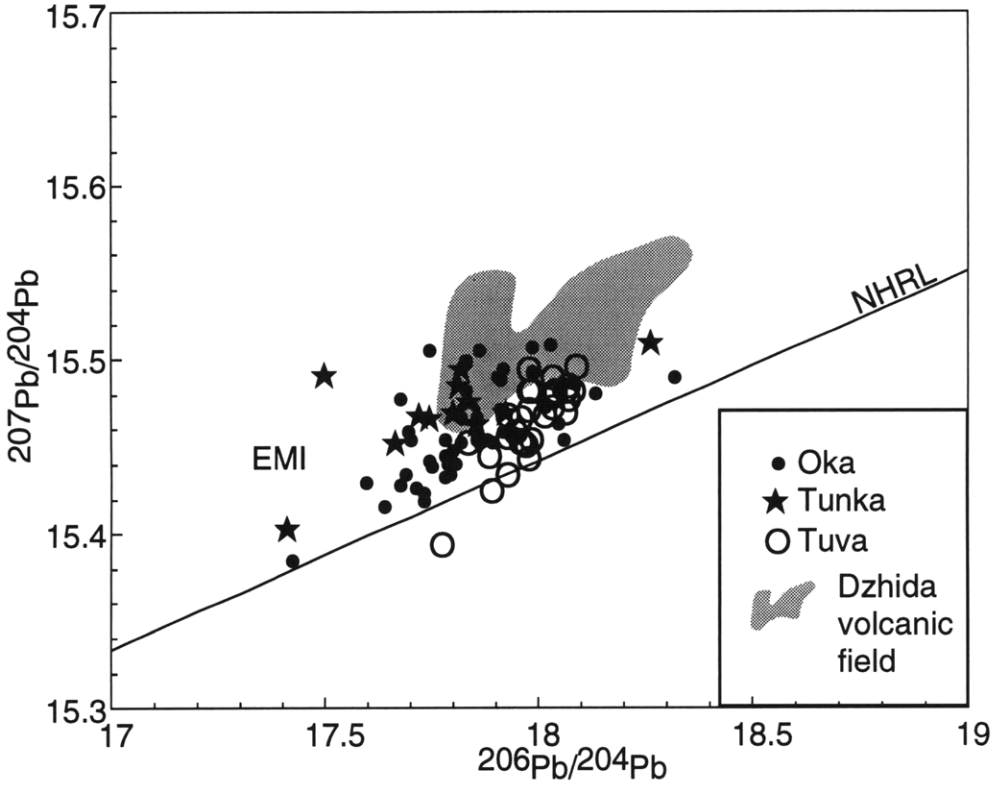
15.7
15.6
15.5
15.4
15.3
17
17.5
18
18.5
19
207Pb/204Pb
206Pb/204Pb
NHRL
EMI
Oka
Tunka
Tuva
Dzhida volcanic field

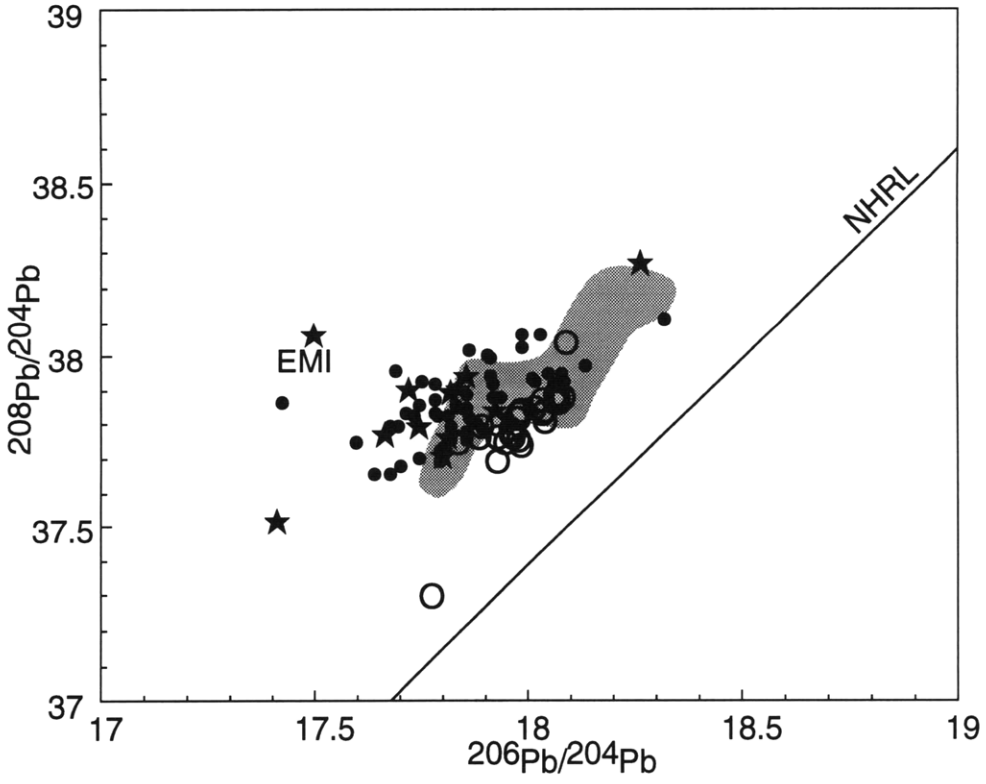
39
38.5
38
37.5
37
17
17.5
18
18.5
19
208Pb/204Pb
206Pb/204Pb
NHRL
EMI

Figure 2.16

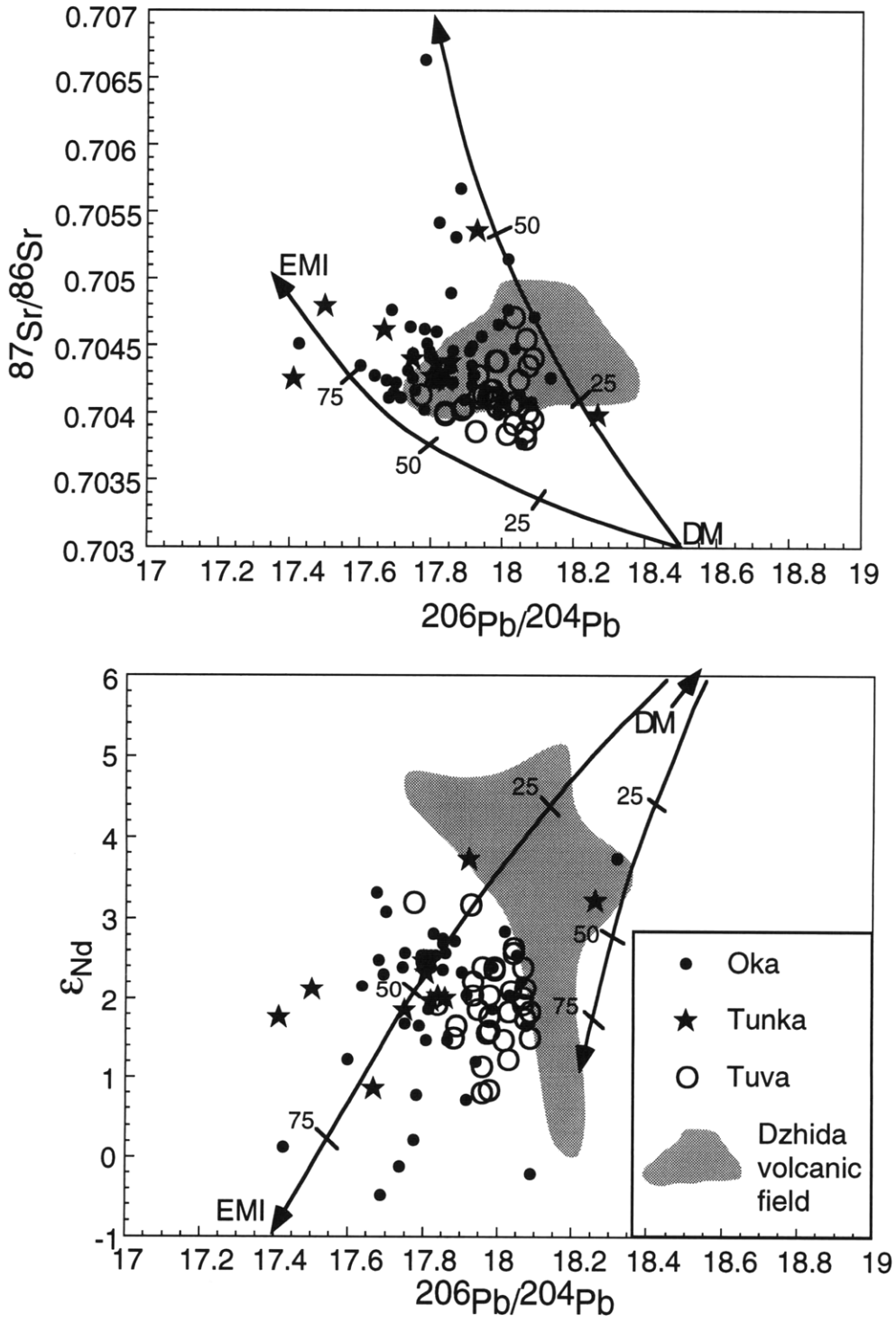
0.707
0.7065
0.706
0.7055
0.705
0.7045
0.704
0.7035
0.703
87Sr/86Sr
17
17.2
17.4
17.6
17.8
18
18.2
18.4
18.6
18.8
19
206Pb/204Pb
EMI
DM
50
75
25
6
5
4
3
2
1
0
-1
εNd
Oka
Tunka
Tuva
Dzhida volcanic field

Figure 2.17

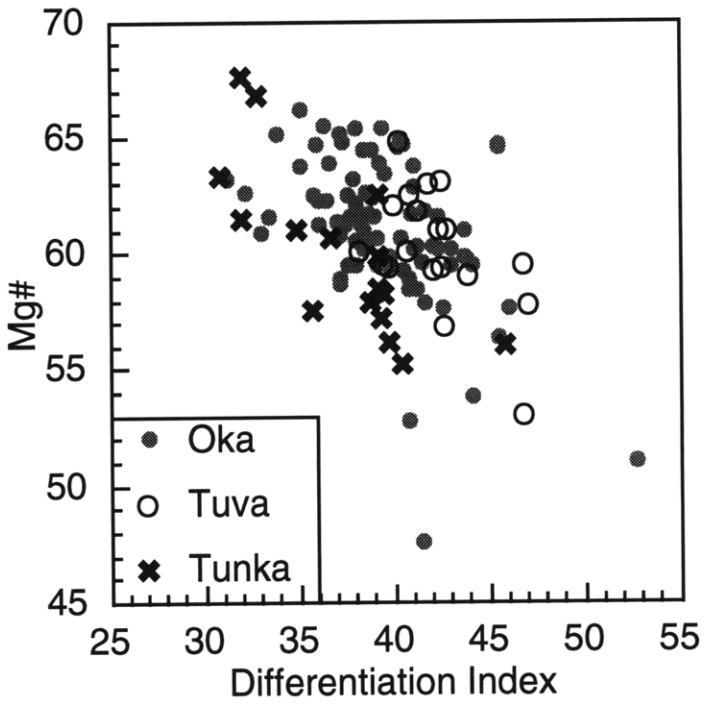
70
65
60
55
50
45
Mg#
Oka
Tuva
Tunka
25
30
35
40
45
50
55
Differentiation Index

Figure 2.18a

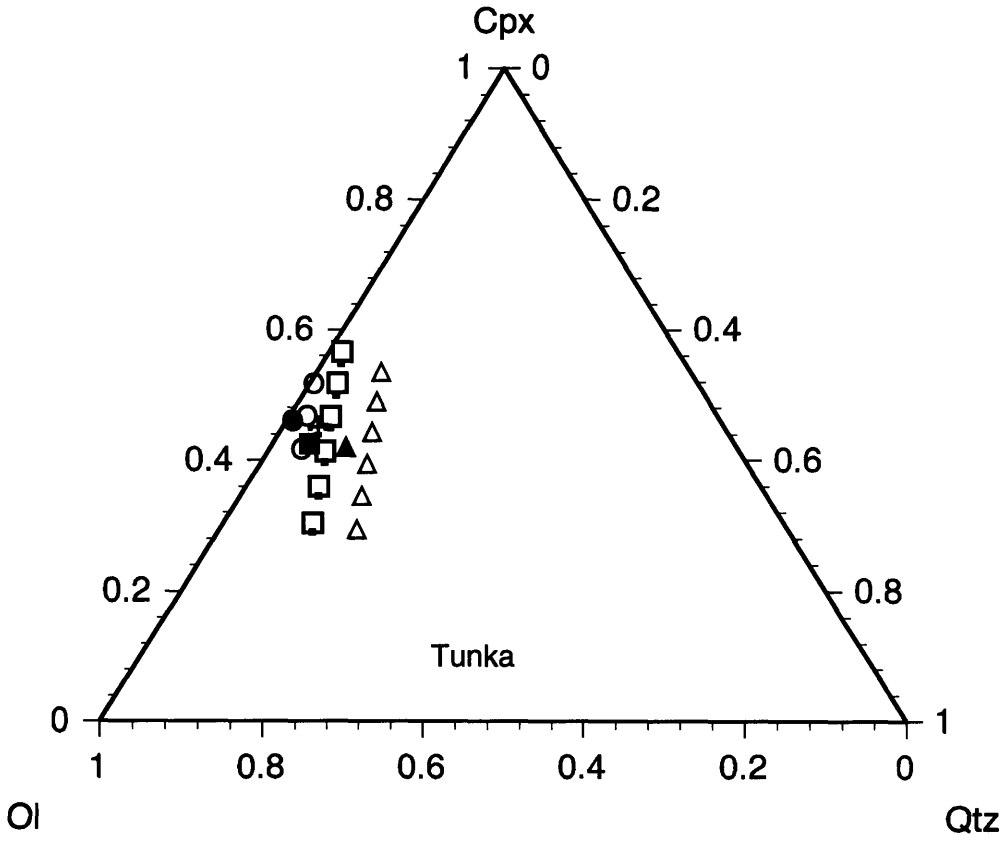

△	BK-1 (5-10kbar): 7.5kbar, 1207°C
▲	BK-1
○	BK-8 (8-10kbar): 9kbar, 1217°C
●	BK-8
□	BK-11 (5-10kbar): 8kbar, 1198°C
■	BK-11
▪	BK-12 (5-10kbar): 7kbar, 1195°C
✣	BK-12

Figure 2.18b

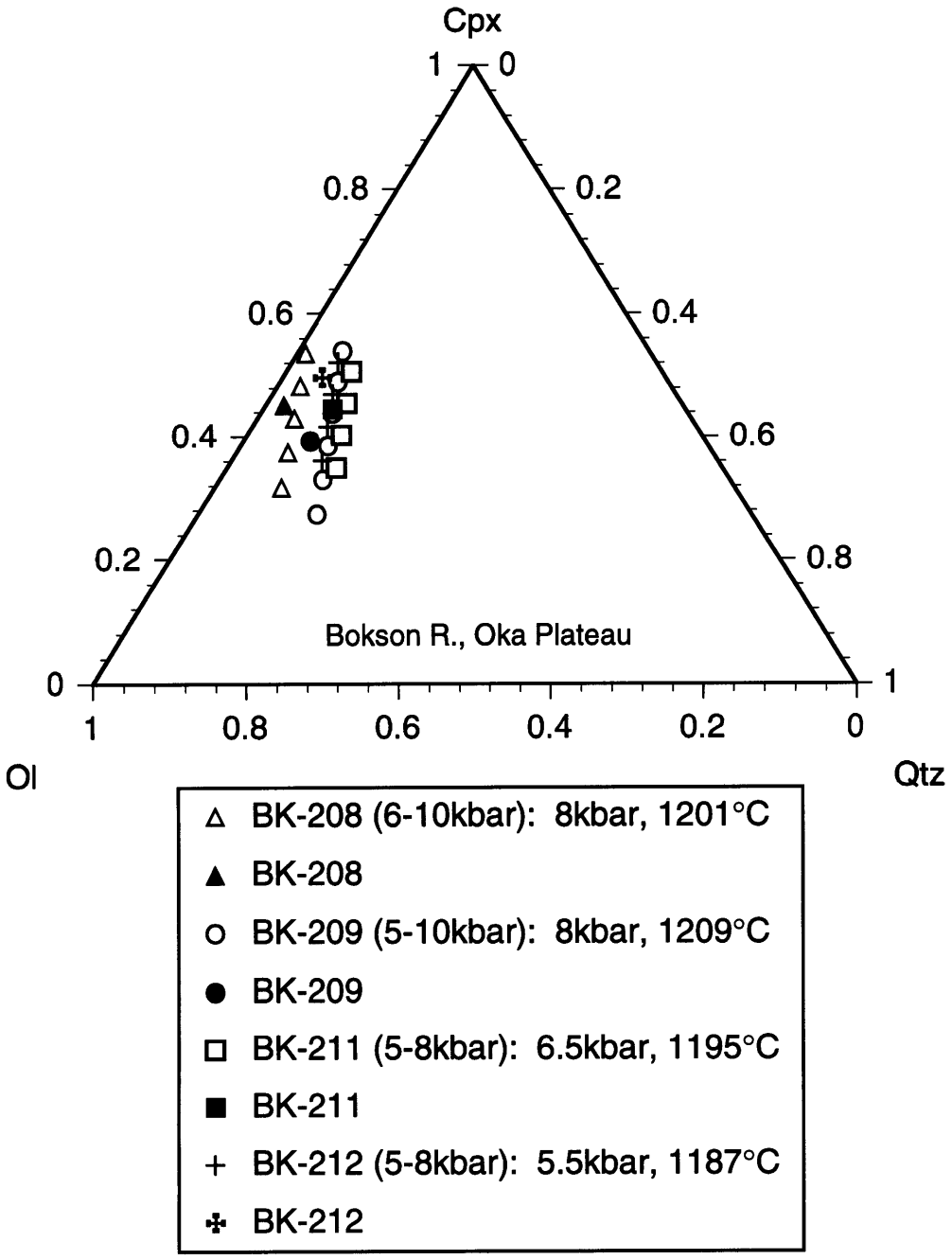
Cpx
1
0
0.8
0.2
0.6
0.4
0.4
0.6
0.2
0.8
0
1
Bokson R., Oka Plateau
1
0.8
0.6
0.4
0.2
0
Ol
Qtz
BK-208 (6-10kbar): 8kbar, 1201°C
BK-208
BK-209 (5-10kbar): 8kbar, 1209°C
BK-209
BK-211 (5-8kbar): 6.5kbar, 1195°C
BK-211
BK-212 (5-8kbar): 5.5kbar, 1187°C
BK-212

Figure 2.18c

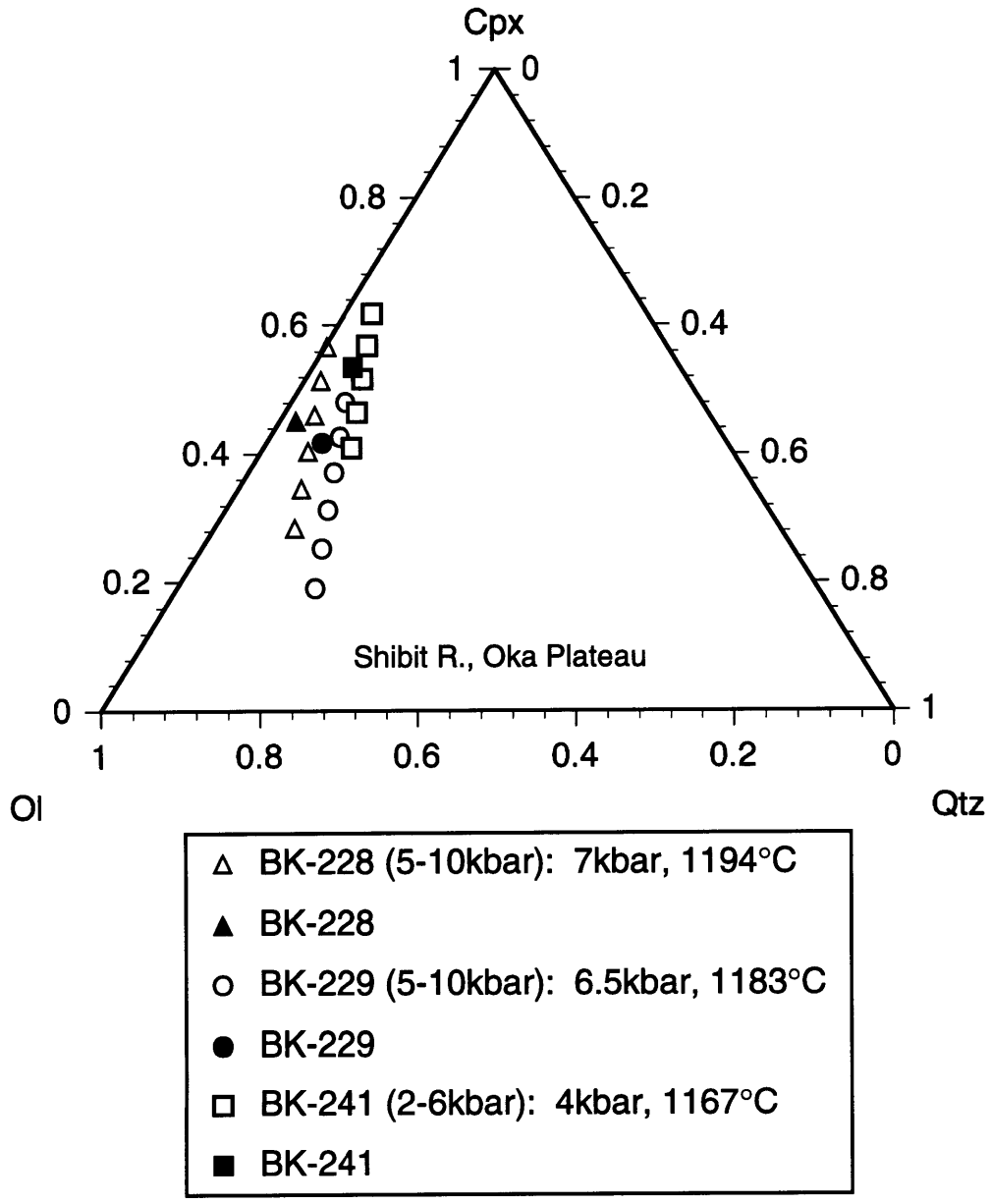
Cpx
1
0
0.8
0.2
0.6
0.4
0.4
0.6
0.2
0.8
0
1
Shibit R., Oka Plateau
1
0.8
0.6
0.4
0.2
0
Ol
Qtz
BK-228 (5-10kbar): 7kbar, 1194°C
BK-228
BK-229 (5-10kbar): 6.5kbar, 1183°C
BK-229
BK-241 (2-6kbar): 4kbar, 1167°C
BK-241

Figure 2.18d

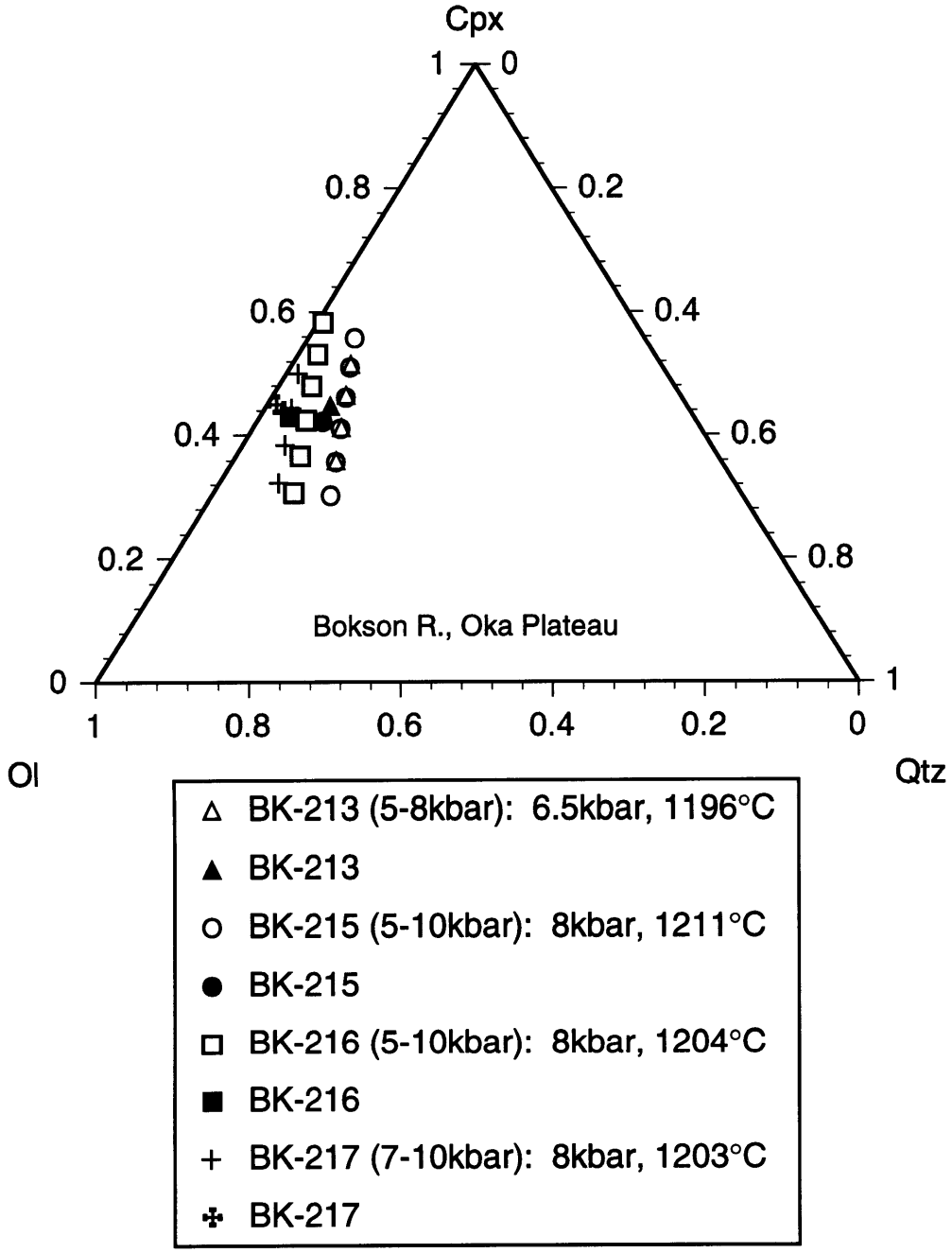
Cpx
1
0
0.8
0.2
0.6
0.4
0.4
0.6
0.2
0.8
0
1
Bokson R., Oka Plateau
1
0.8
0.6
0.4
0.2
0
Ol
Qtz
△ BK-213 (5-8kbar): 6.5kbar, 1196°C
▲ BK-213
○ BK-215 (5-10kbar): 8kbar, 1211°C
● BK-215
□ BK-216 (5-10kbar): 8kbar, 1204°C
■ BK-216
+ BK-217 (7-10kbar): 8kbar, 1203°C
✣ BK-217

Figure 2.18e

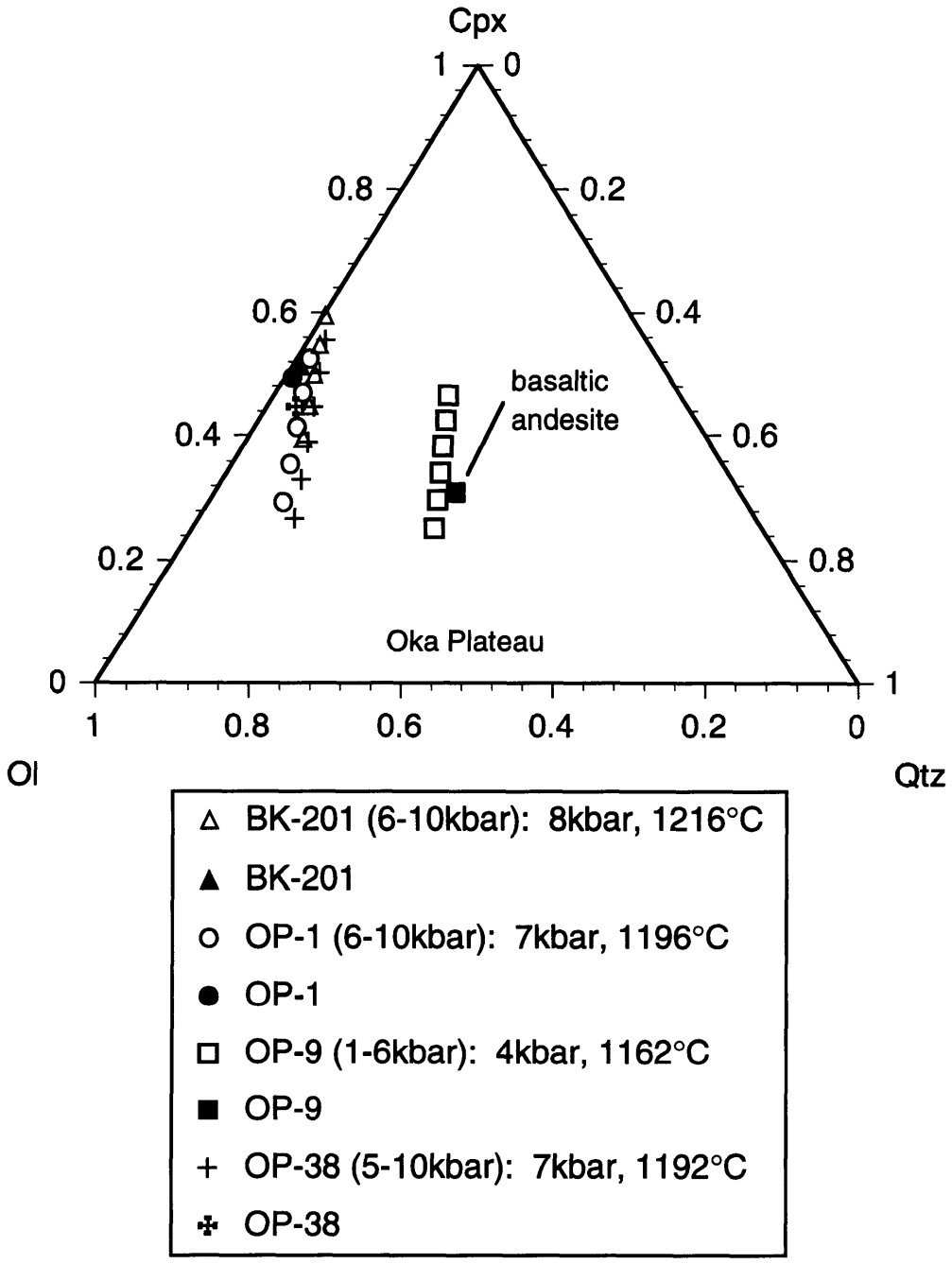
Cpx
1
0
0.8
0.2
0.6
0.4
0.4
0.6
0.2
0.8
0
1
1
0.8
0.6
0.4
0.2
0
Ol
Qtz
basaltic
andesite
Oka Plateau
BK-201 (6-10kbar): 8kbar, 1216°C
BK-201
OP-1 (6-10kbar): 7kbar, 1196°C
OP-1
OP-9 (1-6kbar): 4kbar, 1162°C
OP-9
OP-38 (5-10kbar): 7kbar, 1192°C
OP-38

Figure 2.19

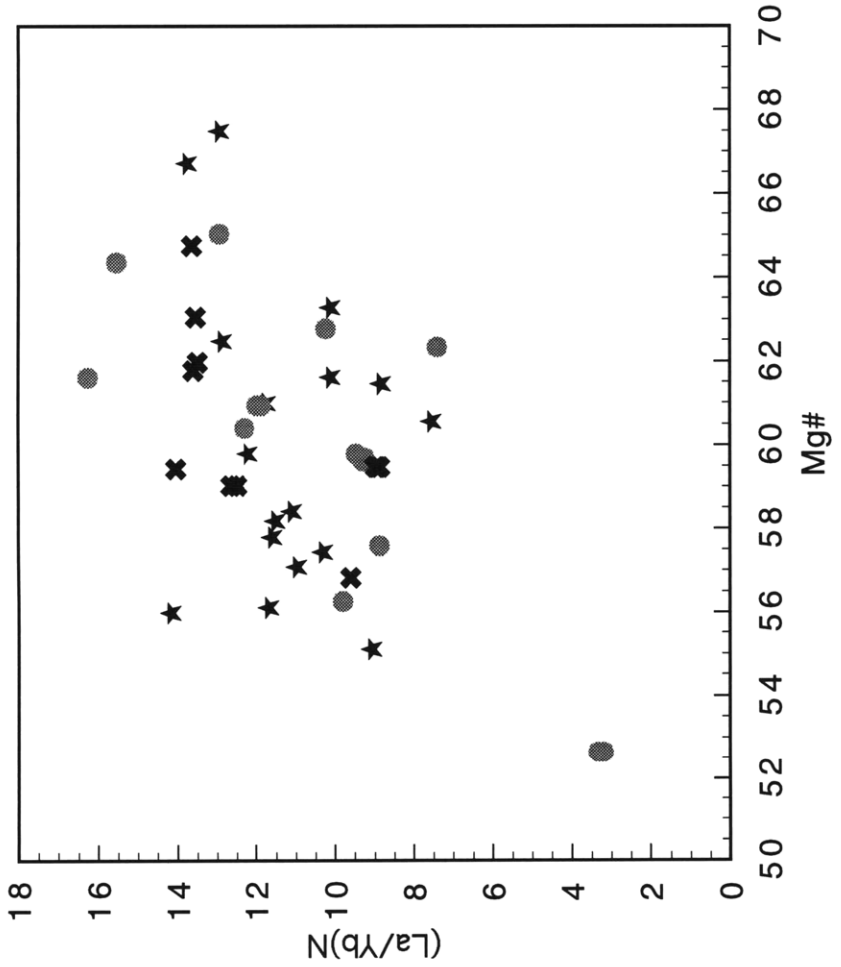

Figure 2.20

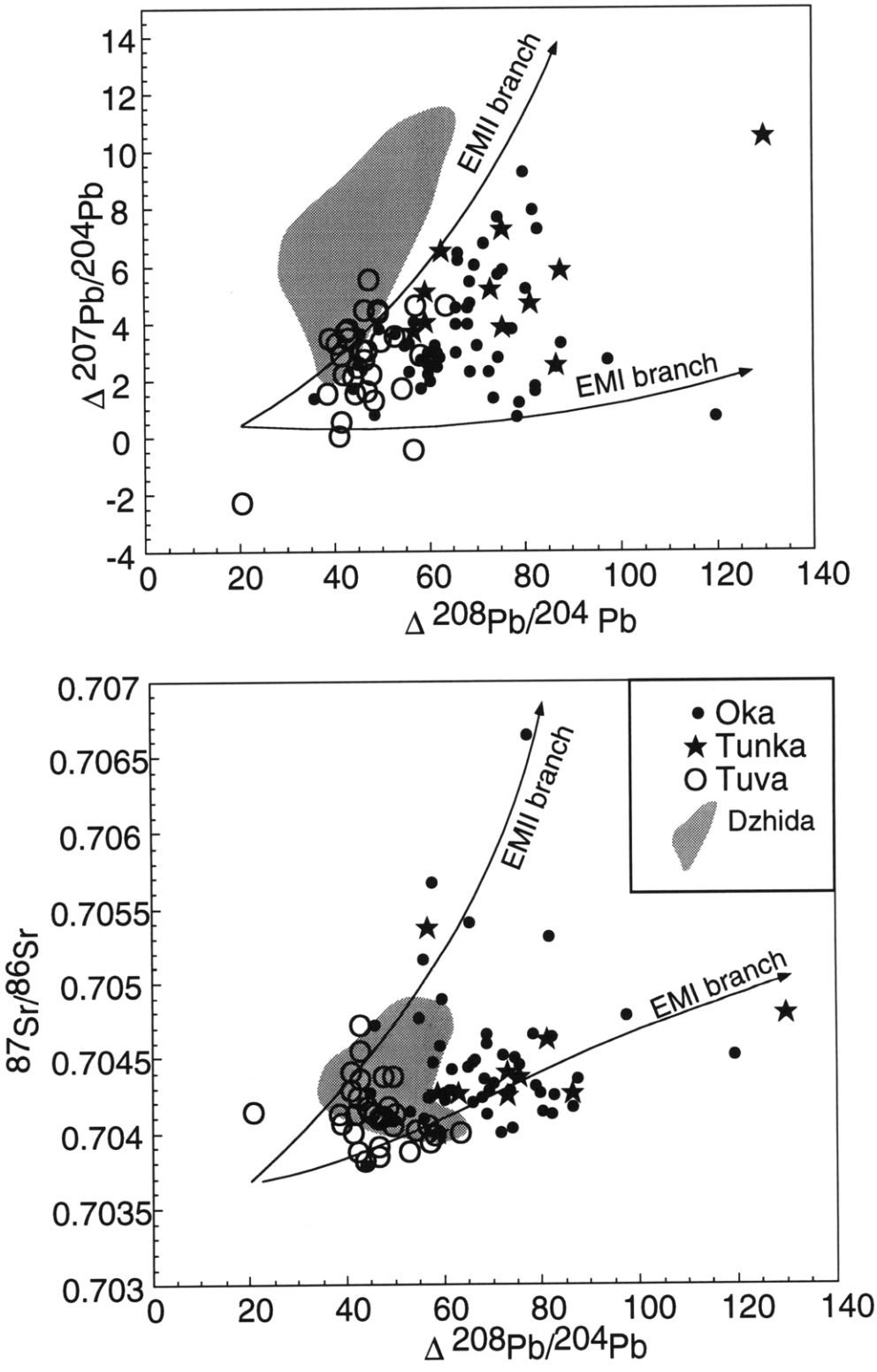
14
12
10
8
6
4
2
0
-2
-4
Δ 207Pb/204Pb
0
20
40
60
80
100
120
140
Δ 208Pb/204 Pb
EMII branch
EMI branch
0.707
0.7065
0.706
0.7055
0.705
0.7045
0.704
0.7035
0.703
87Sr/86Sr
Δ 208Pb/204Pb
Oka
Tunka
Tuva
Dzhida
EMII branch
EMI branch

Figure 2.21

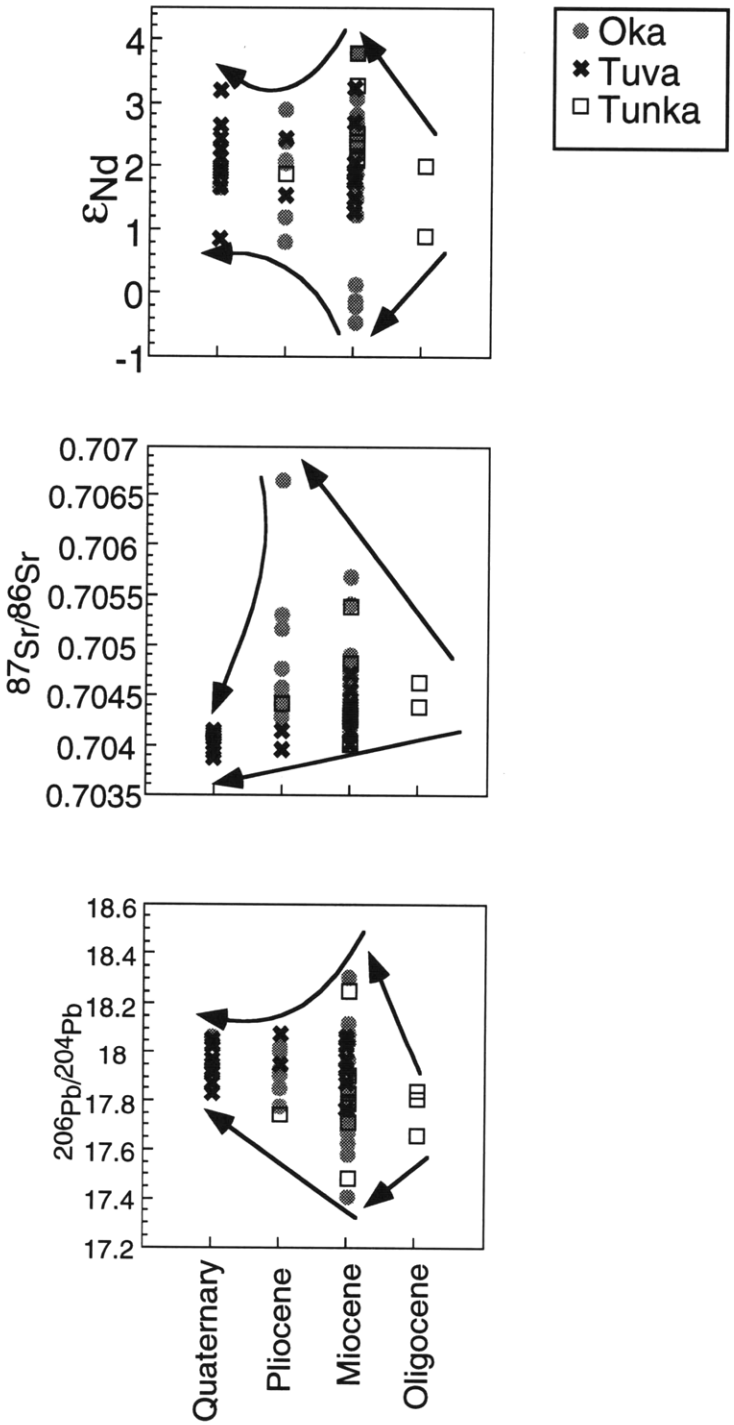
Oka
Tuva
Tunka
εNd
4
3
2
1
0
-1
87Sr/86Sr
0.707
0.7065
0.706
0.7055
0.705
0.7045
0.704
0.7035
206Pb/204Pb
18.6
18.4
18.2
18
17.8
17.6
17.4
17.2
Quaternary
Pliocene
Miocene
Oligocene

Figure 2.22

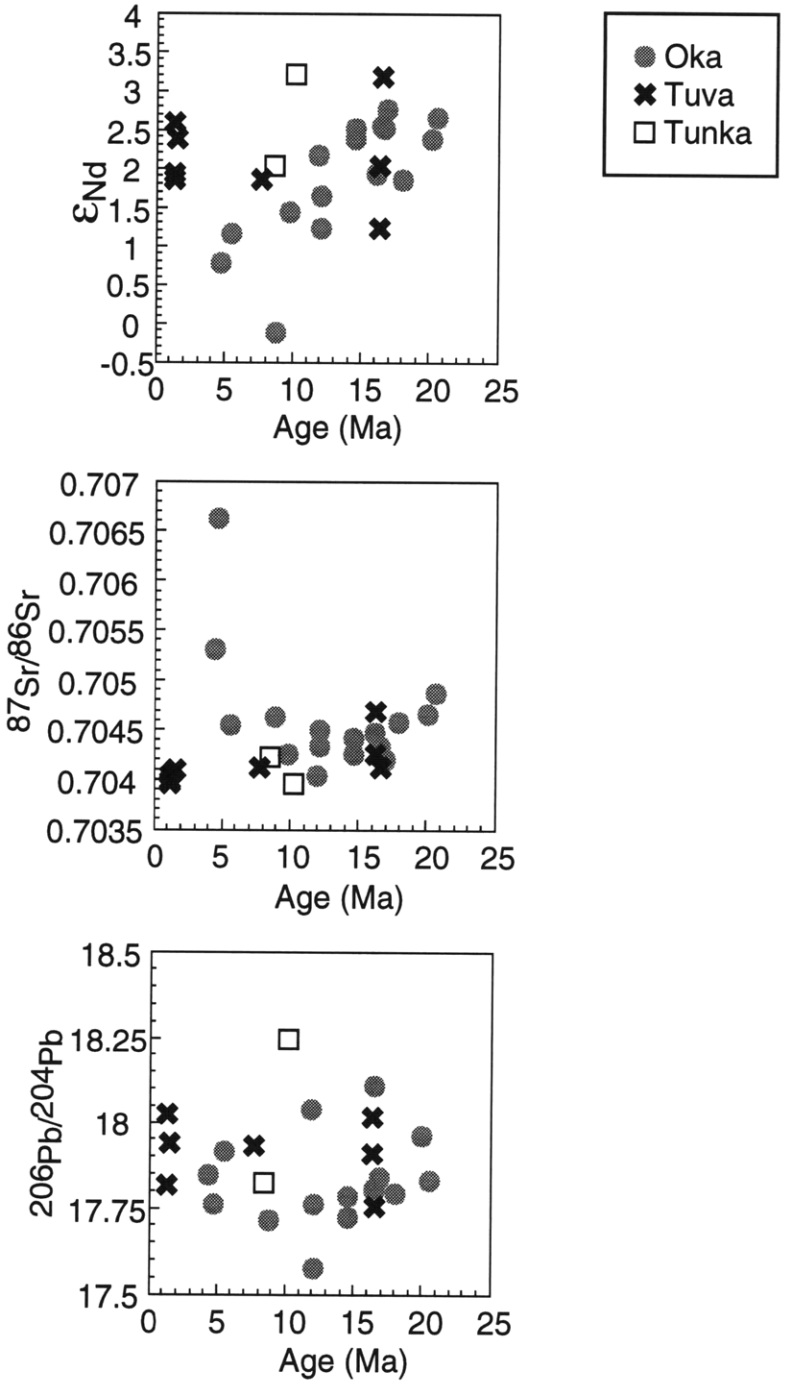
Oka
Tuva
Tunka
ε_{Nd}
Age (Ma)
$^{87}Sr/^{86}Sr$
Age (Ma)
$^{206}Pb/^{204}Pb$
Age (Ma)

Figure 2.23a

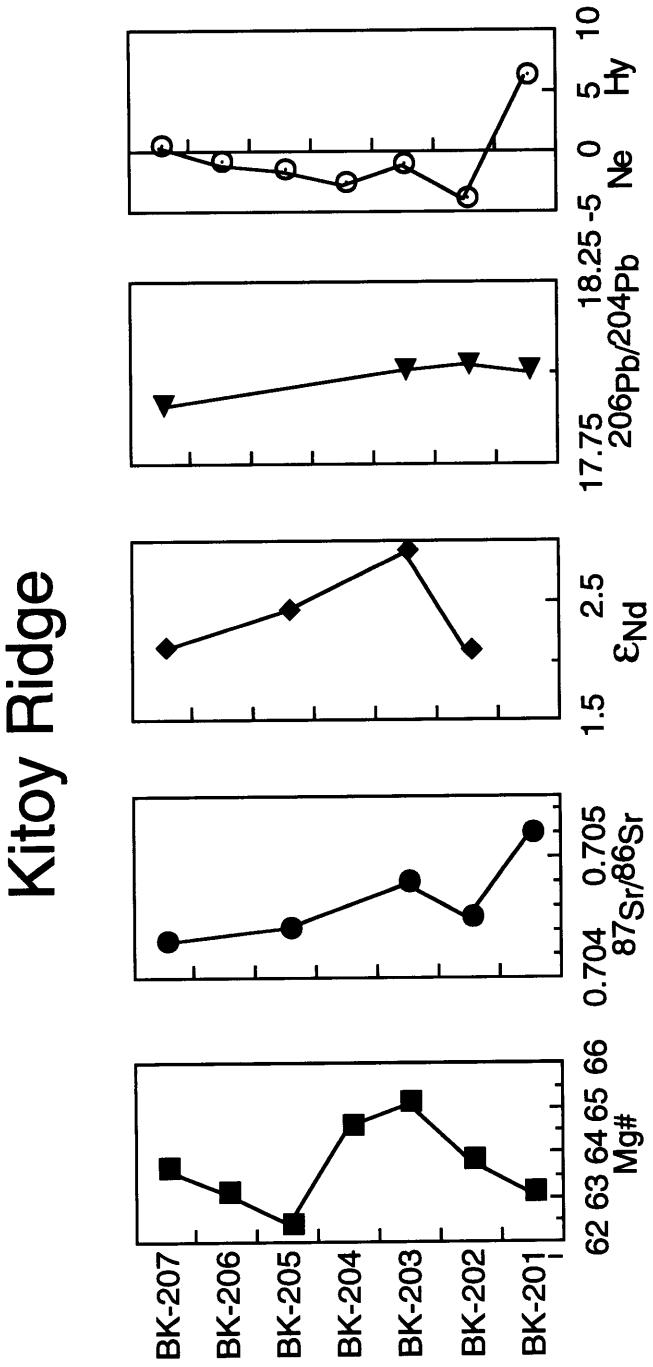
Kitoy Ridge
BK-207
BK-206
BK-205
BK-204
BK-203
BK-202
BK-201
62 63 64 65 66
Mg#
0.704 0.705
87Sr/86Sr
1.5 2.5
εNd
17.75 18.25
206Pb/204Pb
-5 0 5 10
Ne Hy

Figure 2.23b

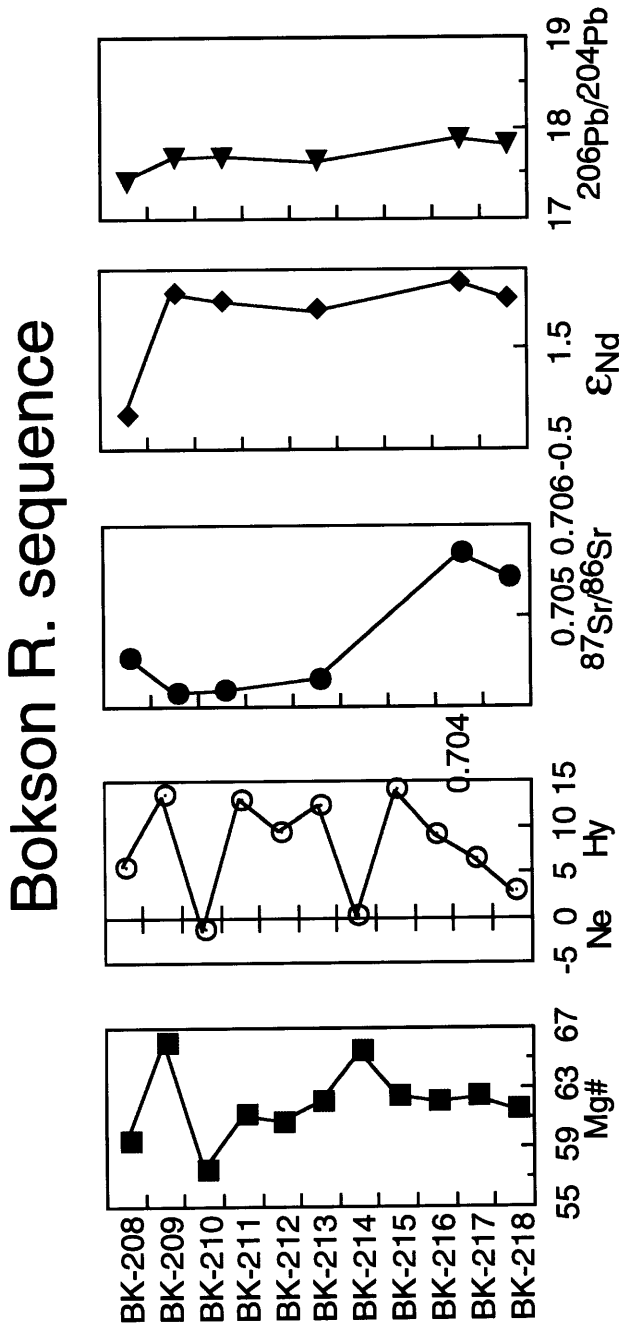
Bokson R. sequence
BK-208
BK-209
BK-210
BK-211
BK-212
BK-213
BK-214
BK-215
BK-216
BK-217
BK-218
55 59 63 67
Mg#
-5 0 5 10 15
Ne Hy
0.704
0.705 0.706
87Sr/86Sr
-0.5 1.5
εNd
17 18 19
206Pb/204Pb

Figure 2.23c

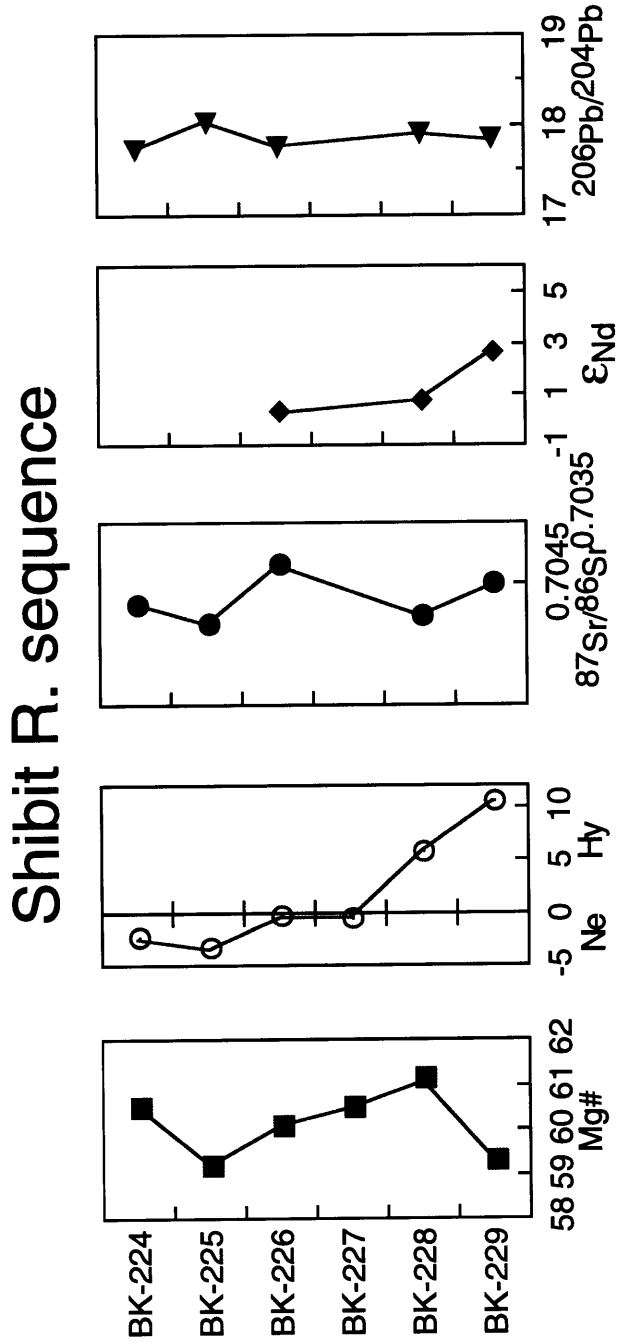
Shibit R. sequence
BK-224
BK-225
BK-226
BK-227
BK-228
BK-229
58 59 60 61 62
Mg#
-5 0 5 10
Ne Hy
0.7045
87Sr/86Sr0.7035
-1 1 3 5
εNd
17 18 19
206Pb/204Pb

Figure 2.23d

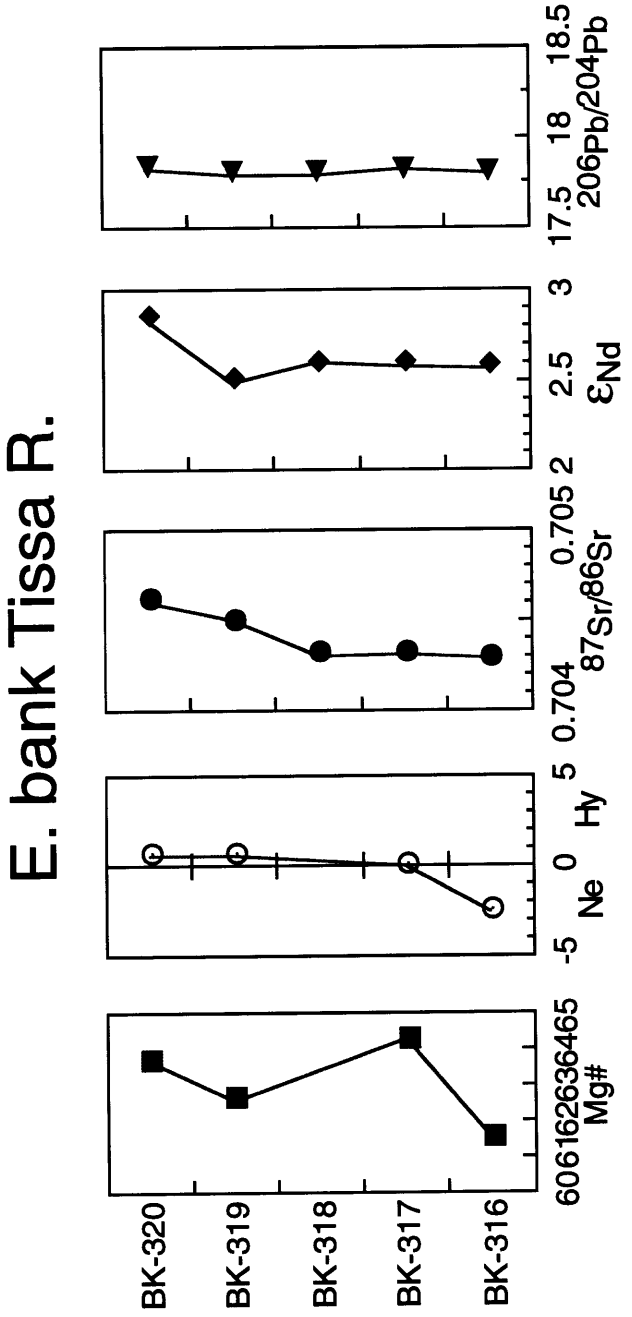
E. bank Tissa R.
BK-320
BK-319
BK-318
BK-317
BK-316
60 61 62 63 64 65
Mg#
-5 Ne 0 Hy 5
0.704 87Sr/86Sr 0.705
2 2.5 3 εNd
17.5 18 18.5 206Pb/204Pb

Table 2.1. $^{40}Ar/^{39}Ar$ Data for the western BRZ

Sample	location	plateau age	±2σ	cum % $^{39}Ar_r$	steps	isochron age	±2σ	steps	$^{39}Ar_r$ (%)	$(^{40}Ar/^{36}Ar)_0$	±2σ	MSWD	^{39}Ar Wtd. Mean age	±2σ
93-OP-5	Oka R.	19.95	±0.24	66.0	1-3	**20.36**	**±0.82**	1-3	66	280.2	±28.7	0.87	19.13	±0.30
93-OP-3	Oka R.	5.15	±0.04	100.0	1-4	**4.31**	**±0.76**	1-3	78.58	368.5	±63.4	0.59	5.14	±0.13
93-OP-3A	Oka R.	5.11	±0.09	100.0	1-4	**5.34**	**±0.18**	1-4	100	286.9	±5.2	0.90	5.06	±0.16
BK-218	Bokson R.												**17.81**	**±0.20**
BK-219	Bokson R.												**4.55**	**±0.10**
93-OP-16	Zabit R.	10.55	±0.09	100.0	1-4	**10.50**	**±0.16**	1-4	100	300.5	±11.9	0.43	10.61	±0.14
93-OP-17	Zabit R.	11.08	±0.09	98.3	2-4	**11.01**	**±0.14**	2-4	98.3	302.5	±6.9	1.41	11.90	±0.20
93-OP-18	Zabit R.					**11.94**	**±0.45**	1-3	46.3	294.7	±23.3	0.12	11.75	±0.15
93-OP-19	Zabit R.	11.52	±0.19	92.6	2-4	**11.74**	**±0.39**	2-4	92.6	292.0	±5.3	0.20	10.86	±0.25
93-OP-33	Oka	9.62	±0.10	100.0	1-4	**9.65**	**±0.19**	1-4	100	294.1	±7.7	2.17	9.67	±0.18
93-OP-34	Oka					**11.09**	**±0.16**	2-4	99.78	312.2	±6.7	1.87	11.29	±0.13
93-OP-36	Oka					**11.38**	**±0.15**	1-3	81.6	315.3	±10.6	1.43	11.83	±0.16
93-OP-37	Oka	11.70	±0.09	100.0	1-4	**11.57**	**±0.17**	1-4	100	308.2	±10.4	1.49	11.88	±0.18
93-OP-38	Oka					**11.94**	**±0.32**	1-4	100	279.5	±8.3	0.63	11.03	±0.30
BK-311	Oka	19.78	±0.17	64.9	3-6	**19.93**	**±0.18**	3-6	64.9	343.8	±19.9	0.57	20.30	±0.19
BK-314	Tissa R.	16.52	±0.11	63.4	3-6	**16.29**	**±0.25**	3-6	63.4	393.0	±85.9	1.86	16.20	±0.11
BK-318(clair72)	Tissa R.	16.97	±0.13	61.1	3-5								16.61	±0.12
BK-318 (clair73)	Tissa R.	17.06	±0.18	72.2	3-6	**16.87**	**±0.28**	1-6	100	348.0	±27.3	0.43	17.46	±0.20
BK-317(clair72)	Tissa R.												**16.77**	**±0.13**
BK-317 (clair 73)	Tissa R.	16.87	±0.14	86.2	2-5	**16.50**	**±0.32**	2-5	96.2	333.8	±25.8	1.92	16.73	±0.15
BK-316	Tissa R.					**14.48**	**±0.36**	1-3	48.44	346.8	±24.5	0.19	15.65	±0.12
BK-322	Oka					**16.85**	**±0.24**	1-3	45.74	282.5	±3.8	0.40	16.15	±0.20
BK-328	Oka	14.71	±0.22	63.1	4-6	**14.56**	**±1.21**	4-6	63.1	305.1	±73.3	2.48	14.11	±0.21
93-OP-8	Hore/Tissa R.	8.73	±0.11	70.5	2-4	**8.66**	**±0.16**	2-4	70.5	312.4	±21.1	1.54	9.29	±0.17
93-OP-12	Oka R.	11.98	±0.21	83.0	1-3	**11.32**	**±1.01**	1-3	83	305.5	±14.7	2.07	11.95	±0.25
TV-94-35	Derbi-Tayga volcano	**1.04**	**±0.28**	90.7	2-6								0.58	±0.31
TV-94-36	Prioserniy volcano	0.68	±0.18	52.7	1-4	**1.09**	**±0.35**	2-4	42.89	274.0	±20.1	0.35	0.32	±0.18

Notes: The preferred age is shown in bold type. Details of the interpretation are given in Appendix 2.A.
Bracketed sequences of rocks are listed by relative stratigraphic position; for example, 93-OP-16 is the highest sample in the series where 93-OP-19 is the lowest sample.

Table 2.2a. Tunka volcanic field major (wt%) and trace element (ppm) data

Sample	BK-1	BK-2	BK-3	BK-4A	BK-4B	BK-4C	BK-5	BK-6A	BK-7	BK-7X2	BK-8	BK-9	BK-10	BK-11	BK-12	BK-13
SiO_2	48.24	47.66	48.10	47.95	47.85	48.07	47.44	48.16	45.29	44.74	47.77	48.03	49.77	48.46	49.69	47.28
TiO_2	2.45	2.40	2.35	1.92	1.93	1.95	2.17	2.04	2.29	2.23	2.26	2.36	2.80	2.52	1.90	2.66
Al_2O_3	13.81	14.88	16.37	15.65	15.71	15.57	15.68	15.62	14.42	14.27	14.52	14.31	14.03	14.56	14.61	14.00
Fe_2O_{3t}	12.02	12.52	11.61	12.79	12.84	12.79	12.61	11.96	11.76	11.68	12.80	11.89	12.86	13.10	11.83	12.97
MnO	0.20	0.18	0.16	0.18	0.17	0.17	0.18	0.18	0.19	0.20	0.17	0.17	0.19	0.18	0.15	0.18
MgO	8.90	7.99	6.34	7.31	7.74	7.64	6.92	7.03	10.12	10.41	8.76	8.50	6.78	7.59	7.80	8.71
CaO	8.31	8.54	7.45	8.08	8.11	7.92	8.02	7.96	9.83	10.05	8.67	8.56	8.22	7.72	7.98	8.56
Na_2O	2.48	4.13	4.51	3.86	4.12	3.85	3.65	3.20	3.67	3.82	2.79	3.91	3.61	3.10	3.52	2.89
K_2O	1.57	1.66	2.43	1.65	1.58	1.69	1.88	1.87	1.98	1.93	1.38	1.83	1.66	1.53	1.08	1.78
P_2O_5	0.51	0.71	0.81	0.59	0.58	0.58	0.71	0.67	0.66	0.63	0.51	0.62	0.57	0.54	0.34	0.54
LOI(%)	1.99	-0.53	-0.26	-0.12	-0.54	-0.29	0.53	0.30	-0.23	-0.30	0.38	-0.37	-0.14	1.05	0.82	0.21
TOTAL	100.47	100.14	99.87	99.85	100.09	99.94	99.79	98.98	99.98	99.66	100.01	99.81	100.35	100.35	99.72	99.78
Mg#	63	60	56	57	58	58	56	58	67	67	61	62	55	57	61	61
Rb	17.0	21.8	29.7	18.1	19.6	19.1	23.0	21.2	35.7	14.3	23.5	19.1	20.0	13.5	24.5	27.6
Sr	531	772	1141	727	742	748	1174	890	840	886	731	562	563	451	702	976
Ba	330	469	710	449	464	478	452	743	556	321	446	435	402	289	396	1768
Sc	20.0	19.2	16.4	20.1	20.0	19.3	17.3	19.1	25.1	26.2	20.5	18.7	18.7	19.2	18.0	17.9
V	174	186	144	159	164	165	140	156	217	173	166	177	172	137	192	243
Cr	283	225	125	208	223	213	170	188	268	296	238	230	179	238	218	211
Co	49.4	45.8	38.6	46.9	48.7	47.0	41.6	42.8	47.6	49.4	51.1	46.4	43.5	48.4	43.2	48.2
Ni	169	101	75	117	136	139	95	100	185	128	155	113	161	104	136	235
Zn	105	105	84	103	103	102	103	88	91	112	102	116	121	109	115	98
Ga	24.2	23.6	21.5	22.5	22.0	20.9	20.3	20.5	19.9	20.5	21.6	25.2	21.4	22.7	22.7	19.4
Y	19.2	22.0	21.6	18.7	18.7	17.2	19.8	21.4	23.4	20.3	19.4	23.8	23.3	17.5	21.4	19.9
Zr	166	199	223	153	150	158	207	208	236	167	204	238	217	151	232	127
Hf	4.19	4.58	4.90	3.66	3.63	3.70	4.65	4.74	5.34	5.11	4.06	4.77	5.75	5.13	3.51	5.13
Nb	29.7	42.3	48.1	31.6	32.2	32.7	41.4	38.5	58.7	28.2	41.5	32.4	31.4	21.2	39.1	26.6
Ta	1.93	2.50	2.96	1.87	1.90	1.93	2.36	2.24	3.75	3.63	1.59	2.52	2.04	1.94	1.29	2.25
Th	2.15	2.30	3.17	1.93	1.96	1.97	2.09	2.56	4.20	3.89	1.95	2.80	2.16	1.99	1.55	2.85
La	21.5	28.8	35.4	24.6	24.4	24.8	28.7	30.0	37.8	36.1	20.2	28.1	25.7	24.9	15.0	27.2
Ce	46.0	59.5	70.7	50.6	49.8	51.1	59.1	61.2	74.8	71.7	42.3	57.7	55.3	50.5	31.6	56.4
Nd	25	30	33	26	26	26	33	31	34	32	24	30	32	29	19	29
Sm	5.88	6.90	6.86	5.53	5.41	5.56	6.73	6.33	7.19	6.99	5.83	6.66	7.30	6.76	4.43	6.64
Eu	1.87	2.24	2.18	1.80	1.77	1.77	2.14	1.99	2.24	2.19	1.88	2.17	2.23	2.13	1.47	2.03
Tb	0.77	0.88	0.83	0.74	0.71	0.72	0.85	0.81	0.89	0.87	0.81	0.87	0.97	0.89	0.64	0.84
Yb	1.47	1.63	1.73	1.55	1.52	1.49	1.70	1.79	1.90	1.93	1.58	1.51	1.96	1.67	1.37	1.60
Lu	0.225	0.244	0.263	0.226	0.234	0.242	0.240	0.257	0.298	0.272	0.221	0.210	0.275	0.248	0.193	0.223

Notes: Major and trace elements determined by XRF at Washington University, St. Louis. REE determined by INAA at Washington University St. Louis. Mg# = 100*atomic Mg/(Mg + Fe^{2+}), calculated with FeO = 0.15*Fe_2O_{3total}.

Table 2.2a. Tunka volcanic field major (wt%) and trace element (ppm) data continued

Sample	BK-161	BK-162	p506	p508	p528/A
SiO_2	48.85	49.31	48.41	48.94	49.26
TiO_2	1.94	1.92	2.42	2.30	2.07
Al_2O_3	14.68	14.68	15.26	15.06	14.61
Fe_2O_{3t}	12.76	12.66	12.21	11.74	11.49
MnO	0.16	0.16	0.16	0.16	0.15
MgO	8.48	8.65	8.14	7.97	8.41
CaO	8.07	8.17	8.72	8.36	7.97
Na_2O	3.07	3.24	3.85	3.83	3.01
K_2O	1.13	1.00	1.88	1.94	1.39
P_2O_5	0.28	0.30	0.63	0.61	0.36
LOI(%)	2.08	1.46	-0.41	0.32	2.30
TOTAL	101.51	101.55	101.27	101.24	101.01
Mg#	61	61	61	61	63
Rb	16	10	20	22	17
Sr	422	388	695	680	592
Ba	215	193	422	441	279
Sc					
V	166	164	172	172	161
Cr	235	237	218	213	248
Co	60	59	56	54	50
Ni	117	116	104	112	90
Zn	105	105	93	98	92
Ga					
Y	22	22	23	24	22
Zr	145	128	215	216	165
Hf					
Nb	23	16	42	42	15
Ta					
Th					
La					
Ce					
Nd					
Sm					
Eu					
Tb					
Yb					
Lu					

Notes: Major and trace elements determined by XRF at Washington University, St. Louis.
Mg# = 100*atomic Mg/(Mg + Fe^{2+}), calculated with FeO = 0.15*Fe_2O_{3total}.

Table 2.2b. Oka Plateau volcanic field major (wt%) and trace element (ppm) abundances.

Sample	OP-1	OP-2	OP-3	OP-3A	OP-4	OP-4(B)	OP-5	OP-6	OP-7	OP-8	OP-9	OP-9*	OP-10	OP-11	OP-12	OP-14
SiO_2	50.21	48.65	48.67	48.77	48.54	48.47	48.08	51.12	50.83	50.06	55.07		46.59	48.90	46.78	46.68
TiO_2	2.14	2.3	2.21	2.25	2.08	2.08	2.39	2.23	2.05	2.06	1.23		2.83	2.32	2.72	2.67
Al_2O_3	15.57	14.76	15.36	15.59	15.15	15.06	14.74	15.66	15.18	15.11	16.52		15.33	15.17	14.73	14.37
Fe_2O_{3t}	10.69	11.03	11.48	11.56	11.08	11.06	11.54	10.78	10.97	11.36	9.98		12.21	11.86	11.49	12.24
MnO	0.15	0.16	0.16	0.17	0.18	0.18	0.16	0.15	0.15	0.16	0.14		0.19	0.19	0.19	0.17
MgO	7.59	8.8	7.42	7.57	8.66	8.77	8.94	5.95	7	7.35	4.76		7.76	7.45	8.07	8.43
CaO	8.22	8.65	7.83	8.31	8.01	8.00	8.14	7.69	7.86	7.89	7.8		8.24	7.79	9.07	8.65
Na_2O	3.53	2.96	4.25	3.34	3.74	3.88	3.51	3.97	4.05	4.18	3.96		4.12	4.48	3.48	3.7
K_2O	1.51	2.06	1.73	1.77	2.04	2.00	1.82	1.99	1.67	1.7	0.48		1.99	1.67	2.32	2.25
P_2O_5	0.55	0.65	0.53	0.6	0.57	0.56	0.71	0.52	0.45	0.46	0.14		0.70	0.54	0.91	0.89
TOTAL	100.16	100.02	99.64	99.93	100.03	100.07	100.03	100.06	100.21	100.33	100.08		99.96	100.37	99.77	100.05
Mg#	62	65	60	60	65	65	64	56	60	60	53		60	59	62	62
Rb	15.3	24.8	20.1	23.6			16	30.1	24.4	24.2	17.8	17.1	25			26
Sr	844	844	811	1127			1097	633	557	588	501	400	573			1010
Ba	315	417	384	388			313	412	341	343	95	85	342			448
Sc	17.7	17.9		16.0			15.0	16.1	17.7		18.4	15.1	17.3			15.8
V	138	147	142	158			146	149	151	143	157		149			161
Cr	(220)	(229)	142	(147)			(222)	(112)	(191)	163	(110)	88	(176)			(187)
Co	39.8	45.6		44.0			46.0	35.2	40.5		32.7	22.7	39.2			45.8
Ni	101	135	108	121			185	43	68	87	65	60	69			105
Cu												65				
Zn	110	113	117	128			127	113	110	110	110	73	113			124
Ga	20	20	22	20			21	23	21	22	18	16	21			23
Y	18	20	19	19			19	22	21	21	12	11	21			22
Zr	168	216	185	198			209	221	187	186	44	41	192			263
Hf	3.68	4.36		3.95			4.19	4.73	4.13		1.25	1.21	4.06			5.41
Nb	29.3	42.2	34.2	36.2			46.5	39.7	32.2	34.2	6.0	6.3	33.2			59.3
Ta	1.66	2.31		1.95			2.42	2.13	1.72		0.33	0.31	1.83			3.08
Th	1.71	2.74		2.16			2.37	3.36	2.69		0.51	0.56	2.65			3.35
U												0.17				
La	15.2	27.5	(17.2)	23.0			25.7	25.3	21.1		5.0	3.9	21.4			35.7
Ce	44.9	62.0	(36.8)	51.3			59.6	57.1	47.3		12.9	7.9	47.8			79.2
Pr												1.2				
Nd	23.9	30.8		26.2			30.5	27.6	24.2		8.5	6.3	23.2			39.5
Sm	5.79	6.73		6.08			7.09	6.16	5.47		2.60	1.82	5.65			8.29
Eu	1.87	2.13		1.94			2.21	1.89	1.80		1.01	0.74	1.80			2.63
Gd												1.96				
Tb	0.64	0.82		0.79			0.79	0.82	0.81		0.42	0.32	0.72			0.88
Dy												1.84				
Ho												0.36				
Er												0.96				
Tm												0.14				
Yb	1.42	1.47		1.29			1.14	1.78	1.54		1.03	0.83	1.60			1.52
Lu	0.19	0.21		0.20			0.17	0.24	0.25		0.16	0.12	0.24			0.22

Notes: Major and trace elements determined by XRF at the University of Massachusetts, Amherst, except samples marked by * where trace elements determined by ICP-MS at M.I.T. Abundances of Sc, some Cr (shown in parentheses), Co, Hf, Ta, Th and REE determined by neutron activation. La and Ce shown in parentheses were determined by XRF. Mg# = 100*atomic $Mg/(Mg + Fe^{2+})$, calculated with $FeO = 0.15*Fe_2O_{3total}$.

Table 2.2b Oka Plateau volcanic field major (wt%) and trace element (ppm) abundances continued

Sample	OP-16*	OP-17	OP-18	OP-18*	OP-19	OP-21	OP-30	OP-32	OP-32*	OP-33	OP-33*	OP-34	OP-38
SiO_2	50.17	49.92	50.08		47.13	48.47	50.13	49.86		51.78		49.74	49.54
TiO_2	2.13	2.24	2.33		2.62	2.53	2.26	2.11		1.8		2.21	2.56
Al_2O_3	14.77	15.06	14.84		14.53	15.95	14.74	14.9		15.76		14.57	14.71
Fe_2O_{3t}	11.04	11.44	10.6		12.44	11.95	11.07	11.65		10.71		11.02	11.63
MnO	0.18	0.18	0.15		0.17	0.15	0.19	0.16		0.15		0.18	0.16
MgO	7.99	7.41	7.1		7.93	5.33	8.21	7.38		6.24		8.89	7.99
CaO	8.12	8.10	8.25		8.43	6.56	8.37	7.49		7.29		7.97	7.6
Na_2O	3.71	3.88	4		3.94	5.24	3.51	4.28		4.46		3.41	3.28
K_2O	1.67	1.36	2.03		1.78	3.09	1.69	1.62		1.37		1.79	1.75
P_2O_5	0.50	0.51	0.61		0.79	0.98	0.55	0.49		0.4		0.59	0.63
TOTAL	100.27	100.10	99.99		99.76	100.25	100.71	99.94		99.96		100.37	99.85
Mg#	63	60	61		60	51	63	60		58		65	62
Rb	21.6		23	21.9	32.9	38		19.8	16.2	13.8	14.6		16.9
Sr	593		760	641	893	1108		657	467	550	467		743
Ba	329		433	390	405	507		308	238	236	231		338
Sc	18.3			16.5					13.8		15.9		
V			157		165	113		126		112			151
Cr	209		190	147	166	84		154	134	141	107		164
Co	44.3			37.0					35.0		38.4		
Ni	111		140	60	81	63		81	93	82	79		107
Cu	32			29					23		29		
Zn	113		99	106	124	144		118	113	126	132		132
Ga	25		22	24	24	26		25	21	23	23		22
Y	22		21	22	23	20		21	20	19	20		23
Zr	212		205	206	292	376		199	169	173	170		226
Hf	4.36			4.54					3.83		3.97		
Nb	37.9		39.1	40.5	65.2	87.4		37.2	33.2	32.1	32.1		41.0
Ta	2.30			2.47					2.07		1.99		
Th	2.31			2.72					1.83		1.80		
U	0.72			0.77					0.65		0.26		
La	21.5		(25.0)	26.1	(33.3)	(43.6)		(21.0)	17.9	(16.3)	17.2		(22.7)
Ce	44.9		(54.3)	54.9	(69.1)	(80.9)		(43.0)	38.0	(36.5)	36.2		(49.1)
Pr	5.8			7.0					5.0		4.6		
Nd	24.2			28.7					20.5		19.1		
Sm	5.76			6.36					4.96		4.70		
Eu	1.91			2.04					1.67		1.61		
Gd	5.08			5.51					4.38		4.15		
Tb	0.79			0.83					0.72		0.69		
Dy	4.08			4.27					3.74		3.64		
Ho	0.74			0.78					0.69		0.67		
Er	1.87			1.93					1.70		1.70		
Tm	0.26			0.27					0.24		0.23		
Yb	1.45			1.52					1.34		1.34		
Lu	0.20			0.21					0.19		0.19		

Notes: Major and trace elements determined by XRF at the University of Massachusetts, Amherst, except samples marked by * where trace elements determined by ICP-MS at M.I.T. Abundances of Sc, some Cr (shown in parentheses), Co, Hf, Ta, Th and REE determined by neutron activation. La and Ce shown in parentheses were determined by XRF. Mg# = 100*atomic Mg/(Mg + Fe^{2+}), calculated with FeO = 0.15*Fe_2O_{3total}.

Table 2.2b. Oka Plateau major (wt%) and trace element (ppm) abundances continued

Sample	BK-201	BK-202	BK-203	BK-204	BK-205	BK-206	BK-207	BK-208	BK-209	BK-210	BK-211	BK-212	BK-213	BK-214	BK-215	BK-216	BK-217
SiO_2	46.88	48.27	47.16	48.35	48.24	47.88	47.62	50.02	48.78	49.91	48.70	49.55	49.44	46.97	46.37	47.84	48.67
TiO_2	2.39	2.40	2.43	2.23	2.26	2.61	2.53	2.15	2.08	2.32	2.19	2.19	2.17	2.35	2.49	2.40	2.44
Al_2O_3	14.53	14.86	14.53	15.11	15.13	14.81	14.76	15.71	15.06	16.05	15.52	15.53	15.57	14.29	14.47	14.83	15.03
Fe_2O_{3t}	11.50	12.01	11.62	11.48	11.58	11.48	11.71	11.75	9.94	10.43	10.12	10.45	10.22	11.23	10.89	11.15	11.33
MnO	0.14	0.16	0.16	0.16	0.16	0.15	0.16	0.16	0.14	0.14	0.14	0.14	0.14	0.14	0.12	0.14	0.14
MgO	8.44	9.07	9.30	8.99	8.23	8.41	8.80	7.39	8.32	6.07	6.83	6.93	7.20	9.11	7.79	7.85	8.06
CaO	9.15	8.66	8.97	8.84	9.06	8.28	8.63	8.13	7.86	8.67	8.16	8.43	8.27	8.11	8.10	7.71	7.80
Na_2O	2.39	3.49	2.80	3.26	3.16	3.09	2.84	3.57	2.86	3.90	3.02	3.21	3.10	2.91	2.40	2.94	3.11
K_2O	1.73	1.82	1.83	1.83	1.76	2.08	1.81	1.25	1.66	1.77	1.56	1.59	1.53	1.82	1.72	1.77	1.82
P_2O_5	0.65	0.52	0.66	0.52	0.53	0.65	0.62	0.40	0.62	0.69	0.62	0.60	0.60	0.69	0.70	0.69	0.70
LOI(%)	2.56	-0.47	1.29	-0.09	0.24	0.78	1.40	0.40	3.30	0.36	3.00	1.86	2.82	2.73	3.85	2.86	1.63
TOTAL	100.36	100.79	100.75	100.68	100.35	100.22	100.88	100.93	100.62	100.31	99.86	100.48	101.06	100.35	98.90	100.18	100.73
Mg#	63	64	65	65	62	63	64	59	66	58	61	61	62	65	63	62	62
Rb	20	19	22	20	19	18	18	14	14	17	13	14	15	20	18	17	17
Sr	1119	755	1062	979	778	894	862	565	654	733	671	709	993	867	1883	1280	828
Ba	341	378	425	353	373	352	356	249	270	286	273	293	321	310	589	334	303
Sc																	
V	177	168	185	182	181	186	207	167	142	160	170	155	158	155	171	156	175
Cr	199	207	242	254	234	212	222	177	216	172	178	198	203	202	187	188	204
Co	56	52	56	57	55	58	61	52	50	41	42	45	47	58	50	54	56
Ni	104	111	130	125	105	115	110	97	119	64	75	85	89	189	144	162	155
Zn	99	97	101	100	93	113	107	117	101	93	98	95	97	103	127	111	117
Ga																	
Y	22	21	22	23	21	22	22	21	20	21	21	20	21	19	20	20	20
Zr	227	204	238	213	202	248	243	178	183	197	186	195	200	212	252	238	218
Hf																	
Nb	37	38	48	37	42	49	36	30	29	37	34	37	35	39	43	40	44
Ta																	
Th																	
La																	
Ce																	
Nd																	
Sm																	
Eu																	
Tb																	
Yb																	
Lu																	

Notes: Major elements and trace elements determined by XRF at Washington University, St. Louis. Mg# = 100*atomic Mg/(Mg + Fe^{2+}), calculated with FeO = 0.15*Fe_2O_{3total}.

Table 2.2b. Oka Plateau major (wt%) and trace element (ppm) abundances continued

Sample	BK-218	BK-219	BK-220	BK-221	BK-222	BK-223	BK-224	BK-225	BK-226	BK-227	BK-228	BK-229	BK-230	BK-231	BK-232	BK-233	BK-234
SiO_2	48.66	48.80	48.64	49.36	49.40	46.55	48.83	49.26	49.51	49.95	50.60	52.09	46.63	47.62	47.05	49.62	46.14
TiO_2	2.45	2.23	2.21	2.13	2.19	2.69	2.35	2.47	2.18	2.35	2.35	2.12	2.53	2.51	2.73	2.28	2.68
Al_2O_3	14.93	15.65	15.57	15.34	15.78	14.74	14.86	15.60	15.08	15.05	15.27	15.66	14.76	15.03	14.75	15.79	14.60
Fe_2O_{3t}	11.45	11.10	11.03	11.29	11.05	12.58	12.31	12.59	12.35	12.06	12.15	11.66	12.38	12.88	13.48	11.54	13.23
MnO	0.14	0.15	0.15	0.15	0.15	0.16	0.16	0.17	0.16	0.16	0.16	0.15	0.16	0.16	0.17	0.15	0.17
MgO	7.85	7.43	7.52	7.76	6.97	7.71	8.09	7.84	7.97	7.94	8.20	7.29	8.54	8.08	8.03	7.50	8.03
CaO	7.95	8.58	8.57	8.19	8.44	8.05	8.21	8.00	8.23	7.94	8.08	7.61	8.35	8.22	8.30	8.50	8.29
Na_2O	3.32	3.04	3.11	3.98	4.06	4.31	3.65	3.39	3.57	3.55	3.11	3.60	3.83	4.09	4.09	4.19	3.49
K_2O	1.76	2.10	2.01	1.69	1.72	1.97	1.76	2.64	1.47	1.87	2.02	1.72	2.34	1.74	2.03	1.87	1.97
P_2O_5	0.71	0.59	0.56	0.48	0.47	0.63	0.55	0.62	0.40	0.48	0.49	0.49	0.57	0.58	0.66	0.50	0.65
LOI(%)	1.10	1.01	1.04	0.85	0.66	0.50	0.10	-1.60	0.32	-0.05	-1.60	-1.65	0.55	0.53	-0.65	-0.72	0.38
TOTAL	100.32	100.68	100.41	101.22	100.89	99.89	100.87	100.98	101.24	101.30	100.83	100.74	100.64	101.44	100.64	101.22	99.63
Mg#	62	61	61	62	60	59	60	59	60	61	61	59	62	59	58	60	59
Rb	17	22	25	19	19	27	22	31	20	21	28	22	30	23	22	19	20
Sr	909	1566	763	582	585	744	624	768	534	593	626	579	721	694	756	609	749
Ba	295	373	390	322	300	384	315	376	266	331	328	258	390	310	359	296	341
Sc																	
V	162	180	184	153	150	185	170	183	158	149	142	127	196	180	174	152	198
Cr	199	166	178	174	173	147	168	146	179	160	143	166	172	149	144	168	169
Co	52	52	51	49	47	56	53	55	55	52	50	49	56	56	57	4949	56
Ni	152	98	103	102	87	104	105	85	93	92	88	88	116	101	103	99	102
Zn	116	103	104	98	94	102	99	111	105	105	104	110	97	103	104	86	111
Ga																	
Y	20	22	22	22	21	22	21	22	24	21	21	22	22	22	22	22	21
Zr	219	243	215	190	182	234	183	248	175	196	190	197	246	200	229	193	219
Hf																	
Nb	40	42	39	30	40	57	34	55	22	41	43	42	58	44	46	40	46
Ta																	
Th																	
La																	
Ce																	
Nd																	
Sm																	
Eu																	
Tb																	
Yb																	
Lu																	

Notes: Major elements and trace elements determined by XRF at Washington University, St. Louis. Mg# = 100*atomic Mg/(Mg + Fe^{2+}), calculated with FeO = 0.15*Fe_2O_{3total}.

Table 2.2b. Oka Plateau major (wt%) and trace element (ppm) abundances continued

Sample	BK-235	BK-236	BK-237	BK-238	BK-239	BK-240	BK-241	BK-242	BK-243	BK-244	BK-245	BK-246	BK-247	BK-247a
SiO_2	47.17	48.83	48.61	47.51	50.50	48.66	51.57	49.37	48.38	49.33	50.29	48.93	47.97	48.46
TiO_2	2.71	2.36	2.45	2.37	2.04	2.29	2.03	2.80	2.62	2.47	2.20	3.15	2.61	3.16
Al_2O_3	14.85	15.24	15.11	15.14	15.31	14.42	15.48	15.12	14.84	14.88	15.56	16.12	14.89	15.10
Fe_2O_{3t}	13.48	12.01	12.43	12.67	11.40	11.90	10.46	12.14	11.99	11.67	9.93	12.63	11.85	11.12
MnO	0.17	0.15	0.16	0.16	0.15	0.15	0.12	0.15	0.16	0.15	0.14	0.16	0.15	0.13
MgO	8.48	7.04	7.48	8.31	7.40	8.05	6.29	8.25	8.21	8.04	6.88	6.30	7.27	4.32
CaO	8.49	7.95	8.07	8.32	7.81	8.05	8.17	8.59	8.59	8.01	8.24	7.74	8.47	8.71
Na_2O	4.15	3.94	4.05	3.92	3.80	3.01	3.91	3.24	3.36	3.81	3.44	3.43	3.18	3.31
K_2O	1.81	1.79	1.73	1.72	1.67	2.09	1.34	1.73	1.90	1.77	2.04	3.13	1.63	2.04
P_2O_5	0.62	0.47	0.53	0.52	0.41	0.47	0.42	0.76	0.59	0.66	0.61	1.08	0.68	0.76
LOI(%)	0.57	0.60	0.39	0.50	0.60	1.99	1.17	-1.33	0.51	0.14	1.49	-2.17	2.18	3.00
TOTAL	102.50	100.38	101.01	101.14	101.09	101.08	100.96	100.82	101.14	100.93	100.82	100.50	100.88	100.11
Mg#	59	58	58	60	60	61	58	61	61	62	62	54	59	48
Rb	20	21	21	22	24	26	14	16	22	18	19	32	15	17
Sr	743	627	620	648	537	640	518	898	909	868	849	1257	837	1085
Ba	326	305	305	320	294	303	257	324	386	315	369	510	288	397
Sc														
V	197	164	182	173	153	153	134	169	168	139	153	180	146	184
Cr	174	153	143	169	182	159	163	170	164	177	198	76	157	59
Co	59	50	54	58	49	56	51	53	55	52	46	52	52	42
Ni	102	88	93	112	90	102	95	104	112	124	63	78	105	27
Zn	104	99	106	98	92	110	107	110	103	103	105	138	108	116
Ga														
Y	23	23	22	22	23	21	21	22	22	21	20	21	22	25
Zr	217	191	197	191	180	195	182	242	223	221	208	344	217	273
Hf														
Nb	42	43	39	40	29	40	31	47	46	45	41	70	45	50
Ta														
Th														
La														
Ce														
Nd														
Sm														
Eu														
Tb														
Yb														
Lu														

Notes: Major elements and trace elements determined by XRF at Washington University, St. Louis. Mg# = 100*atomic Mg/(Mg + Fe^{2+}), calculated with FeO = 0.15*Fe_2O_{3total}.

Table 2.2b. Oka Plateau major (wt%) and trace element (ppm) abundances continued

Sample	BK-310	BK-311	BK-314	BK-316	BK-317	BK-319	BK-320	BK-321	BK-322	BK-323	BK-328
SiO_2	47.37	48.10	48.25	48.77	48.54	48.71	48.94	50.88	50.85	50.84	49.38
TiO_2	2.59	2.54	2.43	2.55	2.46	2.37	2.40	1.99	2.02	2.02	2.25
Al_2O_3	14.37	14.63	14.34	14.96	14.62	14.76	14.97	14.84	14.80	14.75	14.88
Fe_2O_{3t}	11.22	11.41	11.44	11.12	11.42	11.59	10.99	10.19	10.23	10.27	10.89
MnO	0.17	0.16	0.16	0.16	0.15	0.16	0.15	0.14	0.14	0.15	0.15
MgO	9.08	9.00	8.98	7.63	8.84	8.31	8.29	8.00	8.01	7.99	8.19
CaO	8.53	8.28	7.67	7.95	7.94	8.20	8.17	7.20	7.25	7.26	7.99
Na_2O	3.41	3.03	3.59	3.69	3.18	3.22	3.28	4.02	4.14	4.14	3.58
K_2O	2.09	2.00	2.07	2.18	1.99	1.88	1.90	1.98	1.91	1.93	1.88
P_2O_5	0.79	0.70	0.72	0.78	0.70	0.71	0.69	0.56	0.56	0.56	0.70
TOTAL	99.62	99.85	99.65	99.79	99.84	99.91	99.78	99.80	99.91	99.91	99.89
Mg#	65	65	65	62	64	63	64	65	65	64	64
Rb	21	22.5	20.2	20.5	18.3	17.7	18	21.3	19.5	21.7	18.8
Sr	942	864	869	892	863	994	1161	629	681	648	915
Ba	427	427	424	442	399	402	398	317	308	323	413
Sc											
V	171	157	144	148	152	146	141	117	123	132	153
Cr	256	199	236	205	232	238	199	217	222	260	227
Co											
Ni	165	139	157	118	135	141	109	109	117	93	104
Zn	124	126	122	123	119	127	117	111	115	105	107
Ga	20	20	22	22	21	21	21	21	20	21	21
Y	20	19	20	21	19	19	19	17	18	19	20
Zr	233	229	225	237	220	214	210	168	170	173	199
Hf											
Nb	49.8	46.2	46.5	49.5	45.3	43.3	39.9	34.9	36.2	32.3	40.0
Ta											
Th											
La	28.2	32.4	28.3	28.8	28.2	23.4	21.2	19.6	19.4	20.2	25.9
Ce	64.3	60.7	54.1	60.9	57.1	49.4	50.1	34.9	39.7	39.5	50.6
Nd											
Sm											
Eu											
Tb											
Yb											
Lu											

Notes: Major elements and trace elements determined by XRF at University of Massachusetts, Amherst. Mg# = 100*atomic Mg/(Mg + Fe^{2+}), calculated with FeO = 0.15*Fe_2O_{3total}.

Table 2.2c. Major (wt%) and trace element (ppm) abundances in Tuva lavas

Sample	p901/1	p901/1*	p901/2	p901/4	p901/4*	p904/1	p904/1*	p904/6	p904/11	p904/11*	p904/13	p905	p905*	p906/2	p908/4	p908/4*	p908/4-b*
SiO_2	49.99		52.28	49.33		49.07		49.30	49.48		49.48	49.02		47.56	48.30		
TiO_2	2.26		2.27	2.09		2.20		2.23	2.15		2.11	2.20		2.48	2.37		
Al_2O_3	15.34		15.79	14.74		15.10		15.13	14.99		14.90	15.18		15.07	15.70		
Fe_2O_{3t}	10.45		9.97	10.78		11.03		10.64	10.89		10.58	10.95		12.45	10.67		
MnO	0.15		0.11	0.15		0.16		0.16	0.15		0.15	0.15		0.17	0.15		
MgO	6.57		5.84	8.50		7.65		7.13	7.76		7.75	7.66		8.03	6.60		
CaO	7.65		6.75	8.05		8.13		8.57	8.41		8.04	8.67		8.40	8.53		
Na_2O	4.29		4.28	3.33		3.52		3.56	3.52		3.73	3.30		3.88	4.42		
K_2O	2.25		1.75	2.11		2.10		2.40	2.04		2.08	2.39		1.58	2.29		
P_2O_5	0.70		0.57	0.64		0.71		0.85	0.66		0.66	0.65		0.56	0.69		
TOTAL	99.65		99.61	99.72		99.67		99.97	100.05		99.48	100.17		100.18	99.72		
Mg#	59		58	65		62		62	63		61	62		60	59		
Rb	19.1	18.7	14.7	23.3	16.7	26.1	32.0	31.2	21.4	22.5	24.5	23.3	25.1	15.4	26.8	12.2	13.3
Sr	881	722	690	735	467	1227	1160	1181	828	830	1362	723	740	715	819	300	311
Ba	354	340	238	409	261	489	397	422	439	409	430	398	386	357	579	210	222
Sc		13.8			10.2		15.2			15.4			16.0			7.2	7.8
V	133	152	118	123		126		131	130		134	131		143	134		
Cr	265	81	202	193	144	119	182	157	175	191	220	174	197	147	138	65	68
Co		35.8			27.2		40.3			39.9			41.8			15.1	15.9
Ni	42	27	39	86	77	99	126	89	70	102			133			39	42
Cu		24			17		30			30	90	104	32	109	54	15	15
Zn	113	120	126	110	76	112	124	113	108	121	117	108	123	113	92	45	48
Ga	22	25	22	21	19	22	31	21	22	29	22	18	28	22	24	13	14
Y	19	21	18	18	14	22	22	19	19	22	19	18	22	21	21	8	8
Zr	202	204	186	192	135	250	204	207	198	202	203	188	192	195	222	106	113
Hf		4.43			2.89		4.25			4.22			4.04			2.25	2.40
Nb	45.8	47.1	36.2	41.0	31.8	66.7	44.7	43.3	41.1	43.5	43.5	43.0	45.9	38.3	47.8	27.7	29.4
Ta		2.73			1.78		2.55			2.53			2.65			1.54	1.64
Th		2.63			1.82		2.70			2.81			2.63			1.07	1.13
U		1.00			0.65		0.93			0.96			0.89			0.33	0.34
La	26.6	25.9	16.8	23.6	17.2	24.6	27.7	41.9	25.8	27.6	26.7	25.2	26.2	21.2	25.0	9.8	10.4
Ce	50.1	53.2	33.1	42.9	34.6	53.9	56.6	73.9	49.4	55.6	52.7	47.5	52.9	40.3	48.5	20.8	22.1
Pr		6.8			4.3		7.3			7.1			6.8			2.4	2.6
Nd		28.2			18.1		30.9			29.8			28.7			10.0	10.6
Sm		6.41			4.08		6.89			6.67			6.51			2.20	2.34
Eu		2.10			1.34		2.25			2.18			2.14			0.72	0.78
Gd		5.56			3.80		6.26			6.15			6.04			2.05	2.20
Tb		0.82			0.52		0.85			0.85			0.82			0.29	0.31
Dy		4.10			2.62		4.29			4.23			4.19			1.47	1.60
Ho		0.72			0.47		0.76			0.76			0.74			0.27	0.29
Er		1.73			1.14		1.83			1.85			1.78			0.67	0.72
Tm		0.23			0.15		0.25			0.25			0.24			0.09	0.10
Yb		1.28			0.87		1.41			1.41			1.35			0.54	0.57
Lu		0.18			0.12		0.20			0.20			0.19			0.08	0.08

Notes: Major elements determined by XRF at University of Massachusetts, Amherst. Trace elements determined by XRF except samples marked by * which were determined by ICP-MS at M.I.T. Mg# = 100*atomic Mg/Mg + Fe^{2+}, calculated with FeO = .15* $Fe_2O_{3t\ otal}$.

Table 2.2c. Major (wt%) and trace element (ppm) abundances in Tuva lavas continued

Sample	p909/2	p909/3	p909/3*	p915	p915*	p919	p919*	p919-b*	TV-94-12	TV-94-35	TV-94-36	TV-94-41
SiO_2	49.69	49.01		48.97		48.55			46.82	48.81	49.10	48.37
TiO_2	2.12	2.36		2.19		2.32			2.76	2.21	2.44	2.33
Al_2O_3	15.27	15.43		15.29		15.09			15.41	15.51	17.18	15.87
Fe_2O_{3t}	11.01	11.75		11.58		12.06			12.22	11.16	10.60	11.04
MnO	0.15	0.16		0.16		0.17			0.19	0.19	0.19	0.19
MgO	7.38	6.64		7.22		7.60			7.66	7.18	5.12	6.92
CaO	7.97	8.14		8.21		8.35			8.25	8.54	7.89	8.11
Na_2O	4.12	4.27		4.37		3.84			3.97	3.96	4.41	3.89
K_2O	1.69	1.60		1.59		1.56			2.05	1.72	2.34	2.25
P_2O_5	0.54	0.54		0.49		0.53			0.69	0.56	0.76	0.67
TOTAL	99.94	99.90		100.07		100.07			100.02	99.84	100.03	99.63
Mg#	61	57		59		59			59	60	53	59
Rb	18.2	17.2	17.3	17.2	18.5	17.6	17.7	17.9				
Sr	647	626	532	615	614	625	636	639				
Ba	391	318	290	328	323	345	317	316				
Sc			18.1		19.5		19.6	19.8				
V	125	126	163	145		139						
Cr	150	122	84	156	157	142	162	167				
Co			39.3		44.0		46.5	45.3				
Ni	97	76	74	100	126	93	128	133				
Cu			42		41		40	40				
Zn	107	102	123	113	123	113	121	122				
Ga	21	24	23	21	28	23	28	28				
Y	21	22	20	22	23	23	26	26				
Zr	197	191	201	193	197	201	208	209				
Hf			4.43		4.26		4.48	4.57				
Nb	36.2	34.9	38.0	36.6	38.7	36.4	38.2	38.6				
Ta			2.27		2.31		2.27	2.28				
Th			1.96		2.13		2.21	2.17				
U			0.70		0.69		0.73	0.70				
La	21.7	20.7	18.8	19.5	20.9	19.2	22.8	22.8				
Ce	42.2	41.5	40.8	42.4	44.2	45.0	47.3	46.9				
Pr			4.8		5.2		6.0	6.0				
Nd			20.1		21.4		25.5	25.9				
Sm			4.72		4.91		5.92	5.87				
Eu			1.62		1.64		2.00	2.01				
Gd			4.35		4.95		5.90	5.88				
Tb			0.69		0.74		0.87	0.88				
Dy			3.67		3.99		4.69	4.73				
Ho			0.67		0.76		0.88	0.88				
Er			1.69		1.98		2.22	2.24				
Tm			0.23		0.29		0.31	0.31				
Yb			1.35		1.63		1.76	1.76				
Lu			0.19		0.24		0.25	0.25				

Notes: Major elements determined by XRF at University of Massachusetts, Amherst. Trace elements determined by XRF except samples marked by * which were determined by ICP-MS at M.I.T. Mg# = 100*atomic Mg/Mg + Fe^{2+}, calculated with FeO = .15* $Fe_2O_{3t\ otal}$.

Table 2.3a. Tunka isotope data

SAMPLE	$^{87}Sr/^{86}Sr$	±2σ	$^{143}Nd/^{144}Nd$	±2σ	ε_{Nd}	±2σ	$^{206}Pb/^{204}Pb$	$^{207}Pb/^{204}Pb$	$^{208}Pb/^{204}Pb$
BK-1							17.713	15.471	37.914
BK-2	0.70429	±0.00001	0.512732	±0.000006	1.83	±0.12	17.405	15.405	37.528
BK-3	0.70442	±0.00001	0.512735	±0.000007	1.90	±0.14	17.743	15.468	37.804
BK-4A	0.70428	±0.00001	0.512760	±0.000006	2.38	±0.12	17.805	15.488	37.775
BK-4C	0.70429	±0.00001	0.512768	±0.000006	2.54	±0.12	17.792	15.472	37.721
BK-5	0.70540	±0.00001	0.512832	±0.000011	3.79	±0.22	17.917	15.472	37.849
BK-7X2	0.70402	±0.00002	0.512806	±0.000006	3.28	±0.12	18.256	15.512	38.282
BK-8	0.70483	±0.00001	0.512749	±0.000006	2.17	±0.12	17.494	15.494	38.071
BK-9	0.70428	±0.00001	0.512746	±0.000006	2.10	±0.12	17.834	15.478	37.913
BK-10	0.70465	±0.00001	0.512685	±0.000016	0.91	±0.32	17.661	15.454	37.785
BK-12	0.70440	±0.00003	0.512741	±0.000006	2.02	±0.12	17.810	15.496	37.907
BK-13	0.70441	±0.00002	0.512742	±0.000005	2.04	±0.10	17.850	15.466	37.954
BK-161*	0.70495	±0.00001	0.512745	±0.000010	2.09	±0.20	17.741	15.481	38.011
BK-162*	0.70451	±0.00001	0.512725	±0.000005	1.69	±0.10	17.705	15.447	37.904

Notes: Sr and Nd analyses were performed at M.I.T. Sr data are normalized to $^{86}Sr/^{88}Sr = 0.1194$ and corrected for mass fractionation using an exponential law. Replicate analyses of NBS-987 Sr yield $^{87}Sr/^{86}Sr = 0.710227 \pm 0.000017$ (2σ). Nd data are normalized to $^{146}Nd/^{144}Nd = 0.7219$ and corrected for mass fractionation using an exponential law. Replicate analyses of La Jolla Nd yield $^{143}Nd/^{144}Nd = 0.511845 \pm .000008$ (2σ). $\varepsilon_{Nd}(0)$ is calculated with $^{143}Nd/^{144}Nd_{CHUR} = 0.512638$. Pb analyses were performed on a VG354 mass spectrometer at Washington University, St. Louis in single collector mode. Based on replicate analyses of NBS-981, Pb is corrected by 0.06%/mass unit to account for fractionation. Samples marked by * were analyzed for Pb at M.I.T. and corrected by 0.12%/mass unit.

Table 2.3b. Oka Plateau isotope data

SAMPLE	$^{87}Sr/^{86}Sr$	±2σ	$^{143}Nd/^{144}Nd$	±2σ	ε_{Nd}	±2σ	$^{206}Pb/^{204}Pb$	$^{207}Pb/^{204}Pb$	$^{208}Pb/^{204}Pb$
OP-1	0.70451	±0.00001	0.512741	±0.000009	2.00	±0.18			
OP-2	0.70453	±0.00001					17.901	15.490	38.007
OP-3A	0.70534	±0.00001					17.858	15.508	38.026
OP-3	0.70460	±0.00001	0.512700	±0.000017	1.22	±0.34	17.931	15.462	37.893
OP-5	0.70492	±0.00001	0.512778	±0.000007	2.73	±0.14	17.845	15.456	37.790
OP-6	0.70474	±0.00001	0.512633	±0.000007	-0.11	±0.14			
OP-7	0.70480	±0.00001	0.512615	±0.000008	-0.44	±0.16	17.679	15.436	37.967
OP-8	0.70467	±0.00001	0.512634	±0.000005	-0.08	±0.10	17.729	15.421	37.836
OP-9	0.70427	±0.00001	0.512810	±0.000008	3.36	±0.16	17.667	15.480	37.805
OP-10	0.70475	±0.00001	0.512629	±0.000009	-0.18	±0.18	18.080	15.489	37.934
OP-14	0.70446	±0.00001	0.512775	±0.000008	2.66	±0.16			
OP-18	0.70438	±0.00001	0.512704	±0.000006	1.28	±0.12	17.590	15.432	37.758
OP-19	0.70410	±0.00001	0.512753	±0.000007	2.25	±0.14	18.052	15.457	37.928
OP-21	0.70380	±0.00001	0.512770	±0.000006	2.58	±0.12	18.042	15.465	37.871
OP-32	0.70424	±0.00001	0.512716	±0.000006	1.52	±0.12	17.798	15.442	37.741
OP-33	0.70431	±0.00001	0.512714	±0.000010	1.49	±0.20			
OP-38	0.70454	±0.00001	0.512725	±0.000006	1.70	±0.12	17.778	15.442	37.837
BK-201	0.70518	±0.00001					18.004	15.477	37.946
BK-202*	0.70450	±0.00001	0.512745	±0.000009	2.08	±0.17	18.024	15.511	38.074
BK-203	0.70479	±0.00001	0.512787	±0.000005	2.90	±0.10	18.007	15.476	37.939
BK-205	0.70442		0.512762	±0.000009	2.42	±0.18			
BK-207*	0.70430	±0.00001	0.512746	±0.000005	2.10	±0.10	17.909	15.461	37.886
BK-208	0.70454	±0.00001	0.512646	±0.000005	0.16	±0.10	17.416	15.387	37.872
BK-209	0.70414	±0.00001	0.512768	±0.000005	2.54	±0.10	17.670	15.430	37.669
BK-210*	0.70417	±0.00001	0.512760	±0.000015	2.37	±0.30	17.687	15.462	37.807
BK-212	0.70430	±0.00001	0.512751	±0.000005	2.20	±0.10	17.630	15.417	37.668
BK-215	0.70570	±0.00001	0.512780	±0.000005	2.77	±0.10	17.876	15.457	37.811
BK-216	0.70544	±0.00001	0.512764	±0.000005	2.45	±0.10	17.812	15.469	37.809
BK-217	0.70445	±0.00001	0.512769	±0.000006	2.55	±0.12	17.787	15.445	37.741
BK-218*	0.70462	±0.00001	0.512736	±0.000006	1.91	±0.12	17.806	15.470	37.834
BK-219*	0.70667	±0.00001	0.512681	±0.000005	0.83	±0.10	17.775	15.457	37.883
BK-221*	0.70410	±0.00001	0.512725	±0.000005	1.69	±0.10	18.070	15.489	37.962
BK-224	0.70434	±0.00001					17.724	15.426	37.835
BK-225*	0.70416	±0.00001					18.040	15.484	37.960
BK-226	0.70465	±0.00001	0.512651	±0.000006	0.25	±0.12	17.771	15.435	37.927
BK-228*	0.70423	±0.00001	0.512677	±0.000029	0.77	±0.56	17.907	15.496	37.929
BK-229	0.70449	±0.00001	0.512773	±0.000008	2.64	±0.16	17.851	15.467	37.859
BK-230*	0.70402	±0.00001	0.512735	±0.000006	1.89	±0.12	17.980	15.509	38.071
BK-231	0.70405	±0.00001					17.771	15.447	37.846
BK-233	0.70409	±0.00001							
BK-235	0.70412	±0.00001					17.884	15.454	37.800

Notes: All analyses performed at M.I.T., except samples marked by * which were analyzed at Washington University, St. Louis. Sr data are normalized to $^{86}Sr/^{88}Sr = 0.1194$ and corrected for mass fractionation using an exponential law. For M.I.T. data, replicate analyses of NBS-987 Sr yield $^{87}Sr/^{86}Sr = 0.710227 \pm 0.000017$ (2σ). Nd data are normalized to $^{146}Nd/^{144}Nd = 0.7219$ and corrected for mass fractionation using an exponential law. Replicate analyses of La Jolla Nd yield $^{143}Nd/^{144}Nd = 0.511845 \pm .000008$ (2σ). $\varepsilon_{Nd}(0)$ is calculated with $^{143}Nd/^{144}Nd_{CHUR} = 0.512638$. Based on replicate analyses of NBS-981, M.I.T. Pb data is corrected by 0.12%/mass unit to account for fractionation, while Washington University, St. Louis samples are corrected by 0.06%/mass unit.

Table 2.3b. Oka Plateau isotope data continued

SAMPLE	$^{87}Sr/^{86}Sr$	±2σ	$^{143}Nd/^{144}Nd$	±2σ	ε_{Nd}	±2σ	$^{206}Pb/^{204}Pb$	$^{207}Pb/^{204}Pb$	$^{208}Pb/^{204}Pb$
BK-237	0.70419	±0.00001	0.512726	±0.000010	1.72	±0.20	17.743	15.440	37.936
BK-238	0.70415	±0.00001					17.704	15.429	37.843
BK-241			0.512714	±0.000010	1.49	±0.20	17.853	15.455	37.826
BK-242	0.70429	±0.00001					18.124	15.482	37.981
BK-243	0.70439	±0.00001					17.906	15.473	37.950
BK-246			0.512833	±0.000006	3.80	±0.12	18.312	15.491	38.118
BK-309	0.70436	±0.00001	0.512761	±0.000009	2.41	±0.18	17.848	15.459	37.898
BK-310	0.70448	±0.00001	0.512760	±0.000006	2.38	±0.12	17.898	15.491	38.012
BK-311	0.70469	±0.00001	0.512763	±0.000006	2.44	±0.12	17.977	15.495	38.040
BK-314	0.70430	±0.00001	0.512771	±0.000006	2.60	±0.12	17.824	15.485	37.864
BK-316	0.70428	±0.00001	0.512769	±0.000005	2.57	±0.10	17.797	15.443	37.735
BK-317	0.70430	±0.00001	0.512770	±0.000011	2.58	±0.22	17.813	15.455	37.768
BK-318	0.70430	±0.00001	0.512771	±0.000007	2.60	±0.14	17.789	15.450	37.744
BK-319	0.70449	±0.00001	0.512766	±0.000006	2.49	±0.12	17.787	15.437	37.704
BK-320			0.512783	±0.000007	2.84	±0.14	17.822	15.501	37.908
BK-321	0.70425	±0.00001	0.512797	±0.000011	3.11	±0.22	17.694	15.456	37.691
BK-322	0.70425	±0.00001	0.512782	±0.000005	2.80	±0.10	17.849	15.468	37.768
BK-323	0.70428	±0.00001	0.512773	±0.000006	2.64	±0.12	17.739	15.508	37.865
BK-328	0.70446	±0.00001	0.512763	±0.000006	2.45	±0.12	17.738	15.444	37.717

Notes: All data obtained at M.I.T. Sr data are normalized to $^{86}Sr/^{88}Sr = 0.1194$ and corrected for mass fractionation using an exponential law. Replicate analyses of NBS-987 Sr yield $^{87}Sr/^{86}Sr = 0.710240 \pm 0.000016$ (2σ). Nd data are normalized to $^{146}Nd/^{144}Nd = 0.7219$ and corrected for mass fractionation using an exponential law. Replicate analyses of La Jolla Nd yield $^{143}Nd/^{144}Nd = 0.511845 \pm .000011$ (2σ). $\varepsilon_{Nd}(0)$ is calculated with $^{143}Nd/^{144}Nd_{CHUR} = 0.512638$. Based on replicate analyses of NBS-981, Pb is corrected by 0.12%/mass unit to account for fractionation.

Table 2.3c. Tuva isotope data

SAMPLE	$^{87}Sr/^{86}Sr$	±2σ	$^{143}Nd/^{144}Nd$	±2σ	ε_{Nd}	±2σ	$^{206}Pb/^{204}Pb$	$^{207}Pb/^{204}Pb$	$^{208}Pb/^{204}Pb$
p901/1	0.704163	±0.00001	0.512804	±0.000007	3.25	±0.14	17.769	15.396	37.309
p901/2	0.704402	±0.00001	0.512731	±0.000006	1.82	±0.12	17.975	15.496	37.829
p901/3	0.704406	±0.00001	0.512745	±0.000008	2.09	±0.16	17.974	15.485	37.846
p901/4	0.704375	±0.00001	0.512729	±0.000006	1.77	±0.12	18.066	15.488	37.891
p904/1	0.704741	±0.00001	0.512704	±0.000006	1.29	±0.12	18.026	15.481	37.845
p904/6	0.704264	±0.00001	0.512776	±0.000007	2.69	±0.14	18.038	15.484	37.853
p904/11	0.704432	±0.00001	0.512734	±0.000007	1.87	±0.14	18.078	15.485	37.885
p904/13	0.704573	±0.00001	0.512737	±0.000005	1.94	±0.10	18.058	15.484	37.883
p905	0.704301	±0.00001	0.512745	±0.000005	2.09	±0.10	17.926	15.436	37.704
p906/2	0.704143	±0.00001	0.512722	±0.000006	1.64	±0.12	17.973	15.446	37.768
p908/4	0.704143	±0.00001	0.512763	±0.000006	2.44	±0.12	17.951	15.469	37.782
p908/5	0.704072	±0.00001	0.512761	±0.000006	2.40	±0.12	17.982	15.485	37.857
p909/2	0.704160	±0.00001	0.512735	±0.000006	1.90	±0.12	17.941	15.462	37.759
p909/3	0.704041	±0.00001	0.512716	±0.000006	1.53	±0.12	17.877	15.447	37.775
p915	0.704188	±0.00001	0.512700	±0.000006	1.20	±0.12	17.958	15.454	37.773
p919	0.704192	±0.00001	0.512719	±0.000005	1.59	±0.10	17.966	15.453	37.826
TV-94-3	0.703966	±0.00001	0.512718	±0.000009	1.56	±0.18	18.080	15.499	38.053
TV-94-4	0.704063	±0.00001	0.512724	±0.000006	1.68	±0.12	17.884	15.427	37.809
TV-94-6	0.703899	±0.00001	0.512804	±0.000006	3.23	±0.12	17.921	15.471	37.815
TV-94-10	0.703897	±0.00001	0.512763	±0.000010	2.44	±0.20	18.060	15.472	37.877
TV-94-12	0.703932	±0.00001	0.512734	±0.000006	1.87	±0.12	18.026	15.476	37.882
TV-94-13	0.704133	±0.00001	0.512754	±0.000005	2.26	±0.10	17.927	15.458	37.771
TV-94-14	0.703872	±0.00001	0.512716	±0.000006	1.52	±0.12	18.010	15.471	37.861
TV-94-15	0.703842	±0.00001	0.512744	±0.000007	2.06	±0.14	18.060	15.472	37.896
TV-94-20	0.704143	±0.00001	0.512684	±0.000006	0.89	±0.12	17.970	15.474	37.845
TV-94-24	0.704148	±0.00001	0.512764	±0.000007	2.46	±0.14	17.982	15.457	37.749
TV-94-25	0.704129	±0.00001	0.512682	±0.000005	0.86	±0.10	17.955	15.455	37.798
TV-94-27	0.704113	±0.00001	0.512748	±0.000006	2.15	±0.12	18.028	15.491	37.884
TV-94-31	0.704022	±0.00001	0.512749	±0.000011	2.16	±0.22	18.066	15.479	37.875
TV-94-35	0.704087	±0.00001	0.512773	±0.000009	2.64	±0.18	18.037	15.482	37.817
TV-94-36	0.704031	±0.00001	0.512738	±0.000006	1.94	±0.12	17.831	15.472	37.814
TV-94-41	0.704015	±0.00001	0.512739	±0.000005	1.97	±0.10	17.831	15.454	37.761

Notes: Sr data are normalized to $^{86}Sr/^{88}Sr = 0.1194$ and corrected for mass fractionation using an exponential law. Replicate analyses of NBS-987 Sr yield $^{87}Sr/^{86}Sr = 0.710240 \pm 0.000016$ (2σ). Nd data are normalized to $^{146}Nd/^{144}Nd = 0.7219$ and corrected for mass fractionation using an exponential law. Replicate analyses of La Jolla Nd yield $^{143}Nd/^{144}Nd = 0.511845 \pm .000011$ (2σ). $\varepsilon_{Nd}(0)$ is calculated with $^{143}Nd/^{144}Nd_{CHUR} = 0.512638$. Based on replicate analyses of NBS-981, Pb is corrected by 0.12%/mass unit to account for fractionation.

Table 2.4. Ages for BRZ volcanic rocks taken from literature

Sample	location		Age (Ma)	Source
BK-7	Tunka	E. side of Zun-Murin R., SE margin of Tunka Basin	10.1±0.5	Rasskazov, 1989
BK-9	Tunka	same section as BK-7, higher	8.3±0.3	Rasskazov, 1989
p901/1	Tuva	Ulug-Arga Ridge.	16.4±1.8	Rasskazov et al., 1989
p901/2	Tuva	Ulug-Arga Ridge.	27.5±1.7	Rasskazov et al., 1989
p901/4	Tuva	Ulug-Arga Ridge.	26.3±0.7	Rasskazov et al., 1989
p904/1	Tuva	Ulug-Arga Ridge.	16.1	Rasskazov, 1989
p905	Tuva	Ulug-Arga Ridge.	16.1±1.7	Rasskazov et al., 1989
p908/4	Tuva	Ulug-Arga Ridge.	1.3±0.15	Rasskazov, 1989

Table B.1 $^{40}Ar/^{39}Ar$ Furnace Analytical Data for cl72/93-OP-12/WR

T (K)	$^{36}Ar/^{40}Ar$ ±2σ	$^{39}Ar/^{40}Ar$ ±2σ	^{39}Ar(%)	$^{40}Ar^{*}$(%)	Age (Ma)	±2σ
923	0.00192 ± 0.00004	0.0172 ± 0.00005	37.44	43.31	11.79	± 0.31
1073	0.00227 ± 0.00003	0.0127 ± 0.00004	71.16	32.84	12.14	± 0.33
1173	0.00189 ± 0.00013	0.0163 ± 0.00003	82.99	44.05	12.69	± 1.14
1323	0.00239 ± 0.00017	0.0216 ± 0.00035	87.40	29.26	6.36	± 1.07
1473	0.00117 ± 0.00024	0.0249 ± 0.00029	97.12	65.41	12.32	± 1.32
1673	0.00040 ± 0.00053	0.0260 ± 0.00067	100.00	88.14	15.87	± 2.81

J value: 2.61E-4 ± 7.41E-7. All steps of 10 minute duration. $^{40}Ar^{*}$(%) is percentage of measured ^{40}Ar derived from natural decay of ^{40}K.

Table B.2 $^{40}Ar/^{39}Ar$ Furnace Analytical Data for cl72/BK-218/WR

T (K)	$^{36}Ar/^{40}Ar$ ±2σ	$^{39}Ar/^{40}Ar$ ±2σ	^{39}Ar(%)	$^{40}Ar^{*}$(%)	Age (Ma)	±2σ
923	0.00031 ± 0.00005	0.0312 ± 0.00023	16.26	90.88	13.81	± 0.24
1023	0.00132 ± 0.00010	0.0135 ± 0.00006	33.83	60.93	21.40	± 1.06
1123	0.00017 ± 0.00005	0.0233 ± 0.00007	53.20	95.06	19.29	± 0.30
1223	0.00028 ± 0.00007	0.0240 ± 0.00022	64.52	91.82	18.07	± 0.43
1323	0.00039 ± 0.00006	0.0248 ± 0.00052	72.38	88.51	16.92	± 0.49
1473	0.00027 ± 0.00004	0.0252 ± 0.00016	89.64	91.97	17.28	± 0.24
1623	0.00022 ± 0.00019	0.0268 ± 0.00026	100.00	93.43	16.52	± 1.03

J value: 2.64E-4 ± 7.28E-7. All steps of 10 minute duration. $^{40}Ar^{*}$(%) is percentage of measured ^{40}Ar derived from natural decay of ^{40}K.

Table B.3 $^{40}Ar/^{39}Ar$ Furnace Analytical Data for cl72/BK-219/WR

T (K)	$^{36}Ar/^{40}Ar$ ±2σ	$^{39}Ar/^{40}Ar$ ±2σ	^{39}Ar(%)	$^{40}Ar^{*}$(%)	Age (Ma)	±2σ
923	0.00140 ± 0.00012	0.1180 ± 0.00326	12.97	58.71	2.37	± 0.16
1073	0.00207 ± 0.00004	0.0421 ± 0.00032	37.49	38.91	4.39	± 0.15
1173	0.00076 ± 0.00013	0.0746 ± 0.00057	50.75	77.55	4.94	± 0.25
1323	0.00049 ± 0.00008	0.0759 ± 0.00015	68.89	85.54	5.35	± 0.15
1473	0.00069 ± 0.00011	0.0749 ± 0.00037	90.34	79.44	5.04	± 0.20
1673	0.00048 ± 0.00052	0.0860 ± 0.00083	100.00	85.88	4.74	± 0.84

J value: 2.64E-4 ± 7.28E-7. All steps of 10 minute duration. $^{40}Ar^{*}$(%) is percentage of measured ^{40}Ar derived from natural decay of ^{40}K.

Table B.4 $^{40}Ar/^{39}Ar$ Furnace Analytical Data for cl72/BK-314/WR

T (K)	$^{36}Ar/^{40}Ar$ ±2σ	$^{39}Ar/^{40}Ar$ ±2σ	^{39}Ar(%)	$^{40}Ar^{*}$(%)	Age (Ma)	±2σ
923	0.00024 ± 0.00009	0.0274 ± 0.00022	11.67	92.81	15.48	± 0.46
1023	0.00112 ± 0.00005	0.0194 ± 0.00009	36.64	66.80	15.70	± 0.34
1173	0.00019 ± 0.00004	0.0260 ± 0.00011	53.95	94.48	16.57	± 0.21
1323	0.00029 ± 0.00006	0.0253 ± 0.00017	67.40	91.38	16.49	± 0.34
1473	0.00016 ± 0.00003	0.0261 ± 0.00009	88.62	95.34	16.68	± 0.17
1673	0.00000 ± 0.00004	0.0281 ± 0.00018	100.00	100.00	16.24	± 0.21

J value: 2.54E-4 ± 7.81E-7. All steps of 10 minute duration. $^{40}Ar^{*}$(%) is percentage of measured ^{40}Ar derived from natural decay of ^{40}K.

Table B.5 $^{40}Ar/^{39}Ar$ Furnace Analytical Data for cl72/BK-316/WR

T (K)	$^{36}Ar/^{40}Ar$ ±2σ	$^{39}Ar/^{40}Ar$ ±2σ	^{39}Ar(%)	$^{40}Ar^*$(%)	Age (Ma)	±2σ
923	0.00017 ± 0.00005	0.0301 ± 0.00046	12.55	94.96	14.65	± 0.32
1073	0.00093 ± 0.00004	0.0217 ± 0.00011	39.04	72.47	15.50	± 0.25
1173	0.00034 ± 0.00010	0.0285 ± 0.00033	48.44	90.07	14.65	± 0.51
1323	0.00017 ± 0.00005	0.0283 ± 0.00024	63.97	94.96	15.58	± 0.26
1473	0.00016 ± 0.00001	0.0270 ± 0.00015	89.35	95.30	16.36	± 0.12
1673	0.00000 ± 0.00014	0.0282 ± 0.00032	100.00	100.00	16.47	± 0.70

J value: 2.58E-4 ± 7.54E-7. All steps of 10 minute duration. $^{40}Ar^*$(%) is percentage of measured ^{40}Ar derived from natural decay of ^{40}K.

Table B.6 $^{40}Ar/^{39}Ar$ Furnace Analytical Data for cl72/BK-317/WR

T (K)	$^{36}Ar/^{40}Ar$ ±2σ	$^{39}Ar/^{40}Ar$ ±2σ	^{39}Ar(%)	$^{40}Ar^*$(%)	Age (Ma)	±2σ
923	0.00019 ± 0.00006	0.0331 ± 0.00070	10.19	94.27	13.22	± 0.37
1023	0.00097 ± 0.00005	0.0181 ± 0.00006	32.36	71.48	18.30	± 0.35
1173	0.00021 ± 0.00005	0.0261 ± 0.00017	47.82	93.92	16.67	± 0.27
1323	0.00024 ± 0.00007	0.0269 ± 0.00012	65.39	92.90	16.02	± 0.38
1473	0.00018 ± 0.00003	0.0256 ± 0.00005	95.37	94.54	17.10	± 0.15
1673	0.00000 ± 0.00022	0.0254 ± 0.00039	100.00	100.00	18.22	± 1.21

J value: 2.58E-4 ± 7.54E-7. All steps of 10 minute duration. $^{40}Ar^*$(%) is percentage of measured ^{40}Ar derived from natural decay of ^{40}K.

Table B.7 $^{40}Ar/^{39}Ar$ Furnace Analytical Data for cl72/BK-318/WR

T (K)	$^{36}Ar/^{40}Ar$ ±2σ	$^{39}Ar/^{40}Ar$ ±2σ	^{39}Ar(%)	$^{40}Ar^*$(%)	Age (Ma)	±2σ
923	0.00042 ± 0.00020	0.0252 ± 0.00044	6.08	87.62	15.97	± 1.10
1073	0.00108 ± 0.00004	0.0194 ± 0.00008	32.49	68.24	16.20	± 0.28
1173	0.00011 ± 0.00005	0.0257 ± 0.00012	46.00	96.69	17.30	± 0.30
1323	0.00022 ± 0.00004	0.0257 ± 0.00018	65.99	93.45	16.72	± 0.23
1473	0.00018 ± 0.00003	0.0256 ± 0.00009	93.56	94.79	17.00	± 0.18
1673	0.00000 ± 0.00006	0.0297 ± 0.00042	100.00	100.00	15.49	± 0.35

J value: 2.56E-4 ± 7.68E-7. All steps of 10 minute duration. $^{40}Ar^*$(%) is percentage of measured ^{40}Ar derived from natural decay of ^{40}K.

Table B.8 $^{40}Ar/^{39}Ar$ Furnace Analytical Data for cl72/TV-94-36/WR

T (K)	$^{36}Ar/^{40}Ar$ ±2σ	$^{39}Ar/^{40}Ar$ ±2σ	^{39}Ar(%)	$^{40}Ar^*$(%)	Age (Ma)	±2σ
923	0.00260 ± 0.00050	0.2252 ± 0.00185	9.85	23.11	0.46	± 0.29
1073	0.00344 ± 0.00021	0.0296 ± 0.00014	23.87	-1.69	-0.26	± 0.96
1173	0.00230 ± 0.00039	0.1654 ± 0.00174	33.37	31.98	0.87	± 0.31
1323	0.00263 ± 0.00038	0.0837 ± 0.00047	52.74	22.43	1.21	± 0.61
1473	0.00332 ± 0.00018	0.1230 ± 0.00046	94.72	1.95	0.07	± 0.19
1673	0.00395 ± 0.00065	0.1089 ± 0.00110	100.00	-16.71	-0.69	± 0.80

J value: 2.50E-4 ± 1.45E-6. All steps of 10 minute duration. $^{40}Ar^*$(%) is percentage of measured ^{40}Ar derived from natural decay of ^{40}K.

Table B.9 $^{40}Ar/^{39}Ar$ Furnace Analytical Data for cl73/BK-311/WR

T (K)	$^{36}Ar/^{40}Ar$ ±2σ	$^{39}Ar/^{40}Ar$ ±2σ	^{39}Ar(%)	$^{40}Ar^{*}$(%)	Age (Ma)	±2σ
923	0.00046 ± 0.00004	0.0890 ± 0.00054	9.21	86.44	22.38	± 0.41
1073	0.00076 ± 0.00003	0.0870 ± 0.00029	35.07	77.42	20.50	± 0.32
1173	0.00016 ± 0.00019	0.1075 ± 0.00050	45.60	95.26	20.42	± 1.22
1323	0.00020 ± 0.00002	0.1097 ± 0.00030	61.15	93.91	19.72	± 0.25
1473	0.00016 ± 0.00004	0.1113 ± 0.00026	94.94	95.20	19.72	± 0.34
1673	0.00000 ± 0.00016	0.1097 ± 0.00089	100.00	100.00	21.01	± 1.02

J value: 1.28E-3 ± 1.29E-5. All steps of 10 minute duration. $^{40}Ar^{*}$(%) is percentage of measured ^{40}Ar derived from natural decay of ^{40}K.

Table B.10 $^{40}Ar/^{39}Ar$ Furnace Analytical Data for cl73/BK-317/WR

T (K)	$^{36}Ar/^{40}Ar$ ±2σ	$^{39}Ar/^{40}Ar$ ±2σ	^{39}Ar(%)	$^{40}Ar^{*}$(%)	Age (Ma)	±2σ
923	0.00028 ± 0.00013	0.1514 ± 0.00207	5.53	91.58	13.67	± 0.63
1073	0.00075 ± 0.00003	0.1027 ± 0.00029	36.05	77.88	17.11	± 0.22
1173	0.00028 ± 0.00005	0.1260 ± 0.00021	46.87	91.73	16.45	± 0.31
1323	0.00014 ± 0.00014	0.1299 ± 0.00018	65.37	95.88	16.67	± 0.73
1473	0.00025 ± 0.00005	0.1242 ± 0.00032	91.77	92.69	16.86	± 0.28
1673	0.00005 ± 0.00008	0.1272 ± 0.00064	100.00	98.57	17.49	± 0.42

J value: 1.26E-3 ± 7.15E-6. All steps of 10 minute duration. $^{40}Ar^{*}$(%) is percentage of measured ^{40}Ar derived from natural decay of ^{40}K.

Table B.11 $^{40}Ar/^{39}Ar$ Furnace Analytical Data for cl73/BK-318/WR

T (K)	$^{36}Ar/^{40}Ar$ ±2σ	$^{39}Ar/^{40}Ar$ ±2σ	^{39}Ar(%)	$^{40}Ar^{*}$(%)	Age (Ma)	±2σ
923	0.00111 ± 0.00017	0.0801 ± 0.00041	4.11	67.22	18.82	± 1.38
1073	0.00112 ± 0.00008	0.0815 ± 0.00017	27.78	67.01	18.43	± 0.68
1173	0.00016 ± 0.00007	0.1258 ± 0.00032	43.32	95.29	17.00	± 0.40
1323	0.00019 ± 0.00005	0.1240 ± 0.00027	64.61	94.47	17.10	± 0.28
1473	0.00023 ± 0.00006	0.1221 ± 0.00029	93.62	93.16	17.13	± 0.36
1673	0.00038 ± 0.00010	0.1181 ± 0.00054	100.00	88.76	16.86	± 0.56

J value: 1.25E-3 ± 8.60E-6. All steps of 10 minute duration. $^{40}Ar^{*}$(%) is percentage of measured ^{40}Ar derived from natural decay of ^{40}K.

Table B.12 $^{40}Ar/^{39}Ar$ Furnace Analytical Data for cl73/BK-322/WR

T (K)	$^{36}Ar/^{40}Ar$ ±2σ	$^{39}Ar/^{40}Ar$ ±2σ	^{39}Ar(%)	$^{40}Ar^{*}$(%)	Age (Ma)	±2σ
923	0.00318 ± 0.00005	0.0134 ± 0.00004	5.50	6.18	10.34	± 2.32
1073	0.00194 ± 0.00004	0.0607 ± 0.00005	29.80	42.76	15.82	± 0.44
1173	0.00058 ± 0.00004	0.1112 ± 0.00021	45.74	82.83	16.72	± 0.24
1323	0.00059 ± 0.00006	0.1159 ± 0.00015	62.64	82.45	15.97	± 0.34
1473	0.00049 ± 0.00005	0.1124 ± 0.00023	86.40	85.38	17.04	± 0.33
1673	0.00095 ± 0.00007	0.0946 ± 0.00042	100.00	71.94	17.07	± 0.50

J value: 1.25E-3 ± 8.60E-6. All steps of 10 minute duration. $^{40}Ar^{*}$(%) is percentage of measured ^{40}Ar derived from natural decay of ^{40}K.

Table B.13 $^{40}Ar/^{39}Ar$ Furnace Analytical Data for cl73/BK-328/WR

T (K)	$^{36}Ar/^{40}Ar$ ±2σ	$^{39}Ar/^{40}Ar$ ±2σ	^{39}Ar(%)	$^{40}Ar^*$(%)	Age (Ma)	±2σ
923	0.00298 ± 0.00007	0.0162 ± 0.00013	2.96	11.84	16.31	± 2.85
1073	0.00281 ± 0.00005	0.0341 ± 0.00008	16.48	16.96	11.12	± 0.88
1173	0.00140 ± 0.00003	0.0935 ± 0.00017	36.88	58.68	14.01	± 0.26
1323	0.00090 ± 0.00005	0.1110 ± 0.00013	65.67	73.42	14.76	± 0.30
1473	0.00073 ± 0.00008	0.1210 ± 0.00028	91.18	78.41	14.46	± 0.44
1673	0.00053 ± 0.00012	0.1253 ± 0.00073	100.00	84.35	15.01	± 0.63

J value: 1.24E-3 ± 1.01E-5. All steps of 10 minute duration. $^{40}Ar^*$(%) is percentage of measured ^{40}Ar derived from natural decay of ^{40}K.

Table B.14 $^{40}Ar/^{39}Ar$ Furnace Analytical Data for cl73/93-OP-8/WR

T (K)	$^{36}Ar/^{40}Ar$ ±2σ	$^{39}Ar/^{40}Ar$ ±2σ	^{39}Ar(%)	$^{40}Ar^*$(%)	Age (Ma)	±2σ
923	0.00000 ± 0.00028	0.0362 ± 0.00060	0.71	99.84	60.45	± 4.98
1073	0.00167 ± 0.00010	0.1239 ± 0.00052	20.53	50.58	9.07	± 0.56
1173	0.00016 ± 0.00005	0.2446 ± 0.00103	50.92	95.02	8.63	± 0.17
1323	0.00042 ± 0.00005	0.2207 ± 0.00110	71.21	87.55	8.82	± 0.18
1473	0.00073 ± 0.00015	0.1811 ± 0.00075	83.27	78.50	9.63	± 0.54
1673	0.00080 ± 0.00021	0.1899 ± 0.00093	100.00	76.25	8.92	± 0.72

J value: 1.23E-3 ± 1.15E-5. All steps of 10 minute duration. $^{40}Ar^*$(%) is percentage of measured ^{40}Ar derived from natural decay of ^{40}K.

Table B.15 $^{40}Ar/^{39}Ar$ Furnace Analytical Data for cl73/TV-94-35/WR

T (K)	$^{36}Ar/^{40}Ar$ ±2σ	$^{39}Ar/^{40}Ar$ ±2σ	^{39}Ar(%)	$^{40}Ar^*$(%)	Age (Ma)	±2σ
923	0.00460 ± 0.00157	0.6584 ± 0.00292	9.32	-35.76	-1.25	± 1.62
1073	0.00340 ± 0.00019	0.1775 ± 0.00074	31.07	-0.35	-0.05	± 0.72
1173	0.00296 ± 0.00092	0.5904 ± 0.00349	43.04	12.58	0.49	± 1.06
1323	0.00232 ± 0.00034	0.3745 ± 0.00200	51.88	31.33	1.93	± 0.61
1473	0.00263 ± 0.00028	0.4262 ± 0.00189	83.46	22.16	1.20	± 0.44
1673	0.00291 ± 0.00068	0.5542 ± 0.00279	100.00	14.07	0.59	± 0.84

J value: 1.27E-3 ± 1.10E-5. All steps of 10 minute duration. $^{40}Ar^*$(%) is percentage of measured ^{40}Ar derived from natural decay of ^{40}K.

Table B.16 $^{40}Ar/^{39}Ar$ Furnace Analytical Data for cl36/93-OP-3/WR

T (K)	$^{36}Ar/^{40}Ar$ ±2σ	$^{39}Ar/^{40}Ar$ ±2σ	^{39}Ar(%)	$^{40}Ar^*$(%)	Age (Ma)	±2σ
900	0.00169 ± 0.00126	0.8141 ± 0.00502	2.94	49.99	± 3.89	± 2.89
1100	0.00136 ± 0.00002	0.7302 ± 0.00292	64.35	59.61	± 5.17	± 0.07
1300	0.00102 ± 0.00012	0.9159 ± 0.00472	78.58	69.75	± 4.83	± 0.24
1900	0.00035 ± 0.00025	1.0430 ± 0.00694	100.00	89.28	± 5.43	± 0.45

J value: 3.51E-3 ± 1.94E-5. All steps of 10 minute duration. $^{40}Ar^*$(%) is percentage of measured ^{40}Ar derived from natural decay of ^{40}K.

Table B.17 $^{40}Ar/^{39}Ar$ Furnace Analytical Data for cl36/93-OP-3A/WR

T (K)	$^{36}Ar/^{40}Ar$ ±2σ	$^{39}Ar/^{40}Ar$ ±2σ	^{39}Ar(%)	$^{40}Ar^*$(%)	Age (Ma)	±2σ
900	0.00314 ± 0.00007	0.1096 ± 0.00041	6.54	7.14	± 4.12	± 1.23
1100	0.00238 ± 0.00003	0.3759 ± 0.00099	42.61	29.55	± 4.97	± 0.16
1300	0.00108 ± 0.00007	0.8115 ± 0.00363	99.88	67.90	± 5.30	± 0.17
1900	0.00653 ± 0.00646	0.1842 ± 0.03122	100.00	-92.86	-± 32.20	± 66.37

J value: 3.51E-3 ± 1.94E-5. All steps of 10 minute duration. $^{40}Ar^*$(%) is percentage of measured ^{40}Ar derived from natural decay of ^{40}K.

Table B.18 $^{40}Ar/^{39}Ar$ Furnace Analytical Data for cl36/93-OP-5/WR

T (K)	$^{36}Ar/^{40}Ar$ ±2σ	$^{39}Ar/^{40}Ar$ ±2σ	^{39}Ar(%)	$^{40}Ar^*$(%)	Age (Ma)	±2σ
900	0.00037 ± 0.00032	0.2644 ± 0.00061	10.72	88.90	± 21.17	± 2.22
1100	0.00074 ± 0.00005	0.2455 ± 0.00046	37.70	78.06	± 20.03	± 0.39
1300	0.00119 ± 0.00004	0.2061 ± 0.00035	65.97	64.85	± 19.82	± 0.40
1900	0.00061 ± 0.00007	0.3000 ± 0.00083	100.00	81.89	± 17.21	± 0.42

J value: 3.51E-3 ± 1.60E-5. All steps of 10 minute duration. $^{40}Ar^*$(%) is percentage of measured ^{40}Ar derived from natural decay of ^{40}K.

Table B.19 $^{40}Ar/^{39}Ar$ Furnace Analytical Data for cl36/93-OP-16/WR

T (K)	$^{36}Ar/^{40}Ar$ ±2σ	$^{39}Ar/^{40}Ar$ ±2σ	^{39}Ar(%)	$^{40}Ar^*$(%)	Age (Ma)	±2σ
900	0.00179 ± 0.00030	0.2864 ± 0.00212	1.90	47.12	± 10.39	± 1.93
1100	0.00209 ± 0.00008	0.2256 ± 0.00048	11.16	38.21	± 10.70	± 0.66
1300	0.00107 ± 0.00007	0.4036 ± 0.00095	48.70	68.43	± 10.72	± 0.32
1900	0.00043 ± 0.00003	0.5245 ± 0.00188	100.00	87.22	± 10.52	± 0.13

J value: 3.51E-3 ± 1.60E-5. All steps of 10 minute duration. $^{40}Ar^*$(%) is percentage of measured ^{40}Ar derived from natural decay of ^{40}K.

Table B.20 $^{40}Ar/^{39}Ar$ Furnace Analytical Data for cl36/93-OP-17/WR

T (K)	$^{36}Ar/^{40}Ar$ ±2σ	$^{39}Ar/^{40}Ar$ ±2σ	^{39}Ar(%)	$^{40}Ar^*$(%)	Age (Ma)	±2σ
900	0.00000 ± 0.00044	0.1067 ± 0.00116	1.72	99.92	± 58.34	± 7.47
1100	0.00137 ± 0.00041	0.3771 ± 0.00167	6.56	59.35	± 9.95	± 2.00
1300	0.00202 ± 0.00004	0.2225 ± 0.00037	31.62	40.20	± 11.42	± 0.34
1900	0.00035 ± 0.00003	0.5120 ± 0.00165	100.00	89.37	± 11.04	± 0.13

J value: 3.51E-3 ± 8.97E-6. All steps of 10 minute duration. $^{40}Ar^*$(%) is percentage of measured ^{40}Ar derived from natural decay of ^{40}K.

Table B.21 $^{40}Ar/^{39}Ar$ Furnace Analytical Data for cl36/93-OP-18/WR

T (K)	$^{36}Ar/^{40}Ar$ ±2σ	$^{39}Ar/^{40}Ar$ ±2σ	^{39}Ar(%)	$^{40}Ar^*$(%)	Age (Ma)	±2σ
900	0.00076 ± 0.00123	0.3776 ± 0.00192	2.81	77.55	± 12.98	± 6.06
1100	0.00170 ± 0.00007	0.2633 ± 0.00067	12.20	49.64	± 11.91	± 0.51
1300	0.00107 ± 0.00001	0.3620 ± 0.00079	46.33	68.32	± 11.93	± 0.09
1900	0.00035 ± 0.00002	0.4903 ± 0.00158	100.00	89.45	± 11.54	± 0.09

J value: 3.51E-3 ± 8.97E-6. All steps of 10 minute duration. $^{40}Ar^*$(%) is percentage of measured ^{40}Ar derived from natural decay of ^{40}K.

Table B.22 $^{40}Ar/^{39}Ar$ Furnace Analytical Data for cl36/93-OP-19/WR

T (K)	$^{36}Ar/^{40}Ar$ ±2σ	$^{39}Ar/^{40}Ar$ ±2σ	^{39}Ar(%)	$^{40}Ar^*$(%)	Age (Ma)	±2σ
900	0.00330 ± 0.00003	0.0415 ± 0.00011	7.40	2.45	± 3.73	± 1.27
1100	0.00285 ± 0.00004	0.0901 ± 0.00017	21.82	15.83	± 11.08	± 0.78
1300	0.00216 ± 0.00005	0.1993 ± 0.00033	61.45	36.03	± 11.40	± 0.48
1900	0.00186 ± 0.00003	0.2448 ± 0.00074	100.00	44.98	± 11.59	± 0.24

J value: 3.50E-3 ± 4.27E-6. All steps of 10 minute duration. $^{40}Ar^*$(%) is percentage of measured ^{40}Ar derived from natural decay of ^{40}K.

Table B.23 $^{40}Ar/^{39}Ar$ Furnace Analytical Data for cl36/93-OP-33/WR

T (K)	$^{36}Ar/^{40}Ar$ ±2σ	$^{39}Ar/^{40}Ar$ ±2σ	^{39}Ar(%)	$^{40}Ar^*$(%)	Age (Ma)	±2σ
900	0.00272 ± 0.00529	0.5759 ± 0.01786	0.51	19.54	± 2.16	± 17.20
1100	0.00001 ± 0.00069	0.5297 ± 0.00310	4.32	99.63	± 11.91	± 2.41
1300	0.00184 ± 0.00003	0.3011 ± 0.00054	36.84	45.61	± 9.59	± 0.21
1900	0.00035 ± 0.00005	0.5883 ± 0.00249	100.00	89.41	± 9.63	± 0.17

J value: 3.51E-3 ± 8.41E-6. All steps of 10 minute duration. $^{40}Ar^*$(%) is percentage of measured ^{40}Ar derived from natural decay of ^{40}K.

Table B.24 $^{40}Ar/^{39}Ar$ Furnace Analytical Data for cl36/93-OP-34/WR

T (K)	$^{36}Ar/^{40}Ar$ ±2σ	$^{39}Ar/^{40}Ar$ ±2σ	^{39}Ar(%)	$^{40}Ar^*$(%)	Age (Ma)	±2σ
900	0.00662 ± 0.00262	0.2899 ± 0.01804	0.22	-95.59	-± 21.06	± 17.11
1100	0.00165 ± 0.00016	0.2957 ± 0.00082	6.42	51.25	± 10.97	± 0.99
1300	0.00190 ± 0.00003	0.2309 ± 0.00036	29.50	43.74	± 11.98	± 0.27
1900	0.00044 ± 0.00003	0.4912 ± 0.00156	100.00	86.76	± 11.19	± 0.13

J value: 3.51E-3 ± 8.41E-6. All steps of 10 minute duration. $^{40}Ar^*$(%) is percentage of measured ^{40}Ar derived from natural decay of ^{40}K.

Table B.25 $^{40}Ar/^{39}Ar$ Furnace Analytical Data for cl36/93-OP-36/WR

T (K)	$^{36}Ar/^{40}Ar$ ±2σ	$^{39}Ar/^{40}Ar$ ±2σ	^{39}Ar(%)	$^{40}Ar^*$(%)	Age (Ma)	±2s
900	0.00133 ± 0.00003	0.3204 ± 0.00060	33.48	60.60	± 11.91	± 0.20
1100	0.00022 ± 0.00003	0.5127 ± 0.00148	68.80	93.19	± 11.45	± 0.13
1300	0.00065 ± 0.00010	0.4483 ± 0.00125	81.60	80.51	± 11.31	± 0.40
1900	0.00023 ± 0.00020	0.4589 ± 0.00154	100.00	93.05	± 12.77	± 0.81

J value: 3.50E-3 ± 6.49E-6. All steps of 10 minute duration. $^{40}Ar^*$(%) is percentage of measured ^{40}Ar derived from natural decay of ^{40}K.

Table B.26 $^{40}Ar/^{39}Ar$ Furnace Analytical Data for cl36/93-OP-37/WR

T (K)	$^{36}Ar/^{40}Ar$ ±2σ	$^{39}Ar/^{40}Ar$ ±2σ	^{39}Ar(%)	$^{40}Ar^*$(%)	Age (Ma)	±2σ
900	0.00139 ± 0.00036	0.2668 ± 0.00189	1.92	58.97	± 13.91	± 2.50
1100	0.00172 ± 0.00005	0.2563 ± 0.00041	33.88	49.16	± 12.07	± 0.34
1300	0.00047 ± 0.00003	0.4656 ± 0.00126	74.99	85.98	± 11.63	± 0.13
1900	0.00035 ± 0.00015	0.4743 ± 0.00156	100.00	89.44	± 11.88	± 0.57

J value: 3.50E-3 ± 6.49E-6. All steps of 10 minute duration. $^{40}Ar^*$(%) is percentage of measured ^{40}Ar derived from natural decay of ^{40}K.

Table B.27 $^{40}Ar/^{39}Ar$ Furnace Analytical Data for cl36/93-OP-38/WR

T (K)	$^{36}Ar/^{40}Ar$ ±2σ	$^{39}Ar/^{40}Ar$ ±2σ	^{39}Ar(%)	$^{40}Ar^{*}$(%)	Age (Ma)	±2σ
900	0.00332 ± 0.00015	0.0364 ± 0.00027	3.41	1.87	± 3.25	± 7.83
1100	0.00255 ± 0.00007	0.1544 ± 0.00055	14.12	24.75	± 10.11	± 0.83
1300	0.00156 ± 0.00003	0.2959 ± 0.00089	53.82	53.73	± 11.46	± 0.19
1900	0.00122 ± 0.00007	0.3521 ± 0.00177	100.00	63.85	± 11.44	± 0.37

J value: 3.50E-3 ± 4.27E-6. All steps of 10 minute duration. $^{40}Ar^{*}$(%) is percentage of measured ^{40}Ar derived from natural decay of ^{40}K.

CHAPTER 3

MAJOR, TRACE ELEMENT, AND ISOTOPIC CONSTRAINTS ON THE SOURCE REGION OF THE UDOKAN VOLCANIC FIELD, BAIKAL RIFT ZONE, SIBERIA

ABSTRACT

The Udokan Volcanic Field (UVF) is the easternmost expression of the Cenozoic volcanism of the Baikal Rift Zone, Siberia. The UVF lavas were erupted through a complex suture zone between the Archean Aldan Shield and adjacent younger terranes. UVF lavas are the most compositionally variable in the entire rift, and compositions range from strongly undersaturated melaleucitites and basanites to highly evolved trachytes. Trace element signatures are also highly variable, with most lavas (except the evolved trachytes and mugearites/benmoreites) having incompatible elements most comparable to OIB. Trachytes have distinctive incompatible element abundances most likely suggesting evolution at shallower levels involving higher degrees of fractional crystallization of pyroxene, olivine, and plagioclase. The observed range in Sr, Nd, and Pb isotopic compositions is similar to that of OIB. Basanites have the least radiogenic Sr and most radiogenic Nd isotopic compositions, indicative of derivation from a long-term depleted source, while the other lava types trend to isotopic compositions indicative of derivation from or interaction with a more enriched source. The Pb isotopic signatures of the UVF rocks have a complex spatial variation, with steep mixing trends in $^{206}Pb/^{204}Pb$ - $^{207}Pb/^{204}Pb$ and $^{206}Pb/^{204}Pb$ - $^{208}Pb/^{204}Pb$ for each area. Pb isotopic compositions become increasingly radiogenic from north to southeast across the UVF. It is postulated that the

UVF lavas were formed by variable crustal contamination of melts of a mantle source region that may itself also be heterogeneous. Megacrysts of clinopyroxene and anorthoclase have isotopic compositions similar to the regional lavas and support these conclusions.

INTRODUCTION

This work presents part of a large scale project to characterize the geochemistry of rift-related rocks along the length of the Baikal Rift Zone, Siberia (BRZ) (Fig. 3.1). The Udokan volcanic field (UVF) is one of three major volcanic regions in the BRZ and occupies an area of about 3,000 km^2 on the Udokan ridge southeast of the Chara basin (Rasskazov et al., 1997a). Compared to the other volcanic fields of the central and southwestern Baikal Rift Zone, the UVF lavas reveal a large variation in major element and isotopic compositions. The observed variation may reflect melting involving different amounts of relatively old lithospheric mantle and/or crustal components, as well as processes such as fractional crystallization. The fact that the UVF straddles a suture between the Archean Aldan shield and adjacent younger terranes is a likely explanation for the geochemical variation in the lavas.

GEOLOGICAL BACKGROUND

During the last decade, the geology of the crystalline basement in the northeastern BRZ and adjacent areas has been studied intensively (Zonenshain and Savostin, 1981; Glebovitsky and Drugova, 1993; Parfenov et al., 1993; Rundqvist and Mitrofanov, 1993;

Gusev and Hain, 1995). Much of this work has focused on the relative movement between the Siberian and China-Korean cratons and their associated accreted terranes. Motion between these cratons during the Paleozoic and Mesozoic resulted in the closing of the Paleoasian ocean in the eastern Transbaikalia area in the middle Jurassic. The boundary between these two lithospheric plates corresponds to the Mongol-Okhotsk suture, which stretches for 2,000 km from central-western Mongolia in the southwest, through the Transbaikalia area, to the Uda bay in the northeast (Fig. 3.1).

In the Udokan area, the relative tectonic movements involved the Aldan and Baikal-Vitim superterranes (Fig. 3.2). The tectonic block, located west of the Stanovoy terrane between the Mongol-Okhotsk suture and the Aldan terrane, is considered in some geological interpretations as a part of the Archean Siberian craton, although no Archean rocks have yet been found in this block (Rosen et al., 1994 and references therein). Recent geodynamic models (Parfenov et al., 1993; Gusev and Hain, 1995) infer that this block and other terranes comprising the Baikal-Vitim superterrane accreted to the southern edge of the Siberian platform in the latest Precambrian through Paleozoic. Thus, the southern boundary of the Siberian platform is traced along the Dzheltulaksky, Stanovoy, Chukchudu (Dzhugdzhur), Zhuinsky and Baikal-Vitim faults (Fig. 3.2). The Aldan superterrane comprises the Aldan and Stanovoy terranes which are separated from each other by the Stanovoy suture. In the late Cenozoic, oblique NW-SE compression resulted in reactivation of this suture as a right-lateral strike-slip fault (Imaev et al., 1994). Simultaneously, the northeastern portion of the BRZ underwent NW-SE extension and left-lateral strike-slip faulting (Sherman and Levi, 1978).

Local subsidence on the eastern margin of the Aldan shield during the Early Proterozoic is expressed by the Kodar-Udokan foredeep, a depression that stretches ~150 km northwest from the Udokan Range to the Kodar Range. The Kodar-Udokan depression is filled with low-grade metamorphosed sedimentary rocks of the Udokan Group. (Rasskazov et al., 1997a) This portion of the Aldan shield was strongly affected and weakened by Proterozoic tectonic and magmatic processes.

Various models for the initiation of the NW-SE extension in the BRZ have been offered, including the Indo-Eurasian collision (e.g., Molnar and Tapponnier, 1975, 1977; Tapponnier and Molnar, 1979), upwelling asthenospheric material (e.g., Logatchev et al., 1983; Logatchev and Zorin, 1987; Logatchev, 1993), or a combination of the two (Dobretsov et al., 1996). A study of the structural control on late Cenozoic volcanic activity in the Udokan volcanic field and compilation of the data on timing of volcanism in the adjacent areas of southeastern Asia (Rasskazov et al., 1997b) shows that the compression causing right-lateral reactivation of the Stanovoy suture zone could possibly have been produced by collision between the Bonin and Honshu arcs at 12-10 Ma. The mid-plate effect of the collision during the last 10 million years may explain the drastic late Miocene change of stress field in the Japan Sea, east China and the Far East of Russia, as well as the opposite slip motions in the northeastern BRZ and Stanovoy suture (Jolivet et al., 1994; Yoon and Cough, 1995).

STRUCTURAL CONTROL OF VOLCANIC ACTIVITY

The region of the Udokan Volcanic Field can be subdivided into three tectonic zones: the Kodar-Udokan, Chukchudu, and Stanovaya (Figure 3.2). The location of the Chara basin and adjacent smaller depressions of the northeastern BRZ are inferred to be strictly controlled by the reactivated Kodar-Udokan tectonic zone spatially associated with the Kodar-Udokan foredeep on the margin of the shield. The Chukchudu and Stanovaya tectonic zones correspond to the southern margin of the Siberian shield. The Chukchudu tectonic zone stretches from the southeastern to the western part of the UVF (Fig. 3.2). Its southern margin corresponds to the Stanovaya tectonic zone.

Volcanism in the UVF can be divided into three groups roughly corresponding to the Kodar-Udokan, Chukchudu, and Stanovaya zones. Volcanism of the northern part of the UVF overlaps the Kodar-Udokan zone and is therefore considered to be related to rifting. This contrasts with the Chukchudu and Stanovaya zones where volcanism appears to be strongly dependent on the collision-related reactivation of the Stanovoy suture (Rasskazov et al., 1997a, 1997b).

Initiation of the late Cenozoic tectonic reactivation of the Kodar-Udokan zone has been constrained by the first eruptions of alkaline ultramafic lavas in the northern part of the Udokan volcanic field in the middle Miocene at about 14 Ma, coeval with the initiation of subsidence of the Chara basin (Rasskazov et al., 1997a, 1997b). After a long period of volcanic quiescence in the Kodar-Udokan zone, eruptions resumed between 3.2 and 2.4 Ma simultaneously with initiation of subsidence in the smaller rift depressions formed on the flanks of the Chara basin. From 3.2 to 2.6 Ma, lavas of alkali olivine basalt

composition were erupted, followed by final eruptions of basanites between 2.6 and 2.4 Ma (Rasskazov et al., 1997b).

Reactivation of the Chukchudu tectonic zone is expressed by eruptions of differentiated lava series in the time intervals of 9.9 to 7.5 Ma (eastern UVF), 4.0 to 2.6 Ma (central UVF), and from 1.8 Ma through the Holocene (western UVF). ^{14}C dating constrains the latest volcanic eruptions in the Chukchudu weak zone to between 12 and 2.1 ka (Rasskazov et al., 1997b).

Timing of volcanic activity in the Stanovaya zone is not yet well constrained. It is possible that volcanic eruptions in this zone were coeval with those in the Chukchudu tectonic zone in the time intervals of 9.9 to 7.5 Ma and 4.0 to 2.6 Ma (Rasskazov et al., 1997b). Lavas of the Stanovaya zone do not exhibit strong differentiation trends and comprise alkali olivine basalts and basanites.

CHEMISTRY OF UVF VOLCANIC ROCKS

Samples

For the present geochemical and Pb, Sr, and Nd isotopic study, we have selected 33 samples covering all three reactivated tectonic zones (Table 3.1): 14 from the Kodar-Udokan zone, 18 from the Chukchudu zone, and 5 from the Stanovaya zone (Fig. 3.3). These samples were chosen to be representative of the major rock types in the UVF based on the previous work of Rasskazov (1985). All samples were collected by S. Rasskazov and A. Ivanov.

Analytical techniques

Major elements and trace elements were determined by XRF at Washington University, St. Louis according to the methods of Couture et al., (1993) and at the Institute of the Earth's Crust, Irkutsk. Rare earth element (REE) concentrations were obtained by instrumental neutron activation analysis (INAA) at the Massachusetts Institute of Technology, Cambridge, following methods of Ila and Frey (1984). Sample preparation of powders involved crushing rocks to small size, followed by ultrasonic cleaning in deionized water, drying in an oven, and powdering in an alumina ceramic shatterbox.

Isotopic compositions were determined on a VG sector-54 mass spectrometer at M.I.T. Approximately 300 mg of rock powder was dissolved in Teflon beakers in concentrated HF-HNO_3, followed by conversion to chloride form. Rare earth elements were separated by cation exchange columns with HCl as eluant. Sm and Nd were separated using HDEHP-coated BioBead resin with HCl as eluant. Sr separation was accomplished in micro-columns using Sr-spec resin and HNO_3 chemistry. Pb was separated using HBr-based chemistry on anion exchange resin in microcolumns. All reagents used were distilled to reach ultrahigh purity for trace elements.

Sr and Nd isotopic compositions were measured in dynamic multicollector mode. Sr isotopic ratios are normalized to $^{86}Sr/^{88}Sr = 0.1194$, and Nd isotopic ratios are normalized to $^{146}Nd/^{144}Nd = 0.7219$. Based on analyses of NBS-981, Pb isotopic ratios

are corrected by 0.12%/a.m.u. to account for mass fractionation during analysis. Further details are given in Table 2.

RESULTS

Major elements/classification

Major element and trace element data for the analyzed UVF lavas are given in Table 3.1. For classification of volcanic rocks, we follow a common classification based on the total-alkali-silica diagram (TAS diagram) (Le Bas et al., 1986), CIPW normative compositions and modal mineralogy. In the TAS diagram (Fig. 3.4), analyses have been recalculated to 100% on a water-free basis. Normative compositions and mg-numbers ($Mg\# = 100*Mg/(Mg+Fe^{2+})$) were calculated assuming $Fe^{2+} = 0.85*Fe_{total}$.

We distinguish 5 groups of volcanic rocks:

1) Olivine melaleucitites are strongly undersaturated highly alkaline volcanic rocks with normative and modal leucite and Mg# about 70 (Table 3.1). In thin section, these rocks are feldspar-free or contain tiny sanidine and/or plagioclase laths.
2) Basanites are feldspar-bearing highly alkaline volcanic rocks with normative *ne* of 8-19% and Mg# of 66-52. (Fig. 3.6)
3) Alkali olivine basalt and hawaiite have up to 5% normative *ne*. In the samples in this study, Mg# varies from 52 to 62 (Fig. 3.6).

4) A group of evolved hawaiites, mugearites and benmoreites is characterized by Mg# in the range 28-46 and *ne* from 2-5 (Fig. 3.6). Cr and Ni concentrations in these rocks (<25 ppm) are much lower than the rocks of group 4 (Fig. 3.5).

5) Trachytes are highly evolved rocks with > 57 wt.% SiO_2 and Na_2O+K_2O > 10 wt.% (Fig. 3.4). Mg# is highly variable, from 4-21 (Fig. 3.6), while normative *ne* is from 2-6.

The differences between the 5 groups are also readily distinguishable on MgO-major oxide variation diagrams (Fig. 3.7). MgO % is negatively correlated with SiO_2, Al_2O_3, Na_2O, and K_2O, and positively correlated with TiO_2, CaO, and CaO/Al_2O_3. There is no continuous trend for FeO*, but groups 1 - 4 have similar, significantly higher FeO (8 to 11%) than the trachytes. There is a weak negative correlation between MgO and MnO.

Rare earth elements

12 UVF lavas were analyzed for rare earth element abundances, including samples from groups 2, 3, 4, and 5 (Table 3.1). 3 trachytes (group 5) from the western Chukchudu zone have almost identical REE patterns with light rare earth element (LREE) enrichment (La 200 times chondrite), relatively flat heavy rare earth elements (HREE), and a small positive Eu anomaly (Fig. 3.8). In contrast, a trachyte from the central Chukchudu zone has extreme LREE enrichment (La ~500 times chondrite), a large

negative Eu anomaly, and flat HREE. It should be noted that this sample (p367) has the most evolved composition of all analyzed UVF samples (see Fig. 3.4).

Two group 4 lavas from the western Chukchudu zone have roughly parallel REE patterns, with moderate LREE enrichment. The more evolved benmoreite (p61/5) has higher REE abundances than the mugearite (p67/3). In comparison, one group 3 sample (p224/5) from the eastern Chukchudu zone has slightly lower LREE and lower HREE (Fig. 3.8c).

The basanites (group 2) of the western Chukchudu zone are similar to the one analyzed basanite from the Kodar-Udokan zone (p269/4). These samples have moderate LREE enrichment, with La 100-200x chondrite (Fig. 3.8b). One of the basanites from the western Chukchudu zone (p184) differs from the others with steeper LREE and lower HREE. A basanite from the central Chukchudu zone (p411/4) has overall higher REE contents than the other analyzed basanites, with La of ~400 times chondrite.

Incompatible trace elements

Primitive mantle normalized incompatible element diagrams (using values of Sun and McDonough, 1989) demonstrate that the trachytes are strongly affected by fractional crystallization processes (Fig. 3.9). For trachytes of the western Chukchudu zone, incompatible element abundances are very similar (Fig. 3.9). A strong relative Ti and Sr depletion indicates crystallization of an Fe-Ti oxide as well as plagioclase. A trachyte from the central Chukchudu zone (p411/4) has a similar overall incompatible element

pattern, but with much more pronounced relative depletions of Ti and Sr (Fig. 3.9). In this sample, a negative Ba anomaly is also evident.

Basanites of the Kodar-Udokan, western and central Chukchudu zones exhibit similar but somewhat variable incompatible element patterns (Fig. 3.9). Rocks of group 3 (Fig. 3.9) have incompatible elements similar to the basanites. One sample from group 4 (p61/5, benmoreite) has trace elements which more closely resemble the trachyte group, including a relative Ti depletion (Fig. 3.9).

Sr, Nd and Pb isotopic compositions

Isotope data for the UVF lavas are given in Table 3.2. In general, Sr and Nd isotopic compositions of the UVF lavas correlate with their major element chemistry (Fig. 3.10). The five basanites from the Kodar-Udokan zone have very similar Sr and Nd isotopic compositions, with $^{87}Sr/^{86}Sr$ from 0.70374 to 0.70435, and ε_{Nd} from +2.44 to +4.68. With the exception of sample p61/2 (with an anomalously negative ε_{Nd} of -3.0), basanites of the other zones fall within this same range. The melaleucitite (group 1) from the Stanovaya zone (U-94-19) and the one from the Kodar-Udokan zone (U-94-38) have almost identical Sr and Nd isotopic compositions and overlap the basanite range, although on the lower $^{87}Sr/^{86}Sr$, higher ε_{Nd} end (Fig. 3.10). Trachytes (group 5) show the widest range in Sr and Nd isotopic compositions ($^{87}Sr/^{86}Sr$ = 0.70400 to 0.70636; ε_{Nd} = +3.43 to -1.05). It is worth noting that p367, the most evolved trachyte (Fig. 3.4) with the lowest Sr concentration (48 ppm) has the most radiogenic Sr (Fig. 3.10). A plot of $^{87}Sr/^{86}Sr$ vs. 1/Sr (Fig. 3.11) clearly demonstrates that trachytic magmas are being affected by

processes of assimilation and fractional crystallization. The lavas of group 3 have more radiogenic $^{87}Sr/^{86}Sr$ (0.70377 - 0.70535) and less radiogenic ε_{Nd} (+3.69 to -1.45) than most other UVF lavas. The three lavas of group 4 are significantly different from each other. Sample p67/3 is similar to the basanites of group 2. Sample p61/5 and p61/11 have extremely different Nd compositions, even though they are from the same sequence of western Chukchudu zone lavas. However, p61/5 is a benmoreite, while p61/11 is a hawaiite. The Sr concentration of p61/11 is relatively high (950 ppm), making its Sr isotopic composition insensitive to crustal assimilation. Basanite p61/2, also from the same sequence, has ε_{Nd} almost identical to that of p61/5.

The Pb isotopic compositions of the UVF lavas are not as well correlated with rock type (group) as the Sr and Nd isotopic compositions (Fig. 3.12). For example, basanites have the least and most radiogenic $^{206}Pb/^{204}Pb$ of analyzed samples. The trachytes (group 5) and the hawaiite to benmoreites (group 4) have a similar and restricted range of $^{206}Pb/^{204}Pb$ (17.93 - 18.16) and $^{207}Pb/^{204}Pb$ (15.47 - 15.52), and a wider range in $^{208}Pb/^{204}Pb$ (37.92 - 38.27). The basanites from the Kodar-Udokan zone have a restricted range in $^{206}Pb/^{204}Pb$ with a greater variation in $^{207}Pb/^{204}Pb$ and $^{208}Pb/^{204}Pb$. The two group 4 rocks from the same lava sequence, which have very different Nd isotopic compositions (p61/5 and p61/11), have almost identical Pb isotopic compositions.

Spatial variations in UVF lavas

UVF lavas show notable spatial variations. Rocks of the Kodar-Udokan zone are basanites and melaleucitites and have the most unradiogenic Pb and Sr, and most

radiogenic Nd (Fig. 3.13, 3.14). The rocks of the Chukchudu weak zone are highly variable, and include all groups of lavas except for melaleucitite (Fig. 3.14). The Sr and Nd isotopic compositions show larger variations than the Pb isotopic compositions. If we consider the longitudinal variation of the Chukchudu zone (Fig. 3.14), we see that the basanites have very similar low $^{87}Sr/^{86}Sr$ and high ε_{Nd} (with the exception of p61/5). The trachytes (group 5) and group 4 lavas have less radiogenic Sr, Nd and Pb isotopic compositions in the western Chukchudu zone than in the east. The sequence of two group 4 rocks (p61/5, p61/11) and one basanite (p61/2) from the same lava series have essentially identical Pb isotopic composition but varying Sr and Nd, probably indicating the sensitivity of Pb to crustal assimilation.

In Figure 3.12, fields are drawn around lavas of each zone. It can be seen on the $^{206}Pb/^{204}Pb$ - $^{207}Pb/^{204}Pb$ and $^{206}Pb/^{204}Pb$ - $^{208}Pb/^{204}Pb$ diagrams (Fig. 3.12) that rocks from each area show variation that can be attributed to mixing of different components in various proportions. The least radiogenic trend is that of the Kodar-Udokan zone. As described above, the western Chukchudu lavas are less radiogenic than the central and eastern Chukchudu lavas. The central and eastern Chukchudu lavas have quite distinct and higher $^{208}Pb/^{204}Pb$ than the other areas, while the Kodar-Udokan and western Chukchudu lavas have almost parallel trends on the $^{206}Pb/^{204}Pb$ - $^{208}Pb/^{204}Pb$ diagram. The two lavas from the Stanovaya weak zone have different $^{206}Pb/^{204}Pb$, but similar $^{207}Pb/^{204}Pb$ and $^{208}Pb/^{204}Pb$ that is of intermediate composition.

$^{206}Pb/^{204}Pb$ - $^{87}Sr/^{86}Sr$ and $^{206}Pb/^{204}Pb$ - ε_{Nd} diagrams (Fig. 3.15) show the data has a triangular shape, perhaps indicating the involvement of three different components. The

western Chukchudu and central/eastern Chukchudu lavas have a similar range in $^{87}Sr/^{86}Sr$ and ε_{Nd} with different, almost non-overlapping $^{206}Pb/^{204}Pb$.

DISCUSSION

Sources of UVF magmas: crustal contamination vs. mantle heterogeneity

The geochemical characteristics of the analyzed rocks, as described above, indicate that generation of the UVF lavas involved both mantle and crustal sources. However, while some of the most evolved lavas (groups 4 and 5) have clearly been affected by crustal interaction, it is more difficult to discern whether or how much the other groups of lavas have been affected by crustal contamination. Given the intraplate setting of UVF magmatism, there is a wide variety of components that could contribute to the geochemical signatures of the lavas. The possible sources include old lithospheric mantle, upwelling asthenospheric mantle related to the current rifting, or even perhaps lithospheric mantle thermally converted to asthenosphere. The lithosphere in the Udokan region has a complex history of multiple episodes of magmatism and accretion/suturing, and therefore the crust, too, is comprised of a wide range of lithologies of various ages.

The UVF lavas which are the least evolved (highest Mg#, Ni, and Cr abundances) (Fig. 3.5, 3.6) and therefore likely to be most representative of their mantle source are the basanites and melaleucitites. The rocks of this group have high Sr concentrations (670 - 1380 ppm) and relatively high Nd concentrations (28 - 67 ppm) which make them relatively insensitive to small amounts of crustal assimilation. The basanite group has the most depleted (although variable) Sr and Nd isotopic compositions (OIB-like), and is not

correlated with Mg#. On Figure 3.10, three UVF clinopyroxene (cpx) megacrysts are shown to be slightly less radiogenic in Sr and more radiogenic in Nd isotopic composition than the basanitic hosts (Harris et al., in prep. and Chapter 5 of this thesis). Harris et al. considered these megacrysts to have formed from a magma related to but not exactly the same as their host rock. The fact that the megacrysts are less radiogenic in Sr and more radiogenic in Nd than the UVF lavas suggests that the Sr and Nd isotopic compositions of UVF lavas may have been affected by crustal contamination after all. As with the lavas, the source region of the megacrysts could be either lithospheric mantle or asthenosphere.

Unlike Sr and Nd, the Pb concentration of the basanites is in the range of 2 - 9 ppm, and therefore the Pb isotopes are much more likely to have been affected by crustal contamination. This appears to be the case, since the basanites have a range in Pb isotopic compositions that encompasses the range of all the other groups of UVF lavas (Fig. 3.12). The more evolved rocks (groups 4 and 5) have slightly higher Pb concentrations than the basanites. As noted above, the Pb isotopic composition of all rock types seems to be correlated with volcanic region, with steep trends in $^{206}Pb/^{204}Pb$ - $^{207}Pb/^{204}Pb$ that shift to more radiogenic $^{206}Pb/^{204}Pb$ from the Kodar-Udokan zone to the western Chukchudu and central/eastern Chukchudu zones. The central and eastern Chukchudu zones have an especially distinctive high $^{208}Pb/^{204}Pb$ signature. The steep trends for each zone may be attributed to mixing of the mantle source with variable amounts of lithosphere, while the differences in range of $^{206}Pb/^{204}Pb$ for each region may reflect interaction with different types/ages of lithosphere. In particular, the high $^{208}Pb/^{204}Pb$ of the central/eastern Chukchudu zone may reflect interaction with crust with

a higher Th/Pb ratio. Two of the cpx megacrysts (from the central/eastern Chukchudu zone) are shown on the Pb variation diagrams. They have lower $^{207}Pb/^{204}Pb$ and $^{208}Pb/^{204}Pb$ than the analyzed UVF lavas, but similar $^{206}Pb/^{204}Pb$. Also shown are anorthoclase megacrysts analyzed by Harris et al. (in prep.; Chapter 5 of this thesis). Harris et al. proposed that the anorthoclase megacrysts formed at lower pressures than the cpx megacrysts. It can be seen that they have a range in isotopic composition similar to that of the UVF lavas. A cpx (p86/3-3) and anorthoclase (p86/G-p) from the same host lava have similar $^{206}Pb/^{204}Pb$, but the anorthoclase has more radiogenic $^{207}Pb/^{204}Pb$ and $^{208}Pb/^{204}Pb$. This may indicate that the parental magma of the anorthoclase was also affected by interaction with crust.

If the cpx megacrysts are considered to be the most likely to reflect the composition of the mantle source, the source region must vary spatially. In particular, the Kodar-Udokan volcanic source region has a less radiogenic Pb isotopic signature than the central/eastern Chukchudu zone. Alternatively, it is possible that the mantle source is relatively homogenous across the entire area, but in the Kodar-Udokan zone (and perhaps the western Chukchudu zone) parental magma interacted with less radiogenic lithospheric mantle. The triangular distribution of the data on the $^{206}Pb/^{204}Pb$ - ε_{Nd} and $^{206}Pb/^{204}Pb$ - $^{87}Sr/^{86}Sr$ diagrams (Figure 3.14) suggests that there are three possible sources to consider. Again, whether this is the outcome of one type of mantle source interacting with different lithosphere in the different regions or a heterogeneous mantle interacting with variable lithosphere is difficult to discern.

Incompatible trace element signatures of the basanites of the Kodar-Udokan and western Chukchudu zones are quite similar (Fig. 3.9). This may support there being a similar source region for these zones. The western Chukchudu trachytes are all almost identical, and extremely different from the basanites, most likely a result of their evolving in shallower magma chambers with more fractional crystallization.

CONCLUSIONS

UVF lavas exhibit a wide range in major element, trace element, and Sr, Nd and Pb isotopic compositions. Based on major elements, five different groups of lavas can be defined. The strongly undersaturated melaleucitites, basanites, and the moderately undersaturated hawaiites were most likely generated at greater depths than the more evolved trachytes, mugearites and benmoreites. It is possible that the melaleucitites and basanites are parental to the trachytes, mugearites and benmoreites. Basanites of all zones have very similar incompatible elements which are most comparable to OIB. The variation in major element oxides, as well as trace element abundances, indicates that fractional crystallization of clinopyroxene, garnet, feldspar, and Fe-Ti-oxide played an important role in the evolution of the transitional group 4 lavas and the trachytes.

The basanites are considered to be the least evolved magmas, and have Sr and Nd isotopic compositions indicative of derivation from a long-term depleted source. Clinopyroxene megacrysts from Udokan have slightly more depleted Sr and Nd isotopic signatures. Trachytes and the other evolved rocks have more radiogenic Sr and less radiogenic Nd isotopic compositions than groups 1-4. The group of trachytes has also

been affected by processes of assimilation and fractional crystallization, as demonstrated by the trend of 1/Sr vs. $^{87}Sr/^{86}Sr$ (Fig. 3.11) .

The Pb isotopic composition of UVF lavas create a more complex picture than the Sr and Nd isotopic data. Basanites have low Pb concentration, and are therefore extremely sensitive to crustal assimilation. There is a spatial variation in Pb isotopic composition of all rock types exhibited by a steep mixing trend on the $^{206}Pb/^{204}Pb$ - $^{207}Pb/^{204}Pb$ and $^{206}Pb/^{204}Pb$ - $^{208}Pb/^{204}Pb$ diagrams (Fig. 3.12), with $^{206}Pb/^{204}Pb$ becoming increasingly radiogenic from north to southeast. The basanites have the highest and lowest $^{206}Pb/^{204}Pb$, $^{207}Pb/^{204}Pb$, and $^{208}Pb/^{204}Pb$, while the evolved group 4 and 5 rocks have intermediate Pb isotopic compositions. By comparison, cpx megacrysts have lower $^{207}Pb/^{204}Pb$ and $^{208}Pb/^{204}Pb$ for their range in $^{206}Pb/^{204}Pb$, and plot close to the NHRL. Anorthoclase megacrysts have the same range in composition as the UVF lavas.

Based on the obtained data, we propose that the UVF lavas most likely originated by partial melting of a common mantle source, followed by variable interaction between the parental melt and crust. The Pb isotope data provide the best evidence that the different tectonic zones in the Udokan area contributed different crustal contamination signatures. However, it is equally possible that the mantle source region is also heterogeneous, both between and within the different tectonic regions, and was further overprinted by crustal contamination. Based on the current data, it does not seem possible to distinguish between these different hypotheses. Further studies of Udokan mantle xenoliths along with isotopic study of the basement rocks through which the UVF lavas intrude are clearly necessary.

REFERENCES

Couture, R. A., Smith, M. S., and Dymek, R. B., 1993, X-ray fluorescence analysis of silicate rocks using fused glass discs and a side-window Rh source tube: accuracy, precision and reproducibility: Chemical Geology, v. 110, p. 315-328.

Dobretsov, N. L., Buslov, M. M., Delvaux, D., Berzin, N. A. and Ermikov, V. D., 1996, Meso- and Cenozoic tectonics of the central Asian mountain belt: effects of lithospheric plate interaction and mantle plumes: International Geology Review, v. 38, p. 430-466.

Glebovitskii, V. F. and Drugova, G. M., 1993, Tectonothermal evolution of the western Aldan Shield, Siberia: Precambrian Research, v. 62, p. 493-505.

Gusev, G. S. and Hain, V. E., 1995, On relations between Baikal-Vitim, Aldan-Stanovoi and Mongol-Okhotsk terranes (south of mid-Siberia): Geotectonica, v. 5, p. 68-83.

Hart, S. R., Gerlach, D. C. and White, W. M., 1986, A possible new Sr-Nd-Pb mantle array and consequences for mantle mixing: Geochimica et Cosmochimica Acta, v. 50, p. 1551-1557.

Hart, S. R., 1988, Heterogeneous mantle domains: signatures, genesis and mixing chronologies: Earth and Planetary Science Letters, v. 90, p. 273-296.

Ila, P. and Frey, F. A., 1984, Utilization of neutron activation analysis in the study of geologic materials, in use and development of low and medium flux research reactors., in O. K. Harlin, L. Clark and P. von der Hardt, eds., Suppl. Atomkernenerg. Kerntech., v. 44, p. 710-716.

Imaev, V. S., Imaeva, L. P., Kozmin, B. M. and Fudzhita, K., 1994, Active faults and modern geodynamics of the Yakutian seismical belts: Geotectonika, v. 2, p. 57-71.

Jolivet, L., Tamaki, K. and Fournier, M., 1994, Japan Sea, opening history and mechanism: a synthesis: Journal of Geophysical Research, v. 99, p. 22,237-22,259.

Le Bas, M. J., Le Maitre, R. W., Streckeisen, A. and Zanettin, B., 1986, A chemical classification of volcanic rocks based on the total alkali-silica diagram: Journal of Petrology, v. 27, p. 745-750.

Logatchev, N. A., Zorin, Y. A. and Rogozhina, V. A., 1983, Baikal Rift: active or passive? - comparison of the Baikal and Kenya rift zones: Tectonophysics, v. 94, p. 223-240.

Logatchev, N. A. and Zorin, Y. A., 1987, Evidence and causes of the two-stage development of the Baikal rift: Tectonophysics, v. 143, p. 225-234.

Logatchev, N. A., 1993, History and geodynamics of the Lake Baikal rift in the context of the eastern Siberia rift system: a review: Bull. Centres Rech. Explor.-Prod. Elf Aquitaine, v. 17, p. 353-370.

Molnar, P. and Tapponnier, P., 1975, Cenozoic tectonics of Asia: effects of a continental collision: Science, v. 189, p. 419-426.

Molnar, P. and Tapponnier, P., 1977, Relation of the tectonics of eastern China to the India-Eurasia collision: application of slip-line field theory to large-scale continental tectonics: Geology, v. 5, p. 212-216.

Parfenov, L. M., Natapov, L. M., Sokolov, S. D., and Tsukanov, N.V., 1993, Terranes and accretionary tectonics of northeastern Asia: Geotectonics, v. 27, p. 62-72.

Rasskazov, S. V., 1985, The Udokan Basaltoids: Novosibirsk, Nauka Publishers.

Rasskazov, S., Ivanov, A., Boven, A. and Andre, L., 1997a, Late Cenozoic reactivation of the early Pre-Cambrian Aldan Shield: trace element constraints on magmatic sources beneath the Udokan Ridge, Siberia, Russia, in Proceedings of the 30th International Geologic Congress, Part 15.

Rasskazov, S. V., Boven, A., Andre, L., Liegeois, J.-P., Ivanov, A. V. and Punzalan, L., 1997b, Evolution of magmatism in the northeastern Baikal Rift system: Petrologiya, v. 5, p. 115-136.

Rhodes, J. M., 1983, Homogeneity of lava flows: chemical data for historic Mauna Loan eruptions: Journal of Geophysical Research, v. 88 (Suppl.), p. A869-A879.

Rosen, O. M., Condie, K. C., Natapov, L. M., and Nozhkin, A. D., 1994, Archean and early Proterozoic evolution of the Siberian Craton; a preliminary assessment, in K. C. Condie, ed. Archean crustal evolution, Developments in Precambrian Crustal Geology, V. 11, p. 411-459.

Rundqvist, D. V., and Mitrofanov, F. P., 1993, Precambrian geology of the USSR, Elsevier, p.

Sherman, S. I. and Levi, K. G., 1978, Transform faults of the Baikal Rift Zone and Seismicity of their terminations, in., Tectonics and seismicity of the continental rift zones: p. 7-18.

Sun, S. and McDonough, W. F., 1989, Chemical and isotopic systematics of oceanic basalts: implications for mantle composition and processes, in A. D. Saunders and M. J. Norry, eds., Magmatism in the Ocean Basins: Special Publication No. 42, p. 313-345.

Tapponnier, P. and Molnar, P., 1979, Active faulting and Cenozoic tectonics of the Tien Shan, Mongolia, and Baykal regions: Journal of Geophysical Research, v. 84, p. 3425-3459.

Yoon, S. H. and Cough, S. K., 1995, Regional strike slip in the eastern coninental margin of Korea and its tectonic implications for the evolution of Ulleung Basin, East Sea (Sea of Japan): Geological Society of American Bulletin, v. 107, p. 83-97.

Zindler, A. and Hart, S., 1986, Chemical geodynamics: Annual Reviews in Earth and Planetary Science, v. 14, p. 493-571.

Zonenshain, L. P. and Savostin, L. A., 1981, Geodynamics of the Baikal rift zone and plate tectonics of Asia: Tectonophysics, v. 76, p. 1-45.

FIGURE CAPTIONS

Figure 3.1 General map of the Baikal Rift Zone (BRZ) showing locations of the major Cenozoic volcanic fields and other major features. TV is the Tuva volcanic field; OP is the Oka Plateau; T is the Tunka Basin, and D is the Dzhida Basin. Other rift basins according to number label are: 1) Busingol, 2) Darkhat, 3) Khubsugul, 4) Barguzin, 5) Upper Angara, 6) Tsipa, 7) Baunt, 8) Muya, 9) Chara, and 10) Tokka. The 1500 m contour line of the Sayan-Baikal domal uplift is indicated.

Figure 3.2 Map of the northeastern BRZ showing major tectonic terranes and faults related sutures.

Figure 3.3 Map of the Udokan Volcanic Field, showing volcanic fields, sedimentary basins, tectonic zones, and sample locations. Sample numbers correspond to sample numbers in Table 3.1 and Table 3.2. KU = Kodar-Udokan zone, ST = Stanovaya zone, CH = Chukchudu zone.

Figure 3.4 Total Alkali Silica Diagram (fields of Le Bas et al., 1986) showing subdivision of UVF lavas.

Figure 3.5 Weight % SiO_2 versus Cr and Ni concentration of UVF lavas.

Figure 3.6 Mg# versus normative *ne*. Mg# = 100*Mg/(Mg+Fe^{2+}) calculated assuming $Fe^{2+} = 0.85*Fe_{total}$.

Figure 3.7 MgO-major oxide variation diagrams. Symbols as in Figure 3.4.

Figure 3.8 Chondrite-normalized rare earth element diagrams for UVF lavas, using values of Sun and McDonough (1989) for C1 chondrite.

Figure 3.9 Primitive mantle normalized (primitive mantle values of Sun and McDonough, 1989) incompatible element diagrams for UVF lavas. a) W. Chukchudu zone lavas by group, b) E. Chukchudu and C. Chuckchudu zone lavas, c) Stanovaya and Kodar-Udokan lavas. Symbols as in Figure 3.4.

Figure 3.10 $^{87}Sr/^{86}Sr$ - ε_{Nd} diagram for UVF lavas. End-member mantle components DMM (depleted MORB mantle), EMI (enriched mantle type 1), and EMII (enriched mantle type 2) are shown (Hart, 1988; Zindler and Hart, 1986).

Figure 3.11 1/Sr versus $^{87}Sr/^{86}Sr$ diagram demonstrating that trachytes (group 5) are affected by assimilation/fractional crystallization processes.

Figure 3.12 $^{206}Pb/^{204}Pb$ - $^{208}Pb/^{204}Pb$ and $^{206}Pb/^{204}Pb$ - $^{207}Pb/^{204}Pb$ diagrams for UVF lavas. Also shown is the Northern Hemisphere Reference Line (NHRL) of Hart (1984). Fields are drawn around lavas of each zone.

Figure 3.13 Variation in Sr, Pb, and Nd isotopic compositions of UVF lavas with latitude. Symbols as in Figure 3.4.

Figure 3.14 Variations in Sr, Pb, and Nd isotopic compositions with longitude for lavas of the Chukchudu zone. Symbols as in Figure 3.4.

Figure 3.15 $^{206}Pb/^{204}Pb$ - $^{87}Sr/^{86}Sr$ and $^{206}Pb/^{204}Pb$ - ε_{Nd} diagrams for UVF lavas. Fields are drawn around lavas of each zone. Symbols are as in Figure 3.10.

Figure 3.1

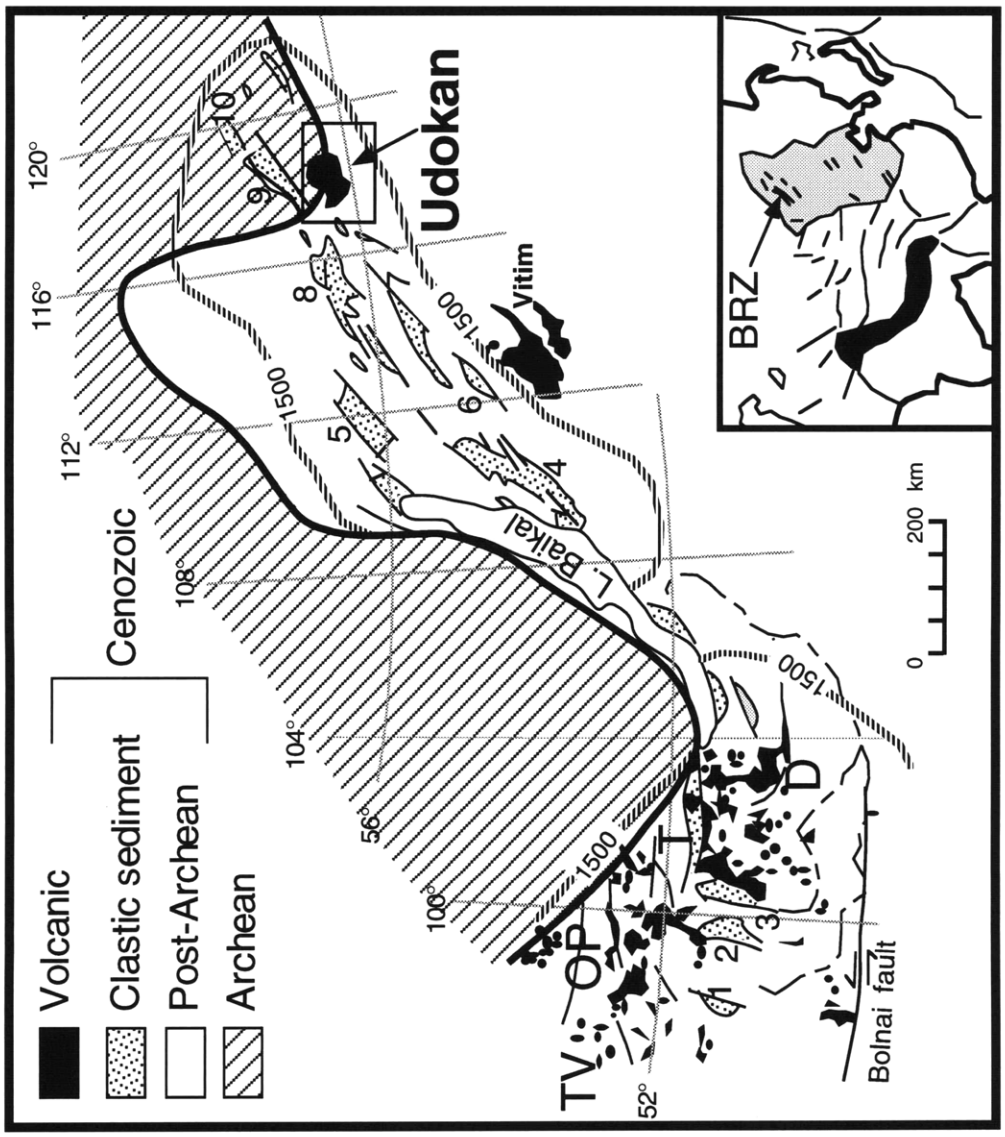
Volcanic
Clastic sediment
Cenozoic
Post-Archean
Archean
Udokan
Vitim
Baikal
BRZ
TV
OP
T
D
Bolnai fault
1500
200 km
0
52°
56°
100°
104°
108°
112°
116°
120°

Figure 3.2

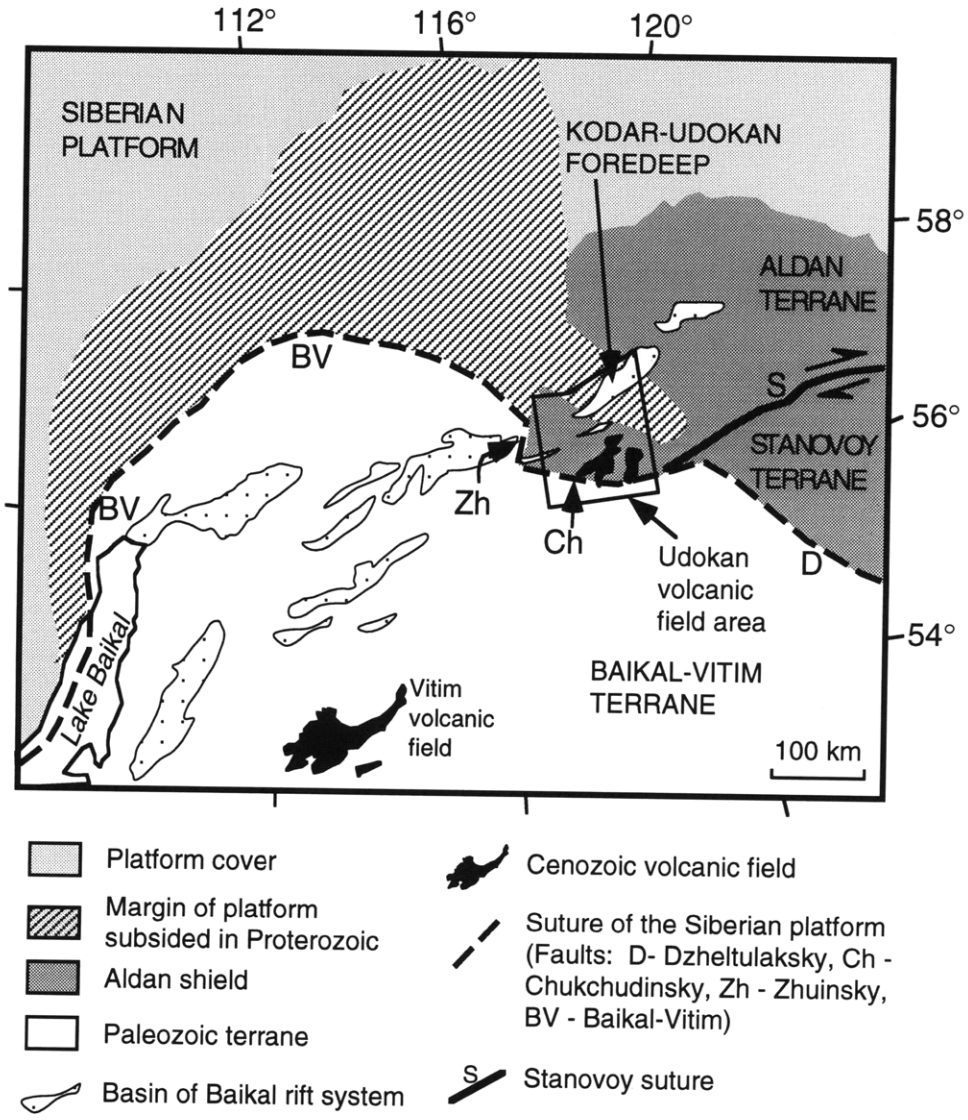
112°
116°
120°
58°
56°
54°
SIBERIAN PLATFORM
KODAR-UDOKAN FOREDEEP
ALDAN TERRANE
STANOVOY TERRANE
BV
BV
S
Zh
Ch
D
Udokan volcanic field area
Lake Baikal
Vitim volcanic field
BAIKAL-VITIM TERRANE
100 km
Platform cover
Margin of platform subsided in Proterozoic
Aldan shield
Paleozoic terrane
Basin of Baikal rift system
Cenozoic volcanic field
Suture of the Siberian platform (Faults: D- Dzheltulaksky, Ch - Chukchudinsky, Zh - Zhuinsky, BV - Baikal-Vitim)
S
Stanovoy suture

Figure 3.3

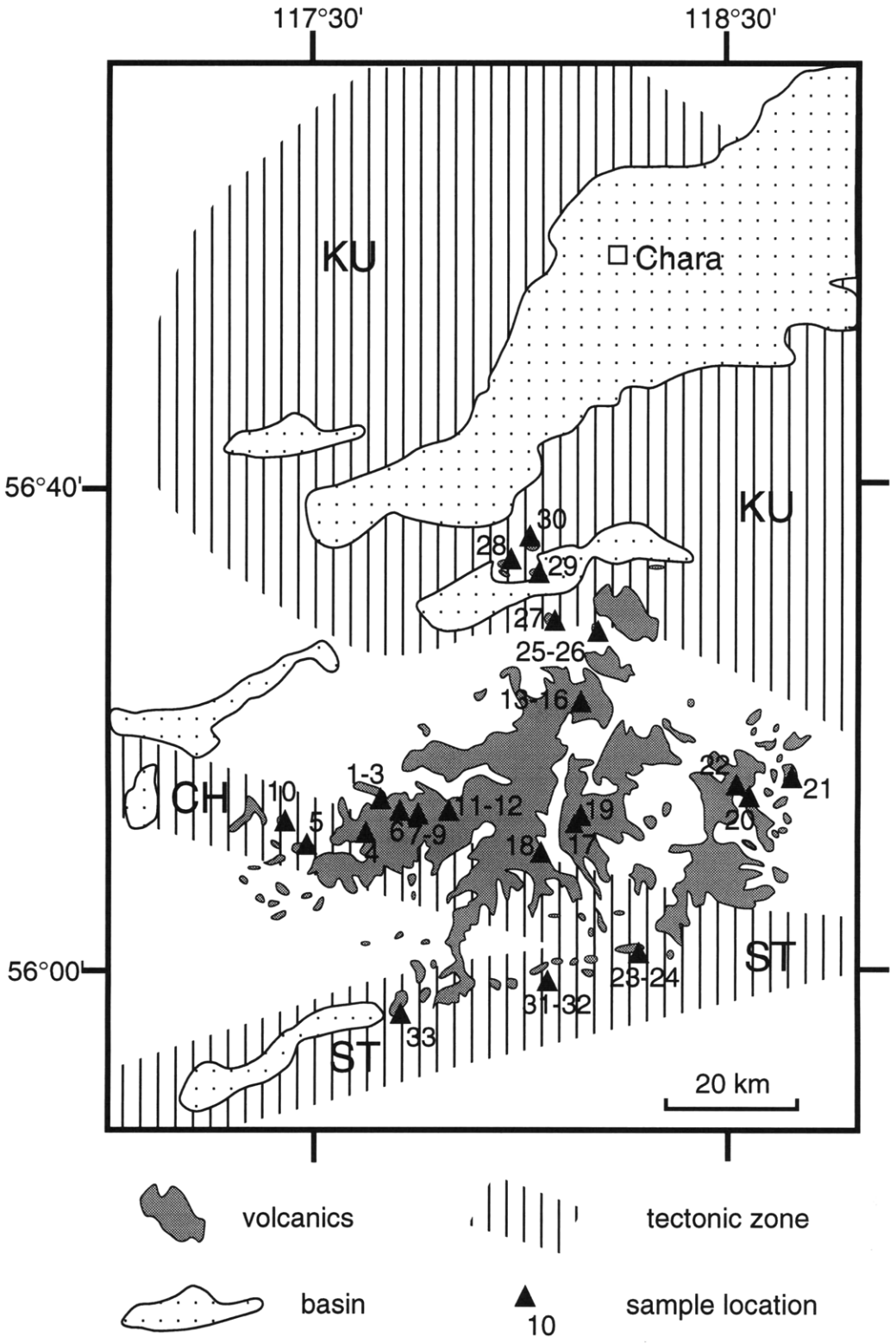
117°30'
118°30'
56°40'
56°00'
KU
Chara
KU
CH
ST
ST
30
28
29
27
25-26
13-16
1-3
10
5
4
6-7-9
11-12
18
19
17
22
21
20
23-24
31-32
33
20 km
volcanics
tectonic zone
basin
sample location
10

Figure 3.4

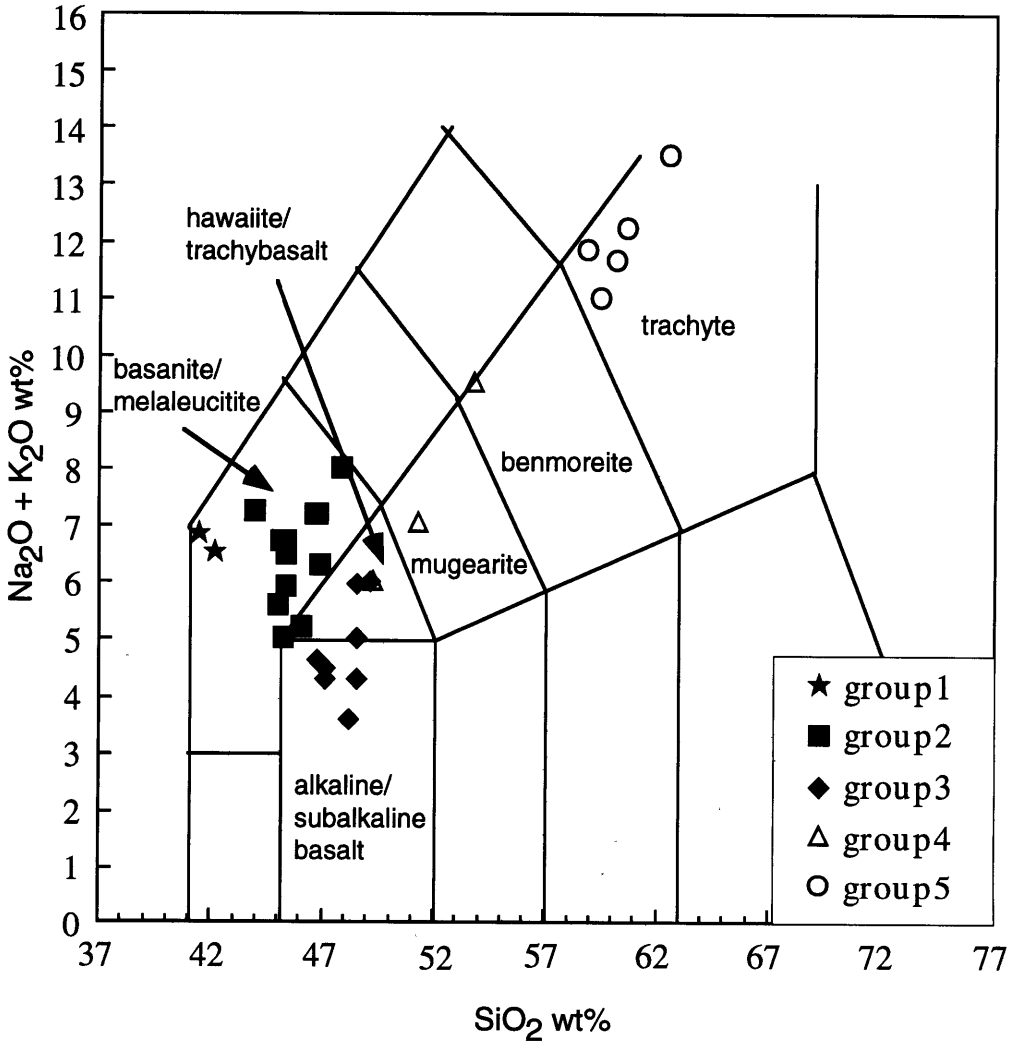
16
15
14
13
12
11
10
9
8
7
6
5
4
3
2
1
0
37
42
47
52
57
62
67
72
77
$Na_2O + K_2O$ wt%
SiO_2 wt%
hawaiite/
trachybasalt
basanite/
melaleucitite
trachyte
benmoreite
mugearite
alkaline/
subalkaline
basalt
group1
group2
group3
group4
group5

Figure 3.5

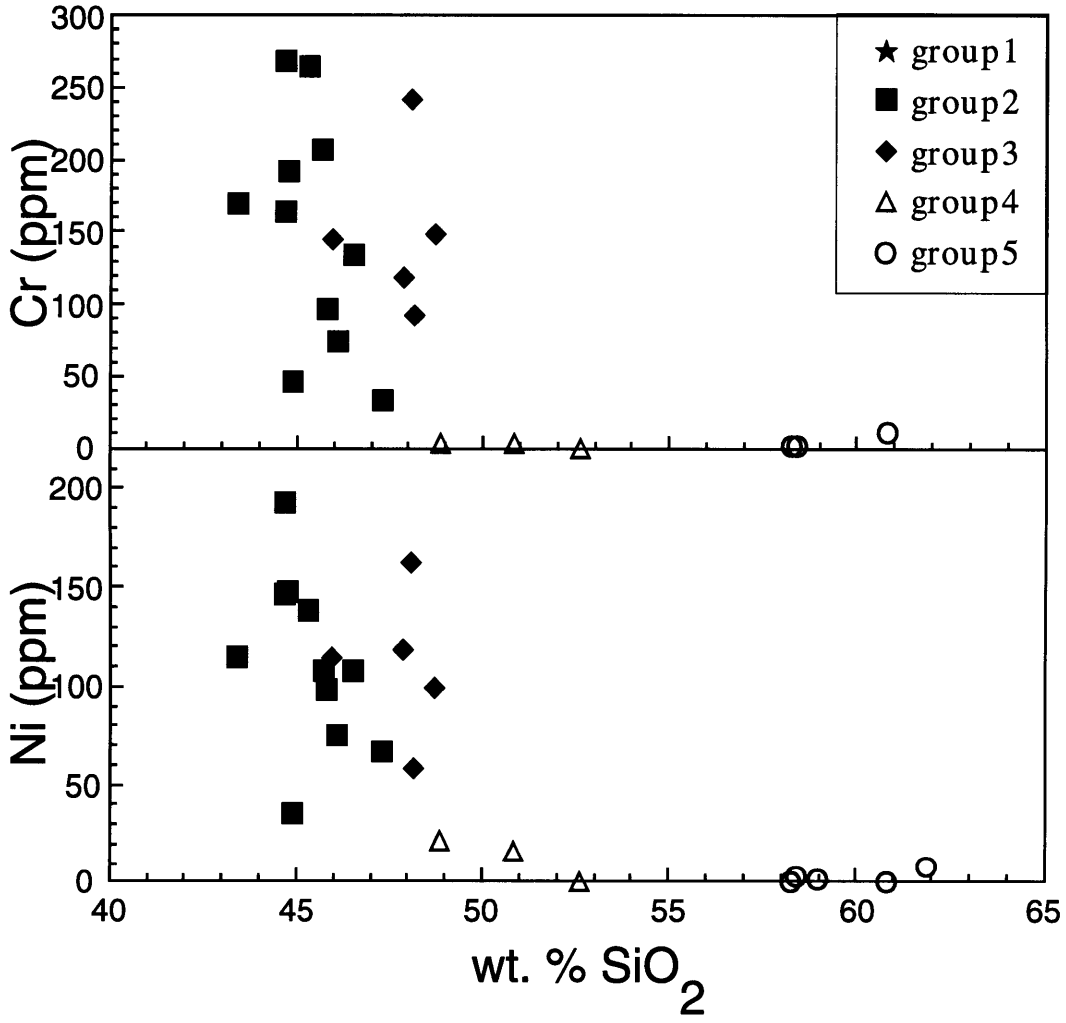
group1
group2
group3
group4
group5
Cr (ppm)
Ni (ppm)
wt. % SiO2
0
50
100
150
200
250
300
40
45
50
55
60
65

Figure 3.6

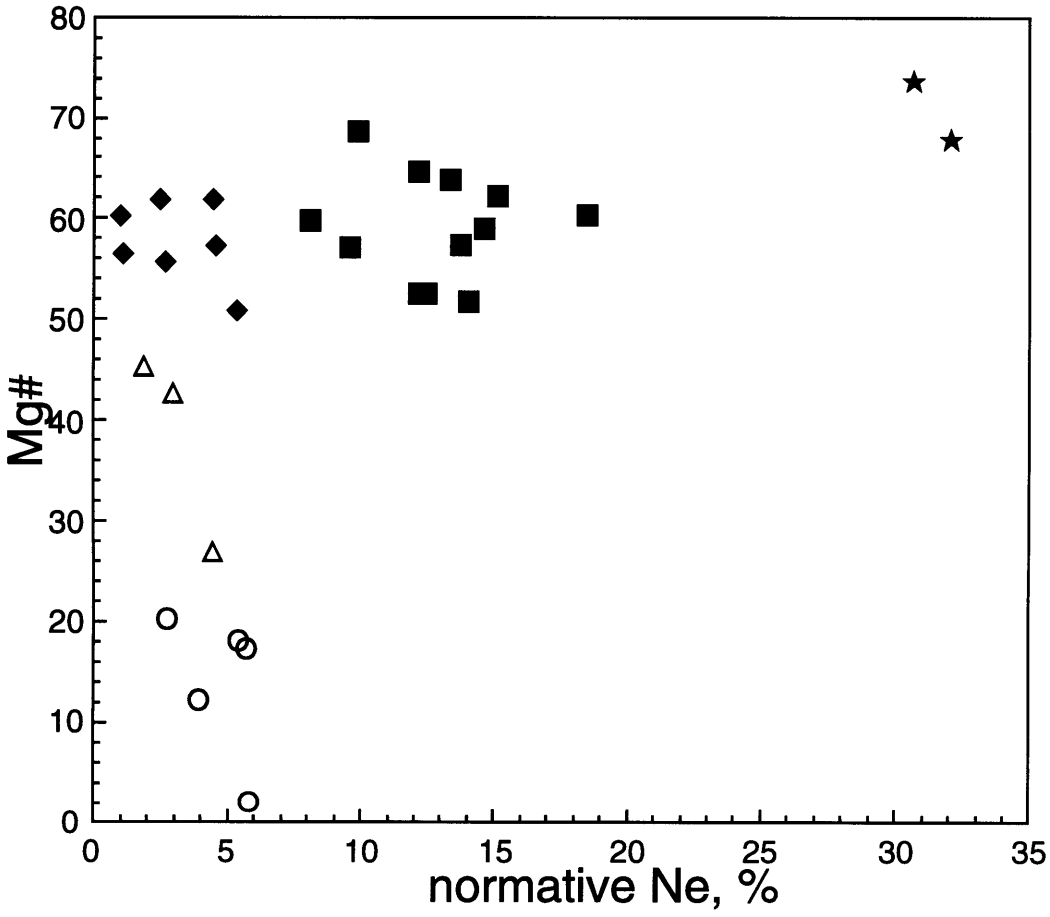

Figure 3.7

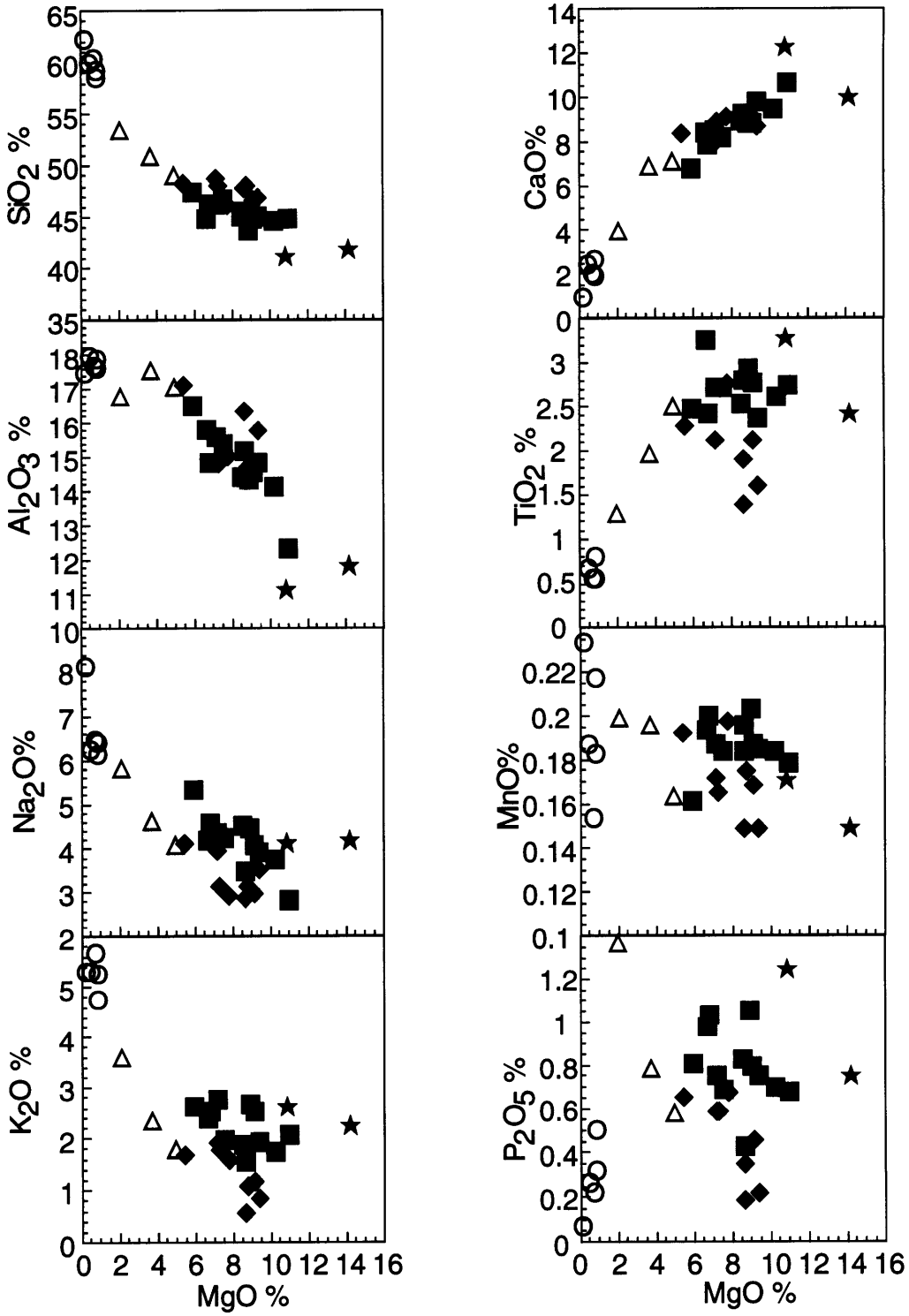

Figure 3.7 continued

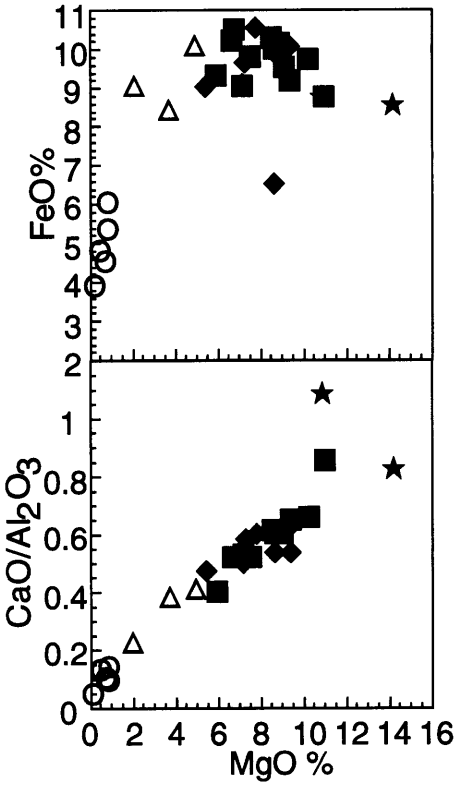

Figure 3.8

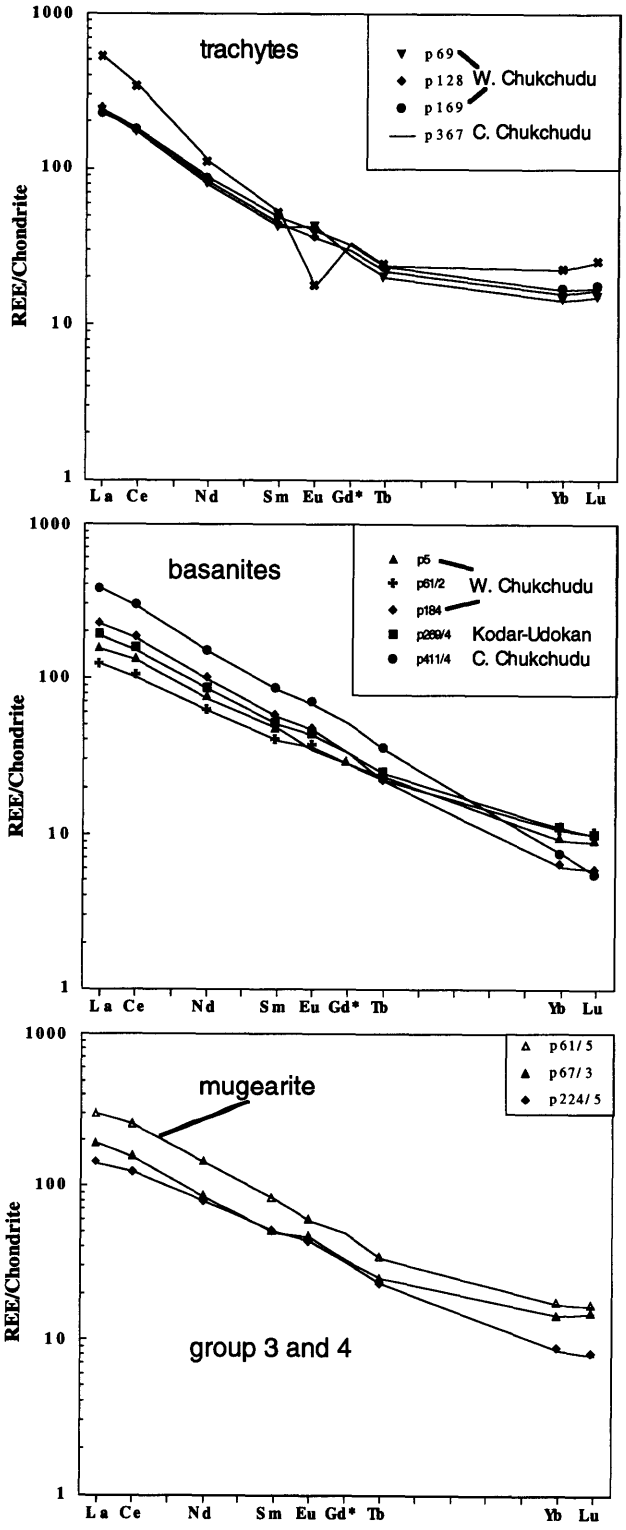
trachytes
p69
p128 W. Chukchudu
p169
p367 C. Chukchudu
basanites
p5
p61/2 W. Chukchudu
p184
p269/4 Kodar-Udokan
p411/4 C. Chukchudu
mugearite
p61/5
p67/3
p224/5
group 3 and 4
REE/Chondrite
1000
100
10
1
La Ce Nd Sm Eu Gd* Tb Yb Lu

Figure 3.9a

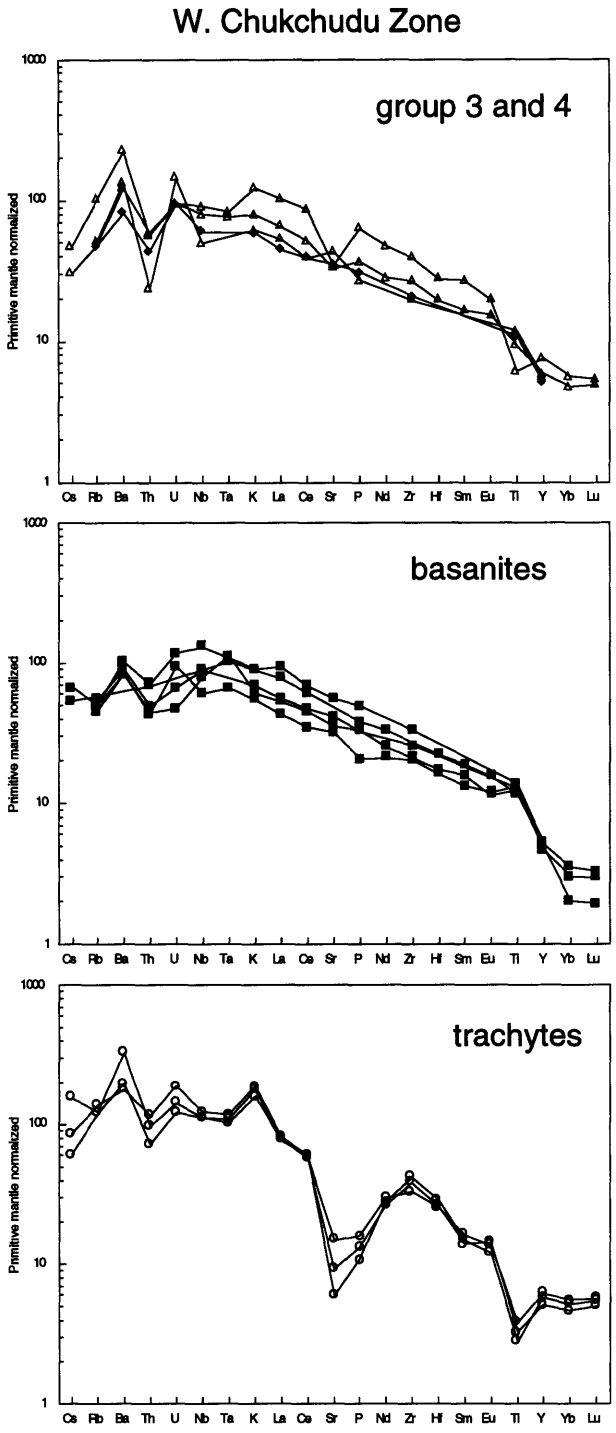
W. Chukchudu Zone
group 3 and 4
basanites
trachytes
Primitive mantle normalized
1000
100
10
1
Cs Rb Ba Th U Nb Ta K La Ce Sr P Nd Zr Hf Sm Eu Ti Y Yb Lu

Figure 3.9b

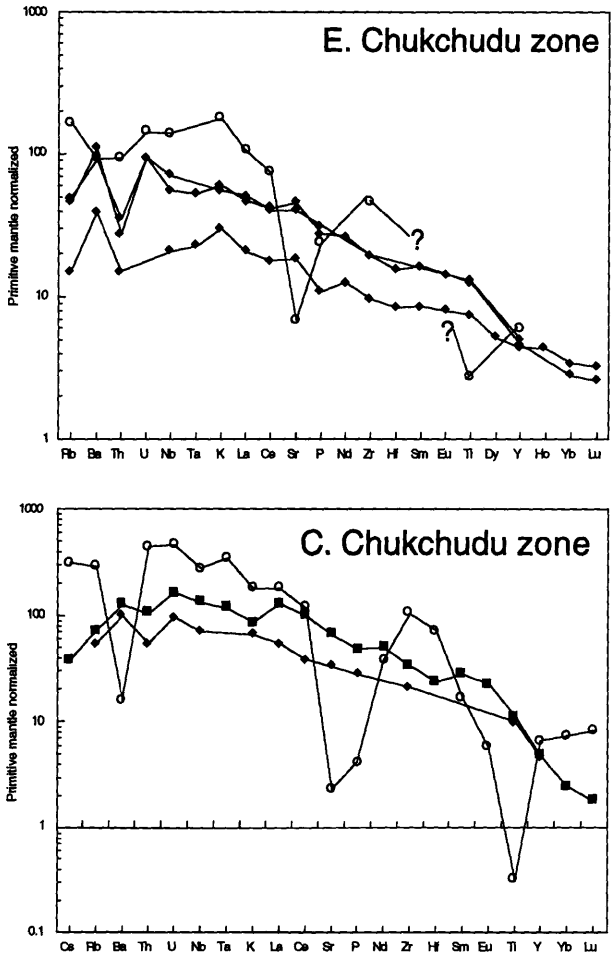
E. Chukchudu zone
Primitive mantle normalized
1000
100
10
1
Rb Ba Th U Nb Ta K La Ce Sr P Nd Zr Hf Sm Eu Ti Dy Y Ho Yb Lu
?
?
C. Chukchudu zone
Primitive mantle normalized
1000
100
10
1
0.1
Cs Rb Ba Th U Nb Ta K La Ce Sr P Nd Zr Hf Sm Eu Ti Y Yb Lu

Figure 3.9c

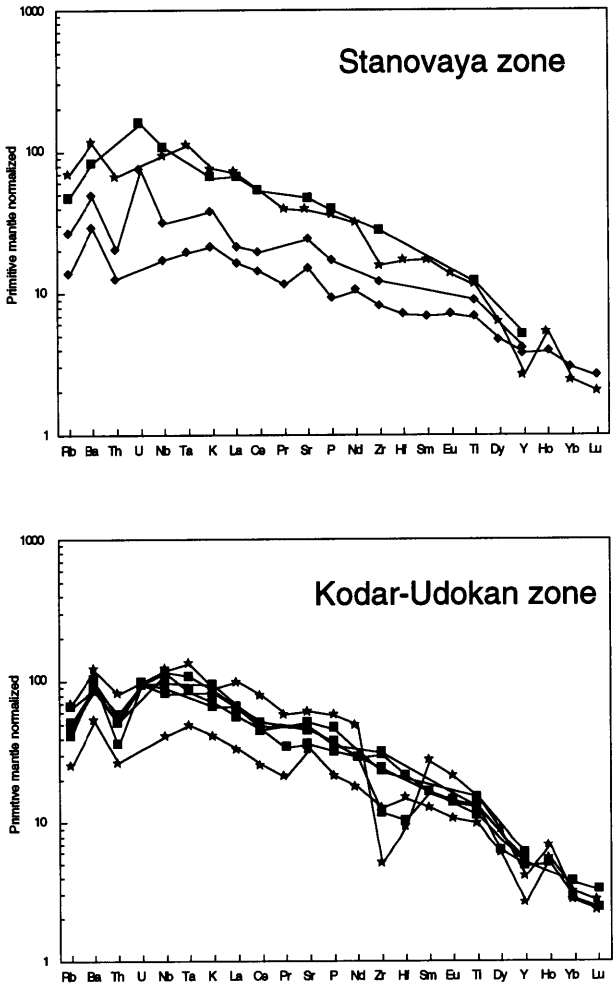
Stanovaya zone
Primitive mantle normalized
1000
100
10
1
Rb Ba Th U Nb Ta K La Ce Pr Sr P Nd Zr Hf Sm Eu Ti Dy Y Ho Yb Lu
Kodar-Udokan zone
Primitive mantle normalized
1000
100
10
1
Rb Ba Th U Nb Ta K La Ce Pr Sr P Nd Zr Hf Sm Eu Ti Dy Y Ho Yb Lu

Figure 3.10

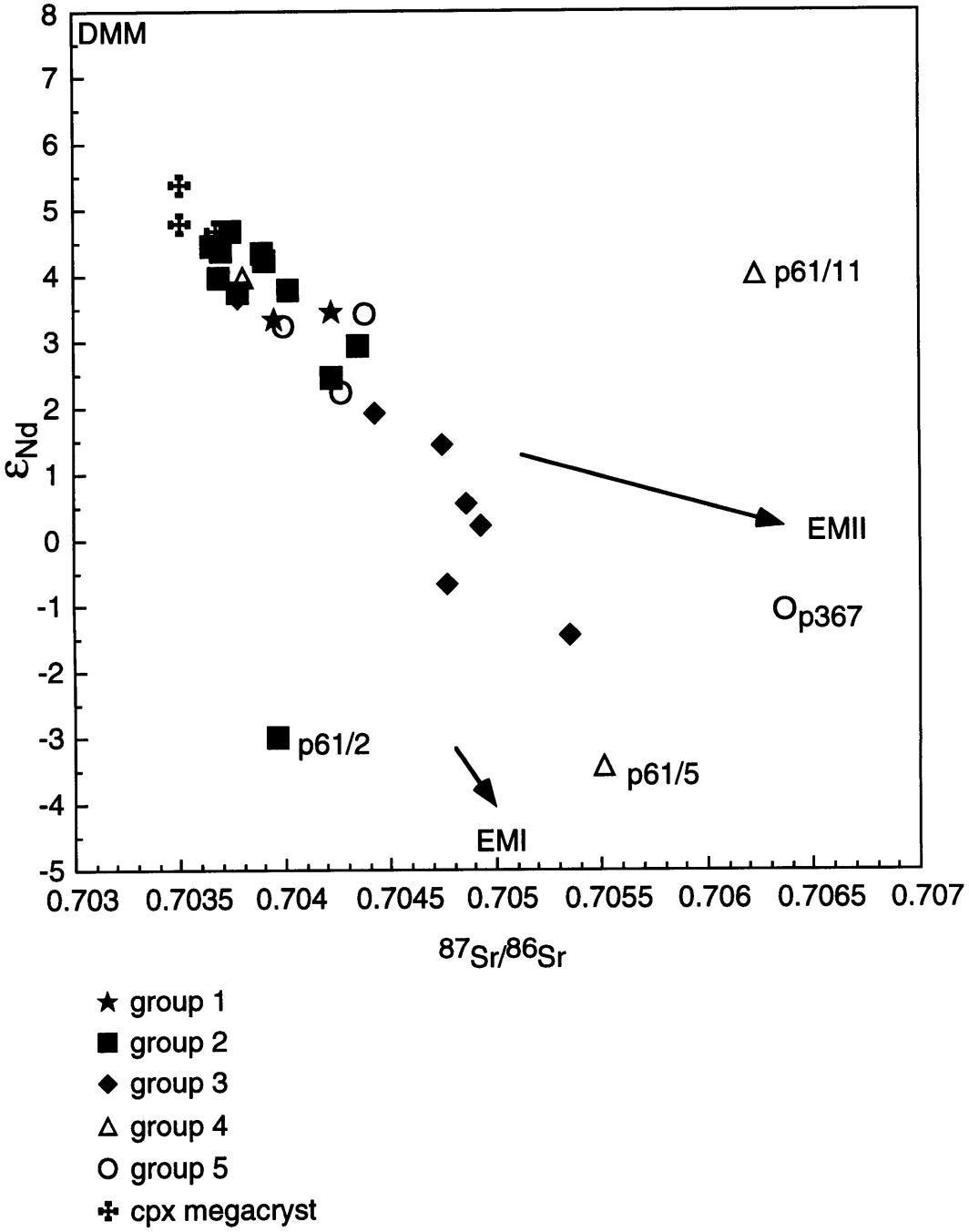
DMM
Δ p61/11
EMII
Op367
p61/2
Δ p61/5
EMI
εNd
87Sr/86Sr
8
7
6
5
4
3
2
1
0
-1
-2
-3
-4
-5
0.703
0.7035
0.704
0.7045
0.705
0.7055
0.706
0.7065
0.707
★ group 1
■ group 2
◆ group 3
Δ group 4
O group 5
✣ cpx megacryst

Figure 3.11

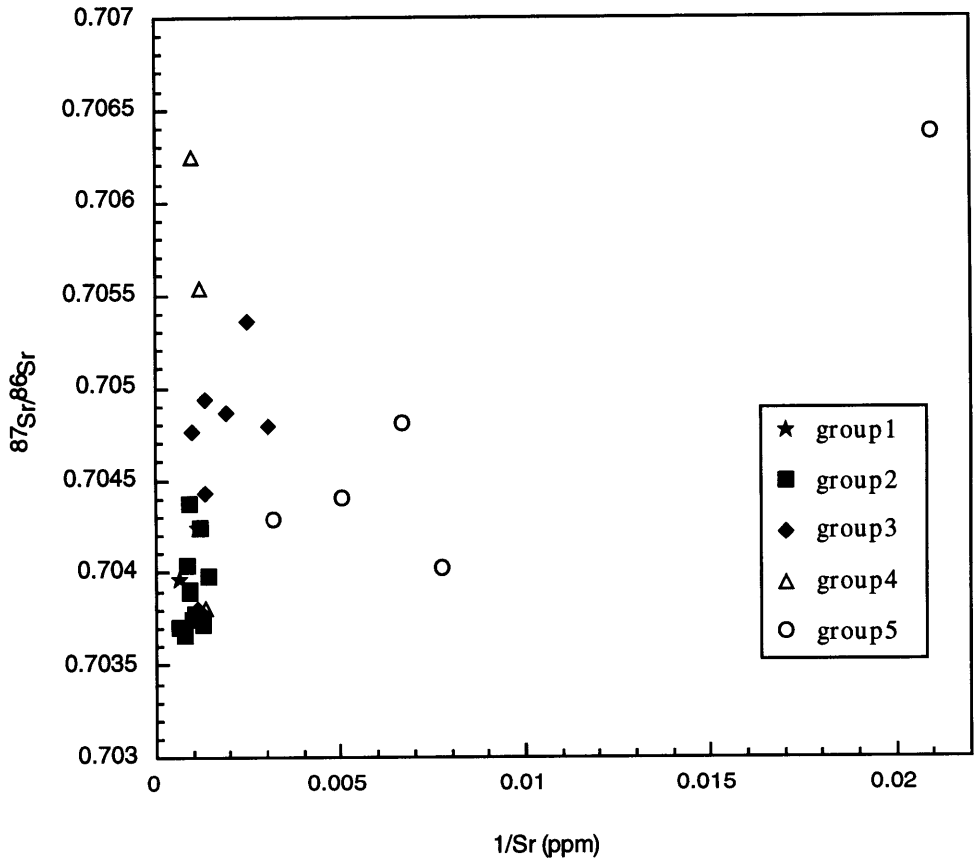
0.707
0.7065
0.706
0.7055
0.705
0.7045
0.704
0.7035
0.703
$^{87}Sr/^{86}Sr$
0
0.005
0.01
0.015
0.02
1/Sr (ppm)
group1
group2
group3
group4
group5

Figure 3.12

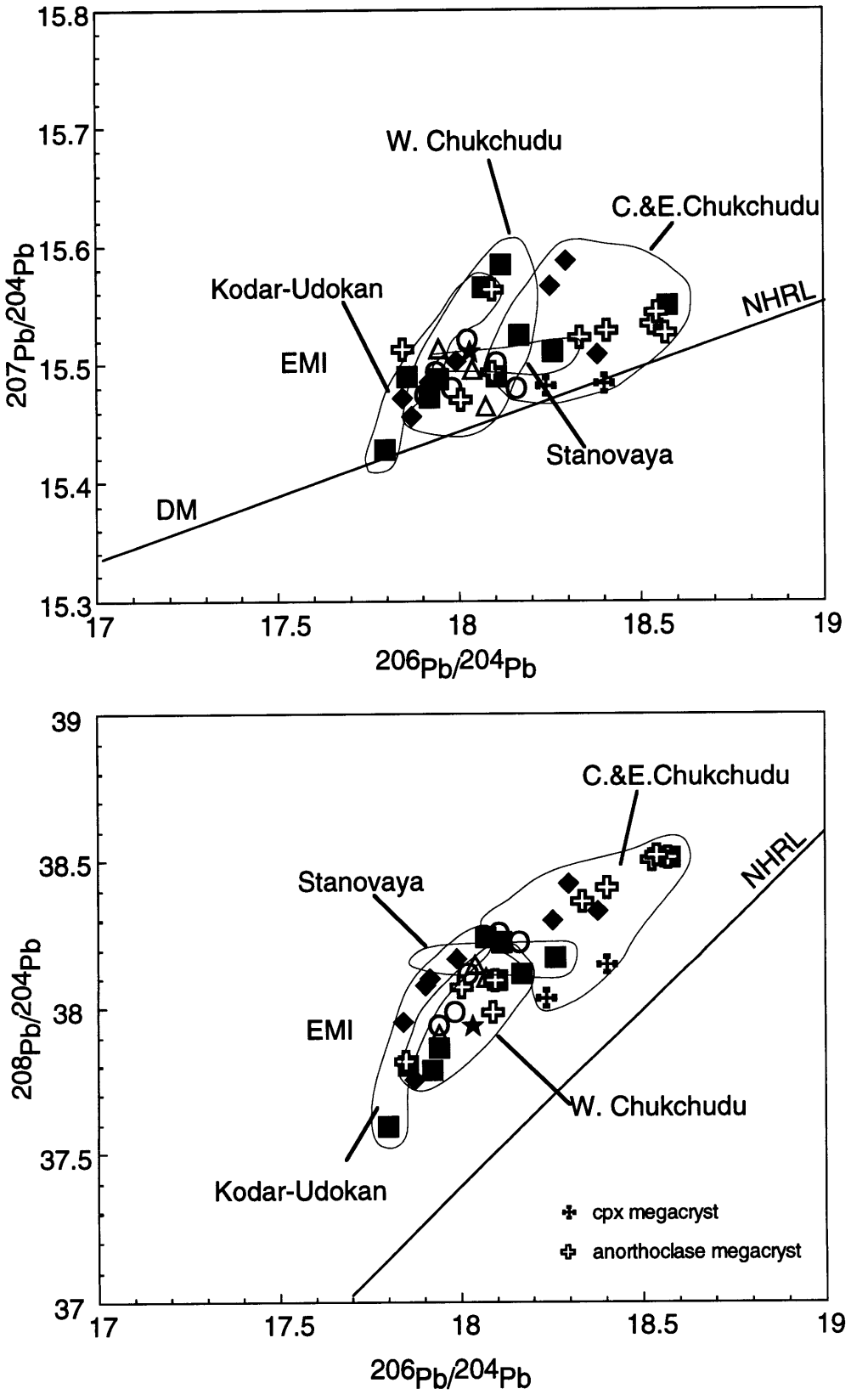
15.8
15.7
15.6
15.5
15.4
15.3
17
17.5
18
18.5
19
$^{207}Pb/^{204}Pb$
$^{206}Pb/^{204}Pb$
W. Chukchudu
C.&E.Chukchudu
Kodar-Udokan
EMI
NHRL
Stanovaya
DM
39
38.5
38
37.5
37
$^{208}Pb/^{204}Pb$
C.&E.Chukchudu
Stanovaya
NHRL
EMI
W. Chukchudu
Kodar-Udokan
cpx megacryst
anorthoclase megacryst

Figure 3.13

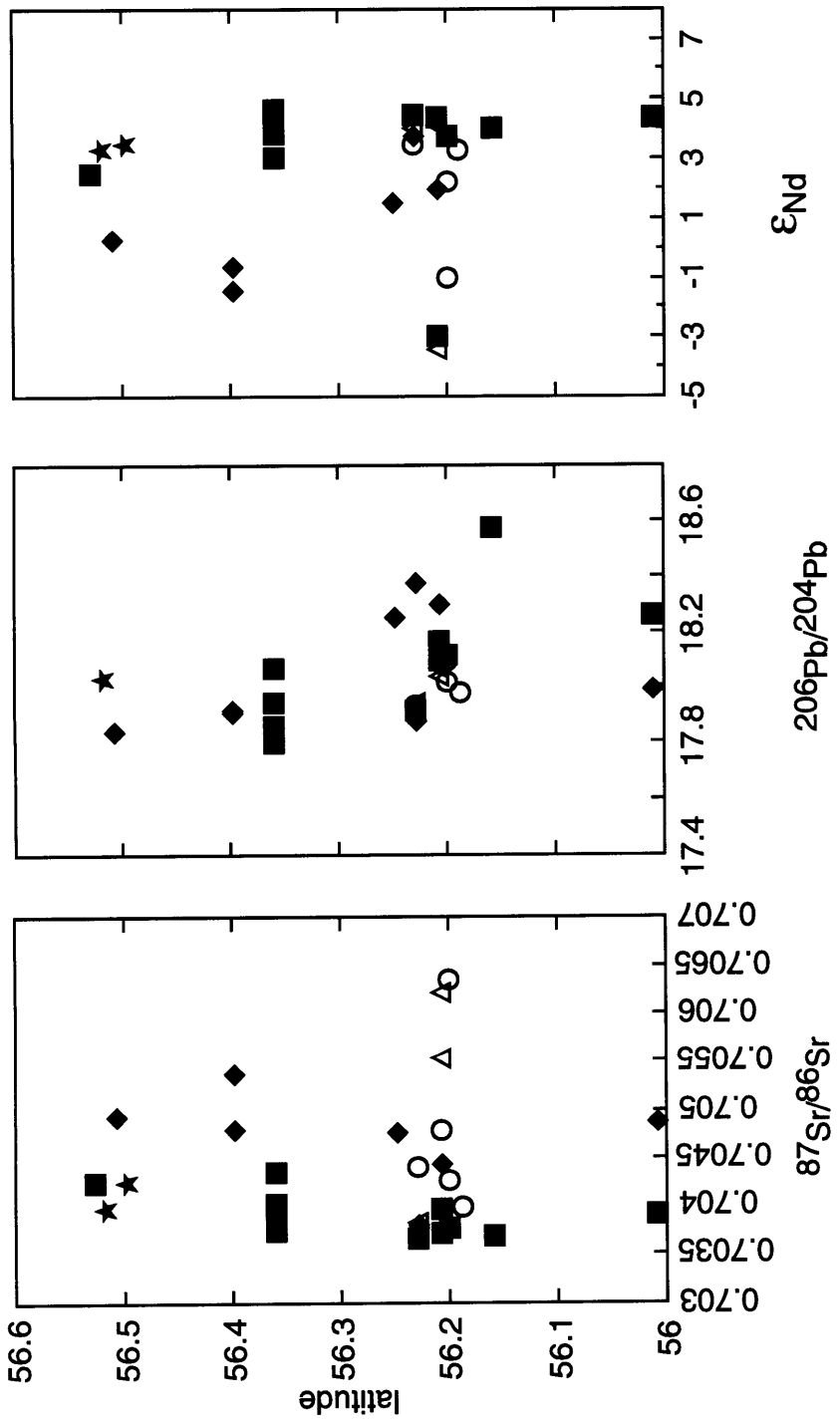
latitude
56.6
56.5
56.4
56.3
56.2
56.1
56
0.703
0.7035
0.704
0.7045
0.705
0.7055
0.706
0.7065
0.707
87Sr/86Sr
17.4
17.8
18.2
18.6
206Pb/204Pb
-5
-3
-1
1
3
5
7
εNd

Figure 3.14

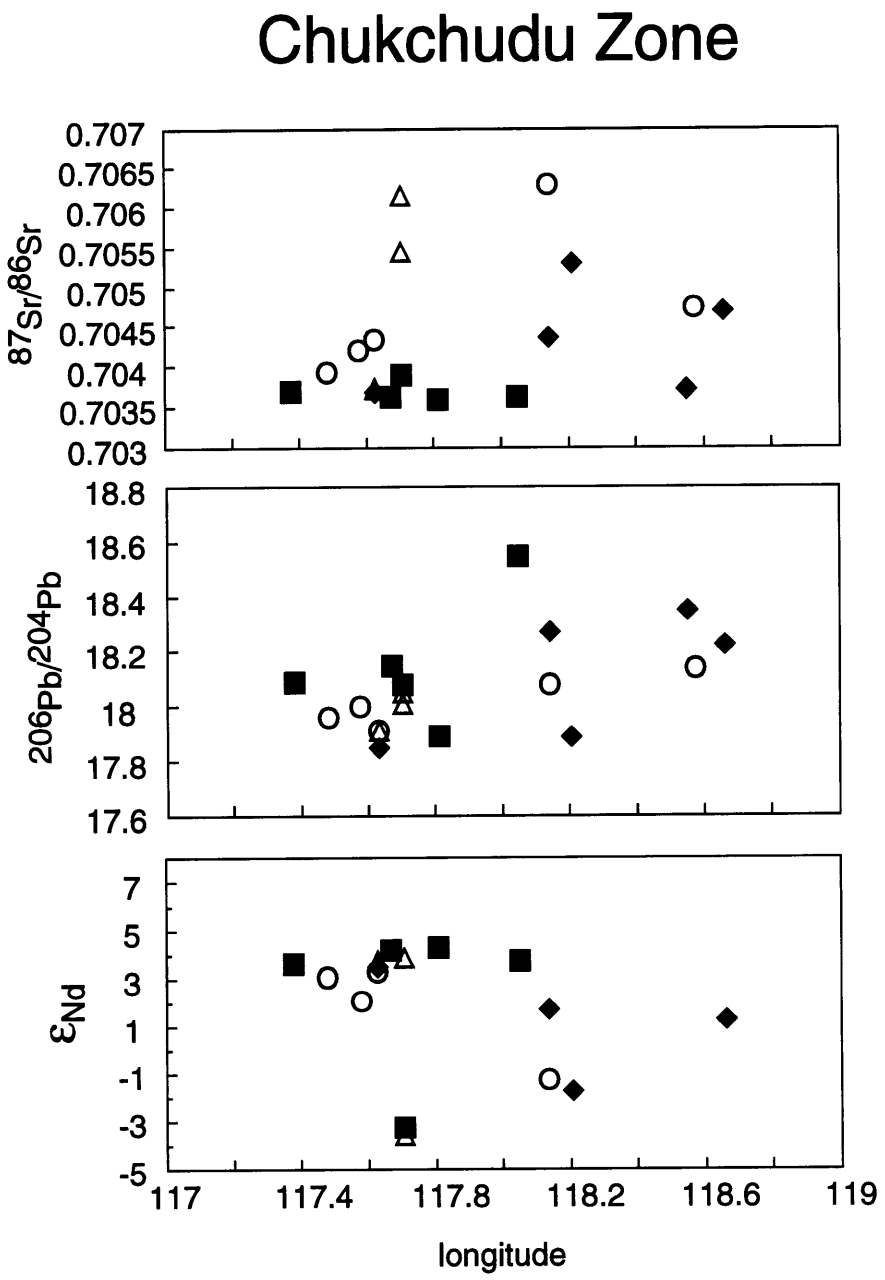
Chukchudu Zone
0.707
0.7065
0.706
0.7055
0.705
0.7045
0.704
0.7035
0.703
87Sr/86Sr
18.8
18.6
18.4
18.2
18
17.8
17.6
206Pb/204Pb
7
5
3
1
-1
-3
-5
εNd
117
117.4
117.8
118.2
118.6
119
longitude

Figure 3.15

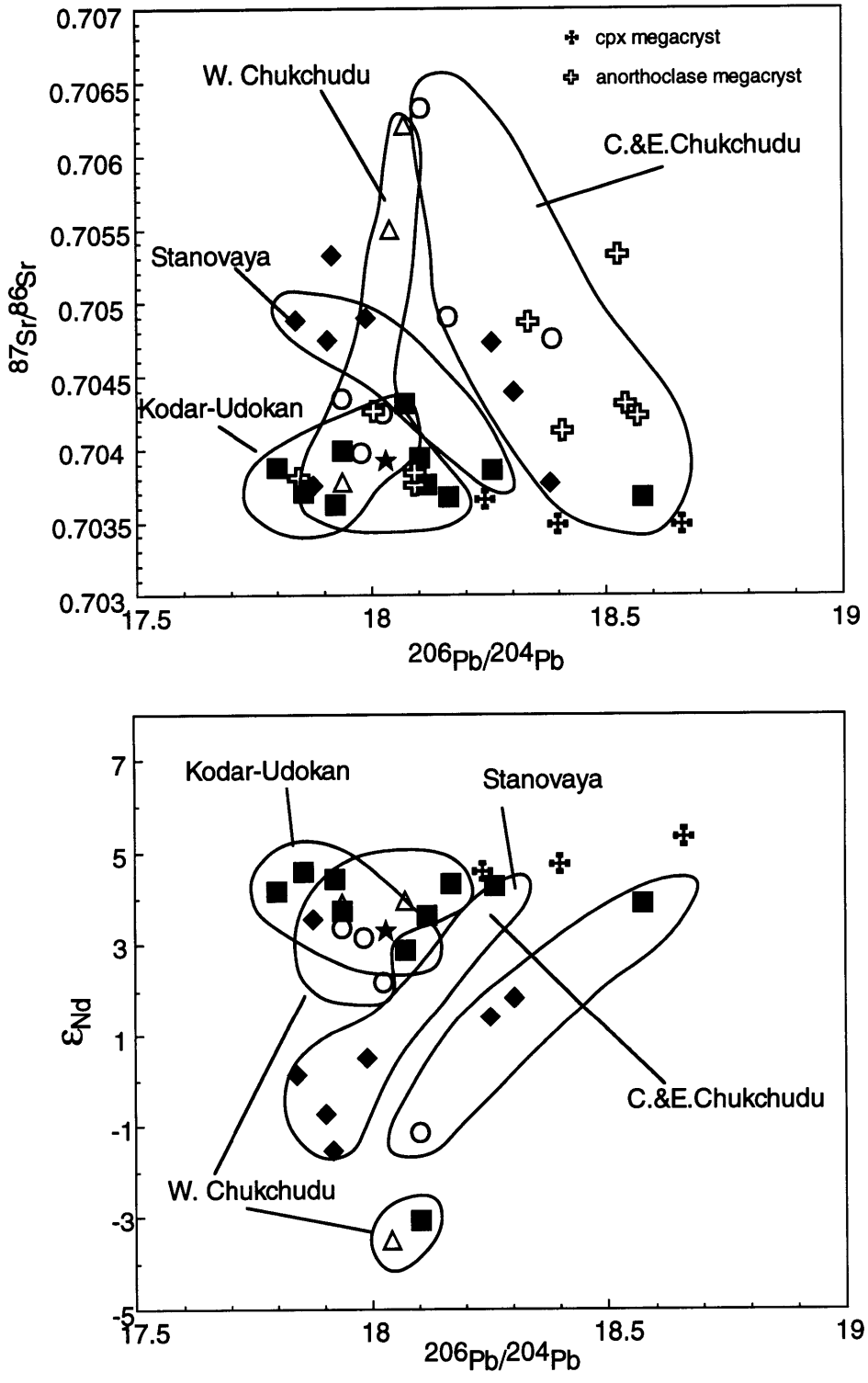
cpx megacryst
anorthoclase megacryst
W. Chukchudu
C.&E.Chukchudu
Stanovaya
Kodar-Udokan
0.707
0.7065
0.706
0.7055
0.705
0.7045
0.704
0.7035
0.703
$^{87}Sr/^{86}Sr$
17.5
18
18.5
19
$^{206}Pb/^{204}Pb$
Kodar-Udokan
Stanovaya
C.&E.Chukchudu
W. Chukchudu
7
5
3
1
-1
-3
-5
ε_{Nd}
17.5
18
18.5
19
$^{206}Pb/^{204}Pb$

Table 3.1a. Major (wt%) and trace element (ppm) abundances in UVF lavas

Map #	1	2	3	4	5	6	7	8	9	10	11	12	13	14	15	16	17
Sample	p69	p67/3	p68	p169	p128	p5	p61/2	p61/5	p61/11	p149	p184	p184/8	p269/2A	p269/4	p269/6	p269/7	p367
Group	5	4	3	5	5	2	2	4	4	2	2	2	2	2	2	2	5
Symbol	O	Δ	◆	O	O	■	■	Δ	Δ	■	■	■	■	■	■	■	O
SiO_2	58.43	50.83	48.16	58.99	60.85	44.68	45.71	52.66	48.89	46.51	47.35	43.38	45.35	44.74	46.09	44.89	61.91
TiO_2	0.69	1.98	2.32	0.83	0.61	2.64	2.82	1.29	2.54	2.73	2.49	2.95	2.41	2.81	2.72	3.28	0.07
Al_2O_3	17.53	17.53	17.13	17.89	17.85	14.15	15.16	16.52	17.02	15.31	16.43	14.25	14.90	14.54	15.50	15.78	17.43
Fe_2O_{3t}	6.25	11.09	11.89	7.09	6.07	12.77	13.19	11.68	13.23	12.83	12.26	13.20	12.17	12.52	11.82	13.36	5.24
MnO	0.18	0.20	0.19	0.18	0.16	0.18	0.18	0.20	0.16	0.18	0.16	0.20	0.19	0.19	0.19	0.19	0.23
MgO	0.38	3.57	5.32	0.78	0.58	10.10	8.44	1.88	4.75	7.38	5.72	8.69	9.25	8.93	6.94	6.45	0.05
CaO	2.53	7.01	8.51	2.80	2.13	9.57	9.33	4.03	7.17	8.25	6.88	8.83	9.94	8.95	8.57	8.49	1.04
Na_2O	6.12	4.68	4.21	6.19	6.55	3.79	3.58	5.77	4.13	4.27	5.35	4.48	4.00	4.14	4.37	4.24	8.10
K_2O	5.24	2.38	1.76	4.79	5.77	1.81	1.64	3.60	1.86	2.04	2.67	2.70	1.99	2.58	2.79	2.45	5.31
P_2O_5	0.28	0.80	0.67	0.34	0.24	0.71	0.44	1.36	0.58	0.70	0.81	1.05	0.77	0.80	0.76	0.98	0.09
LOI(%)	1.05	-0.16	-0.79	-0.04	0.14	-0.37	-0.33	0.42	-0.43	-0.31	-0.42	-0.36	-0.37	-0.37	-0.29	-0.51	0.06
TOTAL	98.68	99.88	99.36	99.83	100.94	100.03	100.16	99.39	99.89	99.87	99.68	99.36	100.59	99.80	99.45	99.60	99.54
Mg#	12	43	51	20	18	65	60	27	46	57	52	61	64	62	58	534	2
Rb	78.2	30.9	30.2	75.3	86.9	28.5	31.9	65.0	32.7	34.7	42.4	32.4	26.2	30.1	32.2	26.2	180.9
Sr	193	679	716	308	125	733	672	738	950	844	1029	1126	978	914	968	1047	48
Ba	2307	858	576	1391	1256	593	580	1550	933	630	812	717	683	597	640	696	112
Sc	3.4	11.5		4.1	4.0	21.5	21.4	4.7			10.4			19.5			1.5
V		100	152			211	205		136	168		208	208	210	195	211	
Cr	2	(35)	87	(1)	(5)	(265)	(202)	1	10	113	(48)	144	233	(209)	161	61	
Co	3.3	24.0		4.3	3.7	54.4	24.3	14.4			43.0			46.2			0.7
Ni	3	27	61	9	3	172	104	3	28	99	68	110	132	135	67	42	9
Zn	97	108	102	80	92	99	86	106	96	102	116	109	90	99	86	87	151
Ga	22	23	21	23	24	21	23	20	22	20	26	23	21	21	21	20	27
Y	23	27	23	28	26	21	23	34	25	24	16	24	23	23	24	27	31
Zr	433	294	230	374	468	234	225	434	216	288	315	370	271	338	351	257	1163
Hf	8.03	5.95		7.88	9.03	5.34	4.99	8.41			6.73			6.67			22.55
Nb	78.8	57.1	42.8	79.7	88.7	57.4	43.2	65.4	35.5	62.8	70.8	93.0	63.1	82.2	69.3	57.8	198.4
Ta	4.47	3.15		4.22	4.81	4.64	2.68	3.39			4.16			4.40			14.13
Th	8.23	4.99		6.16	9.75	3.73	3.70	4.83			5.81			4.33			37.38
La	54.4	44.7	(30.4)	53.1	56.0	36.0	29.1	70.2	(36.6)	(37.9)	52.7	(63.8)	(45.2)	44.2	(46.3)	(43.4)	123.7
Ce	102.3	92.8	(69.3)	106.3	106.6	79.0	61.3	153.2	(69.0)	(84.3)	109.0	(120.8)	(90.7)	91.9	(84.8)	(81.5)	207.4
Nd	35.4	38.2		39.8	37.5	33.7	28.2	64.2			44.8			38.8			50.7
Sm	6.16	7.26		7.18	6.53	7.01	5.85	11.91			8.29			7.43			7.65
Eu	2.40	2.59		2.25	2.00	1.92	2.00	3.32			2.61			2.39			0.97
Tb	0.72	0.90		0.85	0.79		0.81	1.22			0.79			0.89			0.86
Yb	2.29	2.31		2.72	2.54	1.49	1.73	2.75			1.01			1.80			3.68
Lu	0.37	0.36		0.42	0.41	0.22	0.24	0.40			0.14			0.24			0.61

Notes: Abundances of Sc, some Cr (shown in parentheses), Co, Hf, Ta, Th and REE determined by neutron activation at M.I.T. All other data obtained by X-ray fluorescence at the University of Massachusetts, Amherst, including La and Ce shown in parentheses. Mg# = 100*atomic Mg/(Mg + Fe^{2+}), calculated with FeO = .15* Fe_2O_{3total} .

Table 3.1a Major (wt%) and trace element (ppm) abundances in UVF lavas continued

Map #	18	19	20	21	22	23	24
Sample	p411/4	p376	p225/6	p224/5	p228	p270/3A	p270/4
Group	2	3	5	3	3	2	3
Symbol	■	◆	O	◆	◆	■	◆
SiO_2	45.84	48.77	58.33	47.87	46.02	44.80	48.14
TiO_2	2.42	2.15	0.59	2.73	2.78	2.53	1.93
Al_2O_3	14.68	15.56	17.54	14.77	14.91	14.30	14.65
Fe_2O_{3t}	13.67	11.92	8.00	12.56	13.72	13.45	12.94
MnO	0.20	0.17	0.22	0.17	0.20	0.19	0.18
MgO	6.54	6.97	0.72	7.11	7.49	8.32	8.50
CaO	7.82	8.07	2.00	8.94	9.23	8.96	9.22
Na_2O	4.57	4.02	6.46	3.19	3.00	4.52	3.22
K_2O	2.55	1.97	5.29	1.80	1.64	1.93	1.12
P_2O_5	1.03	0.60	0.51	0.60	0.68	0.83	0.37
LOI(%)	0.92	-0.48	0.16	0.29	0.30	0.05	-0.67
TOTAL	100.25	99.72	99.81	100.02	99.96	99.89	99.60
Mg#	53	58	17	57	56	59	60
Rb	46.2	34.6	105.4	29.2	31.1	29.6	16.5
Sr	1382	691	147	950	826	984	494
Ba	888	708	646	760	642	581	335
Sc	10.1			16.7			
V	146	152		183	211	173	174
Cr	(97)	156	2	(149)	162	157	202
Co	42.7			46.3			
Ni	95	98	1	108	107	141	146
Zn	189	104	101	116	123	132	104
Ga	27	21	20	21	22	25	22
Y	22	22	27	21	23	23	18
Zr	373	239	524	217	223	309	136
Hf	7.30			4.79			
Nb	94.9	51.0	98.7	39.6	50.8	76.3	22.3
Ta	4.83			2.17			
Th	8.91			2.36			
La	88.6	(37.8)	(72.0)	32.7	(35.3)	(45.8)	(14.9)
Ce	176.0	(69.1)	(131.4)	74.4	(72.1)	(93.6)	(34.9)
Nd	67.4			35.7			
Sm	12.37			7.42			
Eu	3.83			2.44			
Tb	1.26			0.84			
Yb	1.23			1.38			
Lu	0.13			0.19			

Notes: Abundances of Sc, some Cr (shown in parentheses), Co, Hf, Ta, Th and REE determined by neutron activation at M.I.T. All other data obtained by X-ray fluorescence at the University of Massachusetts, Amherst, including La and Ce shown in parentheses. Mg# = 100*atomic Mg/(Mg + Fe^{2+}), calculated with FeO = .15* Fe_2O_{3total} .

Table 3.1b Major (wt%) element abundances in UVF lavas.

Map #	25	26	27	28	29	30
Sample	U-94-9	U-94-10A	U-94-19	U-94-38	U-94-39	U-94-42
Group	3	3	1	1	3	2
Symbol	◆	◆	★	★	◆	■
SiO_2	46.82	48.06	42	40.97	46.82	45.1
TiO_2	1.63	1.45	2.46	3.3	2.15	2.78
Al_2O_3	15.75	16.4	11.9	11.15	14.8	12.4
Fe_2O_3	2.04	5.53	2.97	3.52	2.41	2.98
FeO	10.08	6.59	8.64	8.8	10	8.85
MnO	0.15	0.15	0.15	0.17	0.17	0.18
MgO	9.21	8.5	13.99	10.64	9	10.85
CaO	8.77	9.12	10.07	12.29	9.3	10.8
Na_2O	3.6	2.95	4.26	4.15	3.1	2.93
K_2O	0.91	0.65	2.29	2.66	1.24	2.12
P_2O_5	0.24	0.2	0.76	1.25	0.47	0.69
LOI(%)	0.13	0.1		0.17	0.13	0.07
H_2O+	0.64	0.73	0.76	0.63	0.46	
TOTAL	99.97	100.43	100.25	99.7	100.05	99.75
Mg#	62	70	74	68	62	69

Notes: Major elements determined by XRF at the Institute of the Earth's Crust, Irkutsk.
Mg# = 100*atomic Mg/(Mg + Fe^{2+}), calculated with FeO = .15* Fe_2O_{3total} .

Table 3.2. Sr, Nd and Pb isotopic ratios of UVF lavas

SAMPLE	LOCATION	$^{87}Sr/^{86}Sr$	±2σ	$^{143}Nd/^{144}Nd$	±2σ	$\varepsilon_{Nd}(0)$	±2σ	$^{206}Pb/^{204}Pb$	$^{207}Pb/^{204}Pb$	$^{208}Pb/^{204}Pb$
p5	W. Chukchudu	0.70370	±0.00001	0.512863	±0.000010	4.40	±0.20	18.161	15.527	38.131
p61/2	W. Chukchudu	0.70396	±0.00001	0.512484	±0.000005	-3.00	±0.10	18.095	15.492	38.105
p61/5	W. Chukchudu	0.70551	±0.00001	0.512462	±0.000009	-3.42	±0.18	18.034	15.498	38.161
p61/11	W. Chukchudu	0.70623	±0.00001	0.512845	±0.000008	4.03	±0.16	18.066	15.468	38.117
p67/3	W. Chukchudu	0.70380	±0.00001	0.512842	±0.000007	3.98	±0.14	17.935	15.516	37.924
p68	W. Chukchudu	0.70377	±0.00001	0.512827	±0.000007	3.69	±0.14	17.868	15.459	37.774
p69	W. Chukchudu	0.70438	±0.00001	0.512814	±0.000008	3.43	±0.16	17.932	15.497	37.953
p128	W. Chukchudu	0.70400	±0.00001	0.512804	±0.000007	3.23	±0.14	17.978	15.483	37.998
p149	W. Chukchudu	0.70377	±0.00001	0.512830	±0.000014	3.75	±0.28	18.109	15.586	38.238
p169	W. Chukchudu	0.70427	±0.00001	0.512754	±0.000007	2.26	±0.14	18.019	15.524	38.130
p184/8	W. Chukchudu	0.70365	±0.00001	0.512868	±0.000008	4.49	±0.16	17.915	15.475	37.801
p224/5	E. Chukchudu	0.70475	±0.00001	0.512714	±0.000010	1.48	±0.20	18.246	15.569	38.319
p225/6	E. Chukchudu	0.70479	±0.00001					18.156	15.483	38.241
p228	E. Chukchudu	0.70379	±0.00001					18.375	15.511	38.344
p269/2A	Kodar-Udokan	0.70435	±0.00001	0.512790	±0.000012	2.96	±0.24	18.064	15.568	38.252
p269/4	Kodar-Udokan	0.70374	±0.00001	0.512878	±0.000008	4.68	±0.16	17.851	15.493	37.815
p269/6	Kodar-Udokan	0.70390	±0.00001	0.512854	±0.000009	4.22	±0.18	17.792	15.430	37.611
p269/7	Kodar-Udokan	0.70402	±0.00001	0.512833	±0.000008	3.80	±0.16	17.935	15.491	37.872
p270/3A	Stanovaya	0.70389	±0.00001	0.512861	±0.000007	4.35	±0.14	18.253	15.513	38.185
p270/4	Stanovaya	0.70486	±0.00001	0.512668	±0.000013	0.59	±0.26	17.985	15.506	38.186
p367	C. Chukchudu	0.70636	±0.00001	0.512584	±0.000008	-1.05	±0.16	18.098	15.504	38.273
p376	C. Chukchudu	0.70442	±0.00001	0.512737	±0.000008	1.94	±0.16	18.294	15.591	38.441
p411/4	C. Chukchudu	0.70369	±0.00001	0.512842	±0.000008	3.98	±0.16	18.568	15.552	38.520
U-94-9	E. Chukchudu	0.70535	±0.00001	0.512564	±0.000008	-1.45	±0.16	17.910	15.488	38.115
U-94-10A	Stanovaya	0.70478	±0.00001	0.512605	±0.000006	-0.65	±0.12	17.900	15.478	38.093
U-94-19	Stanovaya	0.70423	±0.00001	0.512814	±0.000013	3.44	±0.26			
U-94-38	Kodar-Udokan	0.70395	±0.00001	0.512810	±0.000005	3.36	±0.10	18.025	15.514	37.959
U-94-39	Kodar-Udokan	0.70493	±0.00001	0.512651	±0.000006	0.25	±0.12	17.836	15.475	37.971
U-94-42	Kodar-Udokan	0.70422	±0.00001	0.512763	±0.000006	2.44	±0.12			
U-95-92/1	Stanovaya	0.70445	±0.00001	0.512774	±0.000006	2.64	±0.12	17.973	15.501	38.013
U-95-92/2	Stanovaya	0.70539	±0.00001	0.512610	±0.000010	-0.54	±0.20	17.903	15.511	38.160
U-95-93	Stanovaya	0.70541	±0.00001	0.512538	±0.000007	-1.94	±0.14			

Notes: Sr data are normalized to $^{86}Sr/^{88}Sr = 0.1194$ and corrected for mass fractionation using an exponential law. Replicate analyses of NBS-987 Sr yield $^{87}Sr/^{86}Sr = 0.710240 \pm 0.000016$ (2σ). Nd data are normalized to $^{146}Nd/^{144}Nd = 0.7219$ and corrected for mass fractionation using an exponential law. Replicate analyses of La Jolla Nd yield $^{143}Nd/^{144}Nd = 0.511845 \pm .000011$ (2σ). $\varepsilon_{Nd}(0)$ is calculated with $^{143}Nd/^{144}Nd_{CHUR} = 0.512638$. Based on replicate analyses of NBS-981, Pb is corrected by 0.12%/mass unit to account for fractionation.

CHAPTER 4

GEOCHEMICAL AND ISOTOPIC CONSTRAINTS ON THE ORIGIN OF VOLCANISM AT THE VITIM VOLCANIC FIELD, BAIKAL RIFT ZONE, SIBERIA

ABSTRACT

The Cenozoic Vitim volcanic field, located ~200 km southeast of Lake Baikal, comprises lavas ranging from alkaline basalt to basanite, hawaiite, and basaltic andesite. This region is well-known for its abundance of upper mantle xenoliths and megacrysts. Lavas have a restricted range in Mg# from 58 to 64, with MgO from 4 to 10%. Trends in major element and compatible element abundances are best explained by partial melting of an inhomogeneous source followed by fractional crystallization of clinopyroxene, olivine, and plagioclase, as well as minor amounts of an Fe-Ti-oxide phase and possibly garnet. Incompatible element abundances of the Vitim lavas are overall quite similar to those reported for ocean island basalts, as well as other occurrences of continental alkalic magmas. Sr and Nd isotopic ratios are also quite similar to the range reported for OIB, with $^{87}Sr/^{86}Sr$ from 0.70374 to 0.70494 and ε_{Nd} from +2.3 to + 7.2. Pb isotopic ratios of the Vitim lavas all lie above the Northern Hemisphere Reference Line (NHRL) of Hart (1984), and include the least radiogenic Pb values measured for the entire BRZ, with $^{206}Pb/^{204}Pb$ from 17.25 to 18.17, $^{207}Pb/^{204}Pb$ from 15.48 to 15.54, and $^{208}Pb/^{204}Pb$ from 37.22 to 38.20. Vitim clinopyroxene megacrysts have a similar range in isotopic composition. Based on the isotopic, major element, and trace element data, we propose

that Vitim lavas originated by variable, small degrees of partial melting of an isotopically heterogeneous source, followed by small amounts of fractional crystallization of clinopyroxene, garnet, feldspar, and Fe-Ti-oxides before their emplacement. Major and trace element data do not seem to reflect significant amounts of crustal contamination. The very unradiogenic Pb isotopic signatures could possibly be the result of crustal contamination, although we favor their being representative of an EM-I like mantle component.

INTRODUCTION

The Vitim volcanic field, located ~200 km southeast of Lake Baikal along the upper Vitim River, forms one of the three major regions of Cenozoic volcanism associated with the Baikal Rift Zone (BRZ), Siberia (Fig. 4.1). As in the other BRZ volcanic fields, volcanism of the Vitim field ranges in age from Miocene to Holocene (Kiselev, 1987). The BRZ has an estimated total volume of volcanic rocks less than 6000 km^3 (Logatchev, 1993). With an area of ~7000 km^2, the Vitim field is the largest area of volcanism in the BRZ. Compositions of lavas are also typical of the BRZ, ranging from alkali olivine basalt to hawaiite and basanite. Other regions of similar Cenozoic volcanism extend south into Mongolia (Tariat and Dariganga volcanic fields), and occur throughout China (e.g., studies of Song et al., 1990; Basu et al., 1991; Menzies et al., 1993; Peng et al., 1986)

The Vitim volcanic field has received much attention due to the abundance of mantle xenoliths, especially rare garnet peridotite xenoliths thought to come from the spinel-garnet transition zone (40 - 90 km) (Ashchepkov et al., 1989; Ionov et al., 1992,

1993, 1994). Megacrysts of clinopyroxene, anorthoclase, garnet, biotite, amphibole, and ilmenite also occur in the lavas (Ionov et al., 1993; Harris et al., in prep.). By comparison, although the alkaline host lavas of the Vitim volcanic field have been studied by Russian scientists for many years (e.g., Esin, 1995; Kovalenko et al., 1990; Gladikh, 1996; Rasskazov and Batyrmurzaev, 1985; Rasskazov, 1993, 1994), they have not been as comprehensively studied and reported in the non-Russian literature. This study presents new major, trace element, and isotopic (Sr, Nd, Pb) data for 25 samples from the Vitim volcanic field.

GEOLOGIC BACKGROUND

The Baikal Rift Zone is one of the world's major continental rifts, extending almost 1800 km from southwest to northeast along a suture between the Archean Siberian shield and younger Paleozoic accreted terranes (Fig. 4.1) The BRZ comprises 13 major rift basins, the two largest of which form Lake Baikal (636 km long, 40 - 50 km wide), the world's deepest (1637 max. depth) freshwater lake, containing ~20% (23,000 km^3) of the world's freshwater resources (Logatchev, 1993). Rift depressions contain fluvial, proluvial, lacustrine, palustrine, glacial, fluvioglacial, and eolian sediments of Oligocene to Recent age (Logatchev, 1993). Seismic imaging of Lake Baikal has revealed that the South Baikal basin may contain up to 8500m of sediments (Hutchinson et al., 1992).

Most of the volcanic regions of the BRZ and surrounding regions correspond to broad domal uplifts (Sayan-Baikal, Barguzin-Ikat, Khangai, Khentei). However, unlike the region of volcanism on the western edge of the BRZ (including the Dzhida, Tunka,

Oka, and Tuva fields) which lies within the Sayan-Baikal domal uplift, or the Udokan Volcanic Field on the eastern edge of the BRZ which lies within the Barguzin-Ikta domal uplift, the Vitim volcanic field occurs just outside the 1500 m contour of the Bargunzin-Ikat domal uplift (Fig. 4.1) (Rasskazov, 1994; Kiselev, 1987). The domal uplifts are areas of high elevation (up to 3500 m) which roughly correspond to a region of anomalous low-velocity mantle thought to represent hot, upwelling asthenosphere (Kiselev and Popov, 1992). Gao et al. (1994) showed that the low-velocity region is closest to the surface beneath the axis of the rift, but asymmetrically dips off to the southeast. Beneath the Vitim highlands, the low-velocity mantle is estimated to be 80 - 100 km below the Moho (Zorin et al., 1989). The thickness of the crust and depth to the anomalous mantle, combined with the position of the Vitim volcanic field more than 100 km from any rift depression, raises many questions about the origin of Vitim magmatism. Although the other areas of BRZ volcanism are closer to rift depressions and faults, they are also not spatially related to any rift structures. The Tunka Basin in the western BRZ is one exception, since volcanic flows are found intercalated with sediments within the depression. Volcanic flows are noticeably absent from the Lake Baikal basins. The relatively low volume of volcanism for a rift of its size (~6000 km^3, an order of magnitude less than the Rio Grande Rift), and great distance from any plate boundaries, has lead to continuing controversy over the origin of the rift (Lipman et al., 1989; Logatchev et al., 1983). A variety of driving mechanisms for rifting have been proposed, including: one to many "active" plumes beneath the rift (Logatchev and Zorin, 1987, 1992; Rasskazov, 1994; Esin et al., 1995), "passive" response to far-field stresses related to the India-

Eurasia collision (e.g., Molnar and Tapponnier, 1975, 1977; Zonenshain and Savostin, 1981), or a more complex combination of the two end-members (e.g., Dobretsov et al., 1996; Delvaux et al., 1995).

GEOLOGIC SETTING AND SAMPLES

The samples included in this study come from areas in both the western (Dzhilinda basin) and eastern (Bol. Amalat River) part of the Vitim volcanic field (Fig. 4.2). A number of samples come from a 286 m deep drill core taken near Lake Mukhal in the Dzhilinda River basin in the western volcanic field, obtained by Rasskazov and colleagues. This drill core (#82) encountered flows of alkali olivine basalt, subalkaline basalt, and basanite intercalated with sediments of siltstone, gravel, and sand. The core is well-described in Rasskazov and Batyrmurzaev (1985) and Rasskazov (1993). Figure 4.3a is a simplified version of a cross-section through the Dzhilinda basin including the drill core analyzed in this study. Rasskazov and Batyrmurzaev (1985) dated several volcanic horizons within this drill core by K-Ar and obtained a range in age from ~14 Ma at the bottom to ~9.6 Ma near the top (data listed in Table 4.1).

In addition to the 82 drill core, a sample from 13 m depth in core 417 (C417/1), and several other western Vitim samples are included in this study (p586/2, p597, p600/1, and p600/2). In the eastern part of the field, samples of the Miocene flows along the Bol. Amalat River, and Dzhilinda River (Fig. 4.3b) as well as Miocene flows from along the road from Romanovka were collected. Samples of flows from the Pleistocene Kandidushka and Yaksha volcanoes were also included in this study.

SAMPLE PREPARATION AND ANALYTICAL TECHNIQUES

All samples were prepared by first crushing to gravel size with a hammer, while wrapped in heavy plastic to avoid contamination with metal from the hammer. The gravel was then ultrasonically cleaned in deionized water to remove fine particles, followed by drying in an oven. Dried samples were carefully examined and the freshest, most inclusion-free fragments were chosen for powdering in an alumina ceramic shatterbox.

Major element abundances were determined by X-ray fluorescence (XRF) at the University of Massachusetts at Amherst according to the methods described by Rhodes (1983). Selected samples were analyzed for trace element abundances, including rare earth elements (REE), by inductively coupled plasma mass spectrometry (ICP-MS) on the Fisons Plasma Quad 4+S at the Massachusetts Institute of Technology. 100 mg of whole-rock powder was dissolved in a two step HF-HNO_3-HCl process in Teflon beakers, following a procedure modified after Eggins et. al (1997). After complete dissolution and dilution to 200 mL, the samples were spiked with a mixed solution of Se, In and Bi as internal drift correction standards. Solutions of the whole-rock samples were introduced into the plasma by standard nebulization using a peristaltic pump with a sample uptake rate of 0.75 ml/min, a nebulizer gas flow of 0.75 L/min, auxiliary gas flow of 0.9 L/min, and a coolant gas flow of 14 L/min. Using an autosampler, up to 44 samples were analyzed during each analytical session including drift monitors, blanks, calibration standards, and unknowns. Time and mass-dependent variations in machine sensitivity were monitored and corrected for using a combination of internal standards and external

monitor solutions run periodically (every 4 - 5 samples) during the course of each analytical session. Analytical blanks were negligible for all masses analyzed, not exceeding 0.5% of the total counts for each mass. Calibration curves were generated using multiple USGS rock standards analyzed during each analytical session. Accepted values for the elements in these rock standards were taken from the compilations of Govindaraju (1987) and Eggins et al. (1997). Regression lines were forced through the origin and consistently gave correlation coefficients >0.995. Analytical precision and accuracy were estimated from multiple analyses of standard reference materials analyzed as unknowns over the course of the analytical work. Based on repeat analyses of standards, detection limits range from <1-10 ng/g for elements with mass >80 amu, and <10 ng/g to 1 μg/g for elements with mass <80 amu. Analytical precision (1σ) for elements with mass >80 amu is <2% RSD (relative standard deviation), and that for elements with mass <80 amu is <4% RSD. Residuals between average and accepted values for all elements commonly were less than the estimated analytical precision, confirming the quality of the data. Additionally, as a check on reproducibility, a number of aliquots both from the same prepared solution and from different dissolutions of the same sample were analyzed. In all cases the values obtained for these samples were in agreement within the estimated analytical precision.

Isotopic compositions were determined on a VG sector-54 mass spectrometer at the Massachusetts Institute of Technology. Approximately 300 mg of rock powder was dissolved in Teflon beakers in concentrated HF-HNO_3, followed by conversion to chloride form. Rare earth elements were separated by cation exchange columns with HCl

as eluant. Sm and Nd were separated using HDEHP-coated BioBead resin with HCl as eluant. Sr separation was accomplished in micro-columns using Sr-spec resin and HNO_3 chemistry. Pb was separated using HBr-based chemistry on anion exchange resin in microcolumns. All reagents used were distilled to reach ultrahigh purity for trace elements. Total procedural blanks are estimated to be <100 pg for Sr, <400 pg for Nd, and <10 pg for Pb.

Sr and Nd isotopic compositions were measured in dynamic multicollector mode. Sr isotopic ratios are normalized to $^{86}Sr/^{88}Sr = 0.1194$, and Nd isotopic ratios are normalized to $^{146}Nd/^{144}Nd = 0.7219$. Sr and Nd isotopic ratios are corrected using an exponential fractionation law. Pb isotopic compositions were measured in static multicollector mode. Based on analyses of NBS-981, Pb isotopic ratios are corrected by 0.12%/a.m.u. to account for mass fractionation during analysis.

A whole-rock basalt $^{40}Ar/^{39}Ar$ method was used to date several Vitim lavas. The freshest and most fine-grained samples were selected for dating. Samples were finely crushed with a mortar and pestle and then sieved to 500 μm mesh size, followed by ultrasonic cleaning in ethanol to remove adhering powder. A Franz magnetic separator was then used to remove any olivine because olivine has been found to cause problems with excess Ar. Any other visible phenocrysts or more magnetic material was also magnetically removed. ~100 mg of sample was packaged for irradiation. All samples were irradiated at the research reactor at McMaster University. Fast neutron flux was monitored using Fish Canyon sanidine (27.95 Ma; Cebula et al., 1986). Irradiated samples were analyzed on a resistance-furnace gas-extraction system and MAP 215-50

mass spectrometer at the Cambridge Laboratory for Argon Isotopic Research at MIT. See Hodges et al. (1994) for a thorough discussion of the laboratory procedures. All samples were analyzed by six steps of furnace step-heating.

GEOCHEMICAL RESULTS

Major elements

Vitim lavas range from basanites to alkaline basalts and hawaiites/trachybasalts, as seen in the total alkali silica (TAS) diagram (Fig. 4.4; Table 4.2). Sample C417/1 has an anomalous phonotephrite composition, and there is one sample of basaltic andesite (V9). Basanites (normative nepheline from 7 - 20) have Mg# (Mg# = molecular Mg/(Mg + Fe^{2+})) from 58 to 64, and trend to higher normative nepheline with decreasing Mg# (Fig. 4.5). Alkaline, subalkaline basalts, and potassic trachybasalts have a small range in Mg# from 61 to 64, and <50% SiO_2 (Table 4.2). The lavas from drillcore 82 alternate between subalkaline basalt and basanite.

Major element data are plotted as a function of MgO in Figure 6. MgO ranges from 4 - 10% for the analyzed samples (Table 4.2). The MgO versus SiO_2 plot (Fig. 4.6) illustrates that the basanites behave as a group, with MgO from 7-10%, and <47% SiO_2. The alkaline/subalkaline basalts, and trachybasalts have a small range in MgO (8-9%) and higher SiO_2 than the basanites. The phonotephrite (C417/1), hawaiite (V18) and basaltic andesite (V9) have lower MgO and SiO_2>50%. For a given MgO content, basanites have higher FeO*, K_2O, Na_2O, TiO_2, and P_2O_5 than the other samples. A trend of decreasing

K_2O, Na_2O and P_2O_5 with increasing MgO is evident for the basanites. CaO and Al_2O_3 contents of the basanites and alkaline/subalkaline basalts and trachybasalts overlap.

Trace elements

Rare earth elements (REE)

The group of basanites behaves very coherently on a chondrite-normalized REE diagram (Fig. 4.7), and has overall higher light REE (LREE) and lower heavy REE (HREE) than the alkaline/subalkaline basalts and trachybasalts (Table 4.2). A small variation in (La/Yb) ratio (from 16 to 28) causes a small cross-over in HREE patterns for the basanites. Basanite sample p596/1 has overall lower REE abundances than the other basanites but its pattern parallels the other basanites. Phonotephrite sample C417/1 has the most extreme La/Yb ratio of 60. The basaltic andesite (V9) has the flattest REE pattern and lowest La/Yb ratio of 5. Aside from the phonotephrite, all basanites have La > 100 times chondrite, while all other rock types have La < 100 times chondrite.

Incompatible elements

In Figure 4.8, various incompatible elements (Ba, Rb, Sr, Zr) are plotted as a function of MgO. None of these elements appears to correlate with MgO, although the basanites have higher overall Ba, Zr, and Rb than the alkaline/subalkaline basalts and trachybasalts. There is, however, a positive correlation between the incompatible element Th and other incompatible elements (Ba, Sr, Rb, Zr, Nb, etc.) (Fig. 4.8).

As demonstrated on primitive mantle normalized (Sun and McDonough, 1989) incompatible element diagrams (Fig. 4.9), basanites have sub-parallel trace element patterns, with sample p596/1 having lower abundances than the rest of the basanites. Basanites have relative enrichments in Ba, Nb, Ta, K, and Sr, and relative depletions in Th, Pr, and HREE. Sample p596/1 differs from the other basanites with a larger relative K enrichment, and a relative P and Ti enrichment absent from the other basanites. The alkaline/subalkaline basalts, and trachybasalt and hawaiite have a roughly similar incompatible element pattern to the basanites, but with more extreme relative Ba and Sr enrichments. The basaltic andesite again has a roughly similar pattern, but with lower trace element abundances. The phonotephrite, C417/1, has very high abundances of incompatible elements except for the HREE.

Compatible trace elements

Unlike the incompatible trace elements, the compatible trace elements (Ni, Co, Cr) are generally positively correlated with MgO (Fig. 4.10). Basanites and alkaline/subalkaline basalts and trachybasalts have Ni from 120 to 210 ppm, Cr from 100 to 300 ppm, and Co from 30 to 54 ppm. There is no correlation between MgO and Sc (Fig. 4.10), and basanites have lower Sc (<20 ppm) than other lava types, except the phonotephrite. As demonstrated by the plot of Th versus Ni (Fig. 4.10), there is no correlation between compatible and incompatible elements.

Isotopic data

Isotope data for the Vitim lavas are given in Table 4.3 and Figures 4.11 and 4.12. $^{87}Sr/^{86}Sr$ of the analyzed samples ranges from 0.70374 to 0.70494, and ε_{Nd} ranges from +2.3 to +7.2, within the compositional range reported for ocean island basalts (OIB) (Hart, 1988). Basanites have the largest range in Sr and Nd isotopic composition. The alkaline/subalkaline basalts and trachybasalts and hawaiites fall on the more radiogenic Sr and less radiogenic Nd part of the trend (Fig. 4.11). The basaltic andesite sample V9 and sample V11 (from a similar outcrop) have the most radiogenic Nd isotopic compositions of the measured Vitim samples.

Pb isotopic compositions of the Vitim samples have $^{206}Pb/^{204}Pb$ from 17.3 to 18.2, $^{207}Pb/^{204}Pb$ from 15.48 to 15.54, and $^{208}Pb/^{204}Pb$ from 37.2 to 38.2. As seen in Figure 4.12, the Vitim samples all lie above the Northern Hemisphere Regression Line (NHRL) of Hart et al. (1986), as do other BRZ volcanic rocks. Again, as with the Sr and Nd isotopic data, the basanites have the largest range in Pb isotopic compositions, with $^{206}Pb/^{204}Pb$ from 17.3 to 17.9 (Table 4.3). All other samples have $^{206}Pb/^{204}Pb > 17.9$, up to 18.2. The basaltic andesites (V9 and V11) with $\varepsilon_{Nd} > +6$ have the most radiogenic Pb isotopic composition of any Vitim samples, with the exception of 82/17. The basanites with $^{206}Pb/^{204}Pb$ around 17.3 have the most unradiogenic Pb isotopic composition of any analyzed BRZ lavas. In addition to the extremely unradiogenic $^{206}Pb/^{204}Pb$ values recorded in Vitim lavas, the Vitim data define a linear array with a lower slope on the $^{206}Pb/^{204}Pb$ - $^{207}Pb/^{204}Pb$ diagram (Fig. 4.12) than other BRZ fields, as they have a higher $^{207}Pb/^{204}Pb$ for a given $^{206}Pb/^{204}Pb$. The low $^{206}Pb/^{204}Pb$ basanites also have very low $^{208}Pb/^{204}Pb$

(37.2 to 37.4). It is interesting to note that all of the extremely unradiogenic samples are from the eastern part of the Vitim volcanic field, and are all Pliocene or younger (see Table 4.1). These samples also contain abundant mantle xenoliths.

The $^{206}Pb/^{204}Pb$ - $^{87}Sr/^{86}Sr$ and $^{206}Pb/^{204}Pb$ - ε_{Nd} diagrams (Fig. 4.13) demonstrate that the basanites have a minor trend to more radiogenic Sr and less radiogenic Nd with decreasing $^{206}Pb/^{204}Pb$. Other lava types have a wide range in Sr and Nd isotopic composition with a restricted and more radiogenic $^{206}Pb/^{204}Pb$ composition.

DISCUSSION

Origin of Vitim volcanic rocks

The range of Mg# from 58 to 64 (Table 4.2) makes it unlikely that any of the Vitim lavas represent primary mantle melts in equilibrium with their source. The low Ni (<210 ppm) and Cr (<300 ppm) abundances are also too low to be in equilibrium with mantle as represented by peridotite xenoliths (Hart and Allègre, 1980). The observed geochemical variation in the magmas could be explained by a variety of processes including fractional crystallization, varying degrees of partial melting of a homogeneous source, or partial melting of a heterogeneous source. However, several lines of evidence support derivation of Vitim basanites from a deep (>40 km), garnet-bearing source, followed by fractional crystallization: (1) Mg# decreases with increasing normative nepheline content (Fig. 4.5), (2) major oxides K_2O, Na_2O, CaO, and P_2O5 are positively correlated with MgO (Fig. 4.6), (3) the CaO/Al_2O_3 ratio decreases with decreasing MgO (Fig. 4.14), (4) compatible elements (Ni, Cr, Co) are positively correlated with MgO (Fig.

4.10), (5) LREE are enriched over HREE (Fig. 7), and (5) the $(La/Yb)_N$ ratio increases with decreasing MgO (Fig. 4.14) .

The trend of decreasing CaO/Al_2O_3 with decreasing MgO (Fig. 4.14) is strong evidence that clinopyroxene was an important fractionating phase in the evolution of the basanites. The covariation of MgO with Na_2O, K_2O, and CaO indicates that plagioclase fractionation was also involved (Fig. 4.6). There appears to be a smaller group within the basanite group of decreasing TiO_2 with decreasing MgO, although many basanites at MgO of ~9% fall below this trend (Fig. 4.6). A similar trend occurs with variation of FeO* and may indicate variable fractionation of an Fe-Ti oxide mineral phase.

The lack of correlation between MgO and incompatible elements such as Ba, Rb, Sr, and Zr (Fig. 4.8) indicates that the variation in incompatible element abundances must be explained by a process other than mineral segregation. The high degree of correlation between Th and various other incompatible elements (Fig. 4.8) suggests that the incompatible element abundances are controlled by varying, small degrees of partial melting of a homogeneous source. This would seem to argue against the evidence for fractional crystallization exhibited by the major element and compatible element data, although the same major element trends could possibly be explained by varying degrees of partial melting of an inhomogeneous source, such as a veined garnet and pyroxene lherzolite.

In fact, the isotopic data for the basanites best supports their derivation from a heterogeneous source region. As described above, the basanites have the widest range in Sr, Nd and Pb isotopic compositions of all Vitim lavas (Fig. 4.11, 4.12). There is no

correlation between $^{8}7Sr/^{86}Sr$ and 1/Sr, or ε_{Nd} and 1/Nd (Fig. 4.15), which rules out simple mixing as an explanation for the trends. Additionally, there appears to be no correlation between $^{87}Sr/^{86}Sr$ and $(La/Yb)_N$ or Rb/Sr (Fig. 4.15).

The only other explanation would be that the Sr, Nd, and Pb isotopic ratios of the basanites are controlled by varying degrees of crustal contamination. However, although there is a weak correlation between SiO_2 and $^{87}Sr/^{86}Sr$ (Fig. 4.16), there is no correlation of SiO_2 with ε_{Nd} or $^{206}Pb/^{204}Pb$. The high abundance of Sr (681 - 1098 ppm) and Nd (22 - 39 ppm) in the basanites relative to an average crustal contaminant (granite: Sr = 100 ppm, Nd = 44 ppm; values from compilation in Faure, 1986) would also make it difficult to change the Sr or Nd isotopic ratio without a very significant amount of assimilation. Such a large amount of assimilation would also affect the other trace element and major element abundances, which is not the case. Therefore the only viable explanation for the variation in Sr and Nd isotopic ratios must be heterogeneity in the source region. Since the basanites have a relatively restricted range in $^{87}Sr/^{86}Sr$ and ε_{Nd} when compared to that observed in other BRZ volcanic fields or Chinese Cenozoic intraplate volcanic rocks (Fig. 4.11), the source region need only have minor heterogeneity in Sr and Nd isotopic composition. Data for Vitim clinopyroxene megacrysts (Harris et al., in prep. and Ch.5 of this thesis; shown in Fig. 4.11) exhibit a range in Sr and Nd isotopic ratios similar to that of the basanite, further supporting heterogeneity in the source.

Pb isotopic data: evidence for EM-I?

Contrary to the Sr and Nd isotopic data, the range in Pb isotopic compositions for Vitim basanites is relatively large (Fig. 4.12, Table 4.3). Although, as mentioned above, there is no readily obvious evidence for crustal assimilation in these lavas, the reality is that the low Pb concentration of basanitic magmas (~1-3 ppm) makes them highly susceptible to even with small amounts of assimilant. This sensitivity of the Pb isotopic ratios of lavas to interaction with lithosphere during their ascent and emplacement lends a high degree of ambiguity to interpreting trends in continental volcanic Pb isotopic data and deciding whether the measured ratios are reflective of the source characteristics, even when the Sr and Nd isotopic ratios do not appear to be affected by crustal interaction.

The trend to a higher $^{207}Pb/^{204}Pb$ (and very low $^{208}Pb/^{204}Pb$) for a given $^{206}Pb/^{204}Pb$ compared to other BRZ volcanic fields (Fig. 4.12) suggests two possibilities: (1) the young, extremely unradiogenic basanites from the eastern Vitim volcanic field were derived from a different source than the group of more radiogenic lavas, or (2) the extremely unradiogenic lavas are a result of contamination with a very unradiogenic component. The latter possibility could explain the lower slope on the $^{207}Pb/^{204}Pb$ - $^{206}Pb/^{204}Pb$ diagram by contamination with crustal material of a different age than at other BRZ fields. However, the observed trend is equally well described by mixing between an enriched mantle I (EMI) component and a more depleted mantle component (Fig. 4.12).

Adding to the complexity of the Pb data is that the alkaline basalts with high Mg# form the most radiogenic end of the Pb data array, with $^{206}Pb/^{204}Pb > 17.9$. Since these lavas have higher Pb concentrations than the basanites and are arguably somewhat less

susceptible to Pb contamination, they may be a more reliable representation of the Pb signature of the source region. This conclusion would favor the Pb isotopic composition of the basanites being the result of crustal contamination. However, since the major element data and trace element abundances are systematically different from those of the basanites, it is equally probable that they were derived from a completely different, perhaps shallower, source region.

Pb isotopic data for Vitim clinopyroxene megacrysts overlaps but extends beyond the range observed in the basanites, with $^{206}Pb/^{204}Pb$ of 17.3 to 17.7, $^{207}Pb/^{204}Pb$ of 15.44 to 15.48, and $^{208}Pb/^{204}Pb$ of 37.2 to 37.5 (Fig. 4.12). A Vitim anorthoclase megacryst has an intermediate Pb isotopic composition. If the clinopyroxene megacrysts are crystallized from a melt related to the basanites, as proposed by many researchers (e.g., Harris et al., in prep., Irving and Frey, 1984), they are compelling evidence against crustal contamination, since they most likely would have formed somewhere at or below the crust-mantle boundary and therefore would not have been affected by crustal contamination.

The above line of reasoning suggests that the Vitim Pb isotopic data are actually reflective of the primary Pb isotopic character of their source. Evidence for the existence beneath the continents of the same end-member mantle components (i.e., DM, EMI, EMII, HIMU, etc. of Zindler and Hart, 1986 and Hart, 1988) found in ocean island basalts (OIB) has previously been proposed by numerous researchers for Cenozoic volcanic rocks from eastern (Peng et al., 1986; Liu et al., 1992; Zhi et al., 1990; Song et al., 1990; Basu et al., 1991) and southern China (Tu et al., 1991; Tu et al., 1992; Flower et al.,

1992; Tatsumoto and Nakamura, 1991), as well as Vietnam (Chung et al., 1995). Indeed, the widely accepted view of global mantle convection would necessitate the existence of these components world-wide. It is particularly interesting that evidence for an EMI-type mantle component is found beneath Vitim (and other fields of the BRZ), since a proposed origin for this component is subcontinental lithospheric mantle somehow entrained into the convecting asthenosphere (Hart, 1988). Preliminary Pb isotopic data for two separates of Cr-diopside from Vitim garnet peridotites (shown in Fig. 4.12) indicates that the subcontinental lithospheric mantle below the Vitim plateau may have variable Pb isotopic composition that extends to the unradiogenic, EM-I-like end-member. The extremely depleted nature of the sub-Vitim lithospheric mantle recorded by the Sr and Nd isotopic data of Ionov et al. (1993) for Vitim garnet peridotites suggests that the lithospheric mantle can not be the source of the Cenozoic Vitim magmas. It is also unlikely that ascending magmas could have melted anything out of the old, unradiogenic lithospheric mantle. However, a process such as delamination of the unradiogenic, sub-Vitim lithospheric mantle and incorporation into a more radiogenic asthenosphere some time in the past could have given rise to the existence of the EM-I-type component in the sub-Vitim mantle.

CONCLUSIONS

The geochemical data presented in this paper support the generation of the Cenozoic Vitim basanites and transitional basalts by variable degrees of partial melting of a garnet-bearing source. The small variability of Sr, Nd, and Pb isotopic compositions of

basanites suggests that the source region was isotopically heterogeneous. Basanitic lavas evolved to a small degree before emplacement by fractional crystallization of clinopyroxene, feldspar, and Fe-Ti-oxides, as exhibited by the covariation of MgO and Na_2O, K_2O, TiO_2, and CaO/Al_2O_3 (Fig. 4.6, 4.14).

Vitim transitional lavas are systematically different than the basanites, with overall lower incompatible trace element abundances, and isotopic signatures representative of a less depleted source region (i.e., more radiogenic Sr, less radiogenic Nd, more radiogenic Pb). The basaltic andesite samples have a peculiarly high ε_{Nd}, low $^{87}Sr/^{86}Sr$, radiogenic Pb isotopic signature, and the most chondritic trace element abundances, while the transitional lavas have higher $^{87}Sr/^{86}Sr$, lower ε_{Nd}, moderately radiogenic Pb isotopic signatures, and lower incompatible trace element abundances than the basanites. The phonotephrite, with its extremely high incompatible trace element abundances, is clearly the most evolved of the Vitim lavas. The differences between the various lava types are probably a result of derivation from different, but related, source regions.

In both isotopic ratios and trace element signatures, the Vitim lavas are geochemically very similar to OIB. Furthermore, the Pb isotopic data provide evidence that Vitim basanites are a result of mixing between EM-I and DM-type components the same as those found in the oceanic setting. The other Vitim lava types appear to be derived from a more radiogenic, DM-type reservoir.

As a final note, it is interesting that the youngest Vitim lavas have the most unradiogenic Pb isotopic composition. In other rifts, such as the Rio Grande Rift of

North America, it has been observed that as rifting progresses lavas become more "asthenospheric" after the initial heterogeneities are melted out and greater extension leads to easier eruption with less potential for interaction with the crust (Gibson et al., 1992; Lipman et al., 1987). If this is also the case for the Baikal Rift Zone, then we must conclude that the sub-Baikal asthenosphere has an unradiogenic Pb isotopic signature. Although we have tentatively concluded in this study that this is the case, a more thorough geochronological/geochemical study of the Vitim lavas is necessary to confirm this. In addition, a Pb isotopic study of the abundant Vitim mantle xenoliths may be critical to our understanding of the origin of the EM-I mantle signature.

REFERENCES

Basu, A. R., Junwen, W., Wankang, H., Guanghong, X., and Tatsumoto, M., 1991, Major element, REE, and Pb, Nd and Sr isotopic geochemistry of Cenozoic volcanic rocks of eastern China: implications for their origin from suboceanic-type mantle reservoirs: Earth and Planetary Science Letters, v. 105, p. 149-169.

Cebula, G. T., Kunk, M. J., Mehnert, H. H., Naeser, C. W., Obradovich, J. D., and Sutter, J. F., 1986, The Fish Canyon Tuff, a potential standard for the $^{40}Ar/^{39}Ar$ and fission-track dating methods, in Sixth international conference on Geochronology, cosmochronology and isotope geology.

Chung, S.-L., Jahn, B.-M., Chen, S.-J., Lee, T., and Chen, C.-H., 1995, Miocene basalts in northwestern Taiwan: evidence for EM-type mantle sources in the continental lithosphere: Geochimica et Cosmochimica Acta, v. 59, p. 549-555.

Delvaux, D., Moeys, R., Stapel, G., Melnikov, A., and Ermikov, V., 1995, Palaeostress reconstructions and geodynamics of the Baikal region, Central Asia, Part I. Palaeozoic and Mesozoic pre-rift evolution: Tectonophysics, v. 252, p. 61-101.

Dobretsov, N. L., Buslov, M. M., Delvaux, D., Berzin, N. A., and Ermikov, V. D., 1996, Meso- and Cenozoic tectonics of the central Asian mountain belt: effects of lithospheric plate interaction and mantle plumes: International Geology Review, v. 38, p. 430-466.

Eggins, S. M., Woodhead, J. D., Kinsley, L. P. J., Mortimer, G. E., Sylvester, P., McCulloch, M. T., Hergt, J. M., and Handler, M. R., 1997, A simple method for the precise determination of >or=40 trace elements in geological samples by ICPMS using enriched isotope internal standardisation: Chemical Geology, v. 134, p. 311-326.

Esin, S. V., Ashchepkov, I. V., Ponomarchuk, V. A., Yamamoto, M., Travin, A. V., and Kiselyeva, V. Y., 1995, Petrogenesis of Alkaline Basaltoids from the Vitim Plateau, Baikal Rift Zone: Novosibirsk, Russian Academy of Sciences Siberian Branch, United Institute of Geology, Geophysics and Mineralogy, 58 p.

Faure, G., 1986, Principles of Isotope Geology: New York, John Wiley and Sons, 589 p.

Flower, M. F. J., Zhang, M., Chen, C.-Y., Tu, K., and Xie, G., 1992, Magmatism in the South China Basin 2. Post-spreading Quaternary basalts from Hainan Island, south China: Chemical Geology, v. 97, p. 65-87.

Gao, S., Davis, P. M., Liu, H., Slack, P. D., Zorin, Y. A., Logatchev, N. A., Kogan, M., Burkholder, P. D., and Meyer, R. P., 1994, Asymmetric upwarp of the asthenosphere beneath the Baikal rift zone, Siberia: Journal of Geophysical Research, v. 99, p. 15,319-15,330.

Gibson, S. A., Thompson, R. N., Leat, P. T., Dickin, A. P., Morrison, M. A., Hendry, G. L., and Mitchell, J. G., 1992, Asthenosphere-derived magmatism in the Rio Grande rift, western USA: implications for continental break-up, in Storey, B. C., Alabaster, T., and Pankhurst, R. J., eds., Magmatism and the Causes of Continental Break-up, Geological Society, p. 61-89.

Gladikh, V. S., 1996 (1993?), Upper mantle inhomogeneity and variations in rare-element patterns in Baykal Rift Zone basanitoids and alkali basanitoids: Doklady, v. 329, p. ??

Govindaraju, K., 1987, 1987 compilation report on Ailsa Craig granite AC-E with the participation of 128 GIT-IWG laboratories: Geostandards Newsletter, v. 11, p. 203-255.

Hart, S. R., and Allegre, C. J., 1980, Trace element constraints on magma genesis, in Hargraves, R. B., eds., Physics of Magmatic Processes: Princeton., Princeton University Press, p. 121-139.

Hart, S. R., Gerlach, D. C., and White, W. M., 1986, A possible new Sr-Nd-Pb mantle array and consequences for mantle mixing: Geochimica et Cosmochimica Acta, v. 50, p. 1551-1557.

Hart, S. R., 1988, Heterogeneous mantle domains: signatures, genesis and mixing chronologies: Earth and Planetary Science Letters, v. 90, p. 273-296.

Hodges, K. V., Hames, W. E., Olszewski, W., Burchfiel, B. C., Royden, L. H., and Chen, Z., 1994, Thermobarometric and $^{40}Ar/^{39}Ar$ geochronologic constraints on Eohimalayan metamorphism in the Dinggye area, southern Tibet: Contributions to Mineralogy and Petrology, v. 117, p. 151-163.

Hutchinson, D. R., Golmshtok, A. J., Zonenshain, L. P., Moore, T. C., Scholz, C. A., and Klitgord, K. D., 1992, Depositional and tectonic framework of the rift basins of Lake Baikal from multichannel seismic data: Geology, v. 20, p. 589-592.

Ionov, D. A., Kramm, U., and Stosch, H., 1992, Evolution of the upper mantle beneath the southern Baikal rift zone: an Sr-Nd isotope study of xenoliths from the Bartoy volcanoes: Contrib. Mineral. Petrol., v. 11, p. 235-247.

Ionov, D. A., Ashchepkov, I. V., Stosch, H., Witt-Eickschen, G., and Seck, H. A., 1993, Garnet peridotite xenoliths from the Vitim volcanic field, Baikal region: the nature of the garnet-spinel peridotite transition zone in the continental mantle: Journal of Petrology, v. 34, p. 1141-1175.

Ionov, D. A., Harmon, R. S., France-Lanord, C., Greenwood, P. B., and Ashchepkov, I. V., 1994, Oxygen isotope composition of garnet and spinel peridotites in the continental mantle: evidence from the Vitim xenolith suite, southern Siberia: Geochimica et Cosmochimia Acta, v. 58, p. 1463-1470.

Irving, A., and Frey, F. A., 1984, Trace element abundances in megacrysts and their host basalts: constraints on partition coefficients and megacryst genesis: Geochimica et Cosmochimica Acta, v. 48, p. 1201-1221.

Kiselev, A. I., 1987, Volcanism of the Baikal rift zone: Tectonophysics, v. 143, p. 235-244.

Kiselev, A. I., and Popov, A. M., 1992, Asthenospheric diapir beneath the Baikal rift: petrological constraints: Tectonophysics, v. 208, p. 287-295.

Kovalenko, V. I., Yarmoluk, V. V., Ionov, D. A., Yaguts, E., Lugmair, G. W., and Stosch, H. G., 1990, Mantle evolution in central Asia and development of tectonic structures of the Earth's crust: Geotectonics, v. 24, p. 283-292.

Le Bas, M. J., Le Maitre, R. W., Streckeisen, A., and Zanettin, B., 1986, A chemical classification of volcanic rocks based on the total alkali-silica diagram: Journal of Petrology, v. 27, p. 745-750.

Lipman, P. W., Logatchev, N. A., Zorin, Y. A., Chapin, E. E., Kovalenko, V., and Morgan, P., 1989, Intracontinental Rift Comparisons: Baikal and Rio Grande rift systems: EOS, Transactions American Geophysical Union, v. 70, p. 578-579, 586-588.

Liu, C., Masuda, A., and Xie, G., 1992, Isotope and trace-element geochemistry of alkali basalts and associated megacrysts from the Huangyishan volcano, Kuandia, Liaoning, NE China: Chemical Geology, v. 97, p. 219-231.

Logatchev, N. A., Zorin, Y. A., and Rogozhina, V. A., 1983, Baikal Rift: active or passive? - comparison of the Baikal and Kenya rift zones: Tectonophysics, v. 94, p. 223-240.

Logatchev, N. A., and Zorin, Y. A., 1987, Evidence and causes of the two-stage development of the Baikal rift: Tectonophysics, v. 143, p. 225-234.

Logatchev, N. A., and Zorin, Y. A., 1992, Baikal rift zone: structure and geodynamics: Tectonophysics, v. 208, p. 273-286.

Logatchev, N. A., 1993, History and geodynamics of the Lake Baikal rift in the context of the eastern Siberia rift system: a review: Bull. Centres Rech. Explor.-Prod. Elf Aquitaine, v. 17, p. 353-370.

Menzies, M. A., Fan, W., and Zhang, M., 1993, Palaeozoic and Cenozoic lithoprobes and the loss of >120 km of Archaean lithosphere, Sino-Korean craton, China, in Prichard, H. M., Alabaster, T., Harris, N. B. W., and Neary, C. R., eds., Magmatic Processes and Plate Tectonics, Geological Society, p. 71-81.

Molnar, P., and Tapponnier, P., 1975, Cenozoic tectonics of Asia: effects of a continental collision: Science, v. 189, p. 419-426.

Molnar, P., and Tapponnier, P., 1977, Relation of the tectonics of eastern China to the India-Eurasia collision: application of slip-line field theory to large-scale continental tectonics: Geology, v. 5, p. 212-216.

Peng, Z. C., Zartman, R. E., Futa, K., and Chen, D. G., 1986, Pb-, Sr- and Nd-isotopic systematics and chemical characteristics of Cenozoic basalts, eastern China: Chemical Geology, v. 59, p. 3-33.

Rasskazov, S. V., and Batyrmurzaev, A. S., 1985, Cenozoic basalts of the Vitim Plateau and their age determination: Geologiya i Geofizika, v. 26, p. 20-27.

Rasskazov, S. V., 1993, Magmatism of the Baikal rift zone: Novosibirsk, Nauka, 273 p.

Rasskazov, S. V., 1994, Magmatism related to the eastern Siberia rift system and the geodynamics: Bull. Centres Rech. Explor.-Prod. Elf Aquitaine, v. 18, p. 437-452.

Rhodes, J. M., 1983, Homogeneity of lava flows: chemical data for historic Mauna Loan eruptions.: Journal of Geophysical Research, v. 88 (Suppl.), p. A869-A879.

Song, Y., Frey, F. A., and Zhia, X., 1990, Isotopic characteristics of Hannuoba basalts, eastern China: implications for their petrogenesis and the composition of subcontinental mantle: Chemical Geology, v. 85, p. 35-52.

Sun, S., and McDonough, W. F., 1989, Chemical and isotopic systematics of oceanic basalts: implications for mantle composition and processes, in Saunders, A. D., and Norry, M. J., eds., Magmatism in the Ocean Basins, Geological Society Special Publication, p. 313-345.

Tatsumoto, M., Basu, A. R., Wankang, H., Junwen, W., and Guanghon, X., 1992, Sr, Nd, and Pb isotopes of ultramafic xenoliths in volcanic rocks of eastern China: enriched components EMI and EMII in subcontinental lithosphere: Earth and Planetary Science Letters, v. 113, p. 107-128.

Tu, K., Flower, M. F. J., Carlson, R. W., Zhang, M., and Xie, G., 1991, Sr, Nd, and Pb isotopic compositions of Hainan basalts (south China): implications for a subcontinental lithosphere Dupal source: Geology, v. 19, p. 567-569.

Tu, K., Flower, M. F. J., Carlson, R. W., Xie, G., Chen, C.-Y., and Zhang, M., 1992, Magmatism in the South China Basin 1. Isotopic and trace-element evidence for an endogenous Dupal mantle component: Chemical Geology, v. 97, p. 47-63.

Zhi, X., Song, Y., Frey, F. A., Feng, J., and Zhai, M., 1990, Geochemistry of Hannuoba basalts, eastern China: constraints on the origin of continental alkalic and tholeiitic basalt: Chemical Geology, v. 88, p. 1-33.

Zindler, A., and Hart, S., 1986, Chemical geodynamics: Annual Reviews in Earth and Planetary Science, v. 14, p. 493-571.

Zonenshain, L. P., and Savostin, L. A., 1981, Geodynamics of the Baikal rift zone and plate tectonics of Asia: Tectonophysics, v. 76, p. 1-45.

Zorin, Y. A., Kozhevnikov, V. M., Novoselova, M. R., and Turutanov, E. K., 1989, Thickness of the lithosphere beneath the Baikal rift zone and adjacent regions: Tectonophysics, v. 168, p. 327-337.

FIGURE CAPTIONS

Figure 4.1 General map of the Baikal Rift Zone (BRZ) showing locations of the major Cenozoic volcanic fields and other major features. TV is the Tuva volcanic field; OP is the Oka Plateau; T is the Tunka Basin, and D is the Dzhida Basin. Other rift basins according to number label are: 1) Busingol, 2) Darkhat, 3) Khubsugul, 4) Barguzin, 5) Upper Angara, 6) Tsipa, 7) Baunt, 8) Muya, 9) Chara, and 10) Tokka. The 1500 m contour line of the Sayan-Baikal domal uplift is indicated.

Figure 4.2 Map of the Vitim volcanic field, showing locations of two cross-sections shown in Figure 4.3.

Figure 4.3 Cross-sections across the western (A-B) and eastern (C-D) Vitim volcanic field, as shown in Figure 4.2. a) a sequence of Miocene lava, with locations of drillcores 82 and 417, b) cross-section through the Dzhilinda R. basin showing the Pliocene and Quaternary lavas.

Figure 4.4 Total Alkali Silica diagram for Vitim lavas (Le Bas et al., 1986). Labeled fields are: BA - basaltic andesite; B1 - alkaline/subalkaline basalt; B2 - hawaiite/trachybasalt; U1 - basanite; U2 - phonolite. Symbols used in following tables are defined.

Figure 4.5 Plot of Mg# versus normative nepheline or quartz + hypersthene. Symbols as in Figure 4.4.

Figure 4.6 MgO% - major oxide variation diagrams. Symbols as in Figure 4.4.

Figure 4.7 Chondrite normalized rare earth element (REE) diagrams for Vitim volcanic rocks, using values of Sun and McDonough (1989) for C1 chondrite.

Figure 4.8 Variation in incompatible elements versus MgO and Th, demonstrating that incompatible elements are highly correlated with each other. Symbols as in Figure 4.4.

Figure 4.9 Primitive mantle normalized incompatible element diagrams for Vitim lavas, using values of Sun and McDonough (1989).

Figure 4.10 Diagram showing the correlation of MgO with compatible elements (Ni, Co, Cr, Sc), and lack of correlation between incompatible (Th) and compatible elements (Ni). Symbols as in Figure 4.4.

Figure 4.11 $^{87}Sr/^{86}Sr$ - ε_{Nd} diagram for the Vitim lavas. Labeled for reference are the end-member mantle components DMM (depleted MORB mantle) and EMI (enriched mantle type 1), after Hart (1988) and Zindler and Hart (1986). Symbols as in Figure 4.4.

Figure 4.12 $^{206}Pb/^{204}Pb$ - $^{207}Pb/^{204}Pb$ and $^{206}Pb/^{204}Pb$ - $^{208}Pb/^{204}Pb$ diagrams for Vitim lavas. In addition to the end-member mantle component EMI, the NHRL (Northern Hemisphere Reference Line) is also give (Hart, 1986). Symbols as in Figure 4.4.

Figure 4.13 $^{206}Pb/^{204}Pb$ - $^{87}Sr/^{86}Sr$ and $^{206}Pb/^{204}Pb$ - ε_{Nd} diagrams for Vitim lavas. Symbols as in Figure 4.4. The field for lavas of the western BRZ and Udokan volcanic fields is shown. Calculated mixing lines between hypothetical DM (Sr=150ppm, Pb=1ppm, $^{87}Sr/^{86}Sr$=0.703, $^{206}Pb/^{204}Pb$=18.5) and EMI (Sr=100ppm, Pb=.5ppm, $^{87}Sr/^{86}Sr$=0.705, $^{206}Pb/^{204}Pb$=17.2) components are shown

Figure 4.14 Plot of MgO% versus CaO/Al_2O_3 and $(La/Yb)_N$, with symbols as in Figure 4.4.

Figure 4.15 Variation of $(La/Yb)_N$, Rb/Sr, and 1/Sr versus $^{87}Sr/^{86}Sr$. Symbols as in Figure 4.4.

Figure 4.16 Variation of Sr, Nd, and Pb isotopic compositions as a function of SiO_2 wt%. Symbols as in Figure 4.4.

Figure 4.1

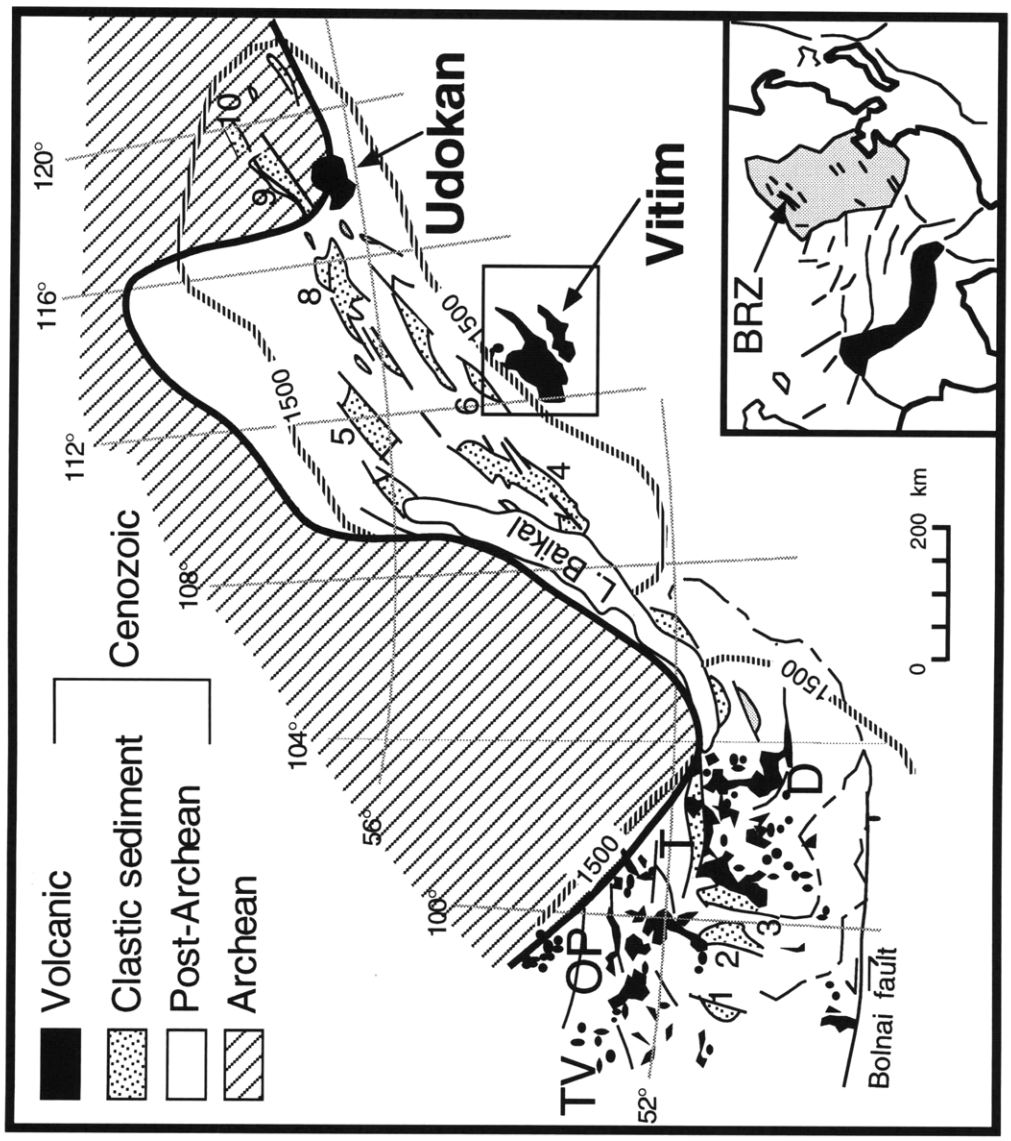
Volcanic
Clastic sediment
Cenozoic
Post-Archean
Archean
Udokan
Vitim
BRZ
L. Baikal
TV
OP
T
D
Bolnai fault
1500
112°
116°
120°
108°
104°
100°
56°
52°
0
200 km

Figure 4.3

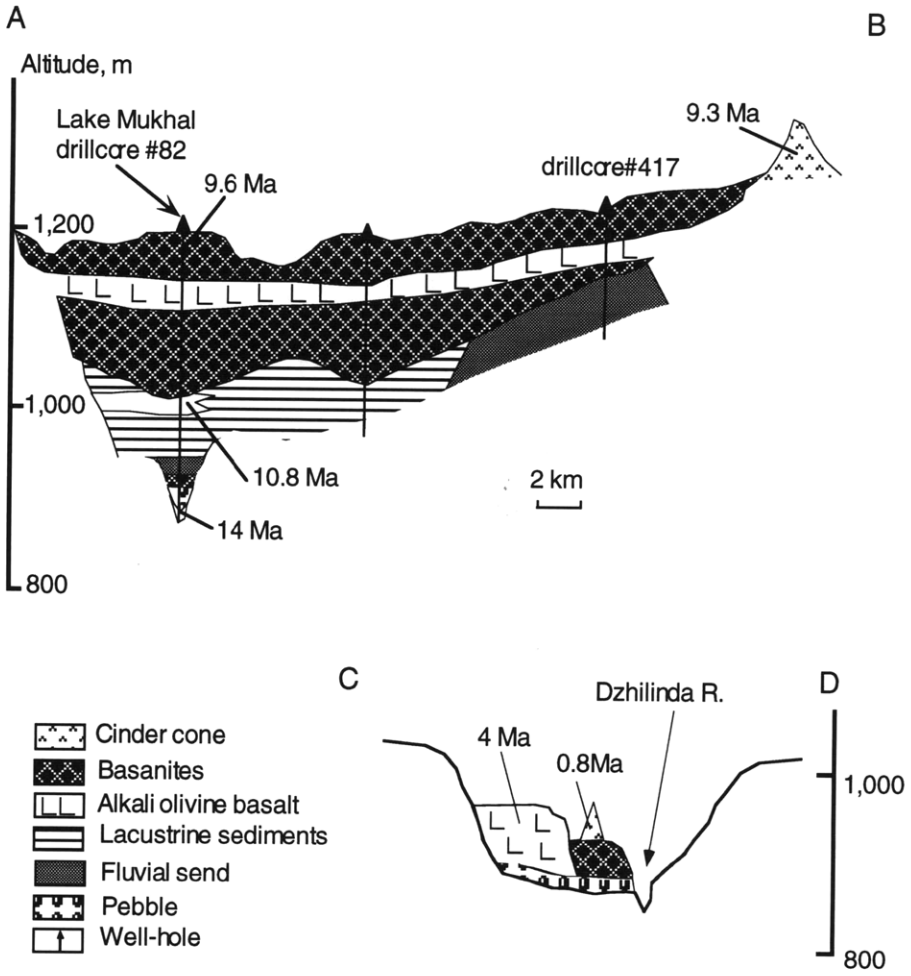
A
B
Altitude, m
Lake Mukhal
drillcore #82
9.6 Ma
9.3 Ma
drillcore#417
1,200
1,000
10.8 Ma
2 km
14 Ma
800
C
D
Dzhilinda R.
4 Ma
0.8Ma
1,000
800
Cinder cone
Basanites
Alkali olivine basalt
Lacustrine sediments
Fluvial send
Pebble
Well-hole

Figure 4.3

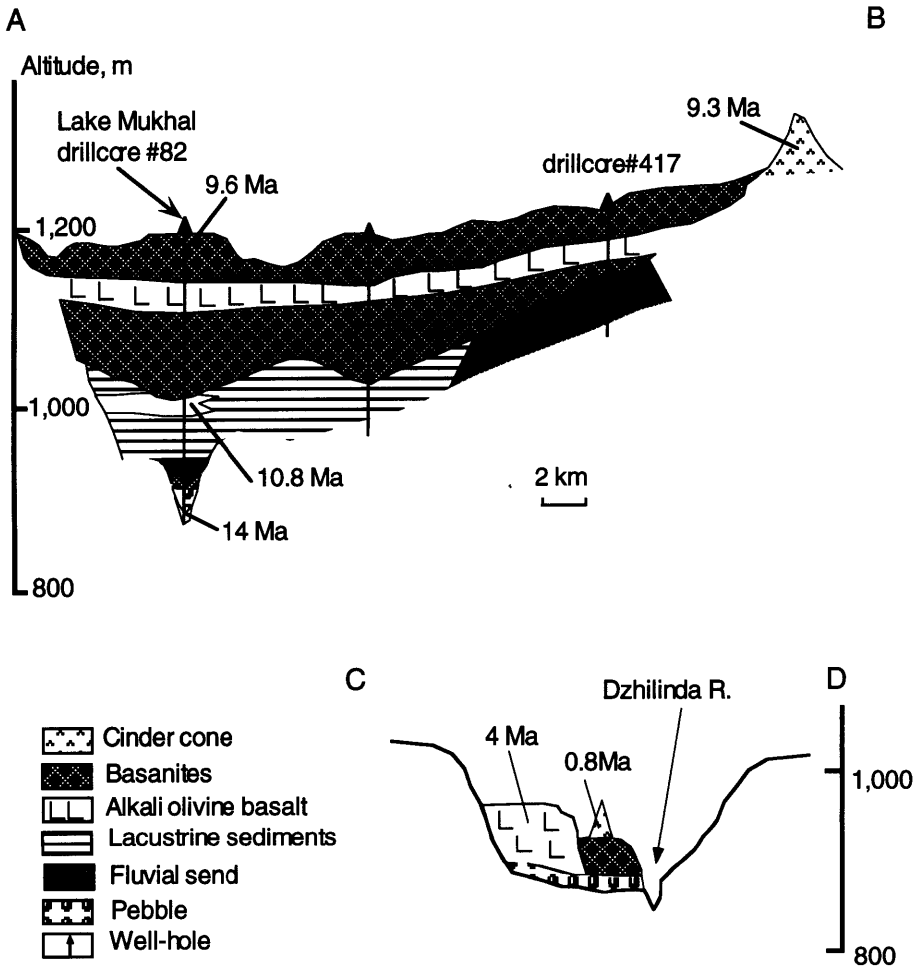
A
B
Altitude, m
Lake Mukhal
drillcore #82
9.6 Ma
9.3 Ma
drillcore#417
1,200
1,000
10.8 Ma
2 km
14 Ma
800
C
D
Dzhilinda R.
4 Ma
0.8Ma
1,000
800
Cinder cone
Basanites
Alkali olivine basalt
Lacustrine sediments
Fluvial send
Pebble
Well-hole

Figure 4.4

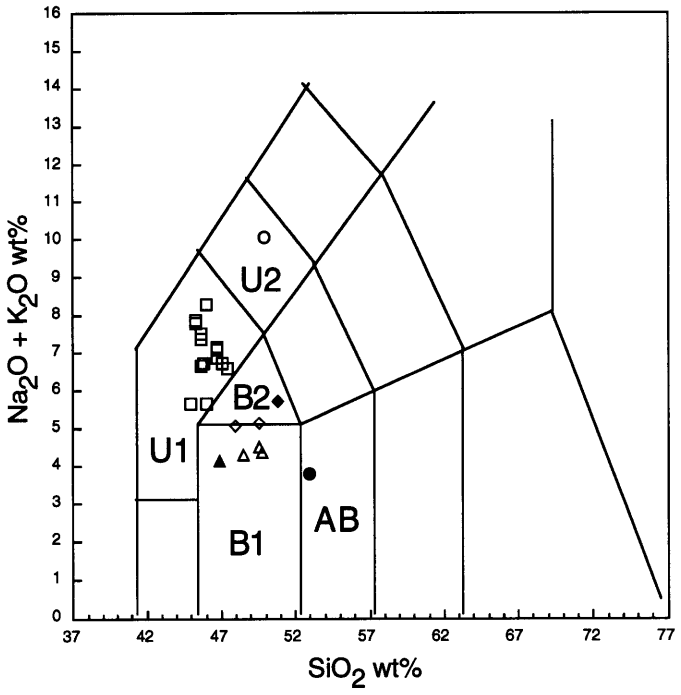
16
15
14
13
12
11
10
9
8
7
6
5
4
3
2
1
0
$Na_2O + K_2O$ wt%
37
42
47
52
57
62
67
72
77
SiO_2 wt%
U2
B2
U1
B1
AB

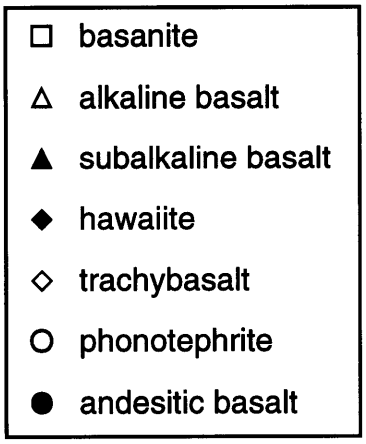
basanite
alkaline basalt
subalkaline basalt
hawaiite
trachybasalt
phonotephrite
andesitic basalt

Figure 4.5

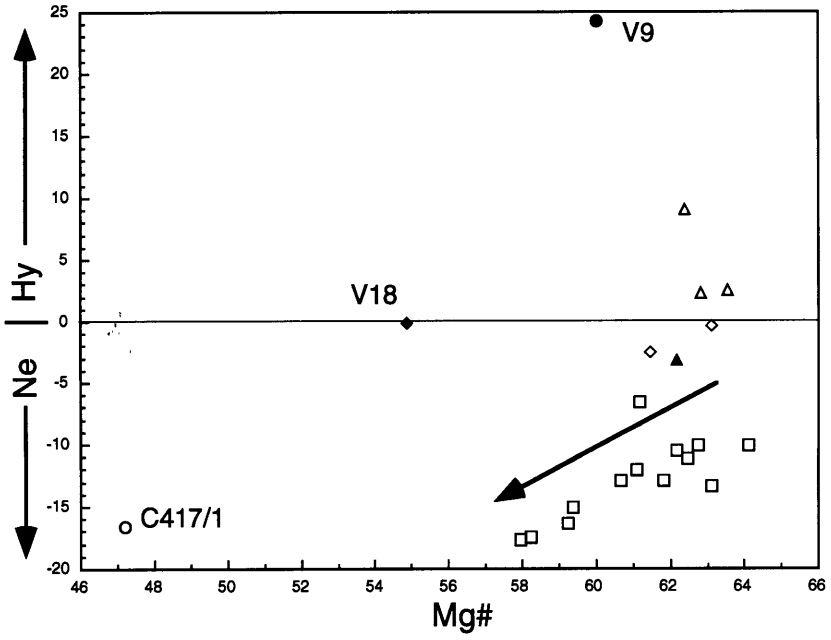
V9
V18
C417/1
Hy
Ne
Mg#
25
20
15
10
5
0
-5
-10
-15
-20
46
48
50
52
54
56
58
60
62
64
66

Figure 4.6

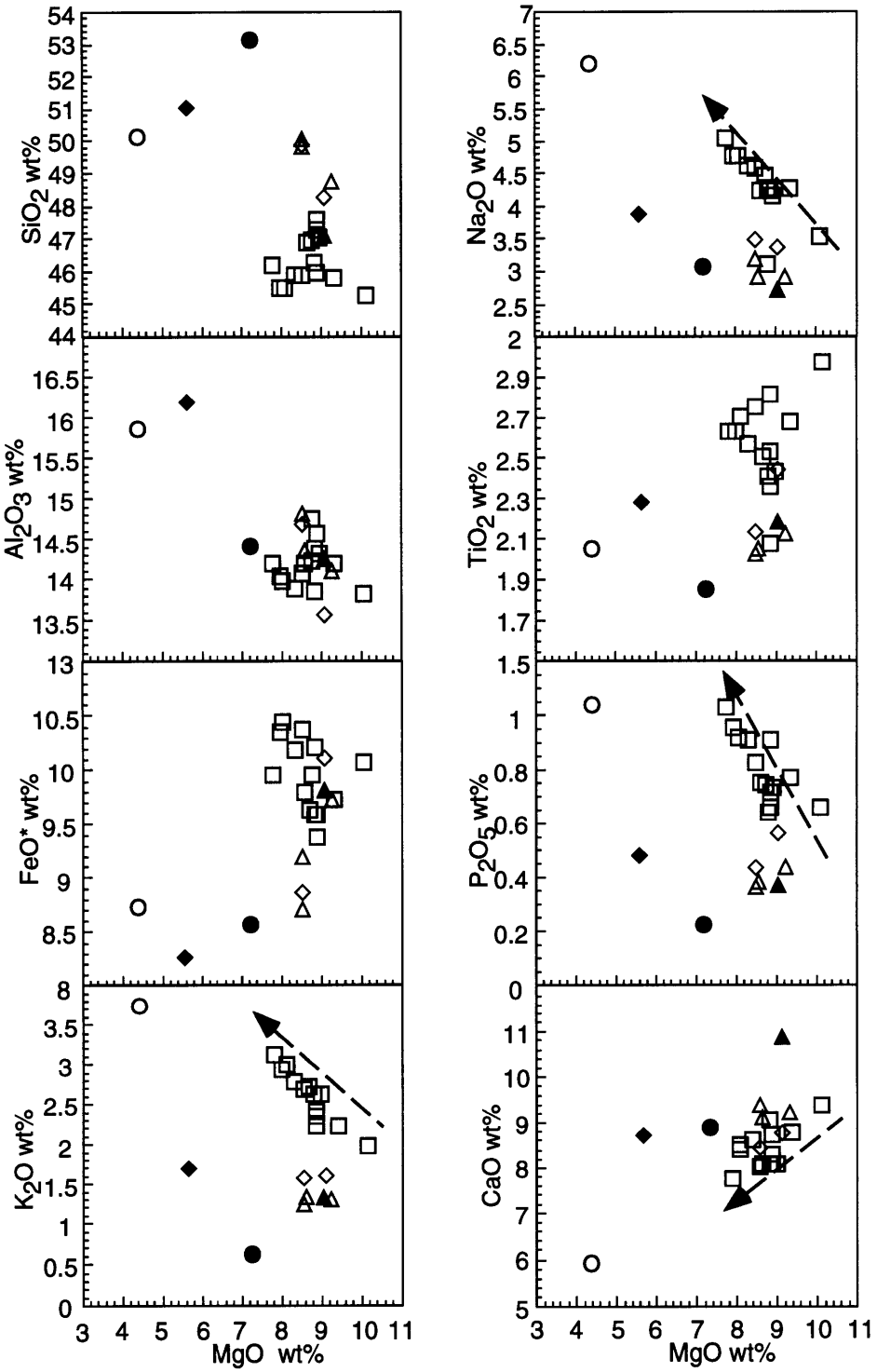
SiO2 wt%
Al2O3 wt%
FeO* wt%
K2O wt%
Na2O wt%
TiO2 wt%
P2O5 wt%
CaO wt%
MgO wt%
MgO wt%

Figure 4.7

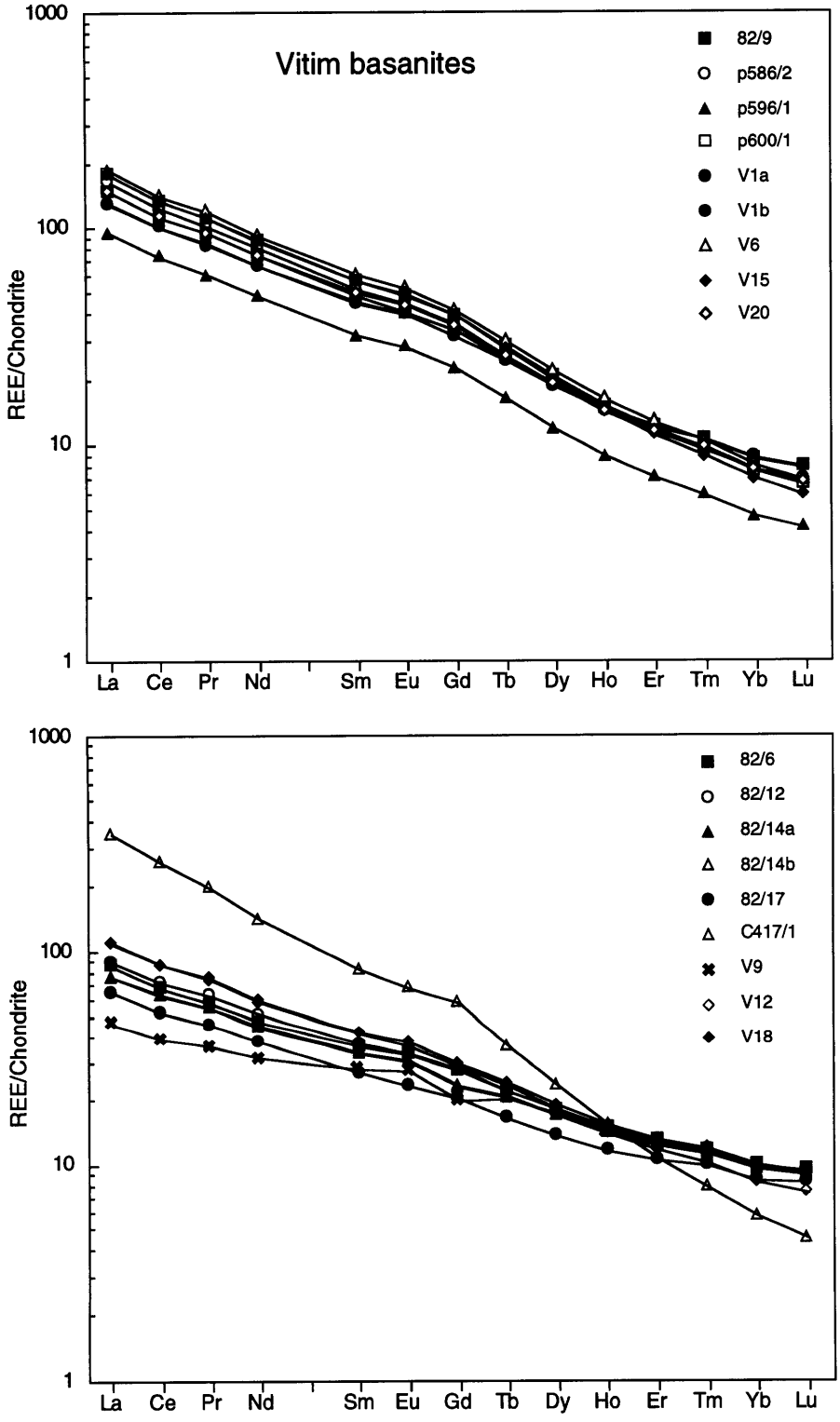
Vitim basanites
REE/Chondrite
1000
100
10
1
La Ce Pr Nd Sm Eu Gd Tb Dy Ho Er Tm Yb Lu
82/9
p586/2
p596/1
p600/1
V1a
V1b
V6
V15
V20
REE/Chondrite
1000
100
10
1
La Ce Pr Nd Sm Eu Gd Tb Dy Ho Er Tm Yb Lu
82/6
82/12
82/14a
82/14b
82/17
C417/1
V9
V12
V18

Figure 4.8

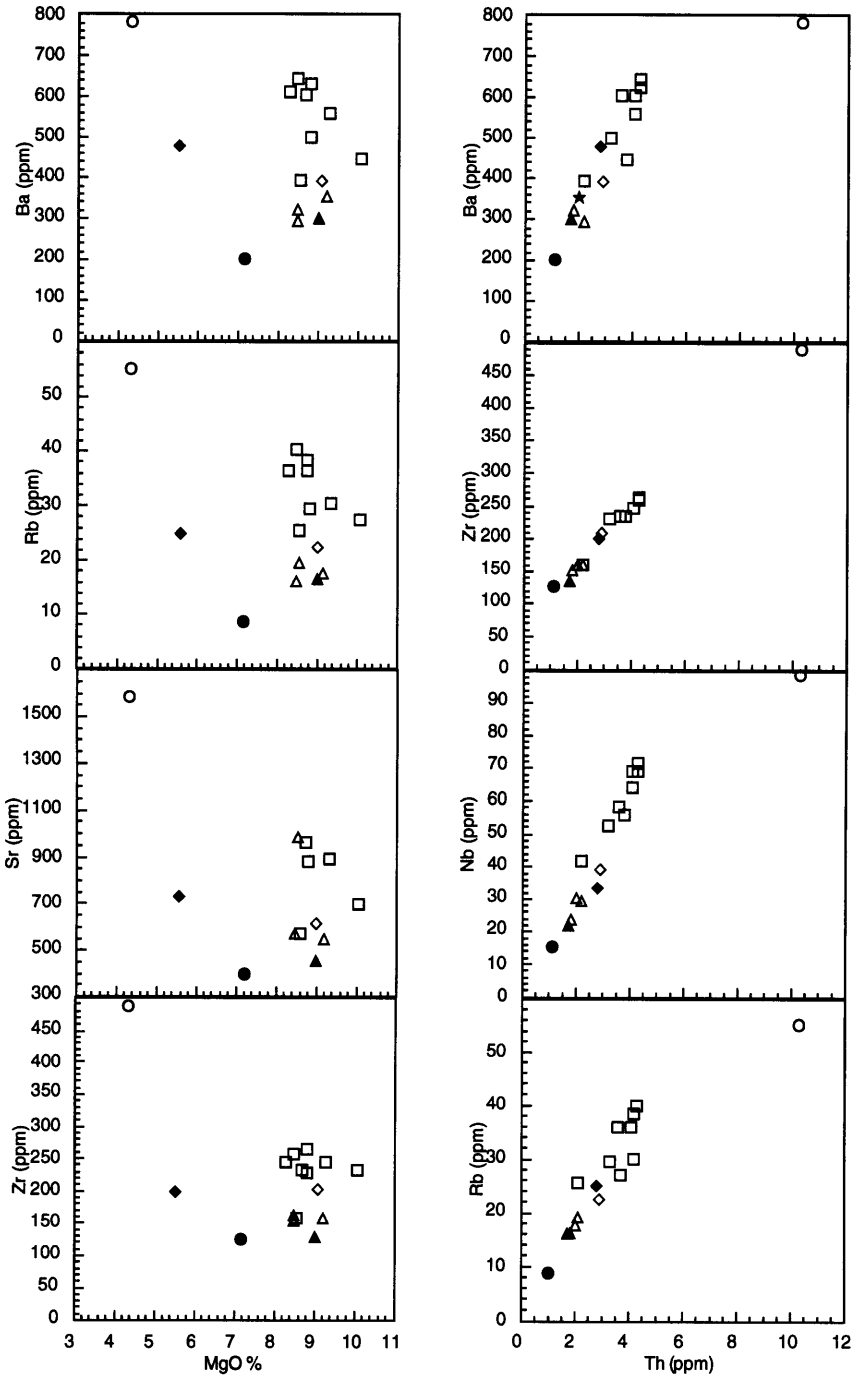

Figure 4.9

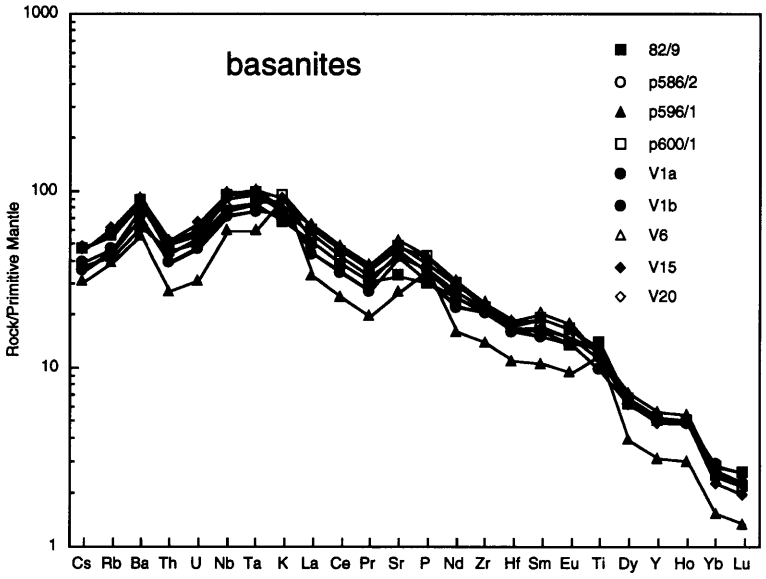
basanites
82/9
p586/2
p596/1
p600/1
V1a
V1b
V6
V15
V20
Rock/Primitive Mantle
1000
100
10
1
Cs Rb Ba Th U Nb Ta K La Ce Pr Sr P Nd Zr Hf Sm Eu Ti Dy Y Ho Yb Lu

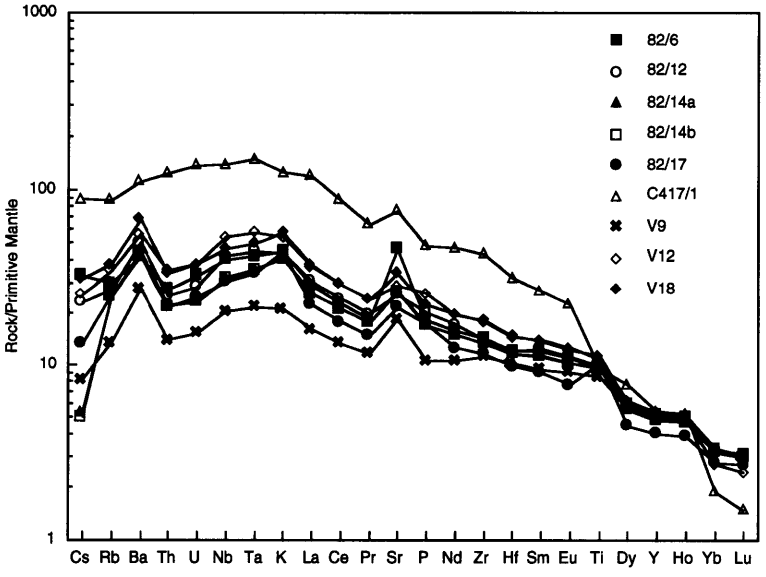
82/6
82/12
82/14a
82/14b
82/17
C417/1
V9
V12
V18
Rock/Primitive Mantle
1000
100
10
1
Cs Rb Ba Th U Nb Ta K La Ce Pr Sr P Nd Zr Hf Sm Eu Ti Dy Y Ho Yb Lu

Figure 4.10

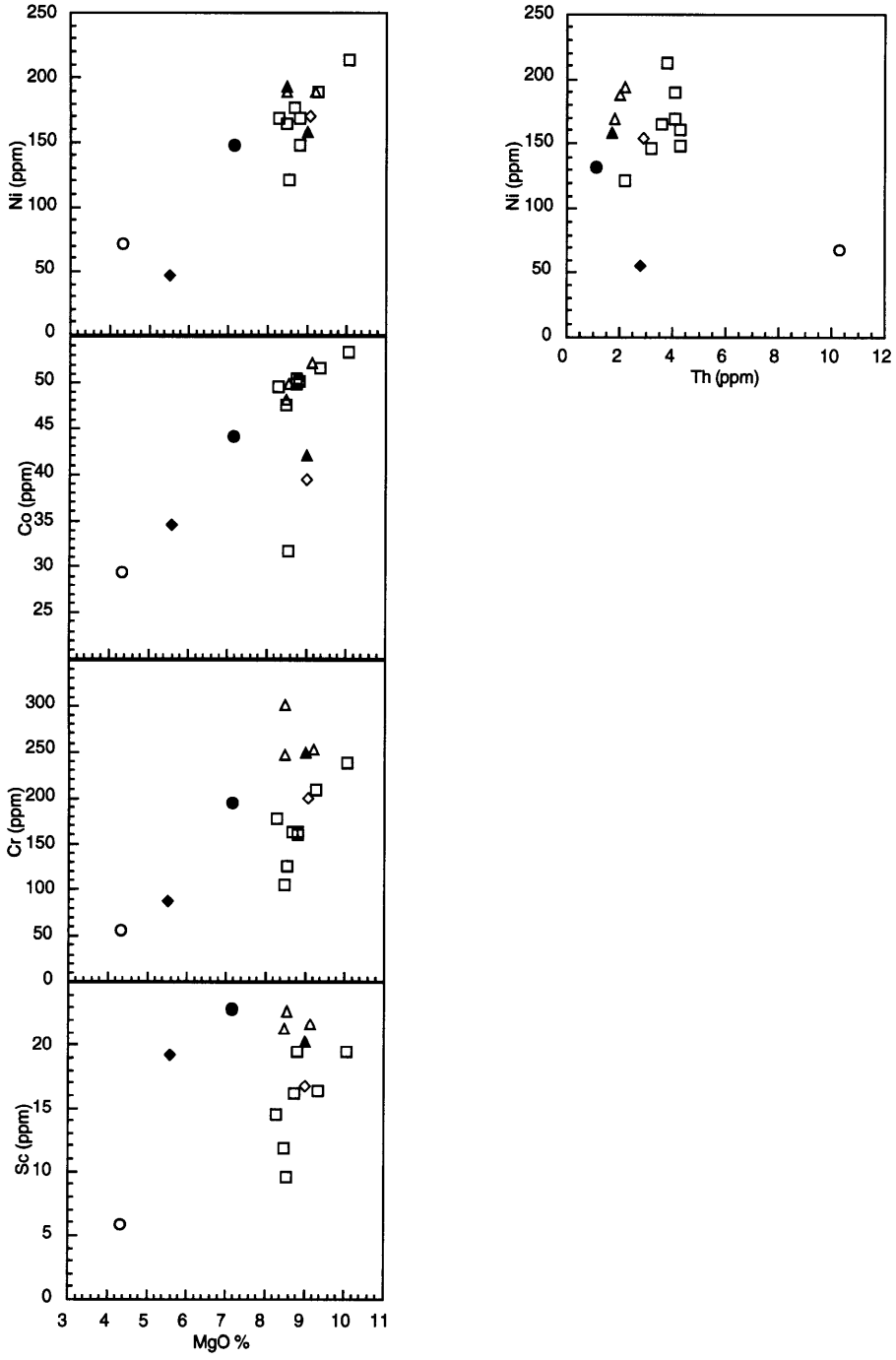

Figure 4.11

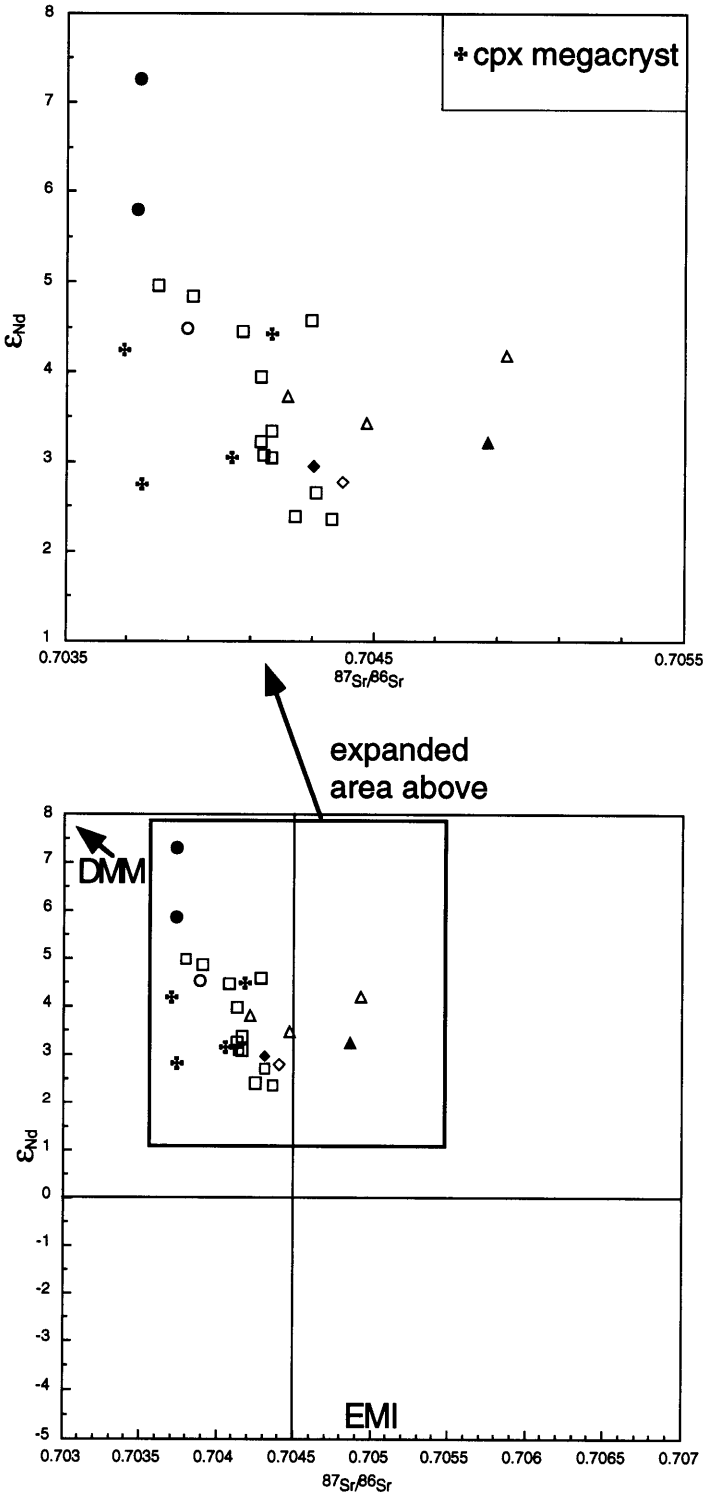
cpx megacryst
ε_{Nd}
$^{87}Sr/^{86}Sr$
0.7035
0.7045
0.7055
expanded
area above
DMM
EMI
0.703
0.7035
0.704
0.7045
0.705
0.7055
0.706
0.7065
0.707

Figure 4.12

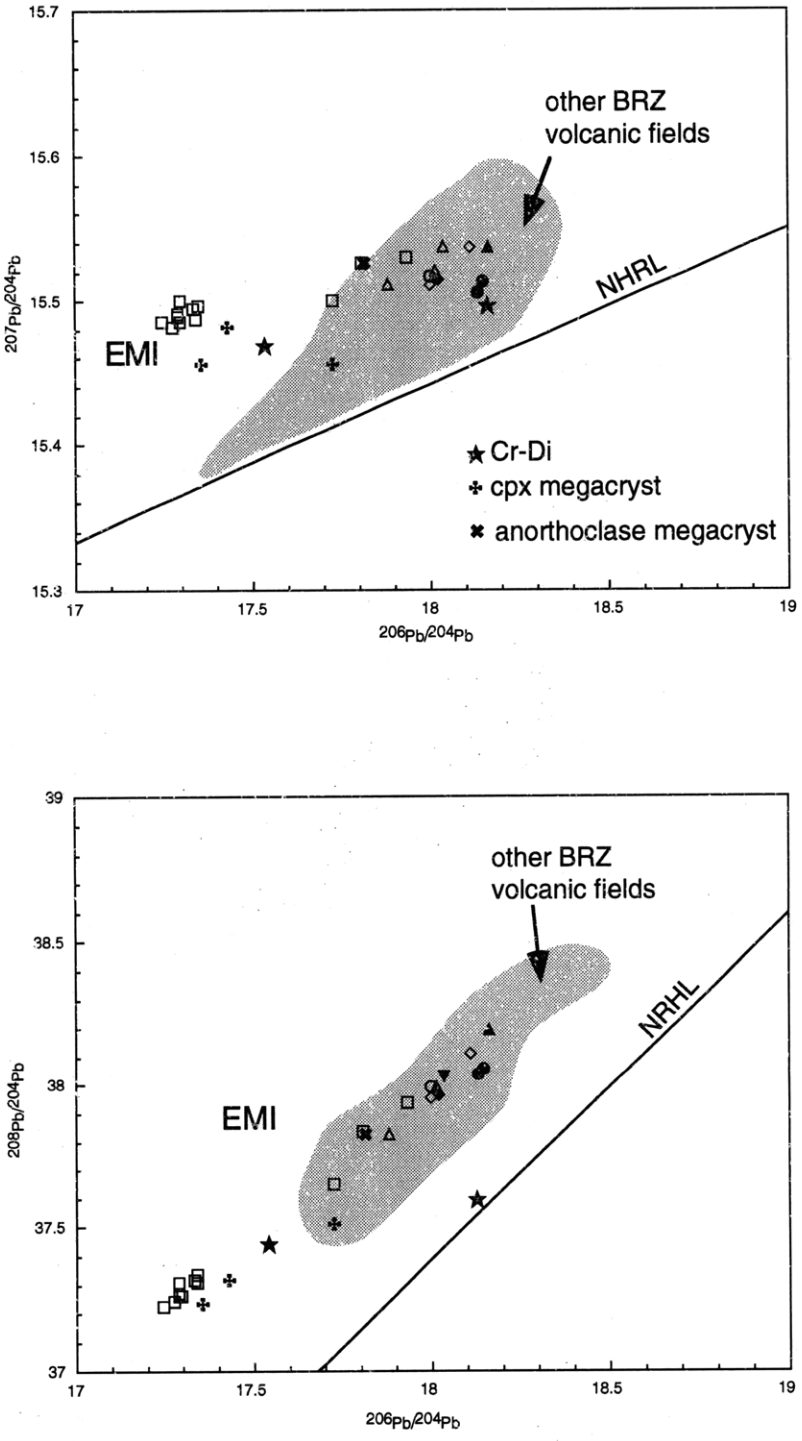
15.7
15.6
15.5
15.4
15.3
17
17.5
18
18.5
19
$^{207}Pb/^{204}Pb$
$^{206}Pb/^{204}Pb$
other BRZ
volcanic fields
NHRL
EMI
Cr-Di
cpx megacryst
anorthoclase megacryst
39
38.5
38
37.5
37
17
17.5
18
18.5
19
$^{208}Pb/^{204}Pb$
$^{206}Pb/^{204}Pb$
other BRZ
volcanic fields
NRHL
EMI

Figure 4.13

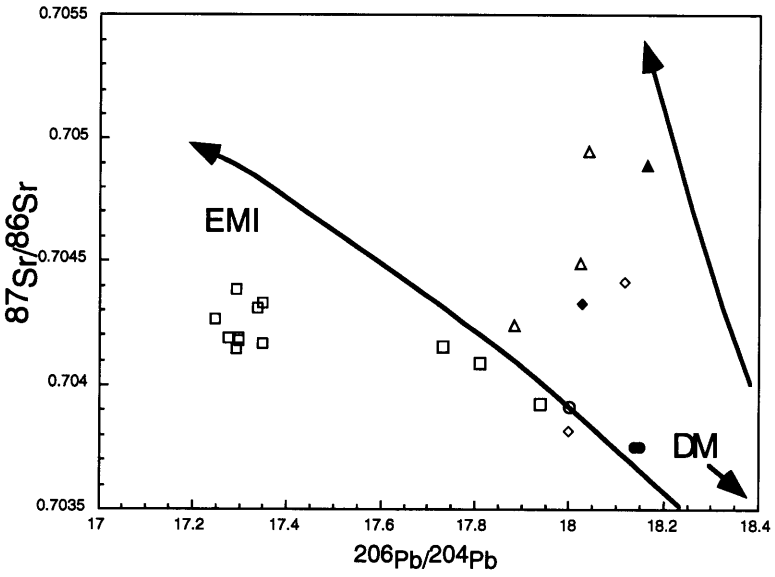
0.7055
0.705
0.7045
0.704
0.7035
87Sr/86Sr
EMI
DM
17
17.2
17.4
17.6
17.8
18
18.2
18.4
206Pb/204Pb

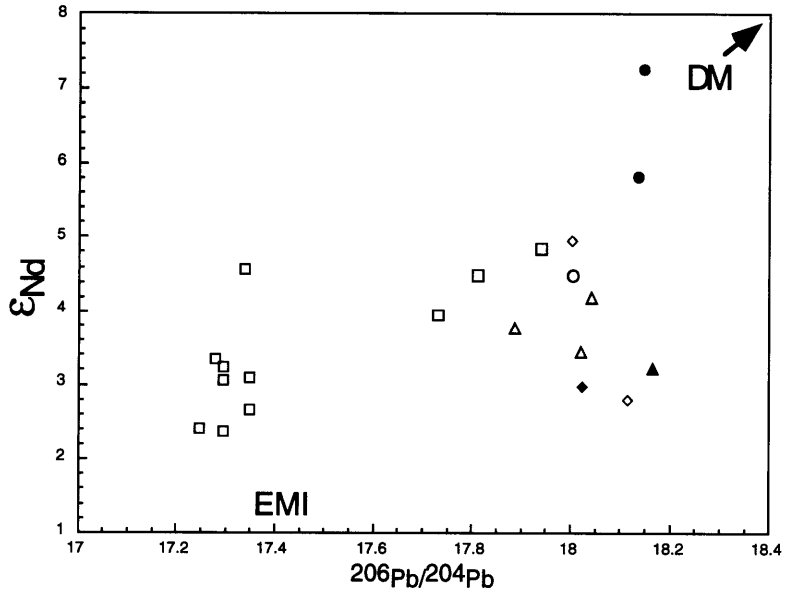
8
7
6
5
4
3
2
1
εNd
DM
EMI
17
17.2
17.4
17.6
17.8
18
18.2
18.4
206Pb/204Pb

Figure 4.14

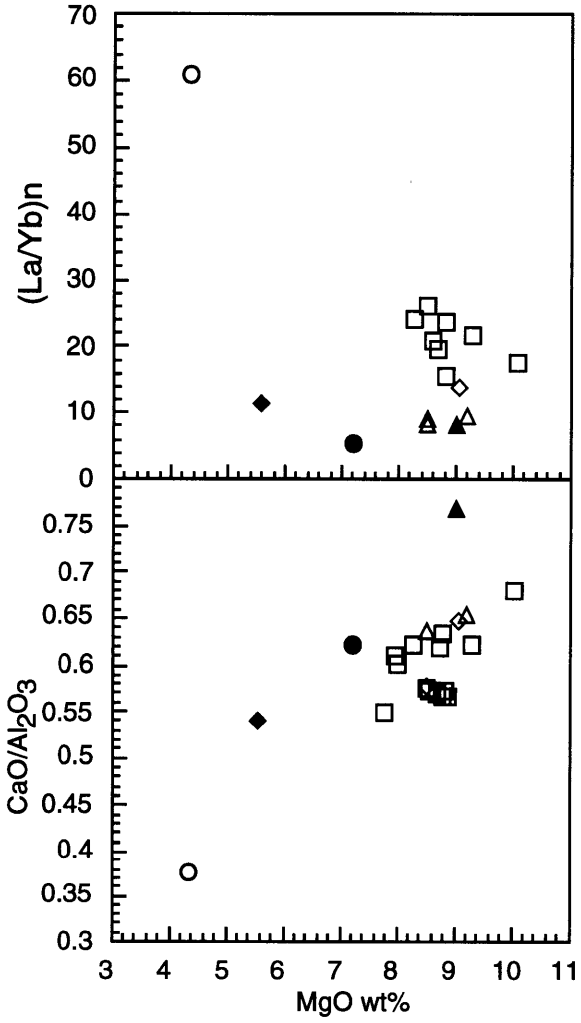
70
60
50
40
30
20
10
0
(La/Yb)n
0.75
0.7
0.65
0.6
0.55
0.5
0.45
0.4
0.35
0.3
CaO/Al2O3
3
4
5
6
7
8
9
10
11
MgO wt%

Figure 4.15

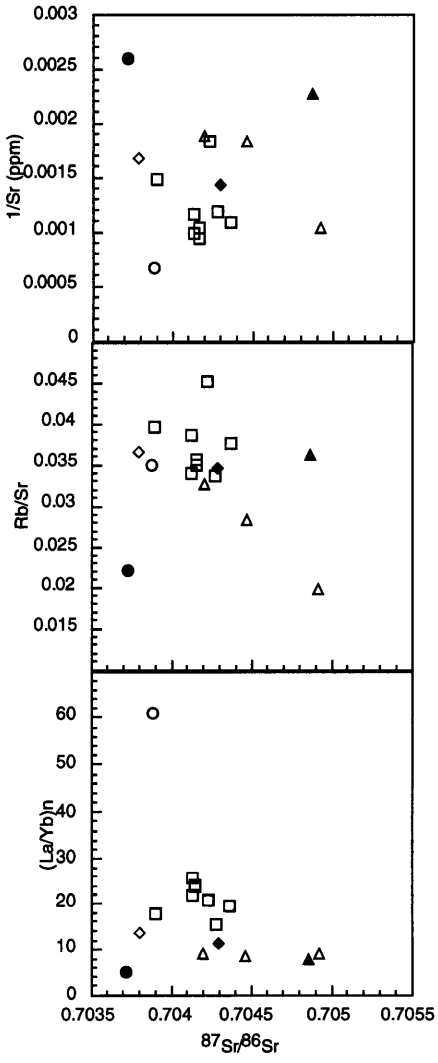
0.003
0.0025
0.002
0.0015
0.001
0.0005
0
1/Sr (ppm)
0.045
0.04
0.035
0.03
0.025
0.02
0.015
Rb/Sr
60
50
40
30
20
10
0
(La/Yb)n
0.7035
0.704
0.7045
0.705
0.7055
87Sr/86Sr

Figure 4.16

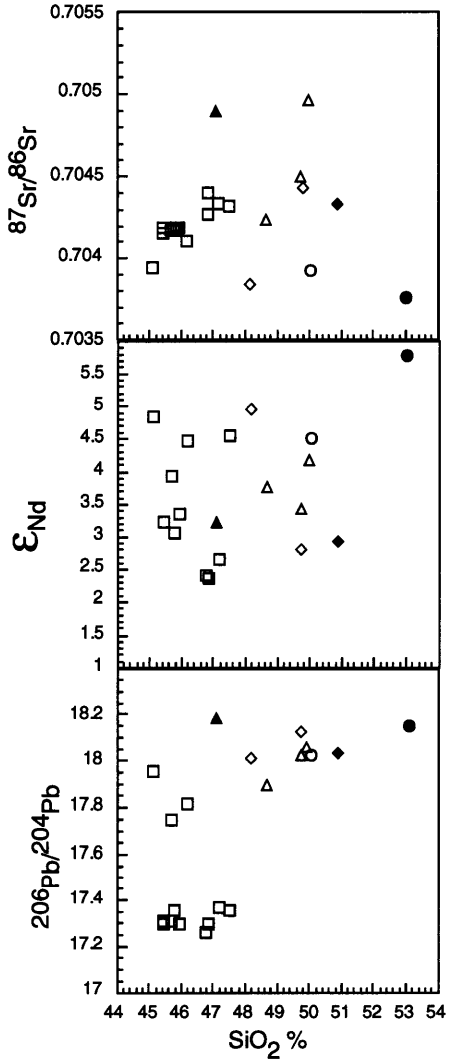
0.7055
0.705
0.7045
0.704
0.7035
$^{87}Sr/^{86}Sr$
5.5
5
4.5
4
3.5
3
2.5
2
1.5
1
ε_{Nd}
18.2
18
17.8
17.6
17.4
17.2
17
$^{206}Pb/^{204}Pb$
44 45 46 47 48 49 50 51 52 53 54
SiO_2 %

Table 4.1a $^{40}Ar/^{39}Ar$ data for Vitim volcanic rocks

Sample	location	plateau age	±2σ	cum % $^{39}Ar_n$	steps	isochron age	±2σ	steps	$^{39}Ar_i$ (%)	$(^{40}Ar/^{36}Ar)_0$	±2σ	MSWD	^{39}Ar Wtd. Mean age	±2σ
V1	Bulykta R.	0.61	±0.10	100 0	1-6	**0.65**	**±0.15**	1-5	94.23	287.9	±14 5	2.52	0.59	±0.13
V8	Kandıdushka V.	**1.01**	**±0.15**	84 4	2-5								1.21	±0.19
V12	E. Vitim	13 35	±0.17	95.1	2-6	**13.52**	**±0.27**	2-6	95 1	286.7	±9.5	0.30	13.92	±0 19

Notes: The preferred age is shown in bold type. Complete data tables for each sample given below.

$^{40}Ar/^{39}Ar$ Furnace Analytical Data for cl72/V1/WR

T (K)	$^{36}Ar/^{40}Ar$ ±2σ	$^{39}Ar/^{40}Ar$ ±2σ	^{39}Ar(%)	40Ar*(%)	Age (Ma)	±2σ
923	0.00222 ± 0 00169	0.2294 ± 0.00198	5.58	34.34	0.67	± 0.98
1073	0.00312 ± 0.00012	0.0708 ± 0.00025	35.56	7.94	0.51	± 0.22
1173	0.00148 ± 0.00050	0.4045 ± 0.00191	57.34	56.10	0.63	± 0.16
1323	0.00320 ± 0.00074	0.2231 ± 0 00111	73.99	5 34	0.11	± 0.44
1473	0.00186 ± 0.00046	0.2521 ± 0.00169	94.23	44.98	0.80	± 0.24
1673	0.00178 ± 0.00096	0.1488 ± 0.00235	100 00	47.36	1.43	± 0.86

J value: 2.50E-4 ± 1.45E-6. All steps of 10 minute duration. $^{40}Ar^*$(%) is percentage of measured ^{40}Ar derived from natural decay of ^{40}K.

$^{40}Ar/^{39}Ar$ Furnace Analytical Data for cl72/V8/WR

T (K)	$^{36}Ar/^{40}Ar$ ±2σ	$^{39}Ar/^{40}Ar$ ±2σ	^{39}Ar(%)	$^{40}Ar^*$(%)	Age (Ma)	±2σ
923	0.00001 ± 0.00099	0.2304 ± 0.00342	11.62	99.61	1.94	± 0.57
1073	0.00318 ± 0.00029	0.0663 ± 0 00032	33.39	5.90	0.40	± 0.57
1173	0.00043 ± 0.00154	0.2916 ± 0.00266	47.86	87 02	1.34	± 0.70
1323	0.00132 ± 0.00069	0.1937 ± 0.00094	64.08	60.90	1.41	± 0.47
1473	0.00186 ± 0.00032	0.2065 ± 0.00084	96.04	45.15	0.98	± 0.21
1673	0.00032 ± 0.00060	0.0988 ± 0.00115	100.00	90.57	4.11	± 0.81

J value: 2.49E-4 ± 1.67E-6. All steps of 10 minute duration. $^{40}Ar^*$(%) is percentage of measured ^{40}Ar derived from natural decay of ^{40}K.

$^{40}Ar/^{39}Ar$ Furnace Analytical Data for cl73/V12/WR

T (K)	$^{36}Ar/^{40}Ar$ ±2σ	$^{39}Ar/^{40}Ar$ ±2σ	^{39}Ar(%)	$^{40}Ar^*$(%)	Age (Ma)	±2σ
923	0.00000 ± 0.00009	0.0835 ± 0.00120	4.88	99.90	26.26	± 0.85
1073	0.00103 ± 0.00008	0.1164 ± 0.00033	28.35	69.62	13.18	± 0.45
1173	0.00025 ± 0.00006	0.1510 ± 0.00041	40.71	92.48	13.50	± 0.29
1323	0.00196 ± 0.00006	0.0713 ± 0.00022	55.60	42.10	13.02	± 0.54
1473	0.00117 ± 0.00005	0.1079 ± 0.00028	94.67	65.29	13.34	± 0.35
1673	0.00026 ± 0.00023	0.1487 ± 0.00060	100.00	92 27	13.68	± 1.02

J value: 1.23E-3 ± 1.30E-5. All steps of 10 minute duration. $^{40}Ar^*$(%) is percentage of measured ^{40}Ar derived from natural decay of ^{40}K.

Table 4.1b Ages for Dzhilinda basin drillcore taken from Rasskazov and Batyrmurzaev, 1985

Sample	Age
82/12	9.5±1 Ma
82/14	10.8±0.8 Ma
82/16	12.4±2 Ma
82/17	14±1.2 Ma
p597	4±0.6 Ma

Table 4.2. Major (wt%) and trace element (ppm) abundances in Vitim lavas

Sample	82/6	82/9	82/12	82/14a	82/14b	82/16	82/17	C417/1	p586/2	p596/1	p597	p600/1	p600/2	V1a	V1b	V3	V6
SiO_2	49.30	44.88	48.04	49.43		45.65	46.45	49.53	45.35	46.06	49.26	45.15	44.98	47.49		45.14	45.65
TiO_2	2.03	2.96	2.10	2.01		2.79	2.16	2.03	2.65	2.47	2.12	2.54	2.60	2.07		2.69	2.52
Al_2O_3	14.16	13.72	13.94	14.71		14.55	14.05	15.72	14.07	13.98	14.54	13.69	13.88	14.56		13.88	13.78
Fe_2O_{3t}	11.87	13.10	12.55	11.33		12.85	12.65	11.30	12.61	12.60	11.49	13.15	13.38	12.25		13.57	13.26
MnO	0.20	0.21	0.20	0.19		0.21	0.21	0.19	0.20	0.20	0.19	0.21	0.20	0.19		0.20	0.20
MgO	8.46	10.06	9.13	8.48		8.72	8.95	4.34	9.27	8.50	8.46	8.21	7.93	8.86		8.03	8.81
CaO	8.97	9.31	9.07	9.31		8.94	10.75	5.85	8.73	7.96	8.35	8.50	8.42	8.28		8.32	8.67
Na_2O	2.89	3.51	2.88	3.19		3.07	2.69	6.11	4.24	4.15	3.47	4.55	4.70	4.24		4.72	4.25
K_2O	1.32	1.99	1.29	1.23		2.39	1.32	3.72	2.23	2.70	1.56	2.75	2.91	2.24		2.98	2.35
P_2O_5	0.39	0.65	0.43	0.36		0.64	0.37	1.03	0.77	0.74	0.43	0.89	0.95	0.65		0.91	0.91
TOTAL	99.57	100.39	99.63	100.24		99.80	99.58	99.83	100.12	99.37	99.85	99.64	99.94	100.83		100.44	100.40
Mg#	62	64	63	64		61	62	47	63	61	63	59	58	63		58	61
Rb	18.9	26.7	17.4	15.7	16.0		16.1	54.8	29.7	25.1		35.7		29.2	28.7		38.0
Sr	976	681	538	560	563		448	1577	884	560		1005		872	871		1098
Ba	291	436	350	312	307		293	774	552	391		603		491	486		621
Sc	22.6	19.3	21.6	21.1	20.8		20.2	5.5	16.2	9.4		14.5		19.3	18.1		16.0
V				180	178			86						164	158		173
Cr	301	233	249	243	206		248	52	206	124		174		158	143		161
Co	49.7	52.8	52.0	47.7	46.1		41.7	29.0	51.5	31.6		49.4		50.0	48.3		49.6
Ni	191	210	185	167	139		156	65	187	119		166		143	116		159
Cu	63	62	65	53	51		57	23	48	27		43		43	39		46
Zn	112	109	115	105	103		80	179	121	84		140		127	122		147
Ga	26	30	28	22	22		20	40	35	23		38		29	28		33
Y	24	23	23	22	22		18	24	22	14		24		23	23		26
Zr	157	230	156	148	147		128	486	241	155		244		226	228		259
Hf	3.70	5.09	3.63	3.51	3.52		3.00	9.85	5.11	3.33		5.30		4.95	4.97		5.61
Nb	28.5	55.0	30.0	22.8	22.6		21.7	98.3	63.7	41.6		67.7		51.8	51.2		70.0
Ta	1.74	3.42	1.81	1.45	1.45		1.38	6.04	3.84	2.43		3.92		3.13	3.13		4.05
Th	2.31	3.86	2.14	1.87	1.84		1.81	10.38	4.24	2.29		4.20		3.35	3.28		4.34
U	0.68	1.06	0.59	0.48	0.48		0.51	2.84	1.19	0.65		1.17		1.01	0.99		1.26
La	19.8	34.5	20.9	17.7	17.7		15.2	81.1	38.2	22.2		41.4		30.1	30.1		43.4
Ce	40.0	68.0	42.7	37.4	37.3		31.2	153.3	73.9	43.7		81.1		60.0	60.4		85.2
Pr	5.0	8.3	5.4	4.8	4.8		4.0	17.3	8.9	5.3		9.8		7.4	7.5		10.5
Nd	21.3	33.3	23.1	20.2	20.0		17.0	63.3	36.0	21.7		39.4		29.7	29.9		41.1
Sm	5.26	7.01	5.46	4.94	4.89		3.96	12.00	7.50	4.63		8.23		6.55	6.61		8.86
Eu	1.81	2.25	1.84	1.71	1.68		1.30	3.69	2.47	1.56		2.70		2.23	2.23		2.92
Gd	5.35	6.58	5.45	4.58	4.51		3.98	11.17	6.95	4.36		7.63		6.14	6.11		8.11
Tb	0.80	0.90	0.80	0.75	0.74		0.59	1.30	0.93	0.59		1.01		0.87	0.88		1.09
Dy	4.36	4.58	4.33	4.09	4.07		3.29	5.60	4.55	2.85		4.90		4.49	4.48		5.28
Ho	0.82	0.80	0.81	0.78	0.77		0.64	0.85	0.78	0.49		0.83		0.80	0.81		0.88
Er	2.06	1.93	2.04	1.96	1.94		1.66	1.69	1.80	1.12		1.87		1.91	1.92		1.98
Tm	0.28	0.25	0.28	0.27	0.27		0.24	0.19	0.23	0.14		0.23		0.25	0.25		0.25
Yb	1.60	1.38	1.59	1.55	1.55		1.36	0.92	1.25	0.75		1.22		1.38	1.40		1.30
Lu	0.23	0.19	0.23	0.22	0.22		0.20	0.11	0.17	0.10		0.16		0.19	0.19		0.17

Notes: Major elements determined by XRF at UMass-Amherst. All trace elements determined by ICP-MS at MIT. Mg# = 100*atomic Mg/(Mg + Fe^{2+}), calculated with FeO = .15* Fe_2O_{3total}.

Table 4.2. Major (wt%) and trace element (ppm) abundances in Vitim lavas continued

Sample	V8	V9	V12	V13	V15	V18	V19	V20
SiO_2	46.37	52.89	47.73	45.85	45.35	50.71	46.70	46.48
TiO_2	2.41	1.85	2.42	2.61	2.72	2.28	2.33	2.38
Al_2O_3	14.14	14.36	13.46	14.09	13.93	16.13	14.21	14.11
Fe_2O_{3t}	12.37	11.18	13.11	12.94	13.42	10.75	12.38	12.49
MnO	0.19	0.18	0.20	0.19	0.19	0.17	0.19	0.19
MgO	8.86	7.23	9.00	7.75	8.45	5.61	8.76	8.70
CaO	7.97	8.87	8.68	7.70	7.95	8.69	8.01	7.98
Na_2O	4.11	3.08	3.33	5.01	4.55	3.88	4.17	4.42
K_2O	2.60	0.63	1.61	3.10	2.67	1.70	2.42	2.60
P_2O_5	0.73	0.23	0.56	1.02	0.81	0.48	0.70	0.74
TOTAL	99.73	100.48	100.10	100.26	100.03	100.41	99.88	100.09
Mg#	63	60	62	58	60	55	62	62
Rb		8.5	22.0		39.6	24.4		35.5
Sr		389	607		1030	713		951
Ba		194	387		637	470		597
Sc		22.7	16.6		11.7	19.0		16.0
V		169	151		135	183		164
Cr		193	198		102	85		160
Co		43.8	39.2		47.2	34.3		50.1
Ni		131	151		146	54		162
Cu		55	54		37	40		42
Zn		110	108		137	104		130
Ga		21	22		32	28		30
Y		23	22		22	24		22
Zr		123	202		254	198		229
Hf		3.12	4.54		5.52	4.47		5.07
Nb		14.5	38.4		68.9	32.7		57.0
Ta		0.88	2.34		4.15	2.03		3.47
Th		1.18	2.99		4.40	2.88		3.74
U		0.32	0.79		1.37	0.81		1.13
La		10.8	25.4		41.4	25.8		34.7
Ce		23.4	51.8		80.8	52.1		68.1
Pr		3.2	6.5		9.9	6.6		8.4
Nd		14.2	26.2		38.7	26.5		33.3
Sm		4.08	6.09		8.22	6.16		7.28
Eu		1.52	2.04		2.70	2.09		2.44
Gd		3.89	5.60		7.73	5.83		6.91
Tb		0.73	0.85		1.00	0.87		0.92
Dy		4.15	4.38		4.78	4.59		4.56
Ho		0.78	0.78		0.79	0.84		0.79
Er		2.00	1.85		1.76	2.08		1.81
Tm		0.28	0.25		0.21	0.29		0.23
Yb		1.57	1.33		1.12	1.63		1.25
Lu		0.22	0.18		0.14	0.22		0.16

Notes: Major elements determined by XRF at UMass-Amherst. All trace elements determined by ICP-MS at MIT. Mg# = 100*atomic Mg/(Mg + Fe^{2+}), calculated with FeO = .15* Fe_2O_{3total} .

Table 4.3. Sr, Nd and Pb isotopic ratios of Vitim lavas

SAMPLE	LOCATION	$^{87}Sr/^{86}Sr$	$\pm 2\sigma$	$^{143}Nd/^{144}Nd$	$\pm 2\sigma$	$\varepsilon_{Nd}(0)$	$\pm 2s$	$^{206}Pb/^{204}Pb$	$^{207}Pb/^{204}Pb$	$^{208}Pb/^{204}Pb$
82/6	Dzhilinda basin	0.70494	±0.00001	0.512851	±0.000008	4.15	±0.16	18.046	15.536	38.026
82/9	Dzhilinda basin	0.70392	±0.00001	0.512884	±0.000006	4.80	±0.12	17.943	15.528	37.935
82/12	Dzhilinda basin	0.70423	±0.00001	0.512828	±0.000009	3.71	±0.18	17.888	15.511	37.826
82/14	Dzhilinda basin	0.70448	±0.00001	0.512813	±0.000012	3.40	±0.24	18.025	15.520	37.985
82/16	Dzhilinda basin	0.70408	±0.00001	0.512865	±0.000006	4.43	±0.12	17.814	15.525	37.827
82/17	Dzhilinda basin	0.70488	±0.00001	0.512802	±0.000006	3.19	±0.12	18.169	15.537	38.197
C417/1	Dzhilinda basin	0.70390	±0.00001	0.512866	±0.000006	4.44	±0.12	18.006	15.516	37.984
p586/2	Bol. Amalat R.	0.70415	±0.00001	0.512839	±0.000006	3.92	±0.12	17.734	15.499	37.646
p596/1	Bol. Amalat R.	0.70425	±0.00001	0.512759	±0.000005	2.36	±0.10	17.250	15.485	37.217
p597	Bol. Amalat R.	0.70441	±0.00001	0.512779	±0.000006	2.75	±0.12	18.120	15.536	38.107
p600/1	W. Vitim	0.70418	±0.00001	0.512793	±0.000006	3.02	±0.12	17.300	15.485	37.259
p600/2	W. Vitim	0.70417	±0.00001					17.299	15.499	37.300
V1	Bulykta R.	0.70430	±0.00002	0.512870	±0.000009	4.53	±0.18	17.340	15.494	37.314
V3	Kandidushka V.	0.70414	±0.00002	0.512802	±0.000008	3.20	±0.16	17.298	15.490	37.269
V6	Kandidushka V.	0.70417	±0.00001	0.512808	±0.000009	3.31	±0.18	17.280	15.481	37.238
V9	E. Vitim	0.70374	±0.00001	0.512934	±0.000009	5.78	±0.18	18.140	15.505	38.031
V11dike	E. Vitim	0.70375	±0.00001	0.513009	±0.000011	7.24	±0.22	18.153	15.513	38.056
V12	E. Vitim	0.70381	±0.00002	0.512890	±0.000005	4.92	±0.10	18.004	15.509	37.952
V15	Kandidushka V.	0.70415	±0.00001	0.512794	±0.000005	3.04	±0.10	17.350	15.486	37.303
V18	Dzhilinda R.	0.70431	±0.00001	0.512788	±0.000006	2.93	±0.12	18.029	15.514	37.964
V19	Dzhilinda R.	0.70432	±0.00001	0.512773	±0.000007	2.63	±0.14	17.351	15.496	37.329
V20	Dzhilinda R.	0.70438	±0.00001	0.512757	±0.000009	2.32	±0.18	17.296	15.487	37.256

Notes: Sr data are normalized to $^{86}Sr/^{88}Sr = 0.1194$ and corrected for mass fractionation using an exponential law. Replicate analyses of NBS-987 Sr yield $^{87}Sr/^{86}Sr = 0.710240 \pm 0.000016$ (2σ). Nd data are normalized to $^{146}Nd/^{144}Nd = 0.7219$ and corrected for mass fractionation using an exponential law. Replicate analyses of La Jolla Nd yield $^{143}Nd/^{144}Nd = 0.511845 \pm .000011$ (2σ). $\varepsilon_{Nd}(0)$ is calculated with $^{143}Nd/^{144}Nd_{CHUR} = 0.512638$. Based on replicate analyses of NBS-981, Pb is corrected by 0.12%/mass unit to account for fractionation.

amphibole, garnet, and biotite, to address the problem of the genesis of megacrysts from the viewpoint of isotopic equilibrium. Cr-diopside from upper mantle xenoliths are also examined for comparison of megacrysts with the sub-Baikal lithospheric mantle. To assess equilibrium, the data for megacrysts from each region of the BRZ and each of the mineral types is compared and contrasted, and discussed within the overall context of the regional host volcanic rock data.

GEOLOGIC SETTING OF THE BAIKAL RIFT ZONE

The Baikal Rift Zone (BRZ) in southeastern Siberia (Fig. 5.1) is one of the world's largest active continental rifts. The BRZ is expressed as an approximately 1800 km-long southwest-northeast oriented system of rift valleys and faults situated along a suture between the Archean Siberian shield and younger Paleozoic fold belts, and is associated with a broad area of domal uplift (Logatchev, 1993). Alkaline volcanic rocks of Oligocene to Recent age are associated with rifting and distributed in three major regions of the rift (Kiselev, 1987): the broad region west of Lake Baikal that includes the Oka Plateau, Tunka, Dhzida, and Tuva volcanic fields; the Udokan volcanic field in the northeast, which partially overlaps the suture with the Siberian craton; and the Vitim volcanic field, situated ~200 km southeast of the rift zone axis on the Vitim Plateau.

The cause of Cenozoic rifting and the associated volcanism in the BRZ has been a subject of considerable debate because of the rift's location thousands of kilometers from any active plate boundary (Fig. 5.1). High heat flow (~1.5 times the background of surrounding areas; Lysak, 1987) and the domal uplift correspond to a region of

Binns et al., 1970; Chapman, 1976; Chapman and Powell, 1976; Ellis, 1976; Irving, 1974; Irving and Frey, 1978; Irving and Frey, 1984; Liotard et al., 1983, 1988; Stuckless and Irving, 1976; Wilkinson and Hensel, 1991; Aspen et al., 1990).

The idea that megacrysts might be high-pressure phases genetically related to their host rocks intrigued early researchers trying to understand the high pressure evolution trend of basaltic magmas (Binns, 1969; Binns et al., 1970; Chapman, 1976). Unlike ultramafic nodules whose mineral compositions and textures usually demonstrate disequilibrium between host and xenolith, megacrysts often occur as large, undeformed, homogeneous single phase crystals with corroded euhedral or subhedral crystal faces. Their physical characteristics as well as lack of exsolution phenomena suggest they were quenched from high temperature, while marginal reaction rims or coronas around the crystals indicate they are unstable in their host at low temperature and pressure. Megacryst compositions usually differ from those of similar groundmass phases in their host or in associated ultramafic nodules (Binns, 1970). On the basis of such features in New South Wales (NSW) lavas, Binns (1969, 1970) concluded that the megacrysts crystallized directly from a melt parental to their host basanite under different P-T conditions than those of the eruption.

One way to assess equilibrium between a megacryst and host is to compare calculated major element partition coefficients with experimentally determined ones, such as $K_D^{Fe2+/Mg}$. An alternative method is to compare the isotopic composition of the megacryst and host. This study examines the Sr, Nd, and Pb isotope systematics of Baikal Rift Zone (BRZ) clinopyroxene and feldspar megacrysts, as well as kaersutite,

are predominantly more radiogenic than regional volcanic rocks. The range of Sr and Pb isotopic compositions for anorthoclase megacrysts from the Udokan and Vitim volcanic fields falls within the range of host rocks. The kaersutite, garnet, and biotite megacrysts also have isotopic compositions similar to their host rocks.

The overall similarity in isotopic compositions suggests that the megacrysts are related in some way to their host rocks. If the megacrysts are derived from a magma related to or parental to the host volcanic rocks, the fact that the clinopyroxene, amphibole, and garnet megacrysts have less radiogenic Sr and more radiogenic Nd isotopic composition than their hosts suggests the host lavas may have been affected by interaction with a low $^{143}Nd/^{144}Nd$, high $^{87}Sr/^{86}Sr$ (crustal?) component before eruption. Megacryst/host relationships may be a reliable indicator of post-melting contamination.

INTRODUCTION

Megacrysts are large (.5 - 15 cm) single crystal inclusions that commonly occur in alkali basalts and are often out of isotopic equilibrium with their host rocks. The world-wide association of megacrysts with alkali basalts has long been thought to imply an inherent relationship between the megacrysts and their host rocks. Current models for the origin of megacrysts were developed from the investigation of occurrences in New South Wales, Australia, East Fife, Scotland, Kakanui, New Zealand, Ross Island, Antarctica and fields in the American southwest, and range from precipitation of megacrysts from a magma related to or similar to their host rock (at high pressure) to precipitation from an unrelated melt, possibly in metasomatized veins (e.g. Binns, 1969;

CHAPTER 5

MEGACRYSTS AND UPPER MANTLE XENOLITHS OF THE BAIKAL RIFT ZONE, SIBERIA: SR, ND, AND PB ISOTOPIC CONSTRAINTS ON THE ORIGIN OF MEGACRYSTS AND IMPLICATIONS FOR THE NATURE OF THE SUB-BAIKAL LITHOSPHERIC MANTLE

ABSTRACT

Clinopyroxene, anorthoclase, and rare amphibole, garnet, and biotite megacrysts from the Baikal Rift Zone, Siberia, provide an opportunity to assess the relationship between megacrysts and host volcanic rocks, and provide insight into asthenosphere/lithosphere interactions beneath the BRZ. In addition, upper mantle xenoliths provide direct evidence about the isotopic composition of the sub-Baikal mantle. Sr, Nd and Pb isotopic data for the megacrysts and upper mantle xenoliths are compared to isotopic data for volcanic rocks from each of the three major volcanic regions of the Rift: the western zone (Oka Plateau and Bartoy center), Udokan, and Vitim.

The data for the upper mantle xenoliths indicates that they derive from a strongly depleted and isotopically heterogeneous mantle, characterized by low $^{87}Sr/^{86}Sr$ (0.70023 to 0.70323) and high ε_{Nd} (+8.7 to +16.9), that is clearly not the source of the megacrysts. In general, the measured isotopic ratios for megacrysts from each area is consistent with the range for volcanic rocks from the same area. However, clinopyroxene megacrysts from the Oka Plateau and Udokan range to less radiogenic Sr and more radiogenic Nd than their host volcanic rocks. Pb isotopic data for the clinopyroxene megacrysts falls within the range of regional host volcanic rocks, except in the Udokan area, where clinopyroxenes

anomalously low-velocity mantle, as seen by seismic and gravity imaging (Gao et al.,1994), leading some researchers to believe the rift is caused by an upwelling plume (Logatchev and Zorin, 1987, 1992). However, the relatively low volume of volcanism for a rift its size (~6000 km^3), as well as the lack of volcanic activity within the Lake Baikal basin itself, have lead other researchers to propose that rifting can be explained by the kinematic effects of tectonic motions at far-away plate boundaries, in particular the India-Eurasia collision (Molnar and Tapponnier, 1975, 1977; Zonenshain and Savostin, 1981.). Most recently, researchers have proposed a compromise between the two end-member theories by recognizing that the BRZ may be the result of a complex combination of far-field stresses and upwelling asthenosphere (Dobretsov et al., 1996; Delvaux et al., 1995).

The BRZ, like other areas of continental alkaline volcanism, contains abundant localities of upper mantle xenoliths and megacrysts. The two most notable and well-documented locations in the BRZ are the Vitim volcanic field (Ionov et al., 1993) and the Bartoy volcanic center (Ionov et al., 1992) in the Dzhida Basin of the western BRZ. Vitim volcanic rocks contain rare garnet-bearing peridotite xenoliths in addition to the more common spinel lherzolites and pyroxenites (Ionov et al., 1993.). The Bartoy volcanic center contains both hydrous and anhydrous peridotite xenoliths. Studies of the xenoliths from these areas has revealed that the sub-Baikal mantle is heterogeneous within the scale sampled at single eruptive centers, and is variably metasomatized.

DESCRIPTION OF THE MEGACRYST SUITE

Clinopyroxene and anorthoclase megacrysts are the most abundant megacryst types found in Baikal Rift Zone volcanic rocks. Usually, both of these megacryst types are found in the same host rock, and may be accompanied by rarer megacrysts of kaersutitic amphibole, Ti-magnetite, ilmenite, garnet, zircon, and Ti-biotite. Megacrysts occur as inclusions in fissure-type volcanic flows, as well as scoria from cinder cones. In all areas, megacrysts are associated with occurrences of mantle xenoliths of peridotite, pyroxenite or garnet lherzolite. Often, locales containing mantle xenoliths and megacrysts also contain small, altered crustal xenoliths.

Clinopyroxene megacrysts

Clinopyroxene (cpx) megacrysts are the most abundant megacryst species found in many of the Baikal Rift volcanic rocks. They range in size from 0.5 cm to 15 cm in length, and generally do not have well-developed crystal faces (Fig. 5.2). Many appear to have been rounded, perhaps during eruption/ascent. Occasionally they are surrounded by a thin (<.2 cm) rim of reaction material, but are otherwise unzoned. Small inclusions of fluids, sulfides, and micas are sometimes observed. Included in this study are 7 cpx from the Oka Plateau, 1 from the Bartoy center in the Dzhida Basin, 3 from Udokan, and 7 from Vitim.

Anorthoclase megacrysts

Anorthoclase megacrysts are the second most common megacryst species in BRZ volcanic rocks. They range in size from 0.25 cm - 7 cm in length (Fig. 5.3), and are optically homogeneous. They occasionally have one or more well-developed crystal faces. Some are very clear, while others may be more cloudy or even reddish. Inclusions of micas and sulfides are quite common, and often appear to be oriented along a plane within the crystal. Tube-like fluid inclusions, also aligned, have been observed in a few of the analyzed megacrysts. The anorthoclases included in this study are 3 from the Bartoy center, 11 from Udokan, and 5 from Vitim.

Kaersutite

Kaersutite amphibole megacrysts are not as common as the cpx or anorthoclase species. Kaersutites range from 0.5 to 5 cm (Fig. 5.4), and are often dark black and glassy in appearance. The kaersutite analyzed for this study is from the Bartoy center.

Mica

Occurrences of mica megacrysts are quite rare, and are usually found in scoria. They occur as mica books, and may contain very abundant apatite inclusions. Two biotite megacryst from the Bartoy center are included in this study. One of the biotites (Bartoy biot-dated) had abundant apatite inclusions, while the other had no visible inclusions.

Garnet

Garnet megacrysts are also extremely rare in BRZ rocks. This variety of megacryst usually appears as somewhat rounded single crystals ~2 cm in diameter. The garnets usually contain significant vein alteration material, but where fresh are ruby red and glassy in appearance (Fig. 5.5). The garnet megacryst included in this study is from the Bartoy center.

Upper mantle xenoliths

As mentioned above, the BRZ lavas contain abundant and varied upper mantle xenoliths. Sr and Nd isotopic data exists for the Bartoy spinel lherzolites (Ionov et al., 1992) and the Vitim garnet and spinel lherzolites (Ionov et al., 1993), but no Pb isotopic data has previously been obtained. Because the emphasis of this study is on the megacryst isotope systematics, we analyzed only a limited number of peridotite xenoliths. In all cases, separates of Cr-diopside were prepared by our Russian colleague Sergei Rasskazov at the Institute of the Earth's Crust, in Irkutsk, Siberia. The pyroxene separates included in this study are from four spinel lherzolites from a single xenolith locale in the Oka Plateau (R-1, R-2, R-87, R-88), a spinel lherzolite from the Dzhilinda River in the Vitim volcanic field (p585/3), and a garnet lherzolite from the picrite tuff (Bereya) quarry in the Vitim area (B1/3-1) that was first described by Ashchepkov and others.

ANALYTICAL METHODS

Mineral compositions of the Baikal Rift megacrysts and lherzolites were determined using the M.I.T 4-spectrometer JEOL 733 superprobe, with a 15 Kev accelerating voltage, 10 nA beam current, and a 10 μm beam size. The data were reduced using Bence and Albee (1968) matrix corrections with the Albee and Ray (1970) modification. Mineral compositions are given in Tables 5.1 - 5.3 and in most cases are the average of several spot analyses. For all analyzed megacrysts, analysis of the edge of the megacryst was compared to analysis of the center, but all were found to be homogeneous within analytical uncertainty.

For isotopic analysis, megacrysts and the Cr-diopside separates were carefully crushed by hand in an agate or a diamonite (synthetic corundum) mortar and pestle, followed by sieving through 250 μm disposable nylon mesh to remove the fine fraction. Crushed grains were then ultrasonically cleaned in ethyl alcohol to remove any powder adhering to grains before using a Franz magnetic separator to remove the most magnetic grains. Grains were then hand-picked in ethanol under a binocular microscope to assure a very high-quality fraction with no visible pieces of basalt, inclusions, or discolorations.

Prior to dissolution, cpx, kaersutite, and garnet grains were leached 30 minutes in 3N HCl at 250° F, 20 minutes at room temperature in 5% HF, and again 30 minutes in 3N HCl. Grains were rinsed in distilled H_2O between each step, and the leachate + rinse was saved for analysis. After leaching, each cpx and kaersutite sample was divided into a fraction for Sr and Nd analysis, and a fraction for Pb analysis, and was spiked accordingly

and dissolved in Savillex beakers with concentrated HF and 50% HNO3, followed by conversion to chloride form. The garnet was dissolved for Sr and Nd analysis only.

Anorthoclase grains were also leached, but with a shorter duration for each step and only at room temperature. Separate fractions of each sample were dissolved for isotopic composition and isotope dilution because of the high concentration of Sr and Pb in feldspar. Anorthoclase was also dissolved in Savillex beakers with concentrated HF and 50% HNO3, followed by conversion to chloride form. In most instances, a complete dissolution of the anorthoclase was achieved only after placing beakers in an ultrasonic bath.

The biotite megacrysts were prepared by carefully separating the sheets of mica and examining them under a binocular microscope for inclusions and alteration. They were then gently rinsed in distilled acetone. The separated mica sheets were leached in 3N HCl at room temperature for ~30 minutes, which successfully removed apatite inclusions. They were then dissolved in HF-HNO3 in Teflon beakers on a hotplate followed by conversion to chloride form. Biotites were analyzed for Sr isotopic composition only. Single grains of apatite included in one of the biotite megacrysts were extracted and dissolved in 6N HCl for Sr isotopic analysis.

Rare earth elements were separated by cation exchange columns with HCl as eluant. Sm and Nd were separated using HDEHP-coated BioBead resin with HCl as eluant. Sr separation was accomplished in micro-columns using Sr-spec resin and HNO_3 chemistry. Pb was separated using HBr-based chemistry on anion exchange resin in microcolumns. All reagents used were distilled to reach ultrahigh purity for trace

elements. Total procedural blanks are estimated to be <100 pg for Sr, <400 pg for Nd, and <10 pg for Pb.

Isotopic compositions were determined on a VG sector-54 mass spectrometer at the Massachusetts Institute of Technology. Sr and Nd isotopic compositions were measured in dynamic multicollector mode, while Pb, Rb, and Sm isotopic compositions were analyzed in static multicollector mode. For some very small samples, Pb isotopic compositions were measured in static Faradaly or singly Daly mode. Sr isotopic ratios are normalized to $^{86}Sr/^{88}Sr = 0.1194$, and Nd isotopic ratios are normalized to $^{146}Nd/^{144}Nd = 0.7219$. Sr and Nd isotopic ratios are corrected using an exponential fractionation law. Based on analyses of NBS-981, Pb isotopic ratios are corrected by 0.12%/a.m.u. to account for mass fractionation during analysis.

RESULTS

Mineral compositions

Compositions of clinopyroxene megacrysts and Cr-diopside separates are given in Table 5.1. Like most other world-wide occurrences of cpx megacrysts (Irving and Frey, 1984; Irving, 1974), the BRZ cpx megacrysts are titaniferous augites with a significant amount of Al (7-10.25 wt% Al_2O_3) assumed to be present as Ca-Tschermak's molecule ($CaAl_2Si_2O_6$). Analyzed Oka Plateau cpx range in Mg# (Mg# = molecular Mg/(Mg + Fe)) from 0.68 to 0.77, Udokan from 0.77 to 0.85, and Vitim cpx from 0.74 to 0.84. Ca, Mg and Fe vary in a systematic fashion that defines a linear trend as shown in Figure 5.6 (Ca-Mg-Fe ternary) and Figure 5.7 (Mg/Mg+Fe vs.Ca/Ca+Mg). The cpx megacrysts from

host basanite BK230 differ from the other analyzed cpx with higher FeO (9.05% to 9.52%) and higher Na_2O (2.16% to 2.46%) (Table 5.1). Cpx megacrysts with similarly high Fe and Na contents are also found in alkaline basalts of Hannuoba, China (Song and Frey, 1990).

Representative feldspar megacryst compositions are given in Table 5.2. As shown in Fig. 5.8 (Ab-Or-An ternary), the analyzed feldspars have a fairly restricted range of composition within the anorthoclase field. Compositions of biotite and garnet megacrysts are given in Table 5.3. The analyzed biotite from Bartoy has high TiO_2 (9.16 wt%), significant Na_2O (0.71 wt%), and low Mg# (0.44) (Table 5.3). The Bartoy garnet is pyrope-rich (Table 3), like other garnet megacrysts world-wide (Irving and Frey, 1978).

Isotopic compositions

Pb, Sr, and Nd isotopic compositions of BRZ clinopyroxene megacrysts, as well as Sr, Sm, Nd, and Pb elemental concentrations from isotope dilution, are presented in Table 4. The Sr isotopic compositions of leachates, if analyzed, are also given in Table 5.4. A plot of leaching step versus $^{87}Sr/^{86}Sr$ (Fig. 5.9) demonstrates that despite careful hand-picking of grains, a high $^{87}Sr/^{86}Sr$ component remains and is removed by the first leaching step (HCl1). Since no inclusions were *visible* in the picked grains, the high $^{87}Sr/^{86}Sr$ component most likely represents surface contamination, although there is always the possibility that Sr-rich fluid inclusions or apatites were simply not visible even under the binocular microscope. The $^{87}Sr/^{86}Sr$ does not change significantly after the

HF leaching step. Isotopic data for the Cr-Di separates and garnet, kaersutite, and biotite megacrysts are given in Table 5.5.

Clinopyroxene megacrysts

Five clinopyroxene megacrysts from the same location (BK230) in the Oka Plateau (plus a duplicate) were analyzed. Four of these five megacrysts have very similar Sr and Nd isotopic compositions ($^{87}Sr/^{86}Sr$ from 0.70374 to 0.70383; ε_{Nd} from +2.6 to +2.9), while one (BK230/6) has a distinctly different isotopic composition ($^{87}Sr/^{86}Sr$ of 0.70365; ε_{Nd} of +3.8), as well as a slightly higher concentration of Sr (133 ppm) and Nd (13 ppm) (Fig. 5.10, Table 5.4). Megacryst BK230/6 was analyzed twice (BK230/6 old and BK230/6), from two separate preparations and dissolutions. $^{87}Sr/^{86}Sr$ agrees within error for the duplicates, while ε_{Nd} does not agree within error. The discrepancy is most likely due to the difficulty in analyzing the Nd isotopic composition for total loads of only ~100 ng of Nd. However, this raises the possibility that the cpx megacryst was not homogeneous in its Nd isotopic composition. In fact, the two preparations have slightly different Nd concentrations: BK230/6old has 13.32±.06 ppm Nd, while BK230/6 has 12.96±.06 ppm Nd. Another possible explanation for the difference in measured Nd isotopic composition is that the leaching steps affected the two preparations in different ways. In any case, cpx megacrysts BK230/1, 2, 3, 5 and 6 all have less radiogenic Sr and slightly more radiogenic Nd isotopic composition than their host basanite (BK230; Oka Plateau; $^{87}Sr/^{86}Sr = 0.070403$; $\varepsilon_{Nd} = +2.15$). The two other cpx megacrysts from the Oka Plateau, R188 and R204, have fairly similar $^{87}Sr/^{86}Sr$. However, R204 has a significantly

lower e_{Nd} than the BK230 megacrysts. The cpx megacryst from the Bartoy center (BK146C), also in the western zone of the BRZ, has a similar $^{87}Sr/^{86}Sr$ (0.70384) to the Oka Plateau samples, but higher ε_{Nd} (+5.0).

The Udokan cpx megacrysts have the most radiogenic Nd isotopic compositions of any of the analyzed megacrysts, ranging from ε_{Nd} of +4.7 to +5.4. Their Pb isotopic composition is also the most radiogenic of any of the analyzed cpx, with $^{206}Pb/^{204}Pb$ from 18.23 to 18.39. Vitim cpx megacrysts have a large range in $^{87}Sr/^{86}Sr$ (0.70348 to 0.70418) and ε_{Nd} (+2.7 to +4.6). Their Pb isotopic composition lies on the less radiogenic end of the data array, with $^{206}Pb/^{204}Pb$ from 17.36 to 17.73.

Anorthoclase megacrysts

Sr and Pb isotopic compositions for the feldspar megacrysts are presented in Table 5.6. The anorthoclases from Udokan clearly have a wide range in Pb isotopic compositions, and form the most radiogenic end of the Pb data array (Fig. 5.11), with $^{206}Pb/^{204}Pb$ from 17.84 to 18.56, $^{207}Pb/^{204}Pb$ from 15.47 to 15.57, and $^{208}Pb/^{204}Pb$ from 37.83 to 38.53. On the $^{206}Pb/^{204}Pb$ - $^{87}Sr/^{86}Sr$ diagram (Fig. 5.12) it is also apparent that they have a wide range in Sr isotopic composition, with $^{87}Sr/^{86}Sr$ from 0.7036 to 0.7054. In contrast, the 3 anorthoclase megacrysts from the Bartoy center have a small range in Sr and Pb isotopic compositions (Table 5.6; Fig. 5.10). The 4 Vitim anorthoclase megacrysts are less radiogenic than the Udokan anorthoclases in Sr and Pb isotopic composition, like the Bartoy anorthoclases (Table 5.6; Fig. 5.10). Three of the megacrysts have almost identical Pb isotopic compositions (p585An1, p588An, p593/1),

while the fourth (p589An) has less radiogenic Pb. Like the Bartoy anorthoclases, the Vitim anorthoclase megacrysts have a small range in $^{87}Sr/^{86}Sr$ (0.70379 to 0.70398).

Kaersutite, garnet, and biotite megacrysts

The kaersutite, garnet, and biotite megacrysts included in this study are all from the same flow at the Bartoy volcanic center in the Dzhida Basin of the western BRZ (Fig. 5.1). It is quite interesting that all of these megacryst species at Bartoy give the same $^{87}Sr/^{86}Sr$ (0.70407) within error that is more radiogenic than the cpx megacryst from the same location (0.70384) (Table 5). Two single grains of apatite plucked from the (Bartoy bt-dated) biotite have the same $^{87}Sr/^{86}Sr$ (0.70401) that is almost the same within error as that of the biotite. The fact that the biotite sample BK-134bt has no visible apatite inclusions but the same Sr isotopic composition rules out the possibility that its Sr composition has been affected by fluids that precipitated the apatites. The Bartoy kaersutite and garnet have very similar Nd isotopic composition, although the garnet has higher ε_{Nd} (+4.6) than the kaersutite (+4.2). The Bartoy cpx has even higher ε_{Nd} (+5.0) than the garnet. If the kaersutite, garnet, and cpx all formed at the same time from the same melt, based on their Sm/Nd ratios we would expect the garnet to evolve to the highest ε_{Nd} with time, followed by the cpx and then the kaersutite. However, although the three megacrysts have different $^{147}Sm/^{144}Nd$, they do not lie on an isochron, and so give no age information. A possible explanation for the cpx having higher ε_{Nd} than the kaersutite and garnet is that it was precipitated at a later time from the same magma as the kaersutite and garnet, and therefore started evolving from a higher $^{143}Nd/^{144}Nd$. It could

not have formed at a very much different time, however, because its Nd isotopic composition is so similar to that of the kaersutite and garnet.

Upper mantle Cr-diopsides

The Cr-diopside separates from the Oka Plateau spinel lherzolites are clearly quite different from the cpx megacrysts in their Sr and Nd isotopic compositions (Fig. 5.10). Although all four samples are from the same xenolith locale, they have a significant range in isotopic composition, with $^{87}Sr/^{86}Sr$ from 0.7024 to 0.7032, and ε_{Nd} from +8.7 all the way to +16.9. The Pb isotopic composition of two of the Oka Plateau Cr-diopside separates is extremely interesting because they are quite unradiogenic, with $^{206}Pb/^{204}Pb$ of 17.45 to 17.57, $^{207}Pb/^{204}Pb$ of 15.35 to 15.42, and $^{208}Pb/^{204}Pb$ of 37.12 to 37.24.

The Vitim Cr-diopside from the picrite tuff quarry has a very similar isotopic composition to the Oka Plateau samples, even though it is from a garnet lherzolite rather than a spinel lherzolite (Table 5.5; Fig. 5.10). Interestingly, the cpx from the Dzhilinda River spinel lherzolite (p585/3) has almost identical ε_{Nd} (+13.7) to the picrite tuff lherzolite, but slightly higher $^{87}Sr/^{86}Sr$ (0.70256). The two Vitim lherzolites have very different Pb isotopic signatures (Fig. 11): p585/3 has low $^{206}Pb/^{204}Pb$ (17.55) like the Oka lherzolites, but higher $^{207}Pb/^{204}Pb$ (15.47) and $^{208}Pb/^{204}Pb$ (37.45), while B1/3-1 has much more radiogenic Pb ($^{206}Pb/^{204}Pb = 18.12$, $^{207}Pb/^{204}Pb = 15.49$, $^{208}Pb/^{204}Pb = 37.52$).

The range in Sr and Nd isotopic compositions for the lherzolites in this study is comparable to that reported for other lherzolites from the Baikal Rift area (Ionov et al., 1993) and Mongolia (Ionov et al., 1994), as shown on Fig. 5.10. It is evident from all of

these studies that the lithospheric mantle sampled by Baikal Rift volcanism, and volcanism in other parts of Asia, is quite heterogeneous. The sub-Vitim mantle has been considered some of the most depleted anywhere in the world (Ionov et al., 1993), while the sub-Bartoy mantle appeared to be less depleted and variably metasomatized, with ε_{Nd} only as high as +10 (Ionov et al., 1993). However, the results for sample R-87 (Oka Plateau) indicate that elsewhere in the western BRZ there is evidently lithospheric mantle similarly depleted to that beneath the Vitim Plateau.

DISCUSSION

Comparison of BRZ megacrysts and regional volcanic rocks

A large-scale geochemical study of BRZ volcanic rocks (Harris et al., in prep and this thesis; Housh et al., in prep.) provides a good database for making regional comparisons between BRZ megacrysts and host lavas. As described elsewhere (Harris et al., in prep., this thesis), BRZ volcanic rocks range in composition from alkaline basalt to basanite, hawaiite, and mugearite in the Vitim volcanic field and the western zone of the BRZ (Oka Plateau, Bartoy). However, lavas of the Udokan volcanic field extend to more evolved compositions that include phonolites and trachytes. In the isotope variation diagrams of Figures 5.10, 5.11 and 5.12, fields for BRZ volcanic rocks of each of the three major regions are shown for comparison. BRZ volcanic rocks have isotopic compositions comparable to the field for ocean island basalts (OIB). Table 5.7 summarizes the range in isotope data for the BRZ megacrysts from each region and gives the range in isotopic composition for volcanic rocks for the same region.

BRZ volcanic rocks of each area have a wide range in Sr and Nd isotopic compositions (Table 5.7). However, megacrysts from each of the regions extend to less radiogenic Sr than any of the whole rocks from that same area. In Figure 5.12, it can be seen that the Pb isotopic compositions of both cpx and anorthoclase megacrysts from each area are remarkably coherent with the regional volcanic rock data. In fact, for all areas, both cpx and anorthoclase megacrysts fall within the same range of Pb isotope ratios as their respective regional rocks. The very unradiogenic component present at Vitim ($^{206}Pb/^{204}Pb \sim 17.4$; most unradiogenic for all of BRZ), is also sampled by two of the Vitim cpx megacrysts. These samples also have a correspondingly higher $^{207}Pb/^{204}Pb$. This unradiogenic signature at Vitim has previously been proposed (Harris et al., 1996) to represent mixing with a lower crustal component which has been highly depleted in U and Th. Alternatively, the lithospheric mantle may have an unradiogenic character which approaches the enriched mantle type I (EM-1) end-member component in ocean island basalts as defined by Hart (1988).

Comparison of the different megacryst species for the BRZ

The Pb isotope variation diagrams (Fig. 5.11, 5.12) show the wide range in Pb isotopic compositions of both clinopyroxene and anorthoclase. Each of the three BRZ volcanic areas has a distinct range in Pb isotope ratios. Vitim has the least radiogenic Pb ($^{206}Pb/^{204}Pb = 17.4 - 17.8$). Udokan forms the more radiogenic end of the trend, with $^{206}Pb/^{204}Pb$ from 17.8 to 18.7, and does not overlap with the Vitim data. The Oka Plateau cpx cluster in the middle of the trend. A $^{206}Pb/^{204}Pb$ - $^{87}Sr/^{86}Sr$ diagram (Fig. 5.12) also

demonstrates the coherency of isotopic data for each area. Again, Vitim cpx and anorthoclase have the least radiogenic $^{206}Pb/^{204}Pb$ coupled with $^{87}Sr/^{86}Sr < 0.7045$, while Oka Plateau cpx form a cluster. In contrast, the Udokan data are much more scattered. Udokan cpx have high $^{206}Pb/^{204}Pb$ and low $^{87}Sr/^{86}Sr$. Udokan anorthoclase are highly variable in $^{87}Sr/^{86}Sr$ but have higher $^{206}Pb/^{204}Pb$ than the Vitim megacrysts.

Implications for the origin of BRZ megacrysts

As shown in Figure 5.3, the BRZ cpx megacrysts have a systematic trend of decreasing Ca/(Ca+Mg) with increasing Mg/(Mg+Fe). There are similar trends of decreasing Si and Mg with increasing Al, Fe, Ti, and Na (Table 5.1). Irving (1974) noted that clinopyroxene megacrysts from particular Newer Basalts, Australia, volcanic centers behaved in this manner, and attributed it to fractionation of a parental magma. This behavior of major elements may imply, as Irving suggested, that a range of clinopyroxene compositions in a single host is possible since a fractionated daughter liquid can, on eruption, contain not only clinopyroxene on its own liquidus, but clinopyroxenes with compositions extending to near-liquidus phases of a parent liquid.

As described in the results section, the BRZ cpx have a high Al content, in the form of Ca-Ts, an indicator of high temperature and moderate to high pressure of equilibration (Chapman, 1976). A plot of calculated Al^{IV} against Al^{VI} (Fig. 13) illustrates that there is probably a significant amount of Al occupying octahedral sites. Experimental studies (Thompson, 1974) indicate that Al tends to occupy the octahedral site at higher pressures, and the tetrahedral site at higher temperatures. Also, Na and Ti

tend to increase along with Al as temperature rises. These experimental and empirical studies would seem to suggest that the Vitim cpx (with the exception of p589/A) formed at higher pressure than the Oka Plateau, Bartoy, and Udokan cpx since they have the highest Al^{VI}/Al^{IV} ratio. The higher crystallization depth suggested for the Vitim samples may be real, since the lithosphere beneath the Vitim Plateau is significantly thicker (>100 km) than that beneath the other volcanic regions (Zorin et al., 1989). The Oka Plateau samples with the high Na_2O (2.16 to 2.46 wt%) have the highest Al^{IV} (Fig. 5.13), perhaps implying they formed at a higher temperature than the other cpx. The reason for a temperature difference at the Oka Plateau is not clear, although the Oka Plateau volcanic field is closer to the major axis of rifting and the lithosphere is thinner.

Because megacrysts occur as discrete single crystals, it is not possible to apply any of the standard pyroxene thermometers that require co-existing phases, but pyroxene barometers and thermometers based on melt/phenocryst equilibrium may be useful. One such clinopyroxene-liquid thermobarometer/barometer is that of Putirka et al. (1996). For the cpx megacrysts where an analysis of the host is available, a pressure and temperature were calculated. Models P1 and T1 of Putirka et al. (1996) are based on the jadeite component in pyroxene. The results are given in Table 5.1. The 5 cpx megacrysts from the same Oka Plateau host BK-230 give almost identical pressures and temperatures: 17.3-17.9 kbar and 1321-1325°C. The two Vitim cpx megacrysts also give very similar results: 16.7-17.1 kbar and 1314-1317°C. It is interesting that the cpx from the two different regions give similar results, especially since the BK230 megacrysts are not in isotopic equilibrium with their host basanite. Calculated mineral/melt distribution

coefficients for [FeO/MgO] ($K_D^{(Fe/Mg)}$) are shown in Table 5.1 and range from 0.29 to 0.64. Irving and Frey (1984) considered $K_D^{(Fe/Mg)}$ of 0.22-0.54 to indicate equilibrium between cpx megacryst and host, with the majority between 0.26 and 0.40. Clearly, the BK230 megacrysts are not in equilibrium with their host.

The calculated pressures for the cpx correspond to a depth of ~50km. Based on estimated crustal thickness in the BRZ (Zorin et al., 1989; Gao et al., 1994), this may correspond to a depth near (perhaps below) the crust-mantle boundary. The experiments of Knutson and Green (1974) were able to produce clinopyroxene similar to that of most cpx megacrysts from an alkalic liquid at pressures from 9-15 kbar, similar to what we have calculated.

The uncertainties in pressure and temperature of formation are equally uncertain for the amphibole and mica megacrysts. However, the fact that all of these megacryst species occur within single flows, and that the cpx, kaersutite, garnet, and biotite from the same Bartoy location of this study have almost identical $^{87}Sr/^{86}Sr$, is very compelling evidence that they formed at similar pressure and temperature.

While there is adequate evidence that clinopyroxene, kaersutite, and garnet could precipitate from basaltic magma at high pressure, the origin of anorthoclase megacrysts from a magma at the same high pressure is problematic. Anorthoclase megacrysts are much more sodic than the low pressure groundmass feldspars of their host, in keeping with experimental results that show plagioclase becomes more sodic with increasing pressure, the anorthite component probably entering clinopyroxene as Ca-Ts component (Binns et al., 1970). However, experiments show that anorthoclase is unstable in a

basaltic melt at pressures greater than 8-9 kb (Chapman, 1976), and has never been produced near the liquidus of an alkali basalt under any conditions (Irving and Frey, 1984). Based on density considerations, Chapman and Powell (1976) suggested that anorthoclase could crystallize in magma with a density similar to anorthoclase, allowing megacrysts to grow large while suspended in the liquid. They further argued that this liquid could be no more basic than trachyandesite. Since anorthoclase megacrysts are also found included in less evolved basalts than trachyandesite, it is difficult to argue that they were precipitated from a magma directly related to their host. Rather, various researchers (Bahat, 1979; Irving and Frey, 1984) have suggested that anorthoclase megacrysts crystallized at shallow depths in isolated highly evolved magmas, and were later entrained by a more primitive magma carrying mafic deep-seated inclusions and possibly clinopyroxene, kaersutite, and garnet megacrysts . Alternatively, Aspen et al. (1990) proposed that anorthoclase-bearing syenitic veins crystallize from trachytic melts in the upper mantle and are later entrained in basanitic magmas. On the basis of a unique mantle-derived fragment in which pyroxene occurred as a druse, Kovalenko et al. (1987) suggested that small pockets of fluidized melt trapped in the upper mantle are capable of growing coarse-grained pyroxenes and garnets which are later disaggregated by ascending alkali melts.

Most studies of Sr and Nd isotope systematics find that clinopyroxene megacrysts are approximately in isotopic equilibrium with their host (Stuckless and Irving, 1976; Stuckless and Ericksen, 1976; Irving and Frey, 1984; Liotard et al., 1983; Liotard et al., 1988; Liu et al., 1992), while anorthoclase is usually in disequilibrium with

its host. Many of these investigators conclude that while there is an overall similarity of the Sr and Nd isotope compositions of clinopyroxene megacrysts and their host, the megacrysts are not strictly cognate in their host. It is more likely that they are cognate in a melt which is parental or derivative to their host. Most authors suggest that a host which is more radiogenic than its megacryst could possibly be contaminated with crustal or other radiogenic material. The greater variation in isotope composition for anorthoclase megacrysts (as in this study) suggests, as discussed above, that they are not in equilibrium or related to their host. If they crystallized at shallower depths (upper crust?), their parental liquid may have been more prone to wall-rock contamination, giving rise to the greater range of isotope compositions observed (Stuckless and Irving, 1976).

In Table 5.7, the isotopic data for the BRZ megacrysts is compared to the range of isotopic data for regional host volcanic rock data. The overall relationship between the Sr and Nd isotope data for cpx megacrysts and regional volcanic rocks is similar to that reported in megacryst studies for other areas of the world: the cpx has slightly less radiogenic Sr and more radiogenic Nd than the host rocks.

Unlike many anorthoclase megacrysts described in the literature, the isotope systematics of BRZ anorthoclase appears to broadly behave the same way as the regional volcanic rocks. In particular, the $^{206}Pb/^{204}Pb$ - $^{87}Sr/^{86}Sr$ diagram (Fig. 5.12) shows that the Udokan megacrysts mirror the two trends seen in the whole-rock data: increasing $^{87}Sr/^{86}Sr$ with little variation in $^{206}Pb/^{204}Pb$, and increasing $^{206}Pb/^{204}Pb$ with little variation in $^{87}Sr/^{86}Sr$. These two trends could represent mixing between three components, such as asthenospheric mantle, and crust of two different ages/types.

If the anorthoclase is a lower-pressure phase and is not directly related to its host volcanic rocks, then the similarity of isotopic trends for anorthoclase and host may imply that the isotopic composition of Udokan volcanic rocks is affected by processes occurring at shallow levels, such as the base of the crust. Alternatively, the anorthoclase may have been formed from an early and smaller degree of partial melting of the same source as the alkali basalts; a subsequent larger degree of melting then produced the alkali basalt magma which entrained the anorthoclases during its eruption.

CONCLUSIONS

The compositional data for BRZ megacrysts indicates they are quite similar to other megacryst occurrences in alkaline volcanic rocks. The high Al and Ti content of the cpx megacrysts agrees with experimental studies suggesting cpx megacrysts form at moderately high pressures (9-20 kb). Calculated temperatures of formation, using the single pyroxene thermometer of Mercier (1976), also give a similar range in temperatures to that predicted by experimental studies (1000-1400°C). The kaersutite, garnet, and biotite megacrysts that co-exist with the cpx megacrysts presumably crystallized under similar conditions. The high albite component in the anorthoclase megacrysts suggests they crystallized at moderately high pressure and temperature also, although probably at a lower pressure than the other megacryst species.

The relationship between megacrysts and host volcanic rocks as indicated by isotopic compositions is also similar to that of previous studies. With the exception of Vitim, cpx megacrysts have less radiogenic Sr, and more radiogenic Nd isotopic

composition than their host volcanic rocks, suggesting that the host magmas have either been affected by interaction with crust shortly before eruption, or were derived from an isotopically distinct source. Cpx megacrysts from the same Oka Plateau host basalt (BK230) show a range in Sr, Nd and Pb isotopic composition, as well as a slight variation in major element composition, suggesting an evolution involving multiple episodes of crystallization.

Finally, one of the most interesting results of this study is that the sub-Baikal lithospheric mantle, as sampled by the lherzolite xenoliths, is heterogeneous on the scale sampled by single eruptions. Intriguingly, most of the analyzed Cr-diopside separates have an unradiogenic Pb isotopic signature. These xenoliths may be sampling the subcontinental mantle that has been proposed as the source of the enriched mantle type 1 (EM-1) component found in oceanic basalts and within-plate volcanism (Hart, 1986, 1988), such as that of the BRZ. Perhaps delaminated, or possibly thermally converted, unradiogenic lithospheric mantle has mixed with the convecting asthenosphere some time in the past, leading to the existence of a sub-Baikal asthenospheric source that is a mixture of EM-1 type mantle and more fertile upwelling mantle. This mixed, heterogeneous mantle is the source of the BRZ volcanic rocks and megacrysts.

REFERENCES

Albee, A. L., and Ray, L., 1970, Correction factors for electron probe microanalysis of silicates, oxides, carbonates, phosphates, and sulfates: Analytical Chemistry, v. 42, p. 1408-1414.

Aoki, K., and Kushiro, I., 1968, Some clinopyroxenes from ultramafic inclusions in Dreiser Weiher, Eifel: Contributions to Mineralogy and Petrology, v. 18, p. 326-337.

Aspen, P., Upton, B. G. J., and Dickin, A. P., 1990, Anorthoclase, sanidine and associated megacrysts in Scottish alkali basalts: high-pressure syenitic debris from upper mantle sources?: Eur. J. Mineral., v. 2, p. 503-517.

Bahat, D., 1979, Anorthoclase megacrysts: physical conditions of formation: Mineralogical Magazine, v. 43, p. 287-291.

Bence, A. E., and Albee, A. L., 1968, Empirical correction factors for the electron microanalysis of silicates and oxides: Journal of Geology, v. 76, p. 382-403.

Binns, R. A., 1969, High-pressure megacrysts in basanitic lavas near Armidale, New South Wales: American Journal of Science, v. 267-A, p. 33-49.

Binns, R. A., Duggan, M. B., Wilkinson, J. F. G., and Kalocsai, G. I. Z., 1970, High pressure megacrysts in alkaline lavas from northeastern New South Wales with chemical analyses: American Journal of Science, v. 269, p. 132-168.

Chapman, N. A., and Powell, R., 1976, Origin of anortholcase megacrysts in alkali basalts: Contributions to Mineralogy and Petrology, v. 58, p. 29-35.

Chapman, N. A., 1976, Inclusions and megacrysts from undersaturated tuffs and basanites, East Fife, Scotland: Journal of Petrology, v. 17, p. 472-498.

Delvaux, D., Moeys, R., Stapel, G., Melnikov, A., and Ermikov, V., 1995, Palaeostress reconstructions and geodynamics of the Baikal region, Central Asia, Part I. Palaeozoic and Mesozoic pre-rift evolution: Tectonophysics, v. 252, p. 61-101.

Dobretsov, N. L., Buslov, M. M., Delvaux, D., Berzin, N. A., and Ermikov, V. D., 1996, Meso- and Cenozoic tectonics of the central Asian mountain belt: effects of lithospheric plate interaction and mantle plumes: International Geology Review, v. 38, p. 430-466.

Ellis, D. J., 1976, High pressure cognate inclusions in the Newer Volcanics of Victoria: Contributions to MIneralogy and Petrology, v. ???, p. 149-180.

Gao, S., Davis, P. M., Liu, H., Slack, P. D., Zorin, Y. A., Logatchev, N. A., Kogan, M., Burkholder, P. D., and Meyer, R. P., 1994, Asymmetric upwarp of the asthenosphere beneath the Baikal rift zone, Siberia: Journal of Geophysical Research, v. 99, p. 15,319-15,330.

Hart, S. R., 1984, A large-scale isotope anomaly in the Southern Hemisphere mantle: Nature, v. 309, p. 753-757.

Hart, S. R., Gerlach, D. C., and White, W. M., 1986, A possible new Sr-Nd-Pb mantle array and consequences for mantle mixing: Geochimica et Cosmochimica Acta, v. 50, p. 1551-1557.

Hart, S. R., 1988, Heterogeneous mantle domains: signatures, genesis and mixing chronologies: Earth and Planetary Science Letters, v. 90, p. 273-296.

Ionov, D. A., Kramm, U., and Stosch, H., 1992, Evolution of the upper mantle beneath the southern Baikal rift zone: an Sr-Nd isotope study of xenoliths from the Bartoy volcanoes: Contrib. Mineral. Petrol., v. 11, p. 235-247.

Ionov, D. A., Ashchepkov, I. V., Stosch, H., Witt-Eickschen, G., and Seck, H. A., 1993, Garnet peridotite xenoliths from the Vitim volcanic field, Baikal region: the nature of the garnet-spinel peridotite transition zone in the continental mantle: Journal of Petrology, v. 34, p. 1141-1175.

Ionov, D. A., Hofmann, A. W., and Shimizu, N., 1994, Metasomatism-induced melting in mantle xenoliths from Mongolia: Journal of Petrology, v. 35, p. 753-785.

Irving, A. J., 1974, Megacrysts from the Newer Basalts and other basaltic rocks of southeastern Australia: Geological Society of America Bulletin, v. 85, p. 1503-1514.

Irving, A. J., and Frey, F. A., 1978, Distribution of trace elements between garnet megacrysts and host volcanic liquids of kimberlitic to rhyolitic composition: Geochimica et Cosmochimica Acta, v. 42, p. 771-787.

Irving, A., and Frey, F. A., 1984, Trace element abundances in megacrysts and their host basalts: constraints on partition coefficients and megacryst genesis: Geochimica et Cosmochimica Acta, v. 48, p. 1201-1221.

Kiselev, A. I., 1987, Volcanism of the Baikal rift zone: Tectonophysics, v. 143, p. 235-244.

Knutson, J., and Green, T. H., 1975, Experimental duplication of a high-pressure megacryst/cumulate assemblage in a near-saturated hawaiite: Contributions to Mineralogy and Petrology, v. 52, p. 121-132.

Kovalenko, V. I., Solovova, I. P., Ryabchikov, E. D., Ionov, D. A., Bogatikov, O. A., and Naumov, V. B., 1987, Fluidized CO2-sulphide-silicate media as agents of mantle metasomatism and megacrysts formation: evidence from a large druse in a spinel-lherzolite xenolith: Physics of the Earth and Planetary Interiors, v. 45, p. 280-293.

Liotard, J.-M., Boivin, P., Cantagrel, J.-M., and Dupuy, C., 1983, Megacristaux d'amphibole et basaltes alcalins associes. Problemes de leurs relations petrogenetiques et geochimiques: Bulletin de Mineralogy, v. 106, p. 451-464.

Liotard, J. M., Briot, D., and Boivin, P., 1988, Petrological and geochemical relationships between pyroxene megacrysts and associated alkali-basalts from Massif Central (France): Contributions to Mineralogy and Petrology, v. 98, p. 81-90.

Logatchev, N. A., and Zorin, Y. A., 1987, Evidence and causes of the two-stage development of the Baikal rift: Tectonophysics, v. 143, p. 225-234.

Logatchev, N. A., and Zorin, Y. A., 1992, Baikal rift zone: structure and geodynamics: Tectonophysics, v. 208, p. 273-286.

Logatchev, N. A., 1993, History and geodynamics of the Lake Baikal rift in the context of the eastern Siberia rift system: a review: Bull. Centres Rech. Explor.-Prod. Elf Aquitaine, v. 17, p. 353-370.

Lysak, S. V., 1987, Terrestrial heat flow of continental rifts: Tectonophysics, v. 143, p. 31-41.

Molnar, P., and Tapponnier, P., 1975, Cenozoic tectonics of Asia: effects of a continental collision: Science, v. 189, p. 419-426.

Molnar, P., and Tapponnier, P., 1977, Relation of the tectonics of eastern China to the India-Eurasia collision: application of slip-line field theory to large-scale continental tectonics: Geology, v. 5, p. 212-216.

Putirka, K., Johnson, M., Kinzler, R., Longhi, J., and Walker, D., 1996, Thermobarometry of mafic igneous rocks based on clinopyroxene-liquid equilibria, 0-30 kbar: Contributions to Mineralogy and Petrology, V. 123, p. 92-108.

Song, Y., Frey, F. A., and Zhia, X., 1990, Isotopic characteristics of Hannuoba basalts, eastern China: implications for their petrogenesis and the composition of subcontinental mantle: Chemical Geology, v. 85, p. 35-52.

Stuckless, J. S., and Ericksen, R. L., 1976, Strontium isotopic geochemistry of the volcanic rocks and associated megacrysts and inclusions from Ross Island and vicinity, Antarctica: Contributions to Mineralogy and Petrology, v. 58, p. 111-126.

Stuckless, J. S., and Irving, A. J., 1976, Strontium isotope geochemistry of megacrysts and host basalts from southeastern Australia: Geochimica et Cosmochimica Acta, v. 40, p. 209-213.

Thompson, R. N., 1974, Primary basalts and magma genesis I. Skye, north-west Scotland: Contributions to Mineralogy and Petrology, v. 45, p. 317-341.

Wilkinson, J. G. G., and Hensel, H. D., 1991, An analcime mugearite-megacryst association from north-eastern New South Wales: implications for high-pressure amphibole-dominated fractionation of alkaline magmas: Contributions to Mineralogy and Petrology, v. 109, p. 240-251.

Zonenshain, L. P., and Savostin, L. A., 1981, Geodynamics of the Baikal rift zone and plate tectonics of Asia: Tectonophysics, v. 76, p. 1-45.

Zorin, Y. A., Kozhevnikov, V.M., Novoselova, M.R., and Turutanov, E.K., 1989, Thickness of the lithosphere beneath the Baikal rift zone and adjacent regions: Tectonophysics, V. 168, p. 327-337.

FIGURE CAPTIONS

Figure 5.1 General map of the Baikal Rift Zone (BRZ) showing locations of the major Cenozoic volcanic fields and other major features. TV is the Tuva volcanic field; OP is the Oka Plateau; T is the Tunka Basin, and D is the Dzhida Basin. Other rift basins according to number label are: 1) Busingol, 2) Darkhat, 3) Khubsugul, 4) Barguzin, 5) Upper Angara, 6) Tsipa, 7) Baunt, 8) Muya, 9) Chara, and 10) Tokka. The 1500 m contour line of the Sayan-Baikal domal uplift is indicated.

Figure 5.2 Photo of clinopyroxene megacrysts. Note the rim surrounding the clinopyroxene in the lower photo.

Figure 5.3 Photo of a variety of anorthoclase megacrysts.

Figure 5.4 Photo of kaersutite megacryst.

Figure 5.5 Photo of altered garnet megacrysts.

Figure 5.6 Ternary diagram of Ca-Mg-Fe for BRZ cpx megacrysts.

Figure 5.7 Diagram of Mg/(Mg+Fe) vs. Ca/(Ca+Mg) for BRZ cpx megacrysts. This diagram essentially shows the compositional variation parallel to the Ca -Mg join of the ternary. Note that Mg/(Mg+Fe) decreases as Ca/(Ca+Mg) increases. Fe is the total molecular Fe.

Figure 5.8 Feldspar ternary diagram. Note that the analyzed BRZ feldspars have a restricted compositional range within the anorthoclase field.

Figure 5.9 Diagram of leaching step vs. measured $^{87}Sr/^{86}Sr$. HCl1 is the first leaching step, HF the second leaching step, and HCl2 the third leaching step (details of the leaching method are described in the analytical methods section of the text). Note that the first leaching step is successful in removing the high $^{87}Sr/^{86}Sr$ component, most likely a post-magmatic surface contaminant. Symbols are the same as Fig. 5.6.

Figure 5.10 $^{87}Sr/^{86}Sr$ - ε_{Nd} diagram for all BRZ megacrysts. In Figure 5.6a, all megacrysts are shown, but 2σ error bars are shown only for the Cr-diopside separates from the BRZ upper mantle xenoliths. Fields around data of Ionov et al. (1992) for the Bartoy center, data of Ionov et al. (1993) for Vitim, and data of Ionov et al. (1994) for Mongolia are also shown. Figure 5.6b is a close-up showing the cpx megacrysts in greater detail. 2σ error bars are only drawn if larger than the symbols.

Figure 5.11 $^{206}Pb/^{204}Pb$ - $^{207}Pb/^{204}Pb$ and $^{208}Pb/^{204}Pb$ diagrams for BRZ megacrysts and upper mantle xenoliths. Fields for each of the BRZ volcanic regions (data of Harris and Housh) are drawn for comparison. NHRL is the Northern Hemisphere Reference Line of Hart (1984). Various end-member mantle components are labeled: EM-I (enriched mantle type 1), EM-II (enriched mantle type 2), and DM (depleted mantle). Symbols are the same as Fig. 5.10.

Figure 5.12 $^{206}Pb/^{204}Pb$ - $^{87}Sr/^{86}Sr$ and $^{206}Pb/^{204}Pb$ - ε_{Nd} diagram for BRZ megacrysts and upper mantle xenoliths. Fields for each of the BRZ volcanic regions are drawn for comparison (data of Harris and Housh). Various end-member mantle components are labeled: EM-I (enriched mantle type 1), EM-II (enriched mantle type 2), and DM (depleted mantle). Symbols are the same as Fig. 5.10.

Figure 5.13 Plot of Al^{IV} (tetrahedral Al) versus Al^{VI} (octahedral Al) for BRZ cpx megacrysts, after Aoki and Kushiro (1968). The solid line is for a ratio of Al^{IV}: Al^{VI} of 1. Dashed line A is an empirical boundary line between eclogitic clinopyroxenes and granulitic clinopyroxenes, while dashed line B is an empirical boundary between eclogites, granulites and other inclusions in basaltics rocks, and those from common igneous rocks (phenocrysts). According to Thompson (1974), increasing Al^{VI} corresponds to increasing pressure, while increasing Al^{IV} corresponds to increasing temperature. Note that the Vitim cpx have the highest proportion of Al^{VI}, while the Oka Plateau cpx have the highest proportion of Al^{IV}. Symbols are the same as Fig. 5.10.

Figure 5.1

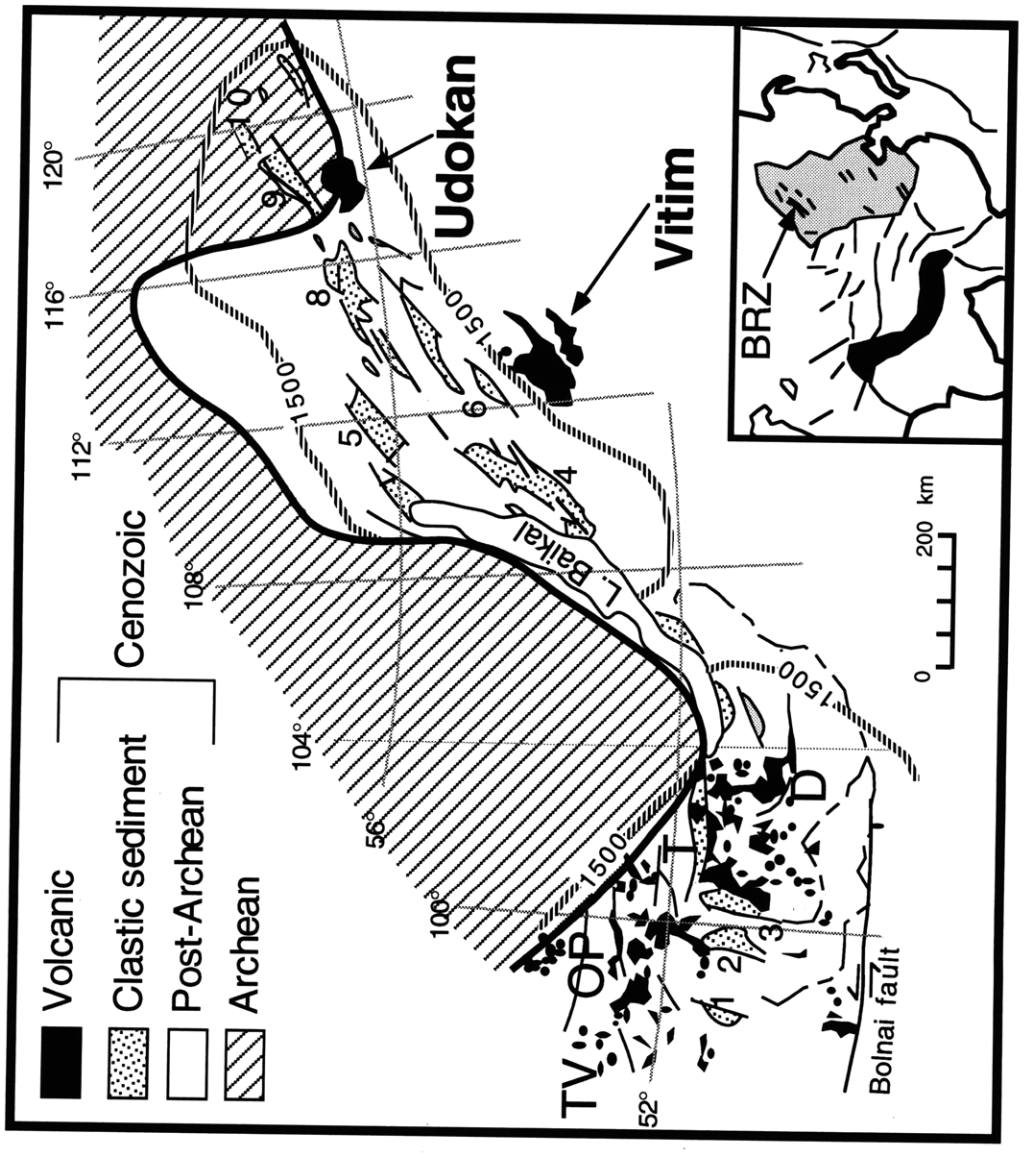
Volcanic
Clastic sediment
Post-Archean
Archean
Cenozoic
Udokan
Vitim
BRZ
Baikal
Bolnai fault
TV
OP
D
1
2
3
4
5
6
7
8
9
10
1500
52°
56°
100°
104°
108°
112°
116°
120°
0
200 km

Figure 5.2

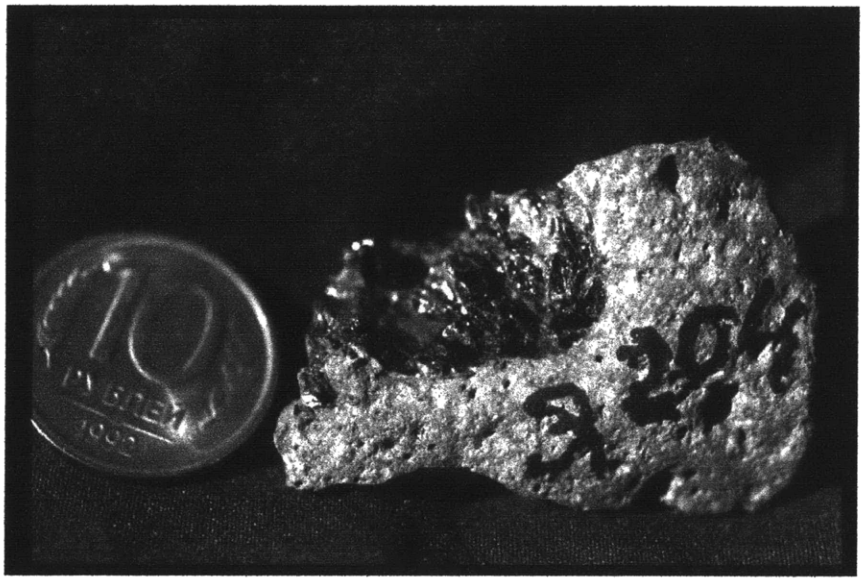

Figure 5.3

Figure 5.4

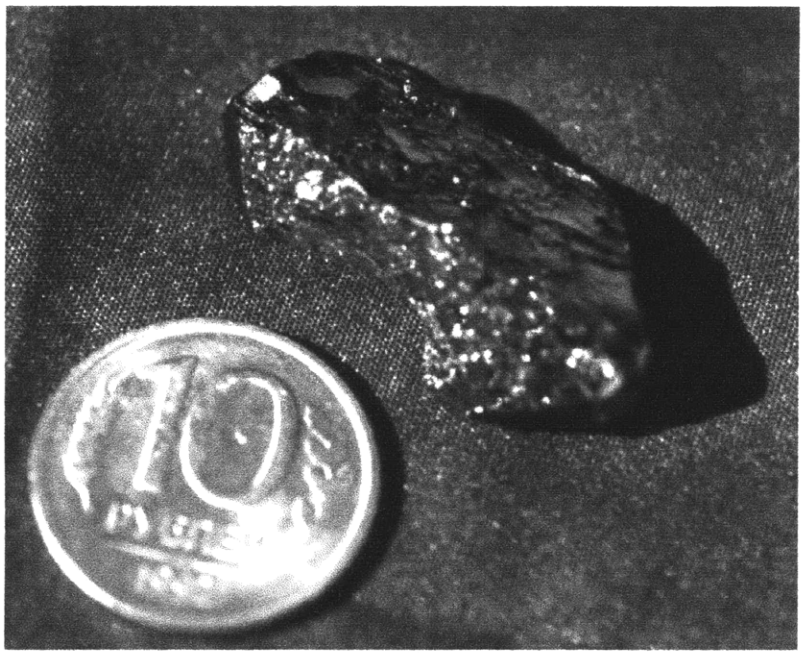

Figure 5.5

Figure 5.6

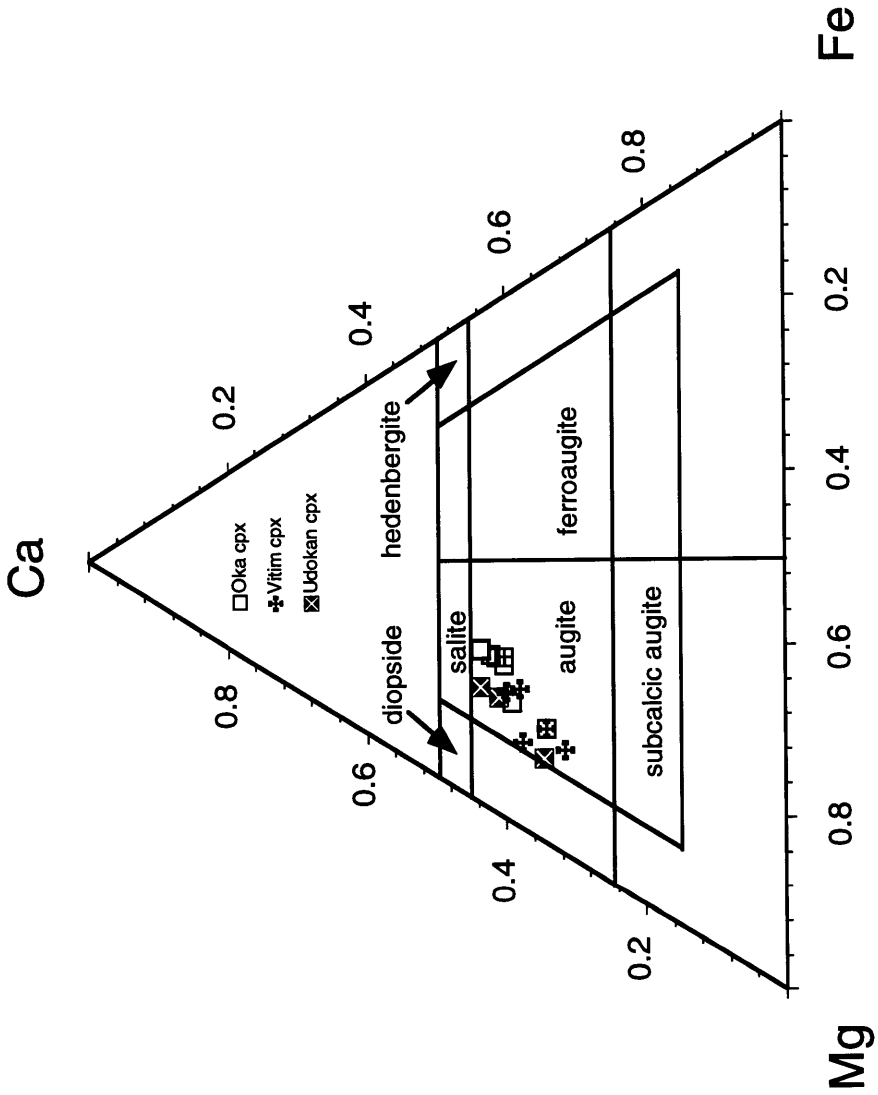
Ca
Fe
Mg
0.2
0.4
0.6
0.8
Oka cpx
Vitim cpx
Udokan cpx
diopside
hedenbergite
salite
augite
ferroaugite
subcalcic augite

Figure 5.7

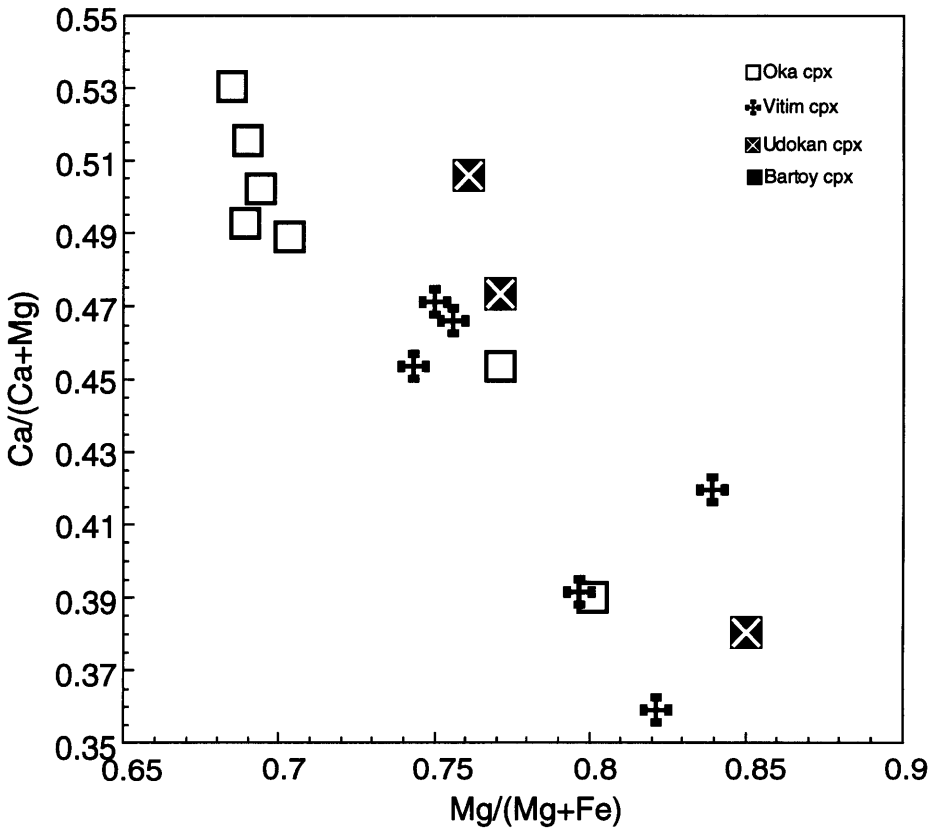
Oka cpx
Vitim cpx
Udokan cpx
Bartoy cpx
Ca/(Ca+Mg)
Mg/(Mg+Fe)
0.55
0.53
0.51
0.49
0.47
0.45
0.43
0.41
0.39
0.37
0.35
0.65
0.7
0.75
0.8
0.85
0.9

Figure 5.8

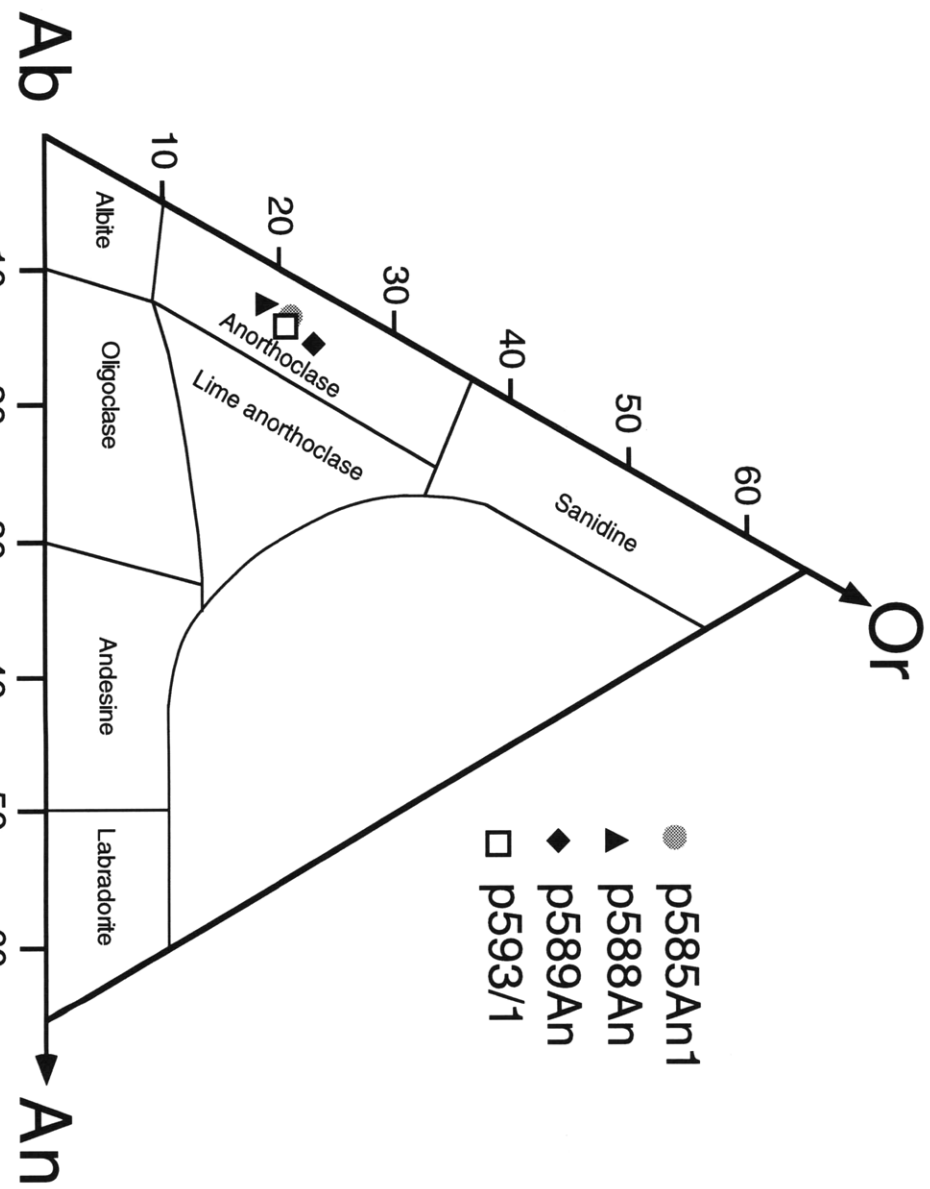
Ab
An
Or
10
20
30
40
50
60
Albite
Oligoclase
Andesine
Labradorite
Anorthoclase
Lime anorthoclase
Sanidine
p585An1
p588An
p589An
p593/1

Figure 5.9

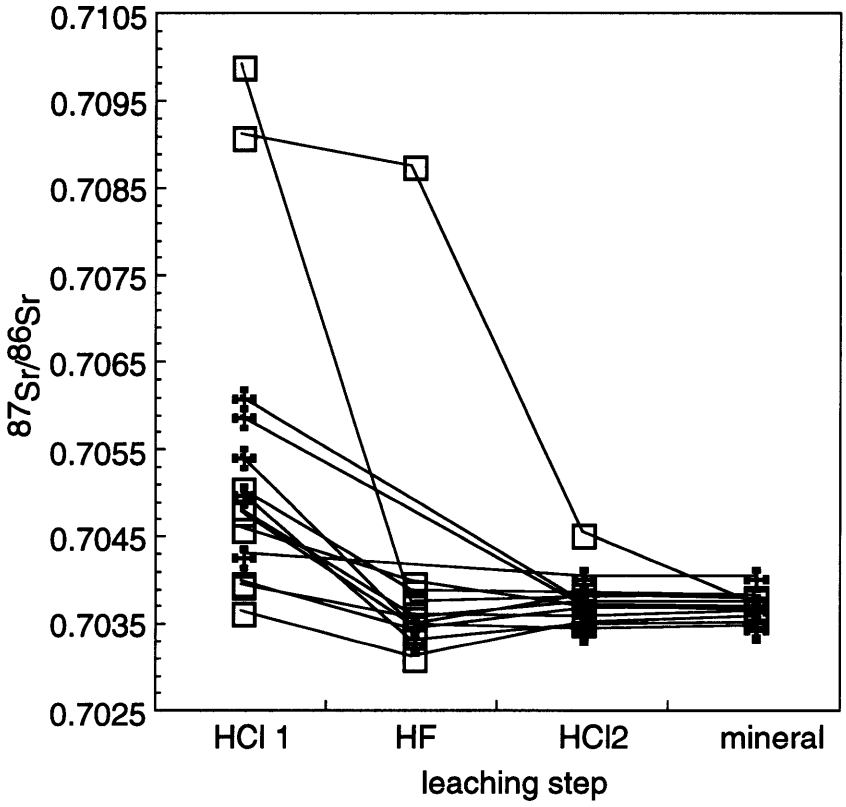
0.7105
0.7095
0.7085
0.7075
0.7065
0.7055
0.7045
0.7035
0.7025
$^{87}Sr/^{86}Sr$
HCl 1
HF
HCl2
mineral
leaching step

Figure 5.10

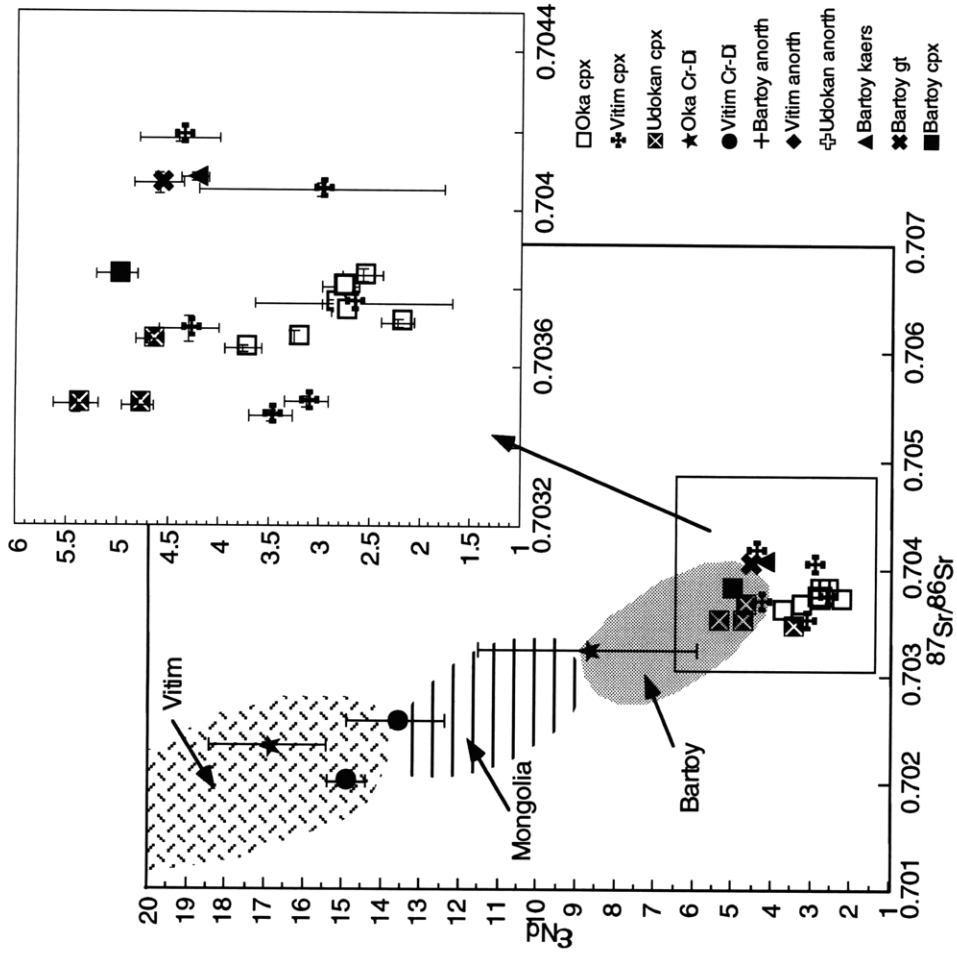
Vitim
Mongolia
Bartoy
εNd
87Sr/86Sr
Oka cpx
Vitim cpx
Udokan cpx
Oka Cr-Di
Vitim Cr-Di
Bartoy anorth
Vitim anorth
Udokan anorth
Bartoy kaers
Bartoy gt
Bartoy cpx

Figure 5.11

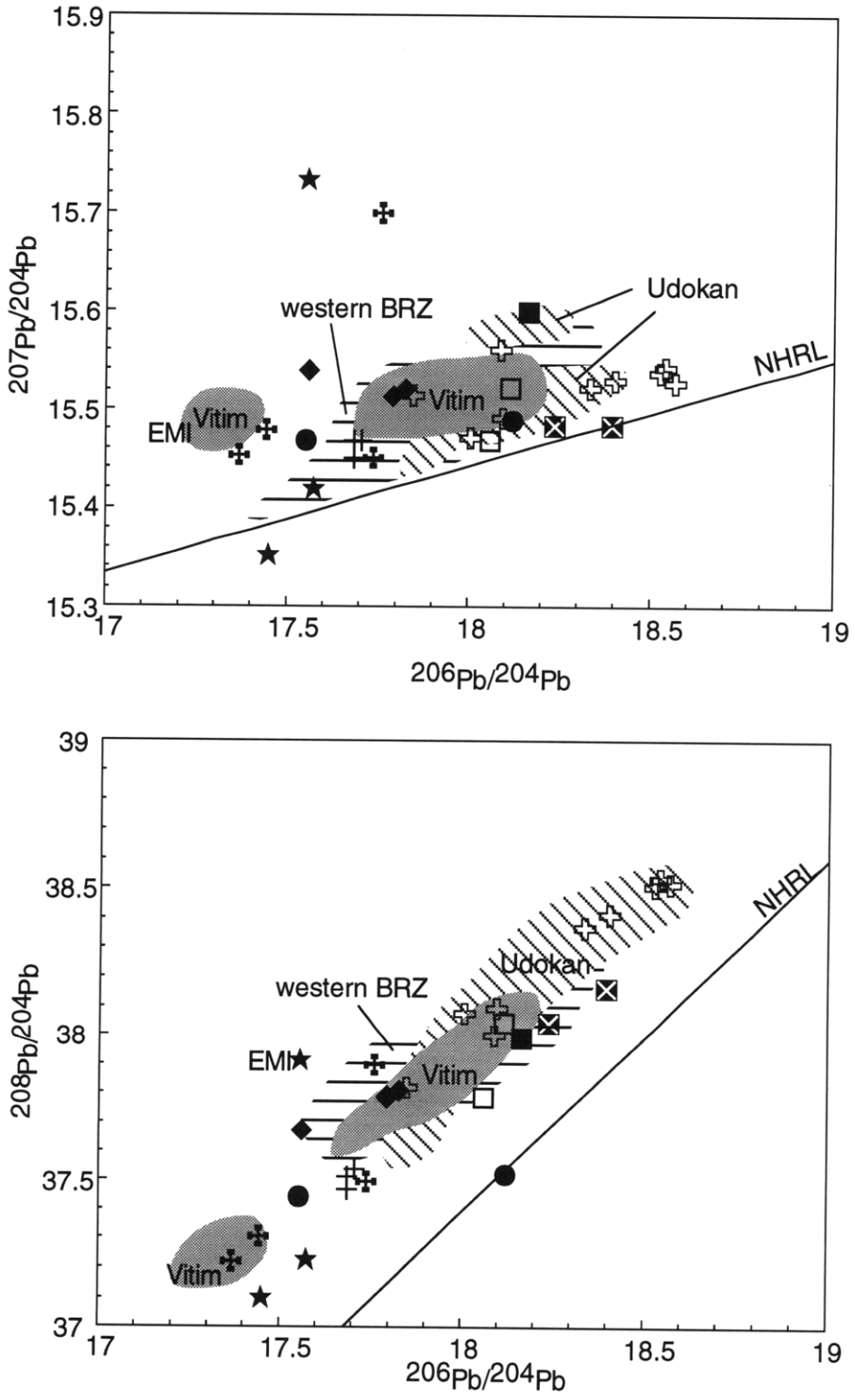
15.9
15.8
15.7
15.6
15.5
15.4
15.3
207Pb/204Pb
17
17.5
18
18.5
19
206Pb/204Pb
western BRZ
Udokan
NHRL
Vitim
EMI
Vitim
39
38.5
38
37.5
37
208Pb/204Pb
17
17.5
18
18.5
19
206Pb/204Pb
NHRL
Udokan
western BRZ
EMI
Vitim
Vitim

Figure 5.12

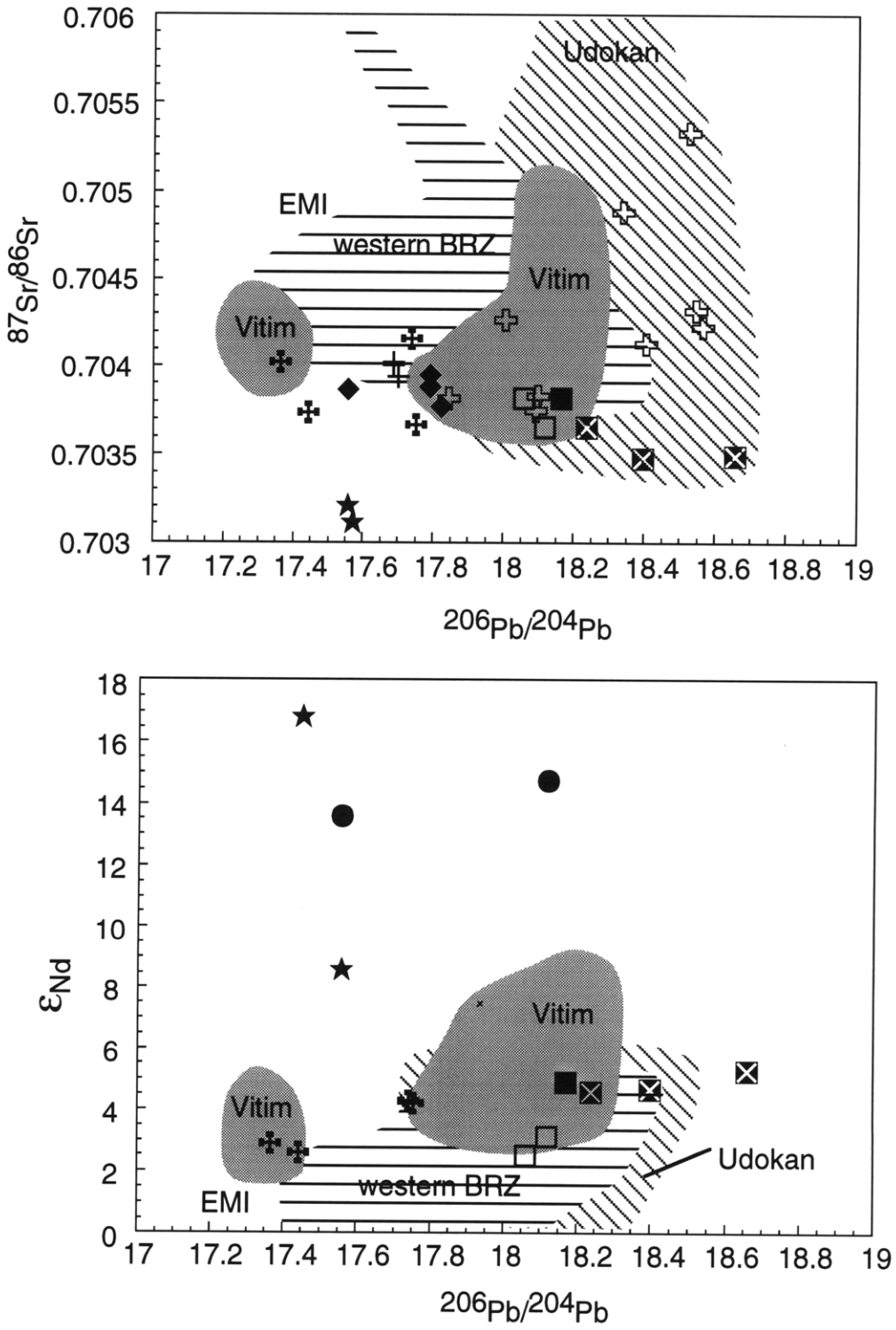
0.706
0.7055
0.705
0.7045
0.704
0.7035
0.703
$^{87}Sr/^{86}Sr$
Udokan
EMI
western BRZ
Vitim
Vitim
17
17.2
17.4
17.6
17.8
18
18.2
18.4
18.6
18.8
19
$^{206}Pb/^{204}Pb$
18
16
14
12
10
8
6
4
2
0
ε_{Nd}
Vitim
Vitim
Udokan
western BRZ
EMI
17
17.2
17.4
17.6
17.8
18
18.2
18.4
18.6
18.8
19
$^{206}Pb/^{204}Pb$

Figure 5.13

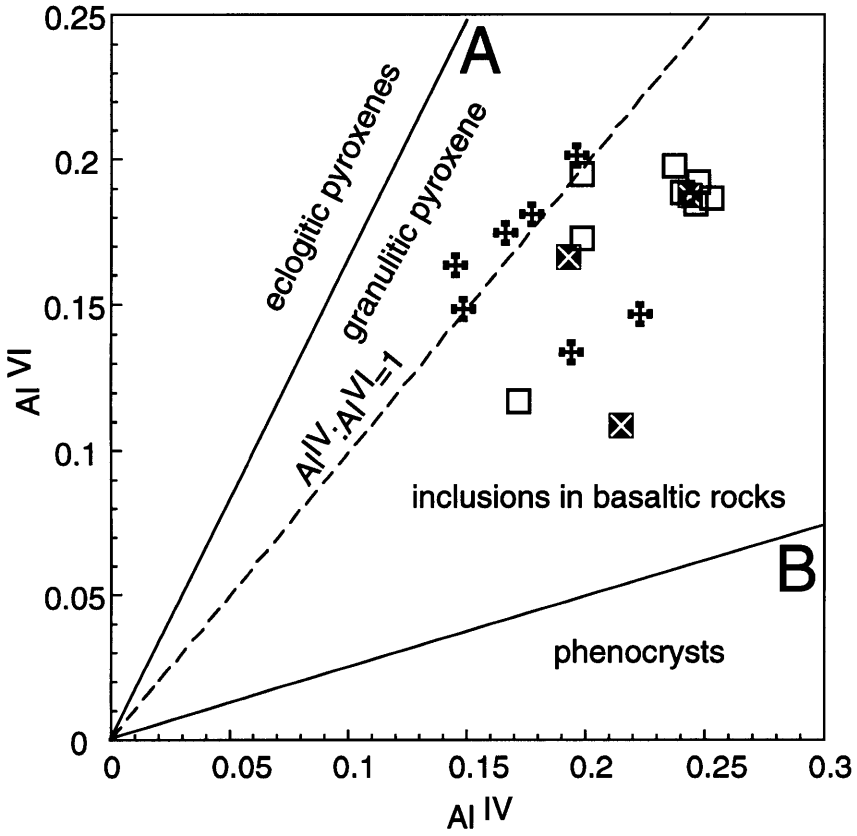
0.25
0.2
0.15
0.1
0.05
0
Al VI
0
0.05
0.1
0.15
0.2
0.25
0.3
Al IV
A
eclogitic pyroxenes
granulitic pyroxene
AlIV:AlVI=1
inclusions in basaltic rocks
B
phenocrysts

Table 5.1 BRZ pyroxene compositions

Sample	BK230/1	BK230/2	BK230/3	BK230/5	BK230/6	R188	R204	p70/4	p86/3-3	p396/7
Location	Oka Plateau	Oka Plateau	Oka Plateau	Oka Plateau	Oka Plateau	Oka Plateau	Oka Plateau	NE Udokan	NE Udokan	central Udokan
SiO_2	47.97	48.12	48.29	48.39	48.36	50.43	49.85	48.59	48.40	50.98
Al_2O_3	10.25	10.03	10.25	10.13	9.99	8.80	9.25	7.47	10.08	8.59
FeO	9.31	9.20	9.52	9.09	9.05	7.56	7.51	7.75	7.11	5.74
MgO	11.73	12.09	11.59	11.22	10.92	16.92	14.10	14.42	12.62	18.27
MnO	0.10	0.14	0.12	0.13	0.12	0.17	0.13	0.17	0.10	0.15
TiO_2	1.97	1.95	2.03	2.02	2.05	0.77	1.05	1.55	1.75	0.49
Cr_2O_3	0.07	0.04	0.04	0.00	0.00	0.09	0.01	0.06	0.00	0.19
CaO	16.61	16.34	16.36	16.68	17.35	14.66	16.40	19.01	18.14	15.67
Na_2O	2.24	2.16	2.29	2.32	2.46	1.39	1.69	0.97	1.90	1.06
Total	100.25	100.05	100.50	99.98	100.27	100.80	99.99	99.99	100.10	101.13
En (Mg)	0.41	0.42	0.40	0.40	0.38	0.53	0.47	0.44	0.43	0.56
Fs (Fe)	0.18	0.18	0.19	0.18	0.18	0.13	0.14	0.13	0.13	0.10
Wo (Ca)	0.41	0.41	0.41	0.42	0.44	0.33	0.39	0.42	0.44	0.34
$Mg/(Mg+Fe_{total})$	0.69	0.70	0.68	0.69	0.68	0.80	0.77	0.77	0.76	0.85
Ca/(Ca+Mg)	0.50	0.49	0.50	0.52	0.53	0.38	0.46	0.49	0.51	0.38
$K_D^{(Fe/Mg)}$	0.61	0.58	0.63	0.62	0.64					
T1 (°C)	1322	1321	1325	1325	1323					
P1 (kbar)	17.5	17.3	17.7	17.9	17.8					

Notes: Major elements determined by electron microprobe at MIT, and are the average of several spots.

Temperature and pressure calculated using model T1 and P1 of Putirka et al. (1996), and is explained in more detail in the text.

Table 5.1 BRZ pyroxene compositions continued

Sample	p567	p596/1-1	p589/A	p599	p601	R-1	R-2	R-87	R-88
						spinel lherzolite	spinel lherzolite	spinel lherzolite	spinel lherzolite
Location	Vitim	Vitim	Vitim	Vitim	Vitim	Oka Plateau	Oka Plateau	Oka Plateau	Oka Plateau
SiO_2	51.97	51.77	48.87	51.15	50.31	51.89	52.31	52.29	52.39
Al_2O_3	7.06	8.16	8.60	8.51	9.41	6.96	6.51	6.17	5.88
FeO	5.79	6.84	8.11	7.38	8.31	2.88	2.85	2.44	3.20
MgO	16.65	17.61	13.79	16.04	13.47	16.38	16.58	16.11	17.17
MnO	0.14	0.14	0.12	0.14	0.15	0.08	0.09	0.07	0.10
TiO_2	0.48	0.52	1.77	0.71	1.07	0.49	0.43	0.37	0.18
Cr_2O_3	0.05	0.17	0.04	0.05	0.06	0.89	0.94	1.14	1.13
CaO	16.80	13.94	17.06	14.64	15.57	19.11	19.47	20.18	18.84
Na_2O	1.59	1.70	1.79	1.98	2.28	1.76	1.63	1.65	1.42
Total	100.53	100.86	100.15	100.60	100.62	100.44	100.81	100.43	100.30
En (Mg)	0.52	0.56	0.45	0.52	0.46	0.52	0.52	0.50	0.53
Fs (Fe)	0.10	0.12	0.15	0.13	0.16	0.05	0.05	0.04	0.06
Wo (Ca)	0.38	0.32	0.40	0.34	0.38	0.43	0.43	0.45	0.42
Mg/(Mg+Fe)	0.84	0.82	0.75	0.79	0.74	0.91	0.91	0.92	0.91
Ca/(Ca+Mg)	0.42	0.36	0.47	0.40	0.45	0.46	0.46	0.47	0.44
$K_D^{(Fe/Mg)}$		0.29	0.46						
T1 (°C)		1314	1317						
P1 (kbar)		16.7	17.1						

Notes: Major elements determined by electron microprobe at MIT, and are the average of several spots.

Temperature and pressure calculated using model T1 and P1 of Putirka et al. (1996), and is explained in more detail in the text.

Table 5.1 BRZ pyroxene compositions continued

Sample	p585/3 spinel lherzolite	B1/3-1 garnet lherzolite
Location	Vitim	Vitim
SiO_2	52.49	52.41
Al_2O_3	7.38	6.09
FeO	2.38	2.99
MgO	14.78	16.29
MnO	0.08	0.08
TiO_2	0.61	0.62
Cr_2O_3	0.80	1.28
CaO	20.07	18.48
Na_2O	2.12	1.94
Total	100.71	100.18
En (Mg)	0.48	0.52
Fs (Fe)	0.04	0.05
Wo (Ca)	0.47	0.43
Mg/(Mg+Fe)	0.92	0.91
Ca/(Ca+Mg)	0.49	0.45
$K_D^{(Fe/Mg)}$		
T1 (°C)		
P1 (kbar)		

Table 5.2 Representative BRZ anorthoclase megacryst compositions

Sample Location	p585An1 Vitim	p588An Vitim	p589An Vitim	p593/1 Vitim
SiO_2	66.67	67.05	66.58	66.62
Al_2O_3	19.53	19.89	20.03	19.81
FeO	0.10	0.11	0.09	0.08
MgO	0.00	0.01	0.00	0.01
CaO	0.52	0.52	0.74	0.66
Na_2O	8.73	9.02	8.35	8.65
K_2O	3.74	3.45	3.93	3.59
SrO	0.26	0.23	0.33	0.33
Total	99.56	100.28	100.06	99.74
An	0.025	0.025	0.036	0.032
Ab	0.761	0.779	0.736	0.760
Or	0.214	0.196	0.228	0.208

Notes: Major elements determined by electron microprobe at MIT and are the average of several spots.

Table 5.3 BRZ biotite and garnet compositions

Sample	Bartoy biotite
Location	Bartoy
SiO_2	35.94
Al_2O_3	15.23
FeO	19.82
MgO	8.62
MnO	0.04
TiO_2	9.16
Na_2O	0.71
CaO	0.01
K_2O	8.59
Total	98.12
Mg/(Mg+Fe)	0.44

Sample	BK146-garnet
Location	Bartoy
SiO_2	41.33
Al_2O_3	22.92
FeO	15.12
MgO	15.29
MnO	0.36
TiO_2	0.64
Cr_2O_3	0.05
CaO	5.53
Total	101.24
Alm	0.30
Py	0.55
Gr	0.14
Sp	0.01

Table 5.4 Sr, Nd, and Pb isotopic compositions of BRZ clinopyroxene megacrysts

Sample	location	Sr (ppm)	$^{87}Sr/^{86}Sr$ ±2σ	Nd (ppm)	Sm (ppm)	$^{147}Sm/^{144}Nd$	$^{143}Nd/^{144}Nd$ ±2σ	$\varepsilon_{Nd}(0)$ ±2σ	$^{206}Pb/^{204}Pb$ ±2σ	$^{207}Pb/^{204}Pb$ ±2σ	$^{208}Pb/^{204}Pb$ ±2σ
BK146C HCl1	Bartoy		0.70506 ± 5								
BK146C HF	Bartoy		0.70390 ± 3								
BK146C HCl2	Bartoy		0.70387 ± 3								
BK146C cpx	Bartoy	84.0	0.70384 ± 2	9.07	3.33	0.222	0.51290 ± 1	5.0 ± 0.2	18.158 ± 0.034	15.601 ± 0.029	37.996 ± 0.072
BK230/1 HCl1	Oka Plateau	118.1	0.70397 ± 1								
BK230/1 HF	Oka Plateau	27.4	0.70359 ± 2								
BK230/1 HCl2	Oka Plateau	142.9	0.70376 ± 1								
BK230/1 cpx	Oka Plateau			9.96	3.72	0.226	0.51279 ± 1	2.9 ± 0.1			
BK230/2 HCl1	Oka Plateau	61.0	0.70913 ± 2								
BK230/2 HF	Oka Plateau	36.6	0.70876 ± 1								
BK230/2 HCl2	Oka Plateau	138.2	0.70457 ± 2								
BK230/2 cpx	Oka Plateau	102.0	0.70374 ± 2	9.77			0.51278 ± 1	2.8 ± 0.1			
BK230/3 HCl1	Oka Plateau	168.0	0.70992 ± 2								
BK230/3 HF	Oka Plateau	25.9	0.70377 ± 1								
BK230/3 HCl2	Oka Plateau	138.7	0.70382 ± 1								
BK230/3 cpx	Oka Plateau	101.6	0.70383 ± 2	9.84			0.51277 ± 1	2.6 ± 0.2	18.052 ± 0.012	15.473 ± 0.011	37.796 ± 0.029
BK230/5 HCl1	Oka Plateau		0.70479 ± 3								
BK230/5 HF	Oka Plateau	11.6	0.70351 ± 3								
BK230/5 HCl2	Oka Plateau	101.3	0.70383 ± 1								
BK230/5 cpx	Oka Plateau		0.70380 ± 1	10.34	3.86	0.226	0.51278 ± 1	2.8 ± 0.2			
BK230/6 HCl1 old	Oka Plateau		0.70481 ± 2								
BK230/6 HF old	Oka Plateau	18.5	0.70361 ± 2								
BK230/6 HCl2 old	Oka Plateau	72.6	0.70360 ± 1								
BK230/6 cpx old	Oka Plateau	133.4	0.70365 ± 1	13.32	4.60	0.209	0.51283 ± 1	3.8 ± 0.2			
BK230/6 HCl1	Oka Plateau	181.9	0.70462 ± 2								
BK230/6 HF	Oka Plateau	49.0	0.70401 ± 2								
BK230/6 HCl2	Oka Plateau	228.1	0.70371 ± 1								
BK230/6 cpx	Oka Plateau	130.7	0.70368 ± 2	12.96			0.51281 ± 1	3.3 ± 0.1	18.110 ± 0.027	15.525 ± 0.023	38.048 ± 0.059
R188 HCl1	Oka Plateau	59.8	0.70365 ± 5								
R188 HF	Oka Plateau	16.5	0.70313 ± 2								
R188 HCl2	Oka Plateau	49.4	0.70352 ± 2								
R188 cpx	Oka Plateau	42.9	0.70360 ± 2								

Notes: Sr data are normalized to $^{86}Sr/^{88}Sr = 0.1194$ and corrected for mass fractionation using an exponential law. Replicate analyses of NBS-987 Sr yield 87Sr/86Sr = 0.710240 ± 0.000016 (2σ). Nd data are normalized to $^{146}Nd/^{144}Nd = 0.7219$ and corrected for mass fractionation using an exponential law. Replicate analyses of La Jolla Nd yield $^{143}Nd/^{144}Nd = 0.511845 \pm .000011$ (2σ). $\varepsilon_{Nd}(0)$ is calculated with $^{143}Nd/^{144}Nd_{CHUR} = 0.512638$. Based on replicate analyses of NBS-981, Pb is corrected by 0.12%/amu to account for fractionation.

Table 5.4 Clinopyroxene megacryst isotopic compositions continued

sample	location	Sr (ppm)	$^{87}Sr/^{86}Sr$ ±2σ	Nd (ppm)	Sm (ppm)	$^{147}Sm/^{144}Nd$	$^{143}Nd/^{144}Nd$ ±2σ	$\varepsilon_{Nd}(0)$ ±2σ	$^{206}Pb/^{204}Pb$ ±2σ	$^{207}Pb/^{204}Pb$ ±2σ	$^{208}Pb/^{204}Pb$ ±2σ
R204 HCl1	Oka Plateau	1.4	0.70400 ± 2								
R204 HF	Oka Plateau	17.1	0.70344 ± 3								
R204 HCl2	Oka Plateau	90.7	0.70369 ± 1								
R204 cpx	Oka Plateau	58.3	0.70371 ± 1	5.87	2.26	0.232	0.51275 ± 1	2.2 ± 0.2			
p70/4 cpx	NE Udokan	78.0	0.70367 ± 1	7.96	2.71	0.206	0.51288 ± 1	4.7 ± 0.1	18.232 ± 0.015	15.486 ± 0.013	38.047 ± 0.032
p86/3-3 cpx	NE Udokan	87.0	0.70350 ± 1	8.94	2.91	0.196	0.51288 ± 1	4.8 ± 0.2	18.394 ± 0.081	15.487 ± 0.068	38.165 ± 0.169
p396/7 cpx	central Udokan	35.6	0.70351 ± 2	3.60	1.34	0.226	0.51292 ± 1	5.4 ± 0.2			
p563/1 HCl1	Vitim	56.0	0.70545 ± 2								
p563/1 HF	Vitim	20.6	0.70350 ± 1								
p563/1 HCl2	Vitim	83.0	0.70346 ± 1								
p563/1 cpx	Vitim	56.4	0.70348 ± 1	3.91			0.51282 ± 1	3.5 ± 0.2			
p567 HCl1	Vitim	279.5	0.70502 ± 1								
p567 HF	Vitim	17.4	0.70333 ± 1								
p567 HCl2	Vitim	79.5	0.70350 ± 1								
p567 cpx	Vitim	58.4	0.70351 ± 1	4.11			0.51280 ± 1	3.1 ± 0.2			
p589/A cpx	Vitim	6.3	0.70418 ± 1	8.84	3.16	0.216	0.51286 ± 2	4.4 ± 0.4	17.733 ± 0.023	15.454 ± 0.021	37.508 ± 0.054
p596/1-1 HCl1	Vitim		0.70612 ± 3								
p596/1-1 HCl2	Vitim		0.70377 ± 3								
p596/1-1 cpx	Vitim	49.5	0.70376 ± 1	3.35	1.23	0.221	0.51278 ± 5	2.7 ± 1.0	17.437 ± 0.012	15.481 ± 0.011	37.310 ± 0.028
p599 HCl1	Vitim		0.70590 ± 3								
p599 HCl2	Vitim		0.70373 ± 4								
p599 cpx	Vitim	65.7	0.70370 ± 3	4.71	1.71	0.220	0.51286 ± 2	4.3 ± 0.3			
p601 HCl1	Vitim		0.70431 ± 3								
p601 HCl2	Vitim		0.70405 ± 4								
p601 cpx	Vitim	91.4	0.70405 ± 2	6.35	2.32	0.221	0.51279 ± 6	3.0 ± 1.2			
Kand-cpx2	Kandidushka			5.32	1.97	0.224	0.51287 ± 1	4.6 ± 0.2			

Notes: Sr data are normalized to $^{86}Sr/^{88}Sr = 0.1194$ and corrected for mass fractionation using an exponential law. Replicate analyses of NBS-987 Sr yield 87Sr/86Sr = 0.710240 ± 0.000016 (2σ). Nd data are normalized to $^{146}Nd/^{144}Nd = 0.7219$ and corrected for mass fractionation using an exponential law. Replicate analyses of La Jolla Nd yield $^{143}Nd/^{144}Nd = 0.511845 \pm .000011$ (2σ). $\varepsilon_{Nd}(0)$ is calculated with $^{143}Nd/^{144}Nd_{CHUR} = 0.512638$. Based on replicate analyses of NBS-981, Pb is corrected by 0.12%/amu to account for fractionation.

Table 5.5 BRZ Cr-Di, apatite, biotite, and kaersutite isotopic compositions

sample	location	Sr (ppm)	$^{87}Sr/^{86}Sr$ ±2σ	Nd (ppm)	Sm (ppm)	$^{147}Sm/^{144}Nd$	$^{143}Nd/^{144}Nd$ ±2σ	$\varepsilon_{Nd}(0)$ ±2σ	$^{206}Pb/^{204}Pb$ ±2σ	$^{207}Pb/^{204}Pb$ ±2σ	$^{208}Pb/^{204}Pb$ ±2σ
R-1 Cr-Di	Oka Plateau	93.8	0.70313 ±2						17.567 ±0.021	15.420 ±0.018	37.236 ±0.043
R-2 Cr-Di	Oka Plateau	109.4	0.70256 ±1	3.78	1.47	0.236	0.51332 ±2	13.3 ±0.4			
R-87 Cr-Di	Oka Plateau	57.7	0.70235 ±2	2.76	1.07	0.234	0.51351 ±8	16.9 ±1.5	17.446 ±0.022	15.354 ±0.019	37.116 ±0.048
R-88 Cr-Di	Oka Plateau	67.7	0.70323 ±1	2.83	0.95	0.203	0.51309 ±14	8.7 ±2.8			
B1/3-1 Cr-Di	Vitim	83.9	0.70201 ±1	4.77	1.56	0.198	0.51340 ±3	14.9 ±0.5	18.115 ±0.024	15.490 ±0.022	37.524 ±0.051
p585/3 Cr-Di	Vitim	109.4	0.70256 ±1	5.72	1.88	0.198	0.51334 ±6	13.7 ±1.3	17.547 ±0.087	15.473 ±0.076	37.446 ±0.190
Bartoy apatite#1	Bartoy		0.70401 ±1								
Bartoy apatite#2	Bartoy		0.70401 ±1								
Bartoy bt-dated	Bartoy	456.9	0.70406 ±1								
BK-134 bt	Bartoy	442.7	0.70407 ±1								
Bartoy kaers-dated	Bartoy	709.0	0.70408 ±1	20.09	6.02	0.181	0.51286 ±1	4.2 ±0.1	17.688 ±0.013	15.486 ±0.011	37.594 ±0.028
BK-146 gt-2	Bartoy	0.4	0.70407 ±3	1.44	1.83	0.771	0.51287 ±1	4.6 ±0.2			

Notes: Sr data are normalized to $^{86}Sr/^{88}Sr = 0.1194$ and corrected for mass fractionation using an exponential law. Replicate analyses of NBS-987 Sr yield 87Sr/86Sr = 0.710240 ± 0.000016 (2σ). Nd data are normalized to $^{146}Nd/^{144}Nd = 0.7219$ and corrected for mass fractionation using an exponential law. Replicate analyses of La Jolla Nd yield $^{143}Nd/^{144}Nd = 0.511845 \pm .000011$ (2σ). $\varepsilon_{Nd}(0)$ is calculated with $^{143}Nd/^{144}Nd_{CHUR} = 0.512638$. Based on replicate analyses of NBS-981, Pb is corrected by 0.12%/amu to account for fractionation.

Table 5.6 Sr and Pb isotopic data for BRZ anorthoclase megacrysts

Sample	location	Sr (ppm)	$^{87}Sr/^{86}Sr$ ±2σ	Pb (ppm)	$^{206}Pb/^{204}Pb$ ±2σ	$^{207}Pb/^{204}Pb$ ±2σ	$^{208}Pb/^{204}Pb$ ±2σ
p585An1	Vitim	1738	0.70398 ± 1	0.30	17.783 ± 0.008	15.516 ± 0.007	37.809 ± 0.018
p588An	Vitim	496	0.70379 ± 1	1.31	17.821 ± 0.040	15.525 ± 0.035	37.822 ± 0.086
p589An	Vitim	1365	0.70390 ± 1	0.28	17.553 ± 0.004	15.544 ± 0.004	37.678 ± 0.009
p593/1	Vitim	2666	0.70391 ± 1	0.31	17.785 ± 0.005	15.516 ± 0.004	37.799 ± 0.010
large Kandidushka	Vitim		0.70396 ± 1				
404/p	central Udokan		0.70383 ± 1	11.39	17.841 ± 0.011	15.516 ± 0.010	37.829 ± 0.024
417/1p	central Udokan		0.70377 ± 1	3.98	18.086 ± 0.021	15.565 ± 0.019	38.004 ± 0.046
K96/3	N Udokan		0.70429 ± 1	0.28	18.000 ± 0.004	15.474 ± 0.003	38.085 ± 0.009
p46/p	W Udokan		0.70386 ± 1	17.26	18.088 ± 0.010	15.496 ± 0.009	38.111 ± 0.021
p79p	NE Udokan		0.70535 ± 1	3.28	18.521 ± 0.029	15.538 ± 0.024	38.519 ± 0.060
p79/p-1	NE Udokan		0.70487 ± 1				
p86/G-p	NE Udokan		0.70425 ± 1	2.90	18.562 ± 0.015	15.530 ± 0.013	38.523 ± 0.032
p88/2	NE Udokan		0.70435 ± 1	2.55	18.536 ± 0.017	15.546 ± 0.014	38.534 ± 0.035
p197/7-p	W Udokan		0.70490 ± 1	1.84	18.328 ± 0.013	15.525 ± 0.011	38.379 ± 0.027
p270/3A	S Udokan		0.70364 ± 1				
p381	central Udokan		0.70415 ± 1	5.91	18.400 ± 0.020	15.531 ± 0.017	38.424 ± 0.042
BK146 feld#1	Bartoy		0.70397 ± 1	1.34	17.694 ± 0.002	15.471 ± 0.002	37.543 ± 0.005
BK146 feld#2	Bartoy		0.70404 ± 1	1.46	17.679 ± 0.002	15.454 ± 0.001	37.483 ± 0.003
BK128-1	Bartoy		0.70403 ± 1	1.54	17.680 ± 0.003	15.469 ± 0.003	37.522 ± 0.009

Notes: Sr data are normalized to $^{86}Sr/^{88}Sr = 0.1194$ and corrected for mass fractionation using an exponential law. Replicate analyses of NBS-987 Sr yield $^{87}Sr/^{86}Sr = 0.710240 \pm 0.000016$ (2σ). Based on replicate analyses of NBS-981, Pb is corrected by 0.12%/amu to account for fractionation.

Table 5.7 Comparison of isotopic data for BRZ megacrysts and regional volcanic rocks

REGION	MINERAL	MEGACRYST RANGE $^{87}Sr/^{86}Sr$	VOLCANIC ROCKS RANGE $^{87}Sr/^{86}Sr$
Oka Plateau	clinopyroxene	0.7036 - 0.70383	0.70380 -00.70667
Bartoy	clinopyroxene	0.70384	0.70400 - 0.70434
	kaersutite	0.70408	
	garnet	0.70407	
	biotite	0.70407	
	anorthoclase	0.70397 - 0.70404	
Udokan	clinopyroxene	0.70350 - 0.70367	0.70365 - 0.70636
	anorthoclase	0.70364 - 0.70490	
Vitim	clinopyroxene	0.70348 - 0.70418	0.70374 - 0.70494
	anorthoclase	0.70379 - 0.70398	

REGION	MINERAL	MEGACRYST RANGE ε_{Nd}	VOLCANIC ROCKS RANGE ε_{Nd}
Oka Plateau	clinopyroxene	+2.2 - +3.8	-0.44 - +3.8
Bartoy	clinopyroxene	+5.0	+3.2 - +4.7
	kaersutite	+4.2	
	garnet	+4.6	
Udokan	clinopyroxene	+4.7 - +5.4	-3.42 - +4.68
Vitim	clinopyroxene	+2.7 - +4.6	+2.32 - +7.2

REGION	MINERAL	MEGACRYST RANGE $^{206}Pb/^{204}Pb$	VOLCANIC ROCKS RANGE $^{206}Pb/^{204}Pb$
Oka Plateau	clinopyroxene	18.05 - 18.11	17.42 - 18.30
Bartoy	clinopyroxene	18.16	17.71 - 18.33
	kaersutite	17.69	
	anorthoclase	17.68 - 17.69	
Udokan	clinopyroxene	18.23 - 18.39	17.84 - 18.57
	anorthoclase	17.84 - 18.56	
Vitim	clinopyroxene	17.44 - 17.73	17.25 - 18.17
	anorthoclase	17.55 - 17.82	

Notes: Range in regional volcanic rocks from data of Harris et al., (in prep. and this thesis) and Housh et al., (in prep.).

CHAPTER 6

SUMMARY

The major scientific contributions of this thesis are:

1) *A general characterization of the geochemistry of nearly every major volcanic field in the Baikal Rift Zone, especially the generation of a new, unique set of isotope data:* This data is crucial to developing a better understanding of the evolution of continental rift volcanism. Although there are subtle systematic differences between each of the volcanic fields, the overall similarity in major, trace element, and isotope geochemistry of volcanic rocks from all areas of the rift strongly suggests that the sub-Baikal source of these rocks - the upwelling asthenosphere - is fairly uniform over a huge region.

2) *Implications for the relationship between megacrysts and host volcanic rocks:* A significant amount of effort was put into generating Sr, Nd, ***and Pb*** isotopic data for megacrysts of different mineral types. An assessment of the isotopic equilibrium between megacrysts and volcanic rocks indicates that the megacrysts are related to the lava they are erupted in, most likely having crystallized from a melt parental to their host. Subtle differences between the mineral types (i.e., clinopyroxene vs. anorthoclase) are related to the sequence of precipitation, as well as the pressure of crystallization. The fact that clinopyroxenes (and kaersutite, biotite, and garnet) all range to slightly less radiogenic Sr and more radiogenic Nd isotopic compositions than their hosts may mean

that the host lavas did interact to a small degree with the crust during their ascent. If the megacrysts are coming through the crust with their geochemistry essentially untouched, then they are the most direct sample of the source region (the asthenosphere). One of the most intriguing results is that some clinopyroxene megacrysts have an EMI-like (unradiogenic) Pb isotopic signature that is mirrored by some of the volcanic rocks. Since crustal contamination with old lithosphere would produce the EMI signature, it is not possible based on the basalt data to unequivocally say that the sub-Baikal asthenosphere may have an unradiogenic Pb isotopic signature. But since the megacrysts also have an unradiogenic Pb isotopic signature, perhaps we can more confidently believe that source region is actually unradiogenic. However, the possibility remains that the melt from which the megacrysts formed was already affected by crustal contamination.

Remaining issues

Clearly, there are many unresolved questions surrounding the evolution of Baikal Rift volcanism. This study provides a good foundation on which to build future research projects. It is necessary to increase our knowledge of all the other aspects of the Baikal Rift (field mapping, structural data, geophysical data, geochronology, etc.) in order to better understand the volcanism. Many large collaborative projects on a wide variety of problems are currently underway, so the future of research in this area appears bright.